University of Southampton

Faculty of Engineering and Physical Sciences

Optoelectronics Research Centre

Developments in the Generation and Measurement of Vortex Modes in Solid-State Lasers

by

Robin Thomas Uren

Thesis for the degree of Doctor of Philosophy

February 2019

University of Southampton

Abstract

Faculty of Engineering and Physical Sciences

Optoelectronics Research Centre

Doctor of Philosophy

Developments in the Generation and Measurement of Vortex Modes in Solid-State Lasers

by Robin Thomas Uren

We have explored several methods of generating Laguerre-Gaussian doughnut modes with the eventual application of laser processing directing our research. These modes have potential in this field due to their increasing mode steepness with azimuthal phase and their potential for carrying orbital angular momentum (OAM). A key research goal has been to obtain such modes with high purity and the ability to select the handedness of the OAM, in a system with robust potential for power scaling. All of which are key in order to fully understand the impact of these modes on laser processing.

Initially we explored intra-cavity, gain shaping methods in Nd:YAG to achieve these goals. This maintains all the advantages of power scaling normally associated with solid state lasers, and has the potential for excellent beam quality. To the best of our knowledge, however, no concrete method has been presented for selecting the handedness within the cavity. We have selectively excited doughnut modes by coupling multi-modal laser diode pump light into capillary fibres and re-imaging the fibre end into a Nd:YAG gain medium. By using a fibre with a 0.8 aspect ratio between its inner and outer radius, we would be able to select higher order doughnut modes that have a steeper intensity profile and more OAM per photon. Through this we have generated Laguerre-Gaussian 'petal' modes up to an azimuthal order of 23. These high order modes exhibit greater intensity steepness but no OAM. These modes have little practical application.

In order to better investigate what governs the selection of the OAM handedness we moved to a ring laser design pumped using a capillary fibre with a 0.5 aspect ratio. This, whilst operating unidirectionally at a single frequency, produces a doughnut mode with an azimuthal order of one and a clear pres-

ence of the helical phase and therefore OAM. This has allowed us to examine such a mode in isolation. Through this we observed that reversing beam propagation direction in the ring cavity also reversed the handedness of the helical phase. We found this effect associated with the Faraday Rotator as it is the only known non-reciprocal effect in the cavity. We also found a similar effect in the highly chiral material, tellurium dioxide. The effects were replicated in a slightly multi-modal ring laser but were not observed in a standing wave laser. Tests in free space were unable to detect this effect, so either another mechanism is responsible or the effect was too weak for our detection methods.

We therefore moved to external methods for creating doughnut modes. We chose to focus on astigmatic mode converters as these can produce perfectly pure beams unlike methods using spiral phase plates or spatial light modulators. We have developed on the previous design by Beijersbergen *et al.* by replacing the cylindrical lenses with off-axis spherical mirrors. We have also expanded the theory of mode converters to apply to off-axis spherical mirrors. The mirrors allow for greater power scaling and wavelength flexibility. The key to this is producing high purity HG_{01} modes. Initially these were produced by placing a slit in a cavity that naturally oscillated on the LG_{01} mode. However there was a significant fundamental mode impurity. We improved this by developing a Nd:YVO_4 laser cavity pumped by two separate circular pump beams. This greatly improved the output power to 175mW as well as the mode quality. This method allows for control of the OAM by rotating the HG_{01} though 90^o. Feeding this through the converter produced a high purity LG_{01} mode with negligible loss.

We also developed a diagnostic technique for analysing the purity of modes generated by a mode converter. As the most likely impurity is a HG_{01} mode from misaligning the converter this can be picked up by measuring the azimuthal symmetry of the Mach-Zehnder spiral interference pattern. A pure mode will generate a spiral with an even azimuthal intensity distribution. A HG_{01} impurity will disrupt this. This can be measured with a virtual rotating slit. Our theoretical predictions of the amount of azimuthal variation a given level of impurity will cause matched extremely well when this method was tested with a real system.

The need for high purity modes has led us to develop further diagnostic techniques to more quantitatively assess the quality of HG_{01} and LG_{01} modes.

For both modes this involves analysing its intensity profile as recorded on a CCD camera. It provides quantitative analysis of key properties of the intensity profile in order to identify impurities. For the HG_{01} mode it compares the evenness of the two intensity maxima and how close to zero the central node is. For the LG_{01} it again measures how close to zero the central null is, the circularity of the beam, and the azimuthal symmetry. Further analysis generates a matching theoretical mode to the image and subtracts it to look at the residual power distribution. This allows us to identify specific modal impurities incoherently combined with the beam and quantify them. Further work is needed to take into account of distortions created by the CCD camera itself as well as general noise.

Finally we Q switched the HG_{01} seed laser. This allowed for greater output power of 460mW without losing mode purity. It produced 24ns pulses with a 147kHz repetition rate. The pulses could be shortened further simply by shortening the cavity. Passing this through a double-pass bounce geometry Nd:YVO_4 slab amplifier; pumped with up to 55W of power we obtained an maximum amplified power of 17W. However some significant mode impurity was added as well as large amount of astigmatism. It was noticed there was damage on the amplifier crystal that may have been the cause of some of this. However amplification is clearly possible, whether by amplifying the HG_{01} or LG_{01} mode.

Acknowledgements

This PhD has been simultaneously the most challenging, engaging, frustrating and rewarding chapter of my life so far. Much like everything in this world it is not the work of one person. It is my name on the front, but the reality is I would never have succeeded without the help of many people. They receive my deepest and sincerest thanks.

First I must thank Andy Clarkson, my supervisor. Thank you for the opportunity you gave me to do this and for helping me every step of the way. Most of the ideas that seeded the work in this thesis either came from you, or from conversations between us. Also thank you for the much deeper understanding of optics and lasers you've given me.

Next I must thank my many fellow students in the research group. Di Lin, Stan Vassilev, Nikita Simakov, Antonin Billaud, Callum Smith, Henry Stenhouse, Florian Leroi, Tom Jefferson-Brain, Mark Burns, Jake Prentice, Silvia Cante and Qiyao Liu. Thanks for all the support, ideas and most importantly the trips to the pub. Particular thanks to Callum for lending me his beam propagation code that was immense help in designing and constructing the mode converter. Also to Nikita for first teaching me to cleave and splice fibres.

I'd also like to thank Sanja Barkovic and the rest of the team in the teaching labs for giving my work another dimension. It was great to relax a bit and have some fun teaching basic physics to first years. I'd also like to thank her for letting me steal bits of kit from the labs every now and again.

I'd also like to thank Bill Brocklesby and Anne Tropper who between them gave me my first taste of research and inspired me to do a PhD in the first place.

An enormous thanks goes to Tim Hoad, the machinist at the ORC. He made some exquisite mounts and heat sinks that formed the backbone of my lasers. They were always beautifully made and in astonishing time for one man serving a whole department.

I also want to thank everyone who helped proof read this thesis. My Dad, Jen, My Wife and my Mother in Law, Mel. An extra special thanks to Mel and Ian who let me bum at their house for a week whilst a wrote a good chunk of this.

I've had the pleasure of working with four post-docs in my time as a PhD, Stefano Valle, Alex Butler, Stephen Beecher and Peter Shardlow. They've all been immensely helpful and taught me more than half of what I know.

Stefano not only helped me set up my first active Q-switch but also directly sourced me the essential schematic for it. Memories of him trying to finish his thesis whilst also having two kids and working also put my own plight into perspective.

Stephen had the initial bright idea of using a prism to redirect the pump into the twin pump system. This directly led to my most important work. He also shared some great whiskey over the years and was always good for a laugh in the pub.

Next Alex gave me my crash course in building lasers and coding their theory right at the start of my PhD. We worked on everything in Chapter 2 of this thesis together and it got my name on a piece of published work for the first time. He also showed me how to build my first fibre laser in some work that unfortunately did not make it into this thesis.

And Peter, who really has taught me half of everything i know, from how to build an bounce amplifier, to design laser mounts properly, to making me better at electronics and the list goes on. He even begged and borrowed off some old friends for some equipment for the final chapter of this thesis. He's also become a good friend over the years and the best person to go to the pub with after a stressful day in the lab.

Next I must thank the scores of friends who've distracted me from the woes and celebrated the highs of this PhD with me. Particular mention to Rach, Spoon, Dave, Josh, Laura, Dev, Dan, Lizzie, Eva and the list goes on too long to write here.

I'm also indebted to my parents who always got me the books on dinosaurs and space that first got my mind whirring and showed me, though I didn't know it at the time, that I wanted to be a scientist. Particularly to my long suffering mum who had to put up with reading all those books to me.

Finally, and most importantly, I thank my wife, Caitlin. Not for convincing me that getting married and finishing a PhD in the same year would be fine (not recommended).

But for always looking after me when I'm stressed, inspiring me to do things when I could otherwise be lazy, and generally just keeping me sane and happy throughout all of this. I love her more than anything and I can't wait for our next adventure together.

Contents

Figures and Tables

List of Figures

List of Tables

Publications

[1] Butler A. C., Uren R. T., Lin D., Hayes J. R., Clarkson W. A., "Simple Technique for High-Order Ring-Mode Selection in Solid-State Lasers," *2015 European Conference on Lasers and Electro-Optics - European Quantum Electronics Conference*, Optical Society of America, June 2015.

[2] R. T. Uren and W. A. Clarkson, "Handedness of Laguerre-Gaussian LG01 Mode in a Unidirectional Ring Laser," in Conference on Lasers and Electro-Optics, OSA Technical Digest (2016) (Optical Society of America, 2016), paper STu1M.6.

[3] R. T. Uren and W. A. Clarkson,"Efficient Astigmatic Mode-Converter Based on Spherical Mirrors," in 2017 European Conference on Lasers and Electro-Optics and European Quantum Electronics Conference, (Optical Society of America, 2017), paper CA˙2˙2.

[4] R. Uren, S. Beecher, C. R. Smith, and W. A. Clarkson,"Novel Method for Generating High Purity Vortex Modes," in Conference on Lasers and Electro-Optics, OSA Technical Digest (online) (Optical Society of America, 2018), paper SW3M.2.

[5] R. Uren, S. Beecher. C. R. Smith, and W. A. Clarkson,"A Novel Method for Generating Measurably High Purity Vortex Modes" Publication Pending

List of Acronyms

HG_{00} The Fundamental Mode.

HG_{01} First-Order Hermite-Gaussian.

HG_{02} Second-Order Hermite-Gaussian.

HG_{nm}^{45} Diagonal Hermite-Gaussian Mode of Orders n and m..

LG_{01} First-Order Laguerre-Gaussian.

LG_{02} Second-Order Laguerre-Gaussian.

ACW Anticlockwise.

AM Angular Momentum.

AMC Astigmatic Mode Converter.

CW Clockwise.

DM Doughnut Mode.

FR Faraday Rotator.

LG Laguerre-Gaussian.

MOPA Master Oscillator Power Amplifier.

Nd:YAG Neodymium Doped Yttrium Aluminium Garnet.

Nd:YVO_4 Neodymium Yttrium Vanadate.

OAM Orbital Angular Momentum.

TeO_2 α - Tellurium Dioxide.

I, Robin Uren, declare that this thesis, "Developments in the Generation and Measurement of Vortex Modes in Solid-State Lasers" and the work presented in it is my own and has been generated by me as the result of my own original research. I confirm that:
1. This work was done wholly or mainly while in candidature for a research degree at this University;
2. Where any part of this thesis has previously been submitted for a degree or any other qualification at this University or any other institution, this has been clearly stated;
3. Where I have consulted the published work of others, this is always clearly attributed;
4. Where I have quoted from the work of others, the source is always given. With the exception of such quotations, this thesis is entirely my own work;
5. I have acknowledged all main sources of help;
6. Where the thesis is based on work done by myself jointly with others, I have made clear exactly what was done by others and what I have contributed myself;
7. Parts of this work have been published as the journal papers and conference submissions listed in "Publications".
Signed:

Date: 24/09/2018

Chapter 1

Introduction

1.1 Laser Fundamentals

Laser stands for light amplification by stimulated emission of radiation. The fundamentals of laser operation are well explained by both Siegman and Svelto in their respective books [1, 2]. Lasers output light that in general is of a narrow range of frequencies, and is both spatially and temporally coherent. This leads to highly directional light that will generally follow the rules of Gaussian optics. Lasers can now be created that operate on wavelengths from the mid-IR to the near-UV. The main wavelength bands being around $10\mu m$ for CO_2 lasers, $2\mu m$ for sources based around thulium and holmium, $1.5\mu m$ for erbium and erbium/ytterbium and $1\mu m$ for neodymium and ytterbium lasers. There are also diode lasers that operate from the mid-IR [3] through the visible spectrum to the near-UV [4]. Each wavelength band has different characteristics that make them suitable for various applications.

There are several distinct classes of lasers. They broadly are: diode lasers, solid-state lasers (of which fibre lasers are a distinct sub group), gas lasers and dye lasers. Dye lasers are generally less common and gas lasers, other than CO_2 lasers, have fallen out of favour due to their poor efficiency, despite high beam quality. Diode lasers represent the most efficient form of laser in terms of electrical to optical power conversion. Nevertheless, to reach high power they need to be stacked into arrays. This allows them to reach staggering peak powers in the multi MW level [5], but compromises beam quality. They are therefore often utilised to pump solid-state lasers, effectively making the solid-state laser a brightness converter, by improving beam quality and changing the characteristics such as wavelength and pulse duration, in exchange for power. Diode lasers have been steadily replacing flash lamps as a pump source for solid-state lasers due to the improved efficiency and beam quality they provide. Solid-state lasers are used very broadly in manufacturing, communications, sensing and many other applications. The recent advent of fibre lasers

has greatly increased the robustness and beam quality of high power laser sources. Solid-state lasers make excellent pulsed sources due to their high levels of energy storage [6].

This thesis is primarily concerned with solid-state lasers that are pumped by diode lasers. *Fig. 1.1* depicts a typical blueprint for such a system. Many variations on this are possible for any given application, however this serves as a good basis.

IC is the input coupler, it is a highly transmissive mirror at the pump wavelength and highly reflective to the lasing wavelength. This is sometimes replaced by an optical coating grown directly on the gain medium. For side pumping or other non end-pumping geometries this will simply be a highly reflective mirror. OC is the output coupler, a mirror that is partially transmissive at the lasing wavelength. The lens is needed to provide cavity stability so that a mode will be self replicating about the cavity. Sometimes the lens is combined with the IC or OC as a spherical mirror; alternatively the thermal lens of the gain medium can be used to stabilise the cavity. These optics form the cavity; which is the feedback mechanism for the amplification. The final part is the gain medium. This will generally either be crystal or glass, doped with a rare earth or heavy metal ion that has an energy band structure suitable for lasing. This medium can take many different geometries which have dramatic impact on the laser's performance. Note that when the gain medium is an optical fibre, both the OC and IC are often, though not always, replaced by either fibre Bragg gratings, or the Fresnel reflections at the ends of the fibre. The cavity stabilisation lens is replaced by the guiding properties of the fibre. There may be many more optics added to a cavity for a variety of purposes; such as frequency, polarisation or transverse mode selection. They may also be added for greater control of the cavity mode size or to enable pulsed operation.

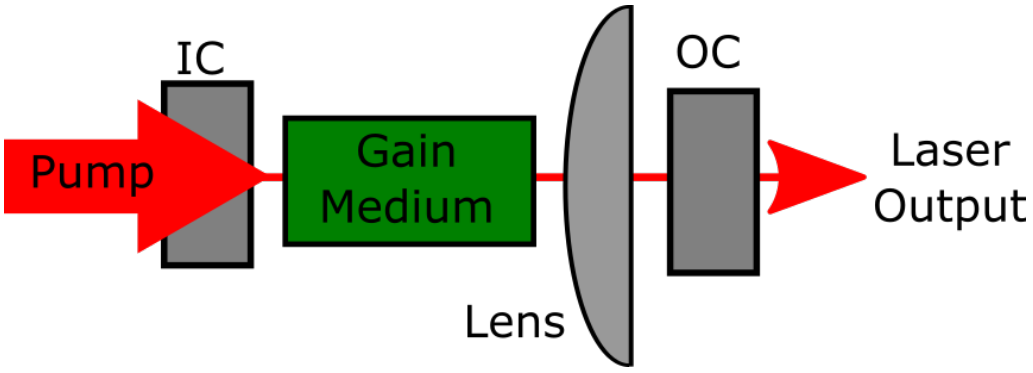

Figure 1.1: A general schematic for a solid-state laser. Sometimes these optics can be combined or more optics may be added. The pump can be transferred to the gain medium in a variety of ways depending on the laser geometry.

For a material to behave as a laser gain medium it needs to create a population inversion. This is where there are more electrons in a higher energy state in an atom compared to lower one. This is thermodynamically impossible between two energy levels when taken in isolation. This is because the rate of absorption per electron in the ground state, and stimulated emission per electron in the excited state is always the same. A population inversion can be made to arise, however, when more than two energy states are considered. There are two main categories where this occurs: 4-level and 3-level gain media. Most of the lasers we consider in this thesis are 4-level systems, we show a diagram of this in *Fig. 1.2*. Initially an electron is excited by incoming pump energy to an excited, unstable energy level. This can be done by either an electron (typically in a diode laser), or a photon of the correct energy. This decays non-radiatively to a meta-stable energy level, $n2$. $n2$ has a radiative decay to another unstable energy level, $n1$. This second unstable state decays non-radiatively back to the ground state. As electrons build up in $n2$ a population inversion occurs between $n2$ and $n1$, meaning that stimulated emission between this and the second unstable level out-paces absorption. This makes the gain medium an amplifier for the energy of light equivalent to the energy gap between two levels. By providing a feedback mechanism that allows for this energy of light to exactly retrace its path through the gain medium we can create a laser. The wavelength of the light must also be equal to an integer multiple of the distance the light travelled to return to its starting point. A 3-level laser is identical to the 4-level except that the second unstable energy level is replaced by the ground state. This gives 3-level lasers higher thresholds before lasing will occur as half the electrons in the ground state need to be excited simultaneously before a population inversion will occur. A third hybrid gain medium known as a quasi-3-level system is also common. This is a system where the lower lasing energy level lies so close to the ground state that thermal effects at room temperature must be taken into account. This means that it and the ground state cannot be treated separately as in a 4-level system, but nor does this state have to be 50% depleted for lasing to occur as in a 3-level system.

1.2 Background on Lasers Applications

Lasers are widespread and thoroughly integrated in modern society. They are key to many aspects of the modern world including manufacturing, remote sensing, communications, scientific research and many more [7, 8, 9, 10]. This thesis will focus on the development of lasers with non-Gaussian spatial distributions, with the ultimate application of materials processing in mind. However, there may be many other potential applications in the fields of communications, optical tweezers and exotic plasma interaction.

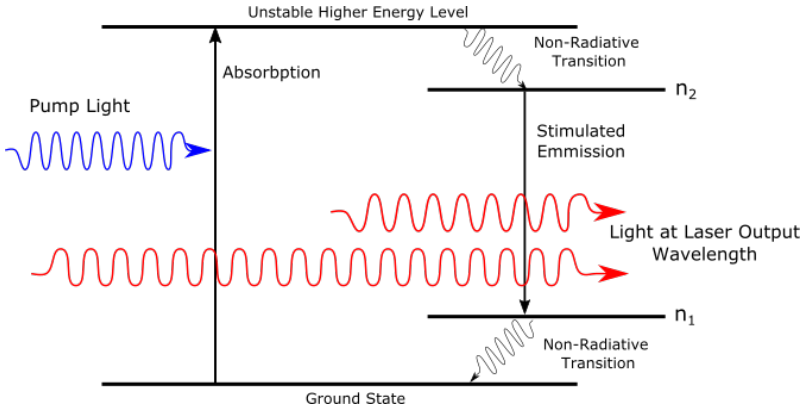

Figure 1.2: This demonstrates the energy levels present in a four level laser material, e.g. Nd:YAG. Pump light excites electrons from the ground state to the 'unstable higher energy level' which quickly decays to n_2. This is quasi-stable and builds up the population inversion over n_1 which is unstable and non-radiatively decays to the ground state.

The laser processing of materials now stands as a multi-billion dollar industry [8]. The laser's potential in this area was clear from its first demonstration in 1960 [11, 12] and has developed successfully ever since. Lasers are effective in many processing areas including welding; drilling; cutting; deposition; surface treatment; annealing; and many more [13]. They are attractive for machining as they can have a small cutting kerf (width of cut) compared to mechanical methods, are simple to automate and can have high precision allowing for more complex cutting profiles and smaller features. They have also given rise to many forms of 3D printing [14, 15]. The use of ultra-short pulses allows material to be removed through ablation, a non-thermal process that can have significant advantages such as not detonating explosive material, removing material transparent to the wavelength being used, or a reduction in the heat affected zone (HAZ) that weakens the material being processed. [16, 17]. Brittle ceramics can also be machined with lasers without the fractures often caused by mechanical shock in conventional processes [18, 19]. This has allowed for both the supplanting of old techniques for machining as well as the development of new and novel ones.

This broad range of benefits can be attributed primarily to the equally broad range of laser designs possible. Wavelength, polarisation, spot size, pulse length and power are all readily customisable and have a dramatic effect on a lasers interaction with materials [20]. Historically the two main classes of laser used for machining have been CO_2 gas lasers and neodymium doped yttrium aluminium garnet (Nd:YAG) solid-state lasers. However, recently many more lasers have been utilised. This includes Ti:Sapphire ultra-fast pulsed lasers used for micro-machining [21, 22, 23]. This offers high precision and the ability to employ 3D internal structuring due to the highly localised ablation delivered by the

ultra-short pulse. It can also allow for machining without the need for post-processing [24]. $2\mu m$ lasers, primarily based on thulium gain sources or optical parametric amplifiers, have seen substantial interest in recent years [25, 26, 27]. The main focus has been in machining semi-conductors, which are transparent at such wavelengths allowing for 'back-side' machining. Furthermore, there has been a general trend away from bulk solid-state lasers towards fibre lasers [28, 29, 30]. The main advantage of this architecture has been the ease of achieving high quality single mode output at high power. This has removed much of the compromise between laser power and beam quality, typically associated with solid-state lasers. In addition they exhibit greater energy efficiency, are more compact and, in an all fibre design, require minimal alignment.

As the cost and efficiency of lasers has improved, so has the specialisation of machining applications. This has led to interest in lasers with more niche attributes. This thesis seeks to investigate the potential for generating two of these attributes at machining powers. The transverse distribution of the light intensity in the form of doughnut modes (DMs) and the presence of orbital angular momentum (OAM) within the beam. Both of these have potential in the application of laser processing, as well as several other domains.

1.3 An Overview of Higher Order Transverse Modes

Modes represent a waveform that is stable over time. In the case of laser cavities these are distributions of electromagnetic waves that are self repeating upon one round trip of the cavity. As these form a complete set, all laser outputs can be described as a superposition of these modes. In general, each mode (unless they are degenerate with another mode) is a unique longitudinal mode. A longitudinal mode is defined by its wavelength, which must be an integer multiple of the round trip length of the cavity. If this is not the case the mode will be out of phase with itself after one round trip and destructively interfere. The frequency spacing of modes within a cavity is defined by the free spectral range of the cavity.

$$\Delta\nu_{FSR} = \frac{c}{nL} \tag{1.1}$$

$\Delta\nu_{FSR}$ is the free spectral range of the cavity in terms of frequency, c is the speed of light in a vacuum, n is the average refractive index of the medium within the cavity and L is the round trip length of the cavity. Each longitudianl mode will also be an allowed transverse mode of the cavity. These are often all the same transverse mode (e.g. every longitudinal mode being in the same fundamental transverse mode) however each longitudinal mode will select its transverse mode independantly and can therefore be different. The transverse mode defines the beam's electric field distribution in the plane orthogonal to the

modes propagation. This gives each transverse mode a different cross sectional intensity. They come broadly in three sets for free space lasers: Hermite-Gaussian (HG) for systems that have rectangular symmetry, Laguerre-Gaussian (LG) for those with cylindrical symmetry, and Ince-Gaussian for elliptical symmetry. This thesis is primarily concerned with HG and LG modes and will ignore Ince-Gaussians. Each set is a solution to Maxwell's equations when applied with the boundary conditions of a laser cavity (for a full derivation see [1]). HG and LG modes both form an infinite set of solutions, with each transverse intensity profile being denoted by two discrete parameters.

For HG modes their defining parameters are denoted m and n and represent how many nodes (points of zero intensity) there are along the x and y axis respectively. HG modes occur in systems with rectangular symmetry. LG modes occur when cylindrical symmetry is present and are denoted by p, which is one less than the number of bands of radial intensity, and l, which denotes how many times there is a full 2π phase shift about the central axis [31]. This is written as HG_{mn} and LG_{pl} respectively. See *Fig. 1.3* for images of the lowest few orders of these beams.

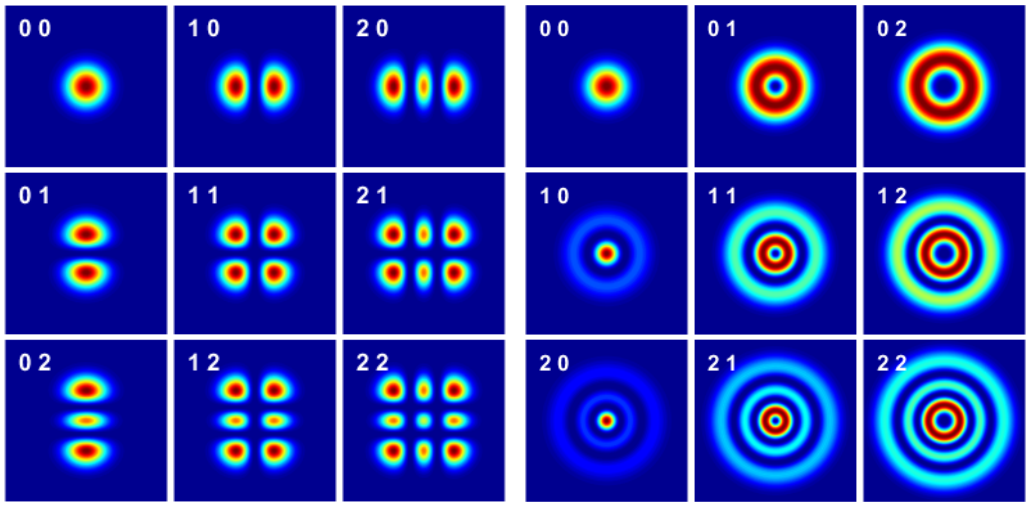

Figure 1.3: (a) The transverse intensity distributions of the nine lowest order HG modes. The first number is the order in x (m) and the second in y (n). *(b)* The transverse intensity distributions of the nine lowest order LG modes. The first number is radial order (p) and the second is the azimuthal order (l). All images are for the same wavelength, and are imaged from the same distance at from the beam waist. Notice that with increasing mode order you get increasing beam diameter and how the lowest order for both Hermite and Laguerre-Gaussian beams are identical. It is therefore often referred to simply as the fundamental mode.

We can define the total mode order, N, of a beam as

$$N = m + n = 2p + l \tag{1.2}$$

N is related to the beam propagation factor, M^2, in that for and ideal beam the M^2 will equal $N+1$. The M^2 is a dimensionless value that is invariant upon propagation and relates the beam's half-angle divergence, θ, to its beam radius at a waist, w_0.

$$\theta = M^2 \frac{\lambda}{\pi w_o} \tag{1.3}$$

where λ is the wavelength. The smallest M^2 value possible is 1 which corresponds to the M^2 of the lowest order Gaussian beam (for a full description of Gaussian beams see [1]). For pure higher order modes the M^2 is given by

$$M^2 = N + 1 \tag{1.4}$$

For a given wavelength and beam waist, the M^2 denotes how fast a beam will diverge relative to the fundamental mode. Beams can have different M^2s along different transverse axes, particularly in the case of HG_{mn} modes which have a minimum M^2 along the x and y axis of $2m+1$ and $2n+1$ respectively. True LG modes have an even M^2 about all axes due to their cylindrical symmetry.

1.4 Review of the Literature

1.4.1 Angular Momentum Within Light

Vortex modes are a subset of LG modes that carry innate Angular Momentum (AM). This is due to their helical phase pattern creating orbital angular momentum (OAM) [32]. In a pure vortex mode, the amount of OAM is equal to $l\hbar$ per photon. The electric field of the vortex mode resembles a helix; its handedness corresponding to the handedness of the OAM. Their are however other forms of LG modes that do not contain OAM, some of which will be discussed later in this thesis. OAM is contrary to the spin AM found in circularly polarised beams that is due to the accumulated spin of individual photons, as demonstrated by Beth *et al.* [33]. OAM, unlike spin AM, can be extrinsic rather than intrinsic to the beam [34]. This means that for AM associated with the polarisation of the beam its value is independent of what axis the AM is measured along, i.e. it is only dependent on the intensity of the beam. Phase generated AM however, will vary depending on the axis of measurement. For example, if one part of the beam is apertured out compared to another, a different AM vector will be measured. The cylindrical symmetry of LG modes mean that the value obtained is only dependent on the radius from the beam

centre and the beam intensity. Practically, this means that when spin AM is transferred to an object it will rotate about its own centre of rotation. In contrast, transfer of OAM will rotate an object about the centre of the beam, provided the object is smaller than the beam itself. A larger object will rotate about its own axis in both cases. It is in this situation that OAM could also be said to be intrinsic [35].

A key additional point to consider is that not all doughnut shaped intensity distributions are vortex modes. It is possible to construct an identical intensity distribution from either a coherent or incoherent superposition of several different modes [36]. If we take the first order LG mode as an example, the LG_{01} mode, we find that it can be de-constructed into two orthogonal first order HG modes, the HG_{01} and HG_{10} modes, see Section 5.2. Depending on the polarisation state and phase delay between these we get different first order LG modes. This is illustrated in *Fig. 1.4* Summing these modes with aligned polarisation and no phase delay gives a HG_{01} mode at 45^0 to the principle axes. Summing them with a $\pi/2$ phase shift give a vortex mode. If they have exotic polarisation states with each lobe having opposing polarisation they can be summed to form either a radial or azimuthal mode. These contain no OAM. Finally, two first order vortex modes with opposite handedness, but the same polarisation, can be summed to make a 'petal' mode. See *Fig. 1.5* for examples of these at higher orders. If two of these, where the two pairs of vortex modes are π out of phase with each other to form petal modes rotated by $\pi/2l$, are summed, either coherently or incoherently, we obtain a first order LG mode with no OAM and the polarisation of the original vortex modes [36]. This list is not exhaustive, but we can already see that there are many modes with vastly different properties that have identical intensity distributions. This highlights the need for careful diagnoses of any given LG mode produced in order to identify its true nature. It also requires careful definition of what exactly constitutes an LG mode. Here we will use 'LG mode' as a broard term that encompasses all modes with a doughnut shaped profile, and then specify whether we are talking about, for example, a vortex or radial DM, when this is relevant.

1.4.2 Doughnut Modes and their Applications

LG modes with an $p = 0$ and $l \geq 1$ form a ring-shaped cross-sectional intensity (see the first row of *Figure 1.3b*). They are commonly referred to as Doughnut Modes or DMs. They are of interest for a variety of applications including machining, optical trapping, driving micro-machines, quantum information processing, communications and plasma interactions [15, 35, 37, 38]. Optical trapping with a typical Gaussian beam traps a transparent particle in the peak intensity region using the gradient force. However, for absorbing particles, the scattering force can destabilise these traps. Therefore DMs are useful as they

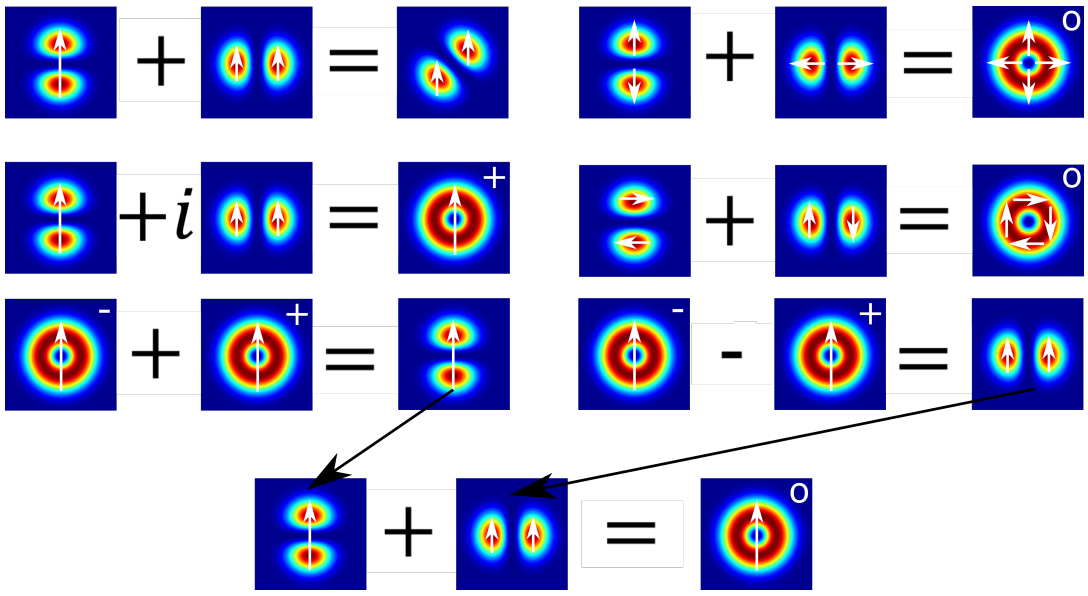

Figure 1.4: Shows how HG_{01} and HG_{10} modes can be summed coherently to form different first order doughnut modes depending on their phase relation and polarisation. The white arrows indicate polarisation direction. The '+' and 'minus' indicate the first order LG mode has OAM and its handedness, a 'o' shows the mode has no OAM. We also show how vortex modes can be summed to form first order HG modes, and then how these can be summed to form an LG mode with no OAM.

can hold absorbing particles more stably in the central intensity null. Here the scattering force is used to trap the particle, as the higher intensity around the central null pusehes inwardly on the object [39]. Furthermore the OAM and spin AM of DMs can be transferred to small particles [40]. It was in this discovery that the transfer of OAM to matter was first accurately measured [35]. OAM and spin AM can transfer separately, with birefringent materials only interacting with spin AM, whereas absorbing particles can also have OAM transferred to them [34]. This transfer of AM has several applications including driving micro-rotors. These are useful for measuring viscosity in fluids or as a pump or mixer in microfluidics [37]. The hollow core of DMs has been theorised to both trap and compress particles when interacting with plasma [15]. The steeper intensity profile of DMs has also been theorised to increase the efficiency of second harmonic conversion in plasma [41]. There are also many applications to communications, mostly concerned with using the OAM of a beam as method to encode data. This has potential in both the fibre and freespace domains [42, 43, 44]. There have also been indications that OAM beams may be more resistant to turbulence. This is of particular interest to free space communications [45].

The interest in DMs for machining comes from three areas: their potential to be radi-

ally or azimuthally polarised due to their intensity null in the centre, their ability to carry OAM as well as benefits from their annular intensity profile.. We also hypothesise that the steeper intensity profile of DMs might reduce the extent of the heat effected zone (HAZ). Radially and azimuthally polarised beams, as well as hybrids between them, form a set of modes often known as 'cylindrical vector modes'. It should be noted that any method of creating a radially polarised mode (henceforth referred to as a radial mode for brevity) can easily be converted to another cylindrical vector mode with the use of an optical rotator [46]. It is important to note that, in general, radial modes and those containing OAM are distinct. Most ways of producing a radial mode will not create the helical phase of a vortex mode and most ways of generating a vortex mode will have a spatially invariant polarisation. The recent development of S-waveplates, however, imparts both a phase delay and alters the polarisation state of an input fundamental Gaussian mode from circular to radial [47]. One should note that this does produce a pure LG_{01} mode. Finally, a mode with a doughnut shaped profile may not exhibit either cylindrical vector polarisation or OAM.

The annular shape of DMs has several advantages for machining. The annular shape spreads the region of peak power over a larger area for the same beam size compared to a Gaussian beam. The central intensity null also reduces the thermal stress in the centre of the irradiated area [17]. This has application in glass bending [48]. This more even heating can also be useful when working with materials which have a narrow processing temperature band (i.e. too high a temperature will cause damage and too low will fail to enact the desired process) [49]. Hnatovsky *et.al.* have demonstrated a novel machining technique using ultra-short pulses of DMs in order to create micron sized rings in silica. These modes exhibited OAM, though it is unclear if this had an effect upon the machining process.

Polarisation has recently been gaining attention as a property that is important to materials processing, due to the different absorption coefficients of S (perpendicular to the plane of incidence) and P (parallel to the plane of incidence) polarised light on an angled surface. In general, this means P-polarised light is absorbed more strongly during laser processing [50, 51]. One might expect linearly polarised light to be favoured for processing, however this is sub-optimal if the cut is multi-directional. Therefore circular polarisation is favoured for its cylindrical symmetry to maintain an even cutting speed. Niziev and Nesterov have theoretically demonstrated that radial polarisation holds significant advantages in the laser processing of metals [52, 53]. Radial polarisation maintains the cylindrical symmetry of circular polarisation, but with the leading edge of the cut always being P-polarised. They theorised that radial polarisation would provide a $1.5-2$

factor improvement in cutting efficiency, defined as the product of cut depth and velocity, compared to circular polarisation. This was then confirmed by Ahmed *et al.* who demonstrated a 50% improvement in efficiency using a radially polarised CO_2 laser [54, 55]. Allegre *et al.* also showed an improvement using a femotosecond laser [56]. Furthermore radial polarisation has shown to be more efficient at shallow bore drilling [50], whilst azimuthal polarisation, due to its lower absorption in the bore side-walls, is better for deeper drilling [24].

There have also been some interesting preliminary studies on the effects of OAM on machining. A vortex mode, with a one micron wavelength, was compared with an equivalent doughnut shaped beam without OAM in the ablation of tantalum [57]. The non vortex beam was not a true mode, being produced by a crude free space diffraction technique. However, it had a similar intensity profile to a true vortex mode and is a valid substitute. It has been shown that both the ablation threshold was lowered and the surface quality was improved when the vortex beam was used in comparison with the non-vortex mode. As the presence of OAM is the greatest difference between these modes, it is assumed to cause these improvements. The smoothing in particular is thought to be from the OAM transferring to the ablated material.

Studies on the ablation effects of picosecond vortex pulses on silicon found that a nanostructure needle formed. This was located within the intensity null of the pulse [58, 59]. The needle reached a height of approximately $40\mu m$ when a region was hit with multiple pulses. Furthermore, the needle appeared to inherit a chirality linked with the OAM of the beam. With more research this could be an effective method of producing novel silicon structures. This could potentially provide needle tips applicable to microscopy that would allow for nano-scale measurements of the chirality and optical activity of molecules. A similar structure had previously been generated in tantalum using the same method. [60]. The needles produced exceed $10\mu m$ in height and were reproducible into a 5 x 6 array of needles. Chirality linked with the OAM was demonstrated in a later paper [61]. Similar structures were also generated in thin silver films on a glass substrate with nanosecond pulses at $512nm$ [62]. By using a unique property of the S-waveplate used to generate their vortex modes, in which two optical vortices with opposite handedness are created, they were also able to simultaneously generate two needles with opposite chirality.

A recent study has shown the writing of sub-diffraction limited features with vortex modes in silver containing glass [63]. It was shown that the size of these features was minimised when the OAM and spin AM were aligned (i.e. the mode is circularly polarised in the same direction as its helical electric field distribution). This is thought to be because,

when focused beyond the paraxial limit, the aligned spins maintain the central intensity null as compared to other polarisations. Whether this is only the case when vortex modes are generated impurely by spatial light modulators (see Section 1.4.3) or is more general, is unclear.

In all the above examples a spiral phase plate, spatial light modulator or S-waveplate were used to produce the vortex mode. These are all impure methods, meaning the beam did not contain the maximum $l\hbar$ per photon of OAM. With better mode quality these effects may be enhanced.

1.4.3 Generating Doughnut Modes External to the Laser Cavity

The main hurdle in developing a technology using DMs for machining is obtaining high enough power. Traditionally DMs have been made external to the laser cavity by converting another laser mode, normally the fundamental or HG_{01} mode, into a vortex mode. This can be done via a spatial light modulator (SLM) [34, 36, 37, 40, 56, 64, 65, 64], a spiral phase plate (SPP) [57, 66, 67, 68, 69] or an astigmatic mode converter (AMC) [58, 70, 71, 72, 73, 74, 75]. The former two have limited efficiency as they cannot create an analytically pure vortex mode as they only act upon the phase of the beam, not the amplitude. A simplified way to look at how an SPP works is that they take the electric field of a fundamental mode and multiply it with a 2π azimuthal phase shift.

$$E^{00}_{HG}(r, \phi, z) \text{ x } e^{i\pi\phi} = E_{SPP} \tag{1.5}$$

Here $E_HG^{00}(r, \phi, z)$ is the electric field the fundamental mode in cylindrical coordinates: radial displacement r, azimuthal angle ϕ and z. Clearly, if we assume the SPP to be 'thin', the beam's intensity immediately after the SPP must be close to a fundamental mode. The central intensity null is then created by destructive interference in the centre of the beam [76]. This beam can be a reasonable approximation of the LG_{01} vortex mode in some planes but will change upon propagation. This can mean a degradation of the mode in the far field as it scatter into higher order LG_{nm} modes [75]. A similar process is undergone when vortex modes are created via SLMs. As LG modes form a complete set of helical modes we can describe the outputs of SPPs and SLMs as a superposition of them. In this view, SPPs have a maximal theoretical power transfer to the LG_{01} vortex mode of 78.5% [66, 67, 77]. Another analysis suggests by having the beam waists of the input the output mode be different sizes, one could yield a conversion efficiency of 97.3% [78]. How this would be physically possible to manifest in a real system though is not stated nor experimentally demonstrated. Spatial light modulators, whilst theoretically capable of creating more pure vortex modes, using the same analysis with LG_{nm} modes as complete

a set of helical modes, with purity up to 93% [79]. The beams presented in this paper however do not appear to have this level of purity. Futhermore, SLMs have power handling and efficiency limitations which restrict their use for machining applications. They are also high cost and produce a pixelated output. Furthermore both SPPs and SLMs are wavelength dependent. This can lead to issues with chromatic aberration when working with pulsed lasers, where a broad bandwidth is required [80].

AMCs extend the phase change over a protracted distance allowing for perfect mode conversion of a HG mode to its corresponding LG mode. They are alignment-sensitive and, to our knowledge, have yet to be applied to a laser processing application. We however believe they have great potential. AMCs will be discussed in detail in Chapter 5.

1.4.4 Generating Doughnut Modes Within a Laser Cavity

An alternative route to generating DMs is to create them directly within a free-space laser cavity. This requires the desired mode to have the lowest threshold within a laser cavity compared to all other modes. This can either be done through gain shaping or loss shaping. In gain shaping one tries to match the spatial distribution to the gain to the shape of the desired mode. In the case of DMs this would be a ring. As the desired mode can spatially access more of the gain than other modes it will have a lower threshold provided the cavity losses are equal. In loss shaping one creates additional loss for modes that would otherwise have a lower threshold than the desired mode. A common application of this is to use a scattering or absorbing spot in the centre of a cavity optic to suppress the fundamental mode. Loss shaping has inherent issues in that there will be gain that cannot be spatially accessed by the main cavity mode. This increases the possibility of other spatial modes oscillating off this unused gain; particularly when the gain is high. The two methods can be combined.

Gain and loss shaping to select transverse modes has been implemented via several methods in bulk solid-state, gas and microchip lasers. DMs have been demonstrated using low-reflectivity regions in the centre of cavity mirrors to force a higher loss for the Gaussian mode [63, 64, 81]. These are often created by simply damaging the mirror. The cavity mode size is then adjusted so the damaged spot is similar in size to the desired mode's central intensity null. This has allowed for modes up to LG_{03} to be generated. However, pushing for higher orders has given rise to 'petal' modes. These are a coherent superposition of two vortex modes with the same mode order but opposite handedness. Here the mode resembles a ring made of a number of lobes equal to twice the azimuthal order, l. These modes contain no OAM provided the contribution from each handedness

is equal. Examples are shown in *Fig. 1.5*. We also show a mode with unequal amounts of each handedness producing a petal mode with wider petals. This contains a limited amount of OAM. Losing both their OAM content and cylindrical symmetry these modes are generally unsuitable, or give no advantage over fundamental mode, for most applications such as: laser processing, remote sensing, optical tweezing, optical communications, etcetera.

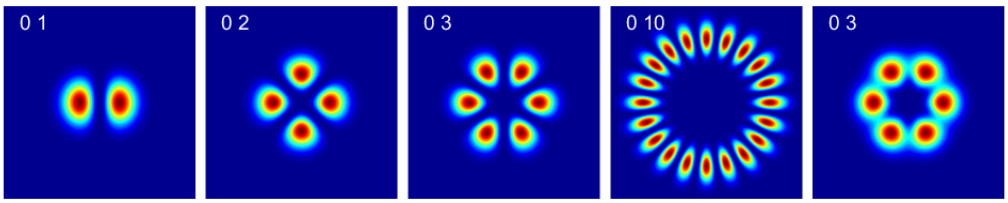

Figure 1.5: Theoretically generated images of petal modes. The examples here are the intensity profiles that result from superimposing both senses of azimuthal phase for the LG_{01}, LG_{02}, LG_{03}, and LG_{010} modes; resulting in petal modes. The final image is a LG_{03} vortex mode combined with the same mode with the opposite handedness but at less power.

In general, gain shaping, rather than loss shaping, has been the more popular method for selecting specific transverse modes. Naidoo *et al.* have also demonstrated DMs in microchip lasers by shaping the pump with a π phase plate to reshape a pure Gaussian pump beam [64]. The plate reformats the pump into a rough ring shape by creating a π phase shift in the centre of the collimated pump. This achieves a reasonable LG_{01} mode. Chen *et al.* have also created DMs in a microchip laser by defocusing the output from a fibre coupled laser diode in order to produce a ring shaped pump profile [82]. This allowed for the creation of very high order 'petal' modes up to $LG_{0,23}$.

Shimohira *et.al.* have found a novel, if highly inefficient method of generating low order LG_{0l} modes in an Yb:YAG disk laser [83]. This was done by pumping the disc with two collimated fibre coupled diodes through the thin edge of the disc, rather than the main face, orthognal to each other. Then by adjusting the overlap between the two beams, i.e. changing the height of the two beams relative to the main face, they found they could switch between exciting high order HG_{0n} modes and the LG_{01} mode. Another novel method that allows for switching between an LG_{01} and Gaussian mode through a double resonator has been developed by D. J. Kim and J. W. Kim [84]. A rough schematic of their set-up is shown in *Fig. 1.6*. Here the cavity is split into two arms that share the same gain medium by using a polarising beam splitter. Both cavities are designed to support the fundamental and LG_{01} modes. In one arm the output coupler (OC) has a higher reflectance giving it a lower threshold, this is the secondary arm. When an aperture

is closed in this arm only the fundamental mode is supported. This saturates the gain in the central region of the laser crystal, causing the other arm to oscillate on the LG_{01} vortex mode. This was reasonably efficient with a 32% slope efficiency at $1.62W$ of output power. By narrowing an aperture in the primary cavity (with lower reflectivity OC) and closing the one in the secondary, a fundamental mode output is produced with 40% slope efficiency and $2.21W$ of output. However, significant power is lost in the output of the secondary cavity. With the secondary cavity closed off and the primary aperture open, a multi-mode output is produced with 44% efficiency and $2.74W$ output. This efficiency loss could be an issue for commercial applications. However, this may be acceptable in an application where rapid switching between the Gaussian and LG_{01} modes is desirable.

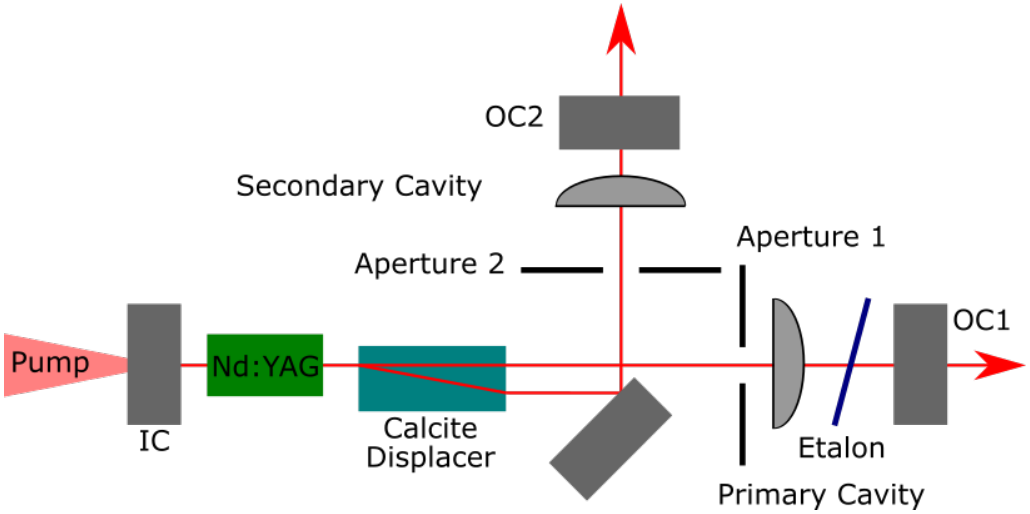

Figure 1.6: Schematic of the laser built by Kim *et al.*. OC2 has a higher reflectivity, both cavities support both the HG_{00} and LG_{01} mode. The apertures can be opened, narrowed or closed to select between the two modes.

Finally, there have been many papers published on the use of capillary fibres to excite DMs within solid-state lasers. Here a multi-mode laser diode is coupled into a capillary fibre. This can be done either through a taper or by focussing the diode output into the wall of the capillary fibre. The output from this is doughnut shaped near the fibre tip before diverging into a top hat profile. However, by using a $4f$ imaging system, see *Fig. 1.7*, the doughnut shape can be re-imaged into a laser crystal. Kim *et al.* have demonstrated this technique for producing DMs up to LG_{03} [85]. No attempt was made to detect the presence of OAM, so these modes may well be the superpositions or petal modes described by Litvin *et al.* in [36] (see Section 1.4.1). More recently Dietrich et al. have used capillary fibres to generate an LG_{01} mode at up to 107W output powers in a Yb:YAG disk laser with radial polarisation [86]. The polarisation was enforced by a mirror that had a higher reflectivity for radial polarisation than other states. The additional interest here was an

improvement in slope efficiency due to apparent better thermal properties. It is thought that as the maximum intensity is spread over the ring rather than concentrated within a central point, as with a fundamental mode, this reduces thermal lensing and makes heat extraction more efficient. This is obviously of interest for machining applications as better thermal efficiency will reduce running costs and limit long term damage to the laser from thermal stress.

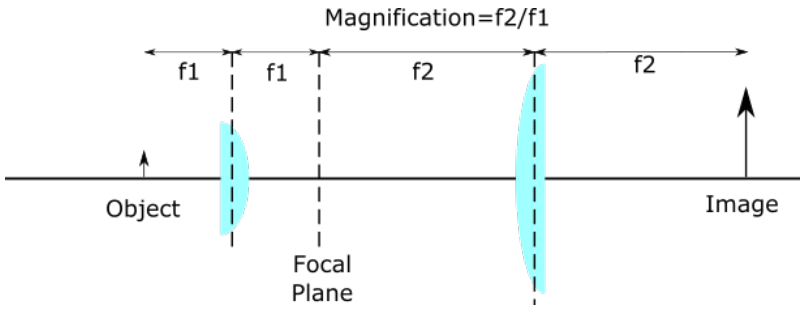

Figure 1.7: Schematic of a $4f$ lens system. This re-images light from the focal plane of $f1$ to the focal plane of $f2$. Copying the image exactly but with a magnification factor of $M = f2/f1$.

One common problem with all methods of generating vortex modes within a cavity is that though no control of the handedness is possible. Often a mode with a measurable sense of handedness is produced but why this was selected over the other handedness is unclear. Furthermore it is possible both handednesses are present in different amounts and are incoherently superimposed. This means the selection of handedness in the system is likely due to small loss differentials of unknown origin. This is evidenced by the ability to alter the apparent balance of handedness by misaligning mirrors [63].

This method of misaligning mirrors has been extended by Kim *et al.* by inserting a tilted etalon into the cavity [87]. They constructed a simple two mirror cavity pumped by a capillary fibre to select for the LG_{01} mode. Initially, they showed this to be operating on two longitudinal modes that were unstable over time. However, the superposition of the two appeared consistent over time. Neither of the longitudinal modes exhibited a clear handedness so we can conclude the cavity was producing something akin to the superposition of petal modes described by Litvin [36]. They then inserted a tilted etalon into the cavity and observed a clear handedness. Furthermore, the handedness could be switched by tilting the etalon. As the electric field in the cavity resembles a helix, they argue that this causes a different loss for each handedness of the helix due to its interaction with the Poynting vector. This result has been replicated by Liu *et al.* [88]. We can, however, think about taking the whole laser cavity and inverting it space (i.e. flipping it upside-down), this is equivalent to tilting the etalon. This therefore should not change the physics of the

laser cavity and select handedness as it violates symmetry arguments. We can therefore assume that this situation is similar to handedness selection by misaligning mirrors, in that it changes the path of the intra-cavity mode to interact with different unknown loss differentials that select the handedness.

The work done by Lin *et al.* has conclusively generated 1^{st} order vortex modes with controllable handedness [89]. This has been achieved through use of novel aluminium strips as a mode selector that exploits the physical distinction between the two senses of phase having oppositely 'twisted' standing wave patterns. The standing wave pattern for a LG_{01} mode is a HG_{01} mode rotating through 360^o every wavelength. However, the direction of the orbital angular momentum dictates which way, clockwise or anticlockwise, the mode rotates. In this way by aligning two strips, that are narrow enough to fit in the intensity null of the HG_{01} mode, at 45^o to each other and $\lambda(n + 1/4)$ apart, where n is an integer, we can create differential loss between the two modes. This works, as for one sense of the phase, both of the strips are going through the intensity null and present minimal loss, whilst for the other, one strip causes a loss as it lies across the two intensity maximums, see *Fig. 1.8*. Whilst this technique has been successful for the lowest order DM, it is unclear whether it will work for higher order modes. This is both because a 'petal' mode has petals equal to twice its azimuthal order; and that the whole electric field distribution rotates l number of times per wavelength. Therefore, the angular difference between the two nano strips will need to decrease by a factor of four per l and the sensitivity in their separation will double. Furthermore the standing wave will have more transverse nodes as it will resemble a higher order HG mode. This means the strips will need to be located off axis, more than one may be needed in each location and the strips will need to be thinner for the same mode size. All of this would present significant engineering challenges. It therefore seems unlikely that this will be practical outside a laboratory environment.

1.5 Doughnut Modes in the Literature

In order to highlight some of the current difficulties in generating high quality DMs we present a selection of LG_{01} beams that have been published in the literature, *Fig. 1.9*. These modes have been produced by different researchers, at different times by different methods. First we can see that it is much easier to observe the quality of the beam in the false colour images. We will therefore endeavour to present all our measured beams in false colour for clarity (we present spiral interference patterns in grey scale as we feel this makes their from easier to identify). The beam produced by Volyar *et al.* in *Fig. 1.9a* is of reasonable quality, there is some interference structure in the mode and an apparent dip in

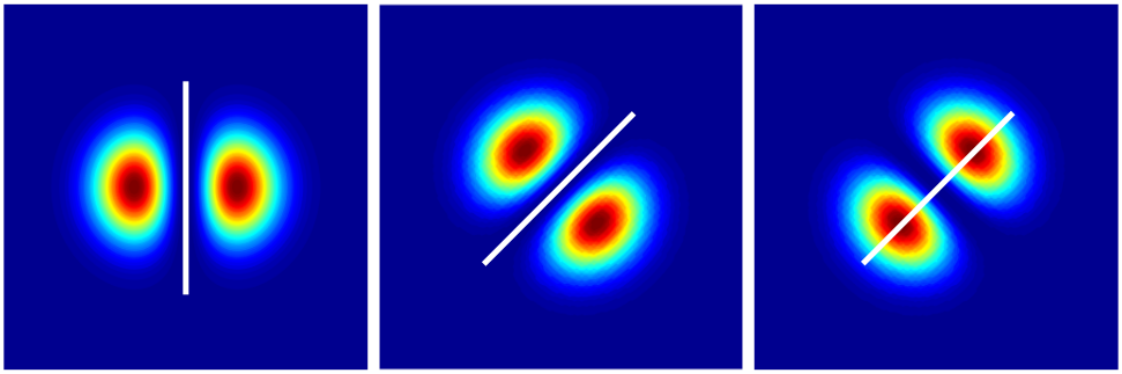

Figure 1.8: This demonstrates the technique used in [89] to select for the handedness of an LG_{01} mode. The left image depicts the orientation of the first aluminium strip (white line) relative to the standing wave pattern of the mode. The centre image is $\lambda(n + 1/4$ further down the beam path and shows the second strip relative to the handedness of the mode that is being selected for. Whilst the right image demonstrates the same strip causing a loss for the counter-rotating opposite handedness.

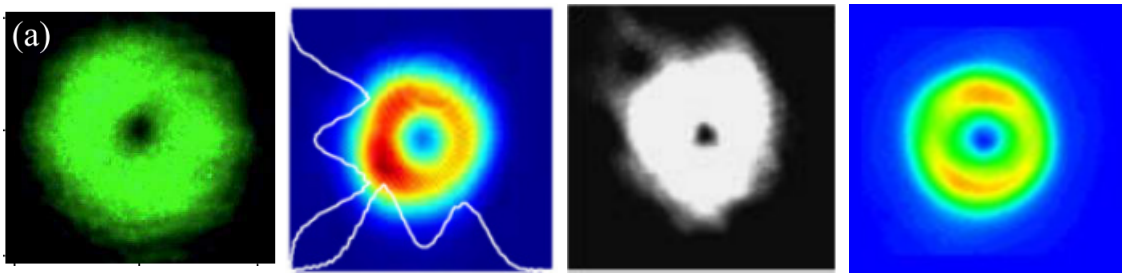

(a) *(b)* *(c)* *(d)*

Figure 1.9: A selection of LG_{01} modes from the literature. *(a)* is from a paper by Volyar *et al.* [90]. *(b)* is from a paper by Tanaka *et al.* [91]. *(c)* is from a paper by Okamoto *et al.* [92]. *(d)* is from a paper by Takahashi *et al.* [58].

the intensity in the top right [90]. More detail than this is hard to make out as it appears the camera has saturated. The beam from Tanaka *et al.* in *Fig. 1.9b* is of significantly worse quality, with a lopsided power distribution and a central intensity null that does not go to zero [91]. The beam made by Okamoto *et al.* in *Fig. 1.9c* is of incredibly poor quality, it being more triangularly shaped than round, and with additional structure outside the main beam [92]. Furthermore, their camera is heavily saturated, possibly obscuring key details about the beam. Finally, Takahashi *et al.* present a beam in *Fig. 1.9d* that is of reasonable quality [58]. There beam is round and with a good central intensity null, however there is clearly an azimuthal variation to the intensity of the beam. This indicates the beam is not a pure LG_{01} mode.

We can therefore see that there is a wide variety in the quality of beams being called

DMs. A more robust way to compare the purity of these modes would help in understanding the various merits of producing DMs in different ways. Furthermore, with a better understanding of the factors that go into DM mode purity, one could improve the design and operation of the systems one used to make these modes and, in turn, improve the modes themselves.

1.6 Thesis Outline

The rest of this thesis deals with our own efforts to both improve old and explore new ways to generate doughnut modes. We have primarily been concerned with generating LG_{01} modes with controllable OAM with both high power and purity, all with the application of laser processing in mind. Whilst a laser was never built that reached machining powers, we believe we have laid the groundwork for building such a laser, whilst gaining a greater sense of both how to measure and control the purity of such beams.

Chapter 2 explores trying to make higher order DMs by using high aspect ratio capillary fibres to reshape the pump for solid-state laser. This discusses the advantages of going to higher mode orders such as greater OAM per photon and steeper intensity profile. It also analytically proves some of the physical trends that appear as the azimuthal order is increased. We present and test a theoretical model for estimating the thresholds at which specific DMs will begin to oscillate. The specifics of preparing a capillary fibre for delivering pump light are discussed, and with this we generate modes up to $LG_{0,23}$ in a 2-mirror Nd:YAG laser. However, all the modes produced are petal modes that have little application.

In Chapter 3 we sought to try to isolate a mechanism for handedness selection within a laser cavity. We initially discuss some key diagnostics that allowed us to detect OAM and individual longitudinal modes. We built a capillary pumped, single longitudinal mode, vortex mode ring laser. This isolates the vortex mode from all others for study. We saw initial promising handedness selection from an unexpected effect in a Faraday rotator. An analogous effect was found in the highly chiral material tellurium dioxide. This effect was not found to be measurable in either free space or in a standing wave cavity.

Chapter 4 is concerned with taking a detailed look at analysing the purity of higher order transverse modes. We initially highlight some key problems that can arise when mode purity is not looked at rigorously and then conduct a review of the literature on the methods used to analyse purity. We then present two new techniques concerned with detecting and quantifying specific impurities that can occur when making HG_{01} or LG_{01}

modes. The first expands on the technique of using a Mach-Zehnder interferometer to check for the presence of a helical phase front. It moves this diagnostic from a binary measurement of whether this is present to a scaled measurement that can estimate the percentage of the beam that carries OAM. The second technique involves basic analysis of the intensity profiles of HG_{01} and LG_{01} modes compared to their theoretical ideal. We show this can reveal small impurities that would otherwise be qualitatively hard to observe. In certain cases we can take this analysis further to estimate what quantity of impurity is present in a given mode.

In order to actually generate a high quality, power scalable vortex mode we decided to investigate using an astigmatic mode converter. Chapter 5 lays out and expands upon the theory of mode converters and the physics underlying them. Our key innovation is to replace the cylindrical lenses typical astigmatic mode converters with spherical mirrors. This provides benefits in terms of power handling, design flexibility and the removal of chromatic aberration. We then present two methods of producing the pre-requisite HG_{01} mode and analyse both the purity of these and the vortex modes they produce. The latter method involves using twin pump spots to select for a pure HG_{01} mode. This produced an LG_{01} vortex mode of high purity with controllable handedness that was suitable for power scaling.

In chapter 6 we introduce a Q-switch to the twin pump spot laser producing a high-quality $25ns$ pulsed HG_{01} laser. After assessing the various amplifier geometries available and conducting a literature review on the amplification of higher order modes we construct a bounce geometry amplifier to scale the power of our HG_{01}. The hope was to scale the power to the $10s$ of watts whilst retaining high beam quality. Up to $17W$ of output was produced but at the expense of the beam quality. The output was of too low a quality to attempt a conversion to the LG_{01} mode. We therefore discuss alternative approaches to this problem.

Finally, chapter 7 summarises the main results from this thesis. We then explain our thoughts on how to progress in the field of high power vortex mode generation.

Chapter 2

Generating High Order Laguerre-Gaussian Modes

Many of the desirable qualities of DMs are enhanced by increasing the azimuthal mode order l. For a pure vortex mode the OAM scales at $l\hbar$. This is probably the main attraction of high order vortex modes for various applications. Furthermore the steepness of the intensity distribution increases with the azimuthal mode order. We derive this in Section 2.2. We believe this has potential application in reducing the undesirable HAZ during machining, as there will be less material being illuminated by laser power that is powerful enough to damage the material, but not to fully melt it. An LG_{01} mode has the a larger cutting area than the fundamental for the same beam size. This is shown by Niziev *et al.* and is stated to be better for cutting materials which have a narrow temperature band in which effective cutting can occur, as less of the beams intensity is either wasted or causing unwanted damage to the material [53].

This chapter describes the work done to extend intra-cavity doughnut mode generation to as high an azimuthal order as possible. This was pursued by expanding on the technique of generating DMs using capillary fibres detailed in Section 1.4.4. We used a higher ratio between the inner and outer diameter of the fibre of 0.8 compared to previous work. This will preferentially select higher order LG modes.

2.1 Selecting Doughnut Modes Within a Cavity

In order to generate a specific DM we need to ensure that it has the lowest threshold. This requires us to have a theoretical understanding of what thresholds to expect from all possible cavity modes. We can then design a laser to select the mode we want. First, when using a doughnut shaped pump beam from a capillary fibre, we can assume that only the set of LG_{0l} modes will have good overlap. HG modes will be suppressed as there

is nothing to break the cylindrical symmetry. We can also largely discount LG modes with a radial order above 0, as the pump has a only single radial null. We therefore need an analytical solution to the pump threshold in the case of DMs. This has been discussed in detail in [85] and will be summarised here. First we must define the cavity photon lifetime, i.e. the rate of decay of the number of photons in the cavity, τ_c. If we take the output power of a laser at time $t = 0$ to be $P_{LO}(0)$ we can ask what the output power will be after a round trip of the cavity, t_r, later. This assumes no more photons enter, or are excited in the cavity, within that time.

$$P_{LO}(t_r) = P_{LO}(0)(1-L)(1-T) \tag{2.1}$$

where $P_{LO}(t_r)$ is the power at time t_r, T is the fractional transmission through the output coupler and L is the fractional loss from all other sources. We can then extrapolate the loss and transmission terms to get

$$(1-L)(1-T) = exp\left(ln\left((1-L)(1-T)\right)\right) = exp\left(\frac{2l_c}{c_n}\frac{c_n}{2l_c}ln\left((1-L)(1-T)\right)\right) \tag{2.2}$$

where l_c is the cavity length (assuming a standing wave cavity) and c_n is the average speed of light within the cavity. By then defining $t_r = \frac{2l_c}{c_n}$ we can then define τ_c as the decay constant for the system. *i.e.* the remaining terms within the exponent. This gives us output power after a round trip as

$$P_{LO}(t_r) = P_{LO}(0)\, exp\left(-\frac{t_r}{\tau_c}\right) \tag{2.3}$$

where

$$\tau_c = -\frac{2l_c}{c_n\left(ln(1-l)(1-T)\right)} \simeq \frac{2l_c}{c_n(L+T)} \tag{2.4}$$

The approximate equality holds as long as both L and T are both $<< 1$. We can then substitute the simplified τ_c into equation (2.4). If we then look at the threshold for a four level laser

$$P_{th} = \frac{h\nu_p(L+T)}{2l_c\sigma_e\tau_f\eta_{abs}\eta_q}\left(\int\limits_{cavity} s_0 r_0 dV\right)^{-1} \tag{2.5}$$

where: h is Planck's Constant; ν_p is the pump wavelength; σ_e is the emission cross section; τ_f is the fluorescence lifetime; η_{abs} is the fraction of the pump light absorbed; η_q is the pumping quantum efficiency, i.e. the fraction of input pump photons that actually cause a unit of inversion; and V is the volume being pumped. The integral is the spatial overlap between the pump and the lasing mode. Within it we find r_0, which is the normalised pump rate density and s_0 is the normalised photon density. We now define the variable A_{eff} as

$$A_{eff} = \left(l_c \int\limits_{cavity} r_0 s_0 dV \right)^{-1} \tag{2.6}$$

This corresponds to the effective area of gain that overlaps with a given mode. If we assume the capillary fibre, when re-imaged into a laser crystal, produces a step index doughnut profile with inner diameter (ID) of a and outer diameter (OD) of b ; and that neither the pump light nor the desired mode diverge significantly over the length of the gain region; we can derive normalised rate density, r_0, of

$$r_0(r,z) = \begin{cases} \dfrac{\alpha_p exp(-\alpha_p z)}{\pi(b^2-a^2)\eta_{abs}} & a < r < b \\ 0 & \text{otherwise} \end{cases} \tag{2.7}$$

where α_p is the absorption coefficient of the pump light in the laser medium [85]. The normalised photon density for a DM of azimuthal order l is described by Phillips and Andrews [93] to be

$$s_0 = \frac{2}{l!\,\pi w^2(z) l_c} \left(\frac{2r^2}{w^2(z)} \right)^l exp\left(-\frac{2r^2}{w^2(z)} \right) \tag{2.8}$$

where $w(z)$ is the spot size of the fundamental mode. We can now substitute (2.7) and (2.8) into (2.6) and resolve the integral to get

$$A_{eff} = \frac{\pi \left(b^2 - a^2 \right)}{\eta_{LP}} \tag{2.9}$$

where η_{LP} is the dimensionless spatial overlap factor between the pumped region and the lasing mode. Effectively the volume being pumped that can be spatially accessed by the cavity mode, given explicitly as

$$\eta_{LP} = \sum_{k=0}^{l} \frac{1}{(l-k)!} \left[\left(\frac{2}{w_0^2} \right)^{l-k} \left(a^{2(l-k)} - b^{2(l-k)} \right) exp\left(-\frac{2(a^2-b^2)}{w_0^2} \right) \right] \tag{2.10}$$

this assumes that the beam waist, w_0, for the lasing mode is within the pumped region. This also assumes that neither the pump nor the cavity beam diverges much over the pumping region. From this we work out theoretical threshold powers for any given DM in a representative laser set-up. To excite a single specific mode we simply need to design the laser cavity and pump architecture in such a way that the desired mode has the lowest threshold. Then provided their are no unused regions of the pump this mode should extract all the gain preventing other modes from oscillating. This is ensured by designing the laser cavity such that both the radius of the cavity mode matches the radius of the pump, and that the width of the mode's ring is equivalent to $b - a$.

2.2 The Gradient of Doughnut Mode Intensity Profiles

As the azimuthal order of DMs increases (i.e. a higher l number) they have a steeper intensity profile on their outside edge given the same measured mode size. It is thought this could help with machining as this will create a 'sharper cut' with less area of the beam under the intensity level needed to remove material. This may lead to a reduction to the damage done to the surrounding material, otherwise known as the heat affected zone, potentially leading to cleaner and more efficient cuts. DMs are ideal for this as they are cylindrically symmetrical and so do not need to be carefully orientated with respect to the cutting angle. The increase in steepness with l can be proven analytically as follows. The electric field intensity for a Laguerre-Gaussian mode in cylindrical coordinates of r, ϕ and z is [31]

$$E_{(r,\phi,z)} = \frac{E_0}{w_{(z)}}\left(\frac{r\sqrt{2}}{w_{(z)}}\right)^{|l|}\exp\left(\frac{-r^2}{w_{(z)}^2}\right)L_p^{|l|}\left(\frac{2r^2}{w_{(z)}^2}\right)\exp\left(-ik\frac{r^2}{2R_{(z)}}\right)\exp\left(il\phi\right) \\ exp(-ikz)\exp\left(i\left(|l|+2p+1\right)\zeta_{(z)}\right) \tag{2.11}$$

Where E_0 is a normalisation constant, $w_{(z)}$ is the Gaussian spot size at position z, l is the azimuthal mode order and p the radial, $L_p^{|l|}$ is the general Laguerre polynomial of orders p and l, k is the wavenumber, $R_{(z)}$ is the wavefront radius at z and $\zeta_{(z)}$ is the Gouy phase shift, also at z. For a DM $p = 0$. From this we set ϕ to 0 for convenience as all DMs are cylindrically symmetrical so this choice is arbitrary. We then multiply by the complex conjugate of the electric field. This gives us $|E|^2_{r,z}$ which is directly proportional to intensity.

$$|E|^2_{(r,z)} = \frac{E_0^2}{w_{(z)}^2}\left(\frac{r\sqrt{2}}{w_{(z)}^2}\right)^{2|l|}\exp\left(\frac{-2r^2}{w_{(z)}^2}\right)\left[L_0^{|l|}\left(\frac{2r^2}{w_{(z)}^2}\right)\right]^2 \tag{2.12}$$

To find the maximum intensity steepness we need to know the gradient of this function in the radial direction. So we differentiate it with respect to r. To make this clearer we set:

$$A = \left(\frac{r\sqrt{2}}{w_{(z)}^2}\right)^{2|l|} \qquad B = \exp\left(\frac{-2r^2}{w_{(z)}^2}\right) \qquad C = \left[L_0^{|l|}\left(\frac{2r^2}{w_{(z)}^2}\right)\right]^2 \tag{2.13}$$

and differentiate each in turn to then recombine using the product rule.

$$\frac{dA}{dr} = \left(\frac{\sqrt{2}}{w_{(z)}^2}\right)^{2|l|} 2|l|r^{2|l|-1} \tag{2.14}$$

$$\frac{dB}{dr} = \frac{-4r}{w_{(z)}^2}\exp\left(\frac{-2r^2}{w_{(z)}^2}\right) \tag{2.15}$$

$$\frac{dC}{dr} = 0 \tag{2.16}$$

$\frac{dC}{dr}$ is zero as $\frac{d}{dx}L_p^l(x) = -L_{p-1}^{l+1}(x)$ and L_{-n}^l is always 0. Enacting the product rule we obtain

$$\frac{d|E|^2}{dr} = \frac{E_0^2}{w_{(z)}^2}\left(\frac{r\sqrt{2}}{w_{(z)}^2}\right)^{2|l|}\exp\left(\frac{-2r^2}{w_{(z)}^2}\right)\left[L_0^{|l|}\left(\frac{2r^2}{w_{(z)}^2}\right)\right]^2\left(\frac{2|l|}{r} - \frac{4r}{w_{(z)}^2}\right) \tag{2.17}$$

If we then plot this expression, *Fig. 2.1b*, we can find the points of maximum intensity steepness as where the gradient of this is zero. It turns out the steepest intensity gradient occurs between the intensity maximum and null in the centre of the doughnut. We are interested in the outer intensity maximum as this is the section of the beam that forms the cutting edge. Normalising to give each mode an equal spot size, where we have defined the spot size as the point at which the intensity drops to $1/e^2$ of its maximum, and equal power we can plot a graph of the maximum steepness against azimuthal mode order, see *Fig. 2.1.* This demonstrates a near linear relationship, clearly showing that higher azimuthal mode orders have greater mode steepness. We should therefore seek to generate higher order DMs in order to investigate their potential for laser processing.

2.3 Experimentally Generating High Order DMs

2.3.1 Theory

In order to generate higher order DMs we have chosen to use capillary fibres with a higher aspect ratio than have previously been tested in order to favour generating higher order modes. This works as with increasing azimuthal mode order the distance from the mode centre to the inner edge of the ring, the intensity 'hole', increases. The ring thickness also decreases. We demonstrate this in *Fig. 2.2.* Both the 'hole' and the ring thickness are defined by the radii at which the beam intensity is $1/e^2$ of the maximum. Higher order modes therefore have an intensity profile that more closely matches a ring with a greater ratio of inner and outer diameters, a and b.

By more closely matching the pump profile with the intensity distribution of higher order modes we hope to selectively generate these modes above lower order ones. From equation (2.10) in Section 2.1 we can see that the relative pump overlap, η_{LP} depends heavily on the mode size within the cavity. Therefore by adjusting the relative mode size within the pump region to the pump size we can select a specific mode. This can be done easily within a two mirror cavity with one plane and one curved mirror. The equation for the spot radius at the beam waist of the fundamental mode is given by [2]

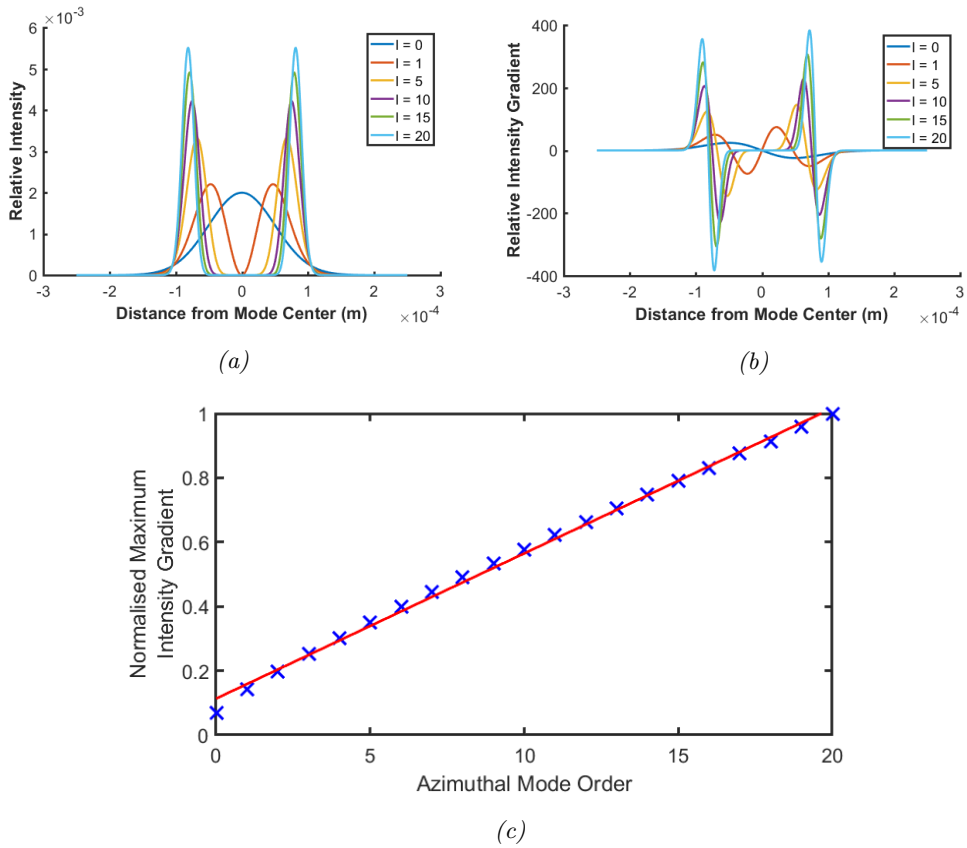

(a) *(b)*

(c)

Figure 2.1: (a) shows the intensity cross sections for DMs with azimuthal mode orders of 0, 1, 5, 10, 15 and 20. All have the same measured beam size and intensity. *(b)* shows the derivatives of these. *(c)* Shows the graph of azimuthal mode order vs the maximum outer intensity gradient, demonstrating a near linear relationship.

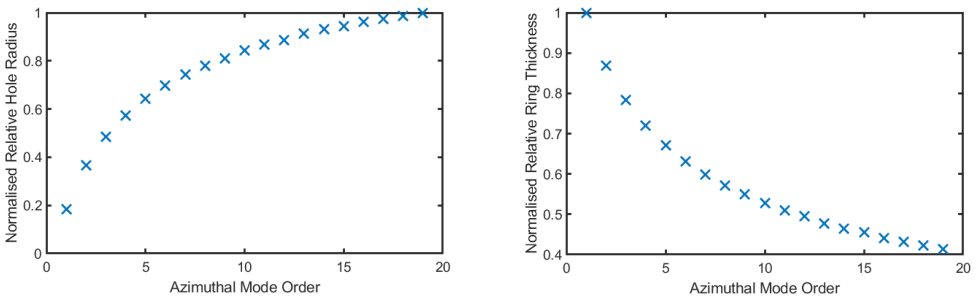

(a) *(b)*

Figure 2.2: (a) shows the logarithmically increasing 'hole' radius of DMs, while *(b)* depicts the logarithmically decreasing ring width. The 'hole' radius is defined as the radial distance from the centre of the mode to the first point that $1/e^2$ of the peak intensity is reached. The ring width is defined as the radial distance from this point to the point of matching intensity on the outer edge of the ring. All modes were normalised for both equal spot size and intensity.

$$w_0 = \sqrt{\frac{z_R \lambda}{\pi}} \tag{2.18}$$

where z_R is the Rayleigh length of the beam. Here, w_0 is the beam radius of the fundamental mode at the waist which is located at the plane mirror. The M^2 of an LG_{pl} mode is given by

$$M^2 = 2p + l + 1 \tag{2.19}$$

The actual measurable radius of a LG mode, w_{0M}, defined as the point at which the intensity has fallen to $1/e^2$ of the maximum, scales with that of w_0 as

$$w_{0M} = w_0 \sqrt{M^2} \tag{2.20}$$

Therefore if we keep the pump radius the same and vary w_0 we will change which order of DM has the best overlap with the pump. In our laser cavity the radius of curvature of the beam, $R_{(z)}$, at a mirror must be equal to the radius of curvature of the mirror. As a beam waist occurs when $R_{(z)} = \infty$ we know the beam waist will occur at the flat mirror. Therefore the distance from the beam waist, z, at the curved mirror is the cavity length l_c. We can then take the formula for the radius of curvature of a Gaussian beam [2] and rearrange for the Rayleigh length, then substitute in l_c for z.

$$R_{(z)} = z\left(1 + \frac{z_R^2}{z^2}\right) \qquad \Rightarrow \qquad z_R = \sqrt{R_{(l_c)} l_c - l_c^2} \tag{2.21}$$

we can then take (2.21) and substitute it into equation (2.18).

$$w_0 = \sqrt[4]{\left(\frac{\lambda}{\pi}\right)^2 \left(R_{(l_c)} l_c - l_c^2\right)} \tag{2.22}$$

thus we can see that by varying the cavity length of a two mirror cavity we can adjust the mode size at the beam waist. We can therefore select a specific DM as the threshold pump power is dependant on the cavity mode size.

2.3.2 Fibre Design and Tapering

We used a custom capillary fibre produced at the Optoelectronics Research Centre at Southampton University by J R Hayes. It has no dedicated cladding, being a simple silica tube with a low index polymer coating. Either the coating or the air if the coating is stripped then acts as the cladding. We selected a fibre with an outer diameter of $210\mu m$ and an aspect ratio between the outer and inner diameters of 0.797. This was chosen as it had the highest aspect ratio of the fibre that it was possible to mechanically cleave. Higher aspect ratios than 0.8 were too brittle and broke when clamped in place during the cleaving process. The fibre was also designed to have the same cross-sectional area of glass as the multi-mode fibre output of the LUMICS^{TM}, $4W$, $808nm$ diode laser used as a pump source. The diode uses a conventional single-clad fibre with a cladding diameter of $125\mu m$ and core diameter of $105\mu m$. The surface area of glass was important in order to reduce loss in splicing the capillary to the pump diode fibre.

The output from the diode laser was coupled into the capillary fibre via means of a taper. When heated under light tension, a capillary fibre will collapse into a solid fibre. The heating was provided by a graphite filament in a Vytran^{TM} GPX-3000 series glass fibre processor. Whilst heated the fibre was put under a low tension, causing the capillary to collapse the smoothly over approximately $10mm$. Heating was then stopped so as not to collapse the fibre further. Such a slow change should be adiabatic to the pump light, resulting in low loss. It also, through the matched surface areas, gave us a collapsed diameter of $125\mu m$ matching the cladding diameter of the diode fibre. This should ensure a low splice loss.

Cleaving the capillary fibres was achieved through propagating a crack under tension. CO_2 laser cleaving was found to be unsuitable as ablation dust was drawn up into the fibre hole causing substantial scattering loss. Mechanical cleaving, however, is not ideal as the fibre has no dedicated cladding. This means defects from the hammer blow, that initiates the crack, may affect the beam quality. It was also found that a small notch was blown out of the surface opposite to the hammer blow. This is thought to be the result of the two shock-waves propagating either side of the ring colliding. *Fig. 2.3* shows both an image of the cleaved fibre and its output after the diode laser was spliced to it. The notch from the hammer blow and the opposing crack are both clearly visible in the cleave image.

However only the crack is visible in the fibre output. This will probably cause a higher than predicted threshold for our modes as it is not accurately modelled in the theory, and represents a mismatch between the pump and laser mode. Furthermore it may encourage non cylindrically symmetric modes to oscillate as the symmetry is now broken. This ring shape is only maintained near the focal plane, trending towards a top hat away from this.

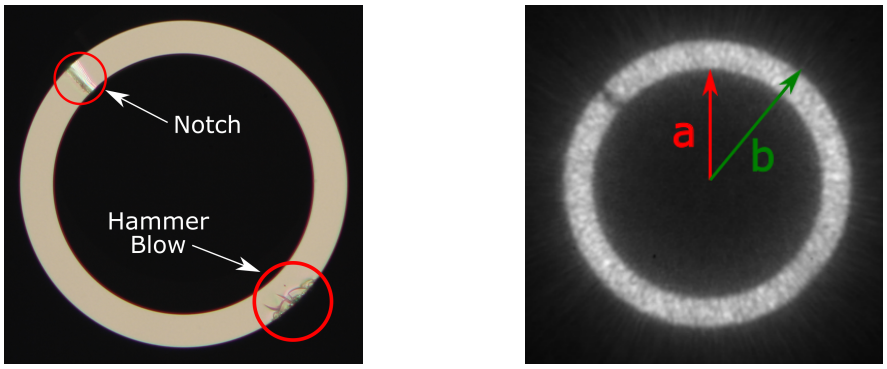

(a) *(b)*

Figure 2.3: (a) Image of the fibre end after mechanically cleaving. The hammer blow and crack where the shockwaves met are both clearly visible. *(b)* Focal image of pump light output. The notch from mechanical cleaving is clearly visible in the top left. The ID, a, and OD, b, are marked.

2.3.3 Laser Design and Modelling

We chose to use a simple two mirror Nd:YAG laser as the basis for our experiments. Nd:YAG has excellent thermal properties and is a well understood solid state gain medium with extensive established use in laser processing [20]. The gain crystal was cylindrical with a $3mm$ diameter and $10mm$ length, doped at $1atm\%$. The LUMICS^{TM} fibre coupled diode source had an M^2 of 21.66 in both axes. The diode was temperature tuned to 31.0^oC in order to match the $808nm$ absorption peak of the laser crystal. This gave a maximum output power of $3.95W$ when driven by $5A$ of current with 98.6% of the pump light being absorbed within the crystal. Immediately after splicing the diode fibre to the taper, the loss was measured at around 10%. This loss was seen to increase with time and regular use over a period of days. It eventually settled at a much more significant loss of 35%, with the maximum output power from the capillary being $2.35W$. It is thought the increased loss is due heating of the low index polymer coating applied to protect the splice and taper, causing it to degrade. This reduces the guiding properties of the taper leading to greater losses. This could potentially be improved by adding a proper cladding to the capillary fibre. This cladding would also minimise the impact from physical cleaving defects.

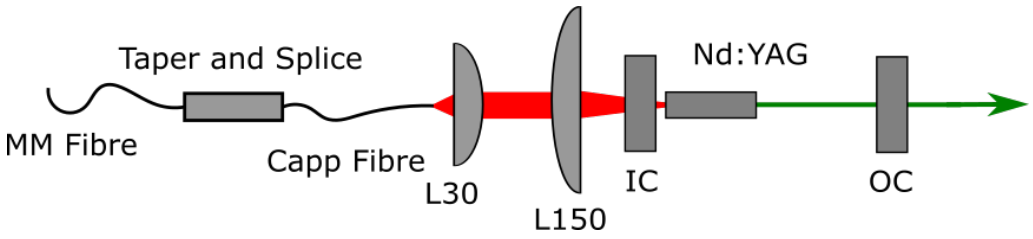

Figure 2.4: Schematic of the capillary pumped laser. LXX is a spherical lens with its focal length, XX, in mm. IC is the input coupler and OC is the output coupler.

The output from the capillary formed a clear ring shape when re-imaged with a $4f$ system of lenses (see *Fig. 1.2*). Bends in the fibre were added to remove higher order modes propagating in the central air hole. The M^2 of the ring shaped pump increased significantly, when compared to the top hat pump, to 111 in the x axis and 115 in y. A $30mm$ focal length spherical lens was used to collimate the pump and a $150mm$ lens to focus it into the crystal. This gave a beam waist radius of $525mm$ and formed ring shape that was subjectively maintained over a distance of $30 \pm 10mm$. We can therefore reliably generate doughnut modes in gain media with absorption lengths shorter than this.

A two mirror cavity with a flat IC and a curved OC with a radius of $200mm$ was constructed, see *Fig. 2.4*. The OC had a 4% transmission at $1064nm$ and a $200mm$ radius of curvature. The Nd:YAG rod was placed $2 - 3mm$ away from the IC, that was highly transmissive at $808nm$ and highly reflective at $1064nm$. This was as close as possible so as to achieve the smallest beam size in the gain region, preferentially lowering the threshold of higher order doughnut modes. A beam's divergence is also lowest near a beam waist. A low divergence beam is a critical assumption in our threshold theory calculations. This design when pumped directly by the laser diode without the capillary fibre produced a fundamental mode output. The laser cavity was optimised for a maximum output power of $1.21W$ at the maximum pump of $4W$. The laser hit threshold with an absorbed pump power of $0 \pm 0.02W$ with a slope efficiency of 31%. The diameter of the pump profile was approximately $263\mu m$.

With the capillary fibre, the focus of the pump was placed towards the front of the laser crystal, where the most of the absorption would take place. This ensured the majority of the gain was in the desired thin ring shape. This gave a pump diameter of $525\mu m$.

We used this information to model our system using equations (2.5), (2.9) and (2.10). The Nd:YAG used for these experiments was produced by CLaser who quote the emission cross section, σ_e, to be 28 x $10^{-24}m^2$ and the upper-state lifetime, τ_f, to be $230\mu s$ [94]. The quantum efficiency for Nd:YAG, η_q, is given as 0.85 by [95]. The absorption

efficiency, η_{abs}, was measured to be 0.986. We estimated the cavity loss to be 1% per round trip. Then inputting the values for the pump size, transmission and wavelengths we can simulate the expected thresholds for each mode order for any given cavity mode size. *Fig. 2.5* shows this model for mode orders up to $l = 25$. Pump thresholds above $2.5W$ are not plotted for clarity. Here we have scaled the cavity mode's beam waist within the laser cavity, w_0, relative to the outer-diameter of the pump ring, b. This theoretical model makes several implicit assumtions. First that the themal lens is both negligible and unchanging at different pumping levels. That neither the pump nor the laser mode diverge significantly over the pumped region. Furthermore, that the gain is being transfered into a singal transverse mode. And finally, that the mode being selected is a pure LG_{0l} mode. All these are approximations not neccessarily true in our laser system, however we felt that any deviations from this in our system would be small and not significantly effect the results.

Looking at our theoretical predictions, we can see that a larger fundamental cavity mode size favours a lower order mode. We also see that the lowest thresholds are reserved for the higher order modes. This makes intuitive sense as lower order modes have thicker rings for the same measured mode size, w_{0M}. So with our thin pump ring more of their intensity profile will be outside the pump region. This is illustrated in *Fig. 2.6*, where we can see the same size pump distribution in two laser cavities with different fundamental beam sizes, w_0. In the first image the lower order mode (blue) is the same size as the pump but much of the mode is outside the pump region. As the cavity mode size decreases the mode's radii decrease the higher order mode (red) aligns with the pump. Its thinner ring profile better matches the pump distribution giving it a lower threshold.

In order to select a specific mode we need to find a point where the threshold for the desired mode is the lowest of all the modes. We can see from the structure in *Fig. 2.5* the graph that we only need to consider the modes adjacent in mode order to the one we wish to operate on. This is because modes more different from the desired one have significantly greater thresholds than those adjacent to it. We should therefore find the mode size at which the two adjacent modes have a threshold equally higher than the target mode. This should minimize the risk of more than one mode oscillating.

2.3.4 Experimental Results

Upon varying the cavity length from $104mm$ down to $25.5mm$ we produced modes from $LG_{0,14}$ through to $LG_{0,23}$. These were not however pure DMs. Instead being what are known as 'petal' modes, see *Fig. 1.5*. These are superpositions between the two handed-

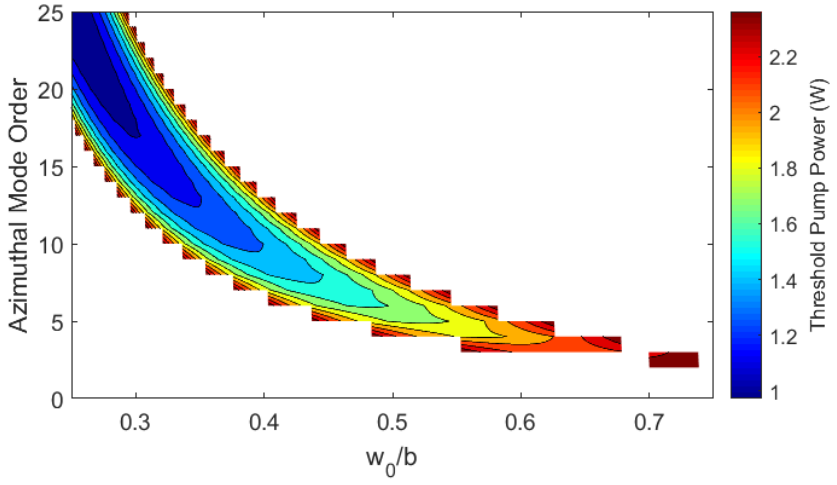

Figure 2.5: A plot of the threshold of a DM within a cavity pumped by a capillary fibre as function of the azimuthal mode order and the cavity mode size, w_0, relative to the outer radius of the pump, b. This plot has assumed 1% loss in the cavity though the true value of this is unknown. Only thresholds up to $2.5W$ have been displayed for clarity.

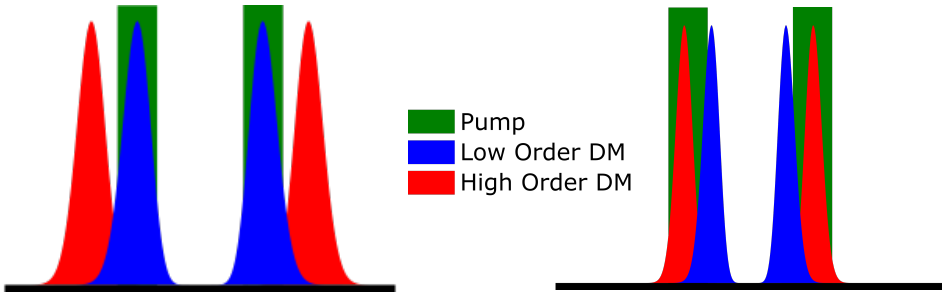

Figure 2.6: Illustration of how changing the cavity fundamental mode radius selects which order of DM attains a lower threshold and preferentially lases. Also why higher-order modes can access lower thresholds due to their thinner ring profile. The green region is the ring shaped pump distribution, the blue a lower order DM and the red a higher order DM. *(a)* shows the situation where the modes have a higher fundamental mode size, and *(b)* when the mode size is reduced. The pump spot size remains constant.

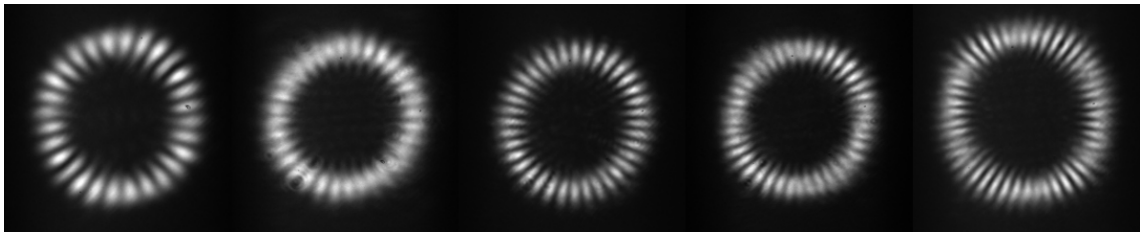

Figure 2.7: Focal images, running from left to right, for the LG_0^{14}, LG_0^{16}, LG_0^{18}, LG_0^{20} and LG_0^{23} petal modes. The petals are distinct enough say with reasonable certainty which mode is dominant in each image. However they do not appear to be pure modes.

ness states of a given LG_{0l} mode. The $l = 14$, 16, 18, 20 and 23 modes are depicted in *Fig. 2.7*. Whilst clearly petal modes, some of the petals are indistinct, indicating there may be more than one petal mode present. This is not unexpected as there is a small difference between the threshold of adjacent DMs according to our model. There is also some structure within the ring of petals indicating there may be non LG_{0l} impurities. If only a petal mode were to oscillate there would be unused gain in the nulls between the petals. This could provide enough gain for secondary modes to lase and may be the cause of our impure beams. These high order modes have little practical application as they lose two of the key properties of DMs, cylindrical symmetry and OAM. They do however retain the increased intensity gradient.

The thresholds obtained for these example modes were significantly higher than theory predicts for all modes. See *Table 2.1*. Here we show (row 1) the fundamental mode size at the plane mirror of the cavity we expect would generate this order of mode observed, if our theoretical model depicted in *Fig. 2.5* is correct. Row 2 then shows the theoretically predicted threshold for this mode, row 3 depicts what was actually measured. We can then use the cavity length to estimate the true mode size at the mirror. We found it to be consistantly larger than what we would expect from the mode orders we achieved. Row 4 and 5 then show the expected thresholds and mode orders we should have obtained from those mode sizes according to the theory in *Fig. 2.5*. Both lower order modes and lower thresholds would have been expected, given the actual mode radii. Most notably the threshold became higher with increasing mode order rather than lower. This demonstrates that our theoretical model was not able to predict the thresholds and mode orders for this laser cavity, nor was it able to explain the actual measured thresholds and mode orders observed. There are clearly key elements missing from this theory.

One possible reason for the failure of our model is that we assumed that the laser would act in only one transverse mode, we have made no attempt to model how the superposition of the two senses of azimuthal phase will effect the threshold. It is likely that the

Azimuthal Mode Order	**14**	**16**	**18**	**20**	**23**
Theoretically Predicted Fundamental Mode Size (μm)	183	179	174	164	159
Theoretically Predicted Threshold (W)	1.19	1.14	1.09	1.05	1.00
Measured Threshold (W)	1.26	1.38	1.34	1.42	1.43
Expected Threshold From Measured Cavity Length (W)	1.24	1.22	1.189	1.13	1.11
Expected Mode Order From Measured Cavity Length	13	13	14	16	17

Table 2.1: Here we compare the theoretically predicted and measured thresholds for the petal modes with what we would expect given the size of the cavity beam waist. Note that the predicted trend of lower thresholds for higher order modes was not true in practice and that much higher mode orders were produced with higher than expected thresholds.

numerous intensity nulls about the petal structure cause a significant enough reduction in the overlap to increase the threshold. Furthermore it appears that there are more modes than a single petal mode competing for the gain. This is again absent from our model leading to the inaccuracies.

The location of the notch in the pump beam might have been expected to be correlated with an intensity null. This would have indicated that this may also have been the cause favouring the production of petal modes. When tested, however, rotating the fibre left the mode unchanged. It therefore seems that another factor has caused the selection of petal modes. Notably, however, other attempts by various methods to produce high order LG modes within a laser cavity have also created petal modes [64, 73, 82]. We can note that at higher orders a petal mode more closely resembles its corresponding pure vortex mode. This indicates that when generating higher order LG_{0l} modes within a laser cavity petal modes will lase preferentially unless a method to differentiate between the two senses of handedness is implemented. We must also therefore conclude that any losses between the two senses of handedness in a standard laser cavity are very small or not present.

2.4 Conclusions

The modes obtained are clearly super-positions of DMs. This technique could be simply extended to develop even higher order modes. There are however, no known applications for petal modes. This method also suffers from low mode purity, with possibly several petal modes being produced simultaneously, along with decreasing efficiency as we approach higher orders. For this technique of higher aspect ratio capillary fibres to be effective, a robust method to select for only one sense of handedness with a single azimuthal order is needed. This would hopefully also improve the efficiency of generating these modes due

to the better inversion overlap.

Chapter 3

Investigating Handedness Selection in Vortex Mode Ring Lasers

In order to improve on the work in the previous chapter, we ideally need to generate a pure LG_{0l} mode so we can robustly study how to control the OAM. To achieve this we have constructed a ring laser. Ring lasers can be made to operate on a single frequency as they can support travelling rather than standing waves. As previously discussed there are many forms of DMs with identical intensity distributions, whereas only vortex modes contain OAM. If one wants the vortex mode specifically, it can be challenging to have this as the only mode operating in a normal laser cavity, as often several different DMs will oscillate simultaneously. By creating a cavity that operates on a single longitudinal mode we hope to isolate it for study. In so doing we hope to discover a way to select this mode preferentially over others. Furthermore, we wish to find a way to control the handedness of the mode within the cavity, something that has not been done robustly thus far.

3.1 Ring Lasers and Faraday Rotators

3.1.1 Ring Lasers

Ring lasers use cavities where a ray of light can return to where it started without retracing its path. Uni-directional ring lasers create a laser cavity with travelling waves rather than standing waves as they do not reflect the intra-cavity beam back upon itself. This eliminates the effect of spatial hole burning. Spatial hole burning occurs when there is unused gain left in the nodes of a standing wave interference pattern. This can then lead to modes oscillating in addition to the one with the lowest threshold. In contrast, a travelling electromagnetic wave will sweep through the gain medium leaving no residual gain

available for competing modes; provided good overlap between the pump and cavity mode. This can lead to single longitudinal mode operation within ring lasers as the first mode to reach threshold can spatially access all the available gain. This is dependant on there only being one direction a cavity mode can travel about the laser: Clockwise (CW) or Anticlockwise (ACW). If the laser operates in both directions these create standing waves which will lead to spatial hole burning and multi-mode operation. Uni-directionality can be solved with the use of a Faraday Rotator (FR).

3.1.2 Faraday Rotators

A FR utilises the magneto-optic effect commonly called the Faraday effect. This is exhibited when a material is in the presence of a magnetic field. By applying such a field, a different phase delay is applied to the two senses of circular polarisation of any light traversing the material that is parallel to the field. As linearly polarised light can be considered as a superposition of the two senses of circular polarisation, this causes the direction of the polarisation to rotate. The direction of this rotation is only dependent on the direction of the magnetic field and not on the direction the light is travelling [96, 97]. This creates one of the few non-reciprocal effects in optics [98, 99]. When combined with either two linear polarisers, or a linearly polarising device along with two half waveplates, an optical isolator can be created. This requires that 45^o of phase rotation is provided by the Faraday effect and leads to light being only able propagate one way through the device. See *Fig. 3.1.* The polarisation is rotated by an amount given in [100]

$$\theta = V \int B.dl \tag{3.1}$$

where: θ is the phase rotation in radians; V is the Verdet constant of the material; B is the magnetic field strength and l is the length of the Faraday material along the axis of beam propagation. A full isolator is not necessary for uni-directionality within a ring laser. Only a loss differential is needed for one direction of beam propagation to reach threshold first and become the only output. This can be achieved with less rotation of the polarisation, so long as one direction of light sees more loss at the polarising element. We can quantify the level of uni-directionality, i.e. how close we are to having all of the photons in the cavity traversing one particular direction, as the ratio of powers in the two outputs.

3.1.3 Scanning Fabry-Perot Etalons

Later in this chapter we will be examining the frequency spectrum of laser outputs using a scanning Fabry-Perot etalon. These devices can give very accurate frequency spectra as

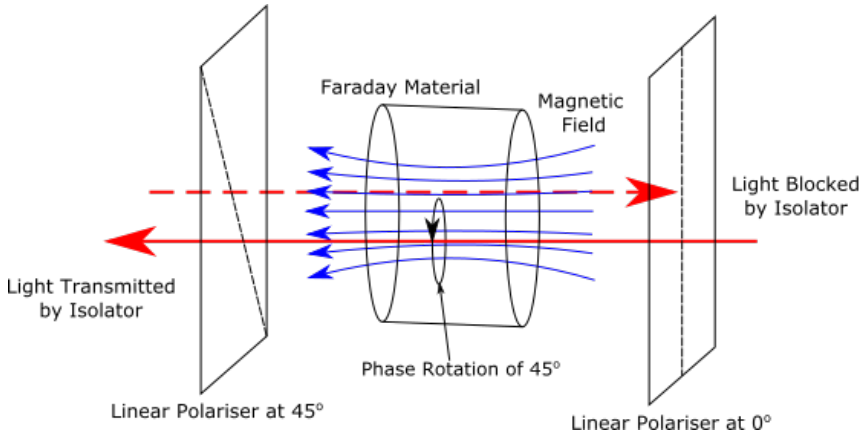

Figure 3.1: Diagram of a Faraday isolator. This forms an optical device similar to a diode in electronics.

they rely on interference properties. They are constructed using two partially transmitting mirrors parallel to each other, into which the light to be studied is inserted at normal incidence (see *Figure 3.2a*). This sets up a standing wave pattern between the two mirrors. If the mirror separation is an integer or half integer multiple of the wavelength, constructive interference occurs, greatly boosting the transmission through the mirrors [101, 102]. If the mirror separation is varied and the transmission monitored on a fast photo-detector connected to an oscilloscope, it is possible to construct a frequency spectrum of the incoming light; *Fig. 3.2b* shows an example. This makes Fabry-Perot interferometers particularly useful for monitoring the frequency spectrum of monochromatic, or near monochromatic lasers, whose frequency separation between longitudinal modes can be easily sub-GHz.

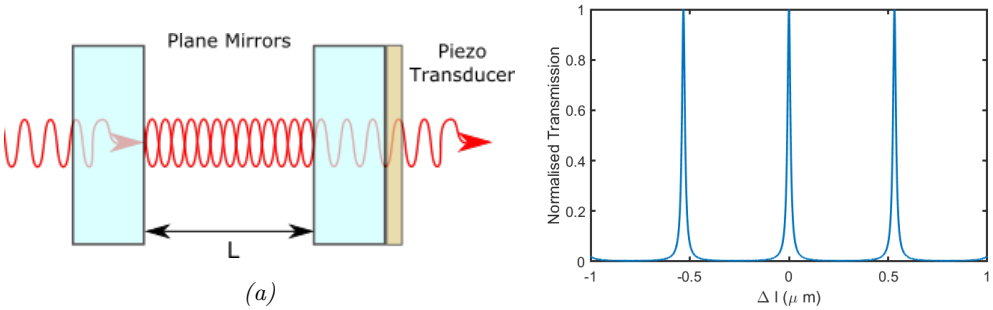

Figure 3.2: (a) depicts a conventional plane-plane scanning Fabry-Perot interferometer. *(b)* shows a typical oscilloscope trace, plotting the variation in separation against the intensity transmitted through the etalon.

Two important properties of a scanning Fabry-Perot interferometer are its free spectral range (FSR) and finesse. The FSR is frequency spacing between its resonant modes;

effectively the bandwidth over which it can scan before the same wavelength will become resonant again [103].

$$\Delta\nu_{FSR} = \frac{c}{2n_g L_m} \tag{3.2}$$

where $\Delta\nu_{FSR}$ is the FSR of the etalon, c is the speed of light in a vacuum, n_g is the group refractive index and L_m is the average mirror separation. The finesse is the FSR of the cavity divided by the bandwidth (as defined by the full width half maximum (FWHM)) of its resonance peaks. The finesse is independent of the mirror separation and is instead dependent only on the reflectivity of the mirrors. The resolution of a scanning Fabry-Perot etalon is its FSR over its finesse. To have a high resolution a high FSR and therefore a large mirror separation is needed. This comes at the cost of the frequency bandwidth that can be analysed simultaneously by the device.

3.1.4 Mach-Zender Interferometers

Mach-Zehnder interferometers are a simple instrument for comparing a light source with a modified version of itself. It employs two beam splitters to separate and then recombine a beam [104]. This allows for one beam to be modified in some way, before being combined back with its other half. It is then possible to look at the resultant interference pattern. The difference in length between the arms should be less than the coherence length of the light being analysed. In our case we will use this to confirm both the existence and direction of helical phase within DMs. By aperturing part of one beam with a pinhole we can create a spherical wave of the same wavelength. Interfering this with the original beam will produce the images seen in *Fig. 3.3b*. We see either a CW, or an ACW, spiral in alignment with the direction of the helical phase fronts. If the beam is a DM with no OAM we will observe concentric circles, see *Fig. 3.3*. Examples of these include superpositions of petal modes. Radially and azimuthally polarised modes will give unusual interference patterns as the small section of beam sampled will not have a polarisation state that matches that of the whole beam. More information on Mach-Zehnder interferometers and their use with vortex modes can be found in Section 4.2

3.2 First Order Laguerre-Gaussian Ring Laser

3.2.1 Experimental Design

For simplicity we are aiming to generate the LG_{01} mode. To facilitate this we are using a capillary fibre with a $200\mu m$ outer diameter and a $100\mu m$ inner diameter. This fibre's lower ratio of outer to innder diameter will favour the generation of the lowest order DM, as it more closely resembles that mode's intensity profile. This is mechanically cleaved by the same method outlined in Section 2.3.2. The cleave was of similar quality to that of

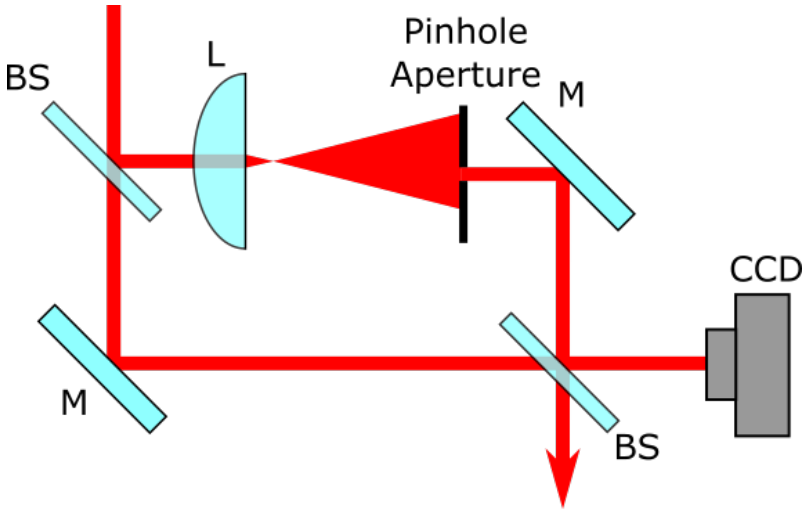

(a)

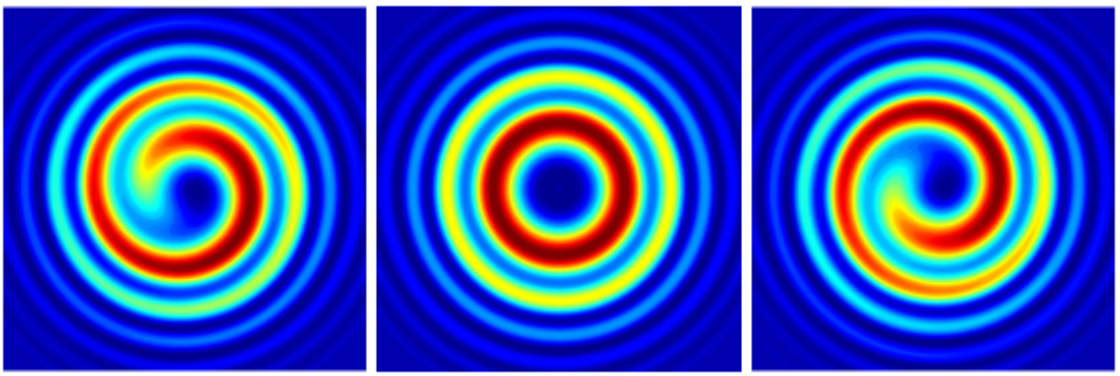

(b)

Figure 3.3: (a) is a typical Mach-Zehnder interferometer for detecting the presence of beam helicity and therefore OAM. BS are non-polarising beam splitters, M are highly reflective mirrors and L a short focal length lens. *(b)* shows theoretical interference patterns observed from a Mach-Zehnder interferometer for the LG_{01} mode. The left image is for a beam with ACW phase fronts, the right for CW and the centre for a DM that does not contain OAM; such as a superposition of petal modes. Thus the interferometer can detect the presence and handedness of OAM.

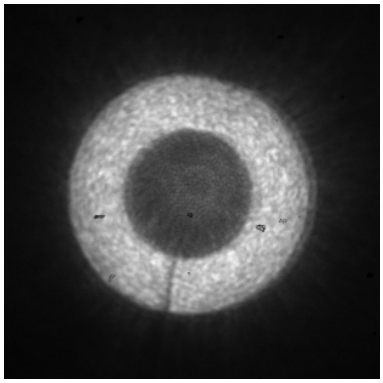

(a)

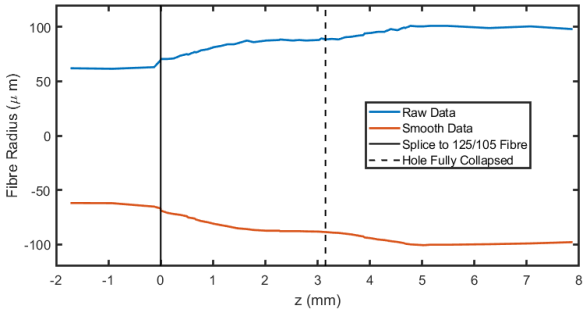

(b)

Figure 3.4: (a) shows the output from the 200/100 capillary fibre imaged in the focal plane. *(b)* shows the radius profile of the taper produced by Gooch and Housego^{TM}. We can see the taper occurs over two distinct regions: the first initial collapse until the hole closes, and then a slower taper until the radius matches that of the diode fibre.

the higher aspect ratio fibre used in Chapter 2, with the same crack opposite the hammer strike. We will assume this has little impact on the quality of DM capable of being produced from the ring laser, as there was no evidence of this defect having much impact previously. An image from the output of this is given in *Fig. 3.4a*. The output from the capillary had an M^2 of 43. The same laser diode from Section 2.3.3 is used however we have a different taper produced by Gooch and Housego^{TM} to connect the capillary to the diode's fibre output. This provided near perfect transmission and therefore an output that was stable over time. Upon examining the tapers, only one substantial difference was found. A different collapse profile has been used, see *Fig. 3.4b*. The taper initially collapses quickly and then finishes its narrowing more slowly. Why this has improved the transmission is unclear.

For the ring laser itself we have used lenses for cavity stability, as although these incur additional losses, they avoid beam astigmatism from off axis reflections on curved mirrors. This is important to achieve a pure LG_{01} without breaking its cylindrical symmetry which would have unknown effects on the beam quality. Furthermore it will cause the mode to shift towards a HG_{01} mode, due to the Gouy phase shift (see Chapter 5). The loss difference between S and P polarised light upon reflection of the cavity mirrors provided the polarisation selection needed for unidirectional operation in combination with the FR. The rotator itself consists of two half waveplates and a $10mm$ rod of terbium gallium garnet (TGG) as the Faraday material. The half waveplates here replace the linear polarisers in a typical faraday rotator. They're orientated so as to ensure the electic field of light travelling in one direction is aligned with the axis of minimum loss on the mirrors, whilst maximising the loss for the other direction. The TGG was anti-reflection coated for

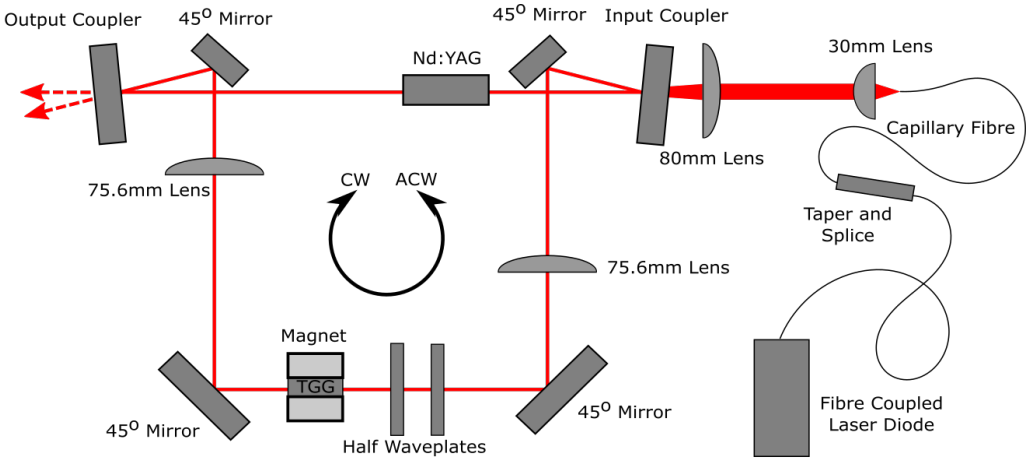

Figure 3.5: Schematic of the uni-directional ring laser. The lenses are positioned so there is a waist within the gain medium in order to match the cavity mode to the pump spot size. We can rotate one of the half waveplates in order to reverse the direction of the cavity mode.

$1064nm$. The magnetic field was produced by two ring shaped neodymium magnets, the poles on the opposing flat faces, surrounding the TGG crystal, providing a magnetic field of approximately $0.29T$. This provided an approximate polarisation rotation of 7^o for linearly polarised $1064nm$ light. A full schematic is in *Fig. 3.5*. The diode could provide up to $3.7W$ of pump at the $10mm$ long, 1% doping concentration cylindrical, Nd:YAG laser crystal. A 5% transmission at $1064nm$, output coupler was used and the cavity length was $520 \pm 20mm$.

When operated without the FR, bi-directional, multi-mode operation is observed. The modes travelling in opposite directions compete for the gain and when we optimise for the maximum total power we observe the outputs in *Fig. 3.6*. This was taken at $3.7W$ of pump power producing $510mW$ of output with a 22.6% slope efficiency. We can see that these beams are not stable with propagation, looking closer to a true LG_{01} in one location but with clear HG_{01} features in another. This could be due to astigmatism and the results of the Gouy phase shift. Astigmatism could have arisen from transmission throug off-axis lenses external to the cavity. On the other hand, we also notice that the orientation of the high power lobes is orthogonal between the beams. This intensity distribution could arise from an incoherent superposition of the lowest order petal mode and a doughnut mode. With the petal modes rotated by 90^o to each other, each exploiting a different region of gain. The total intensity profile of the two beams propagating opposite ways about the cavity would then resemble the lowest order DM. Even though individually they do not match it. This could alternatively explain the lobed appearence of the modes, though not the change in appearence with propagation. Furthermore, the beam depicted in *Fig. 3.6b* seems to have a larger intensity null compared to the beam size, indicating some higher

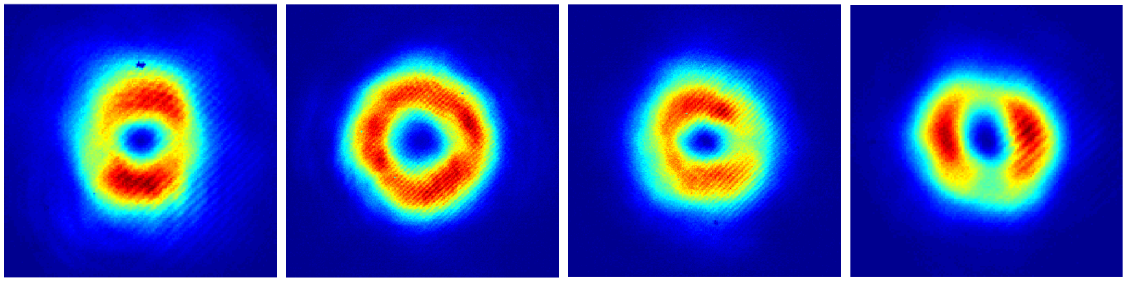

(a) *(b)* *(c)* *(d)*

Figure 3.6: (a) and *(b)* the CW beam in at the focus and in the far field. *(c)* and *(d)* the ACW beam at the focus and in the far field.

order LG_{0l} content. By inserting the FR, we should be able to enforce single longitudinal mode operation and remove the superposition of modes we may be observing.

3.2.2 Handedness Selection

After inserting the FR, the cavity alignment was optimised for both an LG_{01} mode and single frequency operation. We found the beam to exhibit a clear handedness. Single frequency was confirmed using the scanning Fabry-Perot interferometer, see *Fig. 3.7a.* The beam quality has significantly improved, with better cylindrical symmetry and a profile that does not change upon propagation. This handedness was time invariant and robust to small cavity misalignments, even when single frequency operation was broken or mode hopping was observed. This was all observed at the 3.7W of pump power, providing $290mW$ of output with 18.8% slope efficiency. This drop in power and efficiency is to be expected due to the additional losses from the three extra intra-cavity elements. It was found that by adjusting the orientation of the extroadinary axis of one of the waveplates to reverse the direction of propagation about the laser cavity, the handedness of the mode was reversed, *Fig. 3.8.* Reversing the direction of the cavity had no significant impact on the efficiency or mode quality. A CW spiral was observed when the beam traversed the cavity in a CW direction and vice versa. This demonstrates that there is some form of loss or gain differential breaking the degeneracy between the senses of phase. This result was consistent upon multiple repetitions, as long as optimal alignment was maintained. It was also observed to remain true when the cavity design was changed slightly in order to reduce the path length of the cavity. Large misalignments of the cavity mirrors would however, break both the single longitudinal mode operation and the clarity of the spiral in the interference pattern.

We can be certain of the presence of a pure LG_{01} mode from the scanning Fabry-Perot spectrum as only one mode is operating, provided the assumtion that each longitudianl

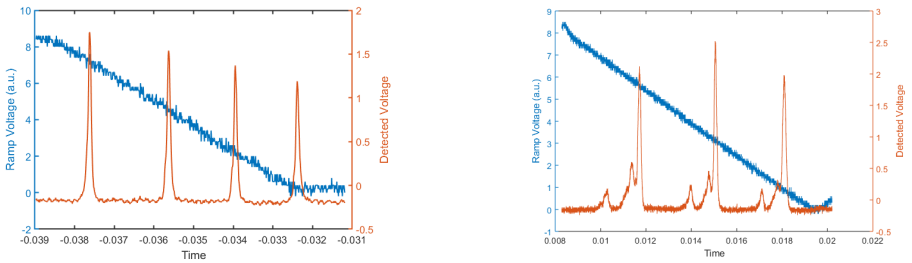

(a) *(b)*

Figure 3.7: Output of scanning Fabry-Perot interferometer for LG_{01} mode ring laser. *(a)* shows the spectrum when properly aligned. We see clear single longitudinal mode operation. *(b)* depicts the spectrum when the mirrors are misaligned, showing clear multi-mode operation.

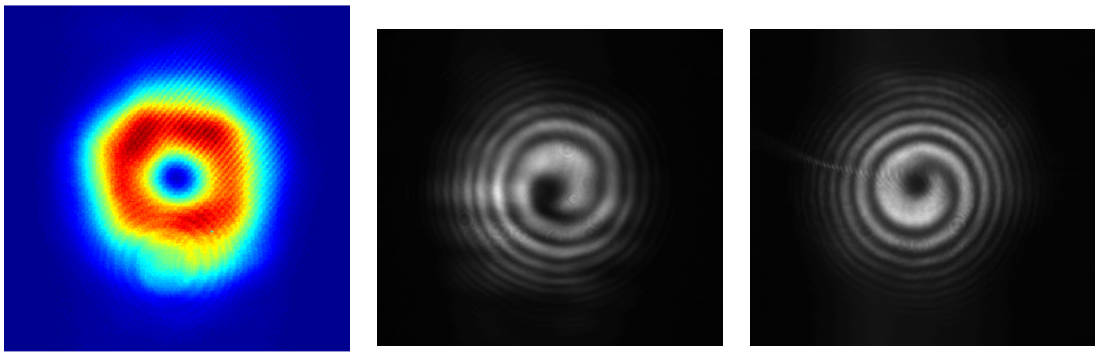

(a) *(b)* *(c)*

Figure 3.8: *(a)* depicts the output beam of the ring laser during single longitudinal mode operation. *(b)* Depicts the interference pattern observed after the Mach-Zehnder interferometer from when the beam is running CW about the cavity. It shows a clear CW spiral indicating CW helicity. *(c)* shows the beam when running ACW about the cavity depicting clear ACW helicity.

mode can only operate on a single transverse mode is correct. The scanning Fabry-Perot interferometer had a mirror spacing was $30.9mm$ and both mirrors had a reflectivity of 95%. This gives a free spectral range of $4.8GHz$ and a finesse of 31. This means we can resolve modes that are separated by greater than $0.15GHz$. The spectrum contains clear single peaks so we can conclude the laser is operating on a single longitudinal mode with bandwidth less than $0.15GHz$. The cavity length is approximately $0.54m$ giving a frequency separation of the cavity modes of $0.54GHz$ so we would expect any secondary longitudinal mode to clearly show up between the resonance peaks shown.

The physical mechanism behind the change in handedness is currently not understood. However, its non-reciprocal nature suggested a non-reciprocal effect is causing the loss differential. The only two such things within the cavity are the magnetic field and the Faraday effect itself. Further investigation was therefore warranted in order to determine

if these were selecting for the handedness of the beam. We also note that, to the best of our knowledge, this is the first demonstration of the handeness selection of vortex modes within a solid state ring laser.

Following this we reversed the direction of the magnetic field by inverting the rotator. This isolated the change in the magnetic field from all variables except any defect within the rotator. This reversed the handedness with respect to the direction the beam was travelling round the cavity. i.e. an ACW spiral is now observed for a CW travelling mode and vice versa. Slight misalignment of the rotator, without inverting the magnetic field, was found not to reverse the handedness. It would occasionally break the single longitudinal mode operation but this could be corrected by re-aligning the cavity mirrors. We can therefore conclude that the handedness selection is linked to either the magnetic field or the Faraday effect, thus confirming a method of handedness selection within a uni-directional ring laser cavity.

3.3 Retro-Reflection Ring Laser

3.3.1 Theory and Literature

In order to further investigate this, we need to separate the mechanism for handedness control from the mechanism for uni-directionality. As we know no other mechanism for selecting handedness, we must find another for enforcing uni-directionality and single longitudinal mode operation. Enforcing uni-directionality is done by creating a loss differential between the two counter-propagating travelling waves [105]. One method of doing this is to retro-reflect one of the outputs back into the gain medium. This is done by simply using a mirror to reflect the output of one direction back through the OC. This suppresses the mode that is being fed into the feedback arm. This method was initially explored early in laser development [1, 105, 106], but was generally discarded in favour of FRs due to poor uni-directionality. It has been explored more recently as it removes intra-cavity optics and thus reduces loss within the laser [107, 108]. However no account of the uni-directionality is given. Shardlow *et al.* have, however, reported excellent, 2500:1, uni-directionality using this method [109]. They attribute this to the high gain in their Nd:YVO_4 bounce geometry laser. An interesting point is that when aligned correctly there is almost no observable power in the feedback arm. Shardlow *et al.* posit that therefore one of the directions has been completely suppressed and the feedback is coming from amplified spontaneous emission (ASE).

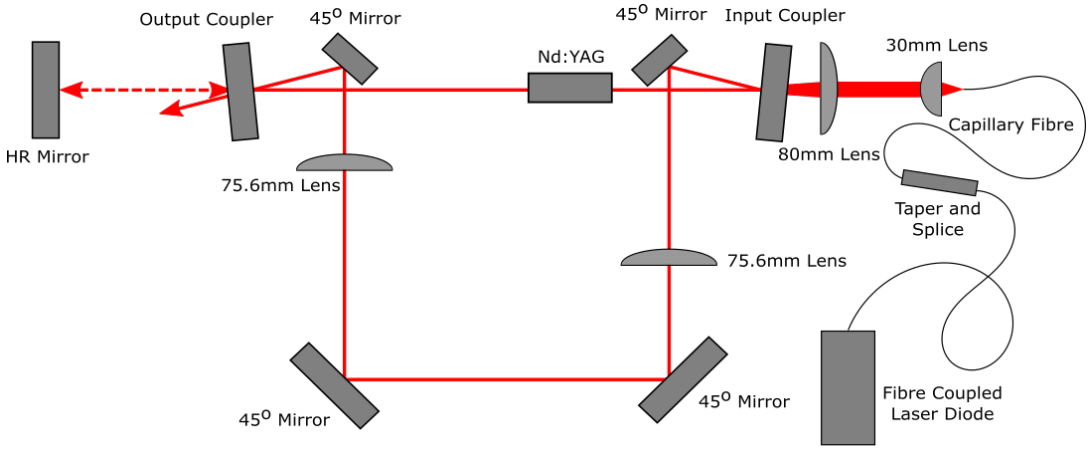

Figure 3.9: Schematic for the ring laser using retro-reflection to enforce uni-directionality. The external mirror creates feedback for the ACW mode, suppressing it.

3.3.2 Experiment

We constructed the laser shown in *Fig. 3.9*. We measured the uni-directionality by optimising the power in the ACW direction and then measuring the total power output from the laser travelling in each direction separately. We found there to be 50 times the power travelling in the ACW direction compared to the other, giving reasonable though not perfect uni-directionality. The mode was still shown to posses CW helicity, however single longitudinal mode operation was not achieved as shown in the frequency spectra in *Fig. 3.10a*. Re-aligning the cavity could, however, reverse the handedness or remove a clear helicity, *Fig. 3.11*. We believe the spiral interference patterns to be degraded compared to the ring laser utilising the FR due to the multi-modal output. This highlights that without a helicity selecting mechanism, clear helicity is possible, but neither stable, nor guaranteed. It also suggests that a spiral interference pattern may not be sufficient to give full information about the OAM content of a mode. We explore this issue further in Section 4.2.

We then re-introduced the FR as a helicity selecting device. No half wave plates were added in order to retain the retro-reflector as the dominant force for uni-directionality. The cavity operated in the ACW direction as before, regardless of the orientation of the FR. However, in both directions the frequency spectrum became more multi-modal, particularly when the magnetic field was pointed against the cavity mode's direction of travel. Though in this case it may have been caused by a retro-reflection from the etalon of the Fabry-Perot interferometer interfering with the gain in the laser. The reason the multi-modal output in the other cases is, however, unclear, but suggests that there are several competing mechanisms occurring within the laser cavity, destabilising it. Nevertheless the

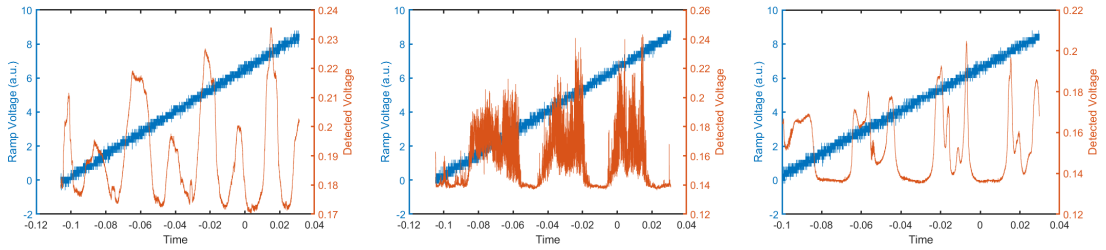

(a) *(b)* *(c)*

Figure 3.10: Fabry-Perot spectra for the retro-reflection ring laser. *(a)* is the spectrum with no FR, *(b)* with the magnetic field of the FR orientated against the cavity mode's direction of travel and *(c)* with the field orientated with the mode.

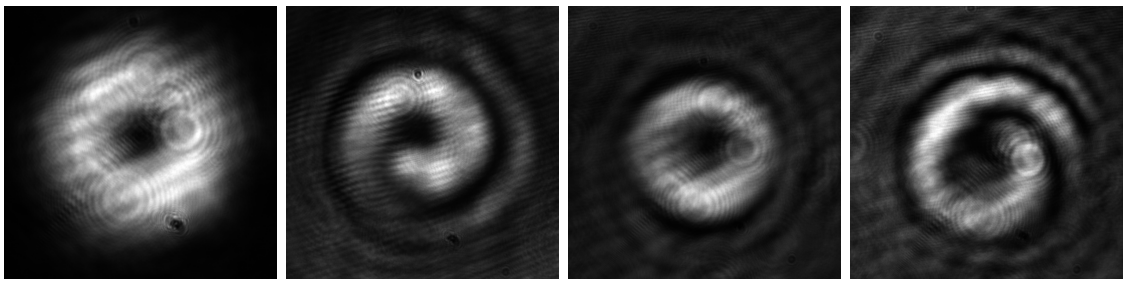

(a) *(b)* *(c)* *(d)*

Figure 3.11: (a) is an image of the typical output from the retro-reflected ring laser. *(b)*, *(c)* and*(d)* are three spiral interference patterns generated from this. The handedness was changed via minor cavity re-alignments.

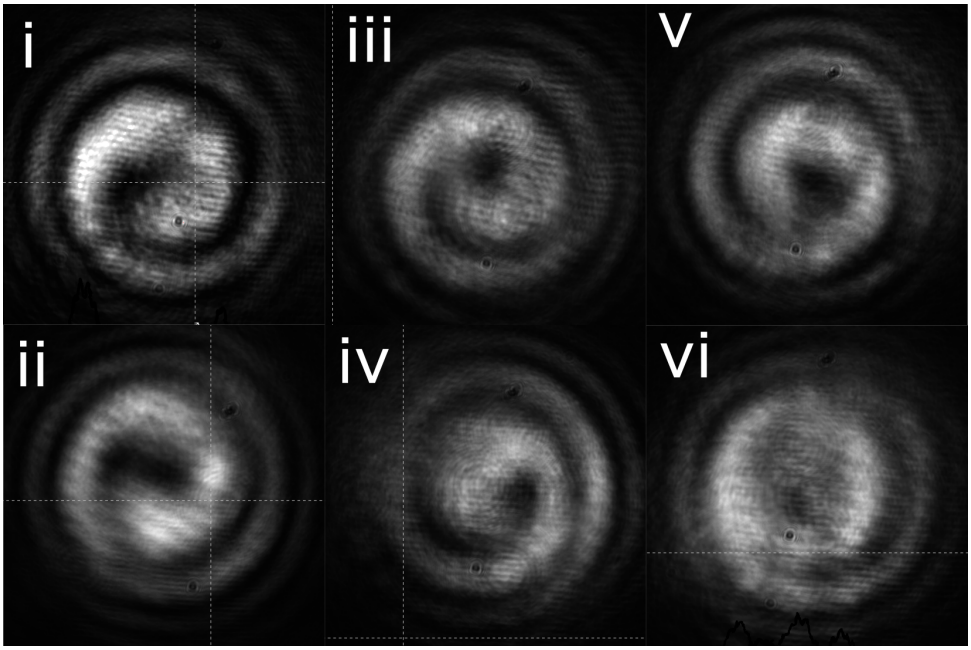

Figure 3.12: Spiral interference patterns from the retro-reflected ring laser. i and ii show clear CW handedness when the laser contains no FR. iii and iv show relatively weak CW and ACW spirals when the FR's magnetic field opposes the cavity mode's propagation. v and vi show ACW and no handedness when the magnetic field co-propagated with the mode.

intensity profile of the laser output remained constant as measured by a camera with a frame rate of $25fps$. Again the handedness was not robust to cavity misalignment.

The cavity was aligned without the rotator for clear CW handedness and then the FR was introduced. Both clear CW and ACW handedness was obtainable with the magnetic field pointing with the beam propagation. With the beam counter-propagating, either ACW or no handedness was obtainable, examples given in *Fig. 3.12*. In general however, it was found that the co-propagating magnetic field favoured a CW and counter-propagating ACW handedness. No realignment of the cavity was done upon introducing the rotator. The FR was removed between each measurement and aligned so as to minimise translation of the output beam. The variance in the handedness demonstrates that the selection mechanism was relatively weak and is not robust when subjected to a multi-mode laser.

We do not propose a clear mechanism for the handedness selection provided by the FR. We do note however that the Faraday effect has a similar physicals effect to optical activity, a phenomenon only found in microscopically chiral materials [110]. As the physical origin of handedness in vortex modes is their chiral phase pattern, we ask the question: do other chiral structures induce the same effect?. If it is found that structures that are chiral on

a microscopic level do cause a loss differential between the two senses of orbital phase, we can name this orbital activity.

3.4 Tellurium Dioxide as a Handedness Selector

We have chosen to study α-Tellurium Dioxide (TeO_2) as a candidate for handedness selection, due to its unusually high optical activity [111]. It is also highly suitable as an optical material as it has high transparency and good thermal properties. We therefore obtained a $10mm$ thick crystal of TeO_2, coated to be anti-reflective at $1064nm$. This had previously been designed for use within an acoustic Q-switch, so was of high optical quality. This was then inserted into the retro-reflective ring laser.

3.4.1 Tellurium Dioxide as a Handedness Selector Within a Ring Laser

The same retro-reflecting ring laser as depicted in *Fig. 3.9* was used to test out the TeO_2 as a handedness selector. The crystal was placed between the two 45^o mirrors opposite the Nd:YAG crystal. The laser was initially aligned to operate with CW handedness without the TeO_2 crystal. Images of the Mach-Zehnder interference patters from this are shown in *Fig. 3.13*. The transverse intensity profile of the mode remained consistent with earlier results. When the TeO_2 crystal was inserted a clear reversal of the handedness, to ACW, was observed. This was independent of the orientation of the TeO_2 crystal as expected with chirality being reciprocal. The output remained multi-mode. We also inserted the FR, in addition to the TeO_2, in both directions into the cavity. The handedness remained ACW in all cases. Unexpectedly having the FR's magnetic field co-propagating with the mode qualitatively improved the spiral interference pattern. This is especially unusual as previously the aligned rotator had favoured a CW handedness. Opposing the magnetic field with the beam propagation had minimal effect on the spiral quality. With the TeO_2 in the cavity the handedness was much more stable. The handedness could only be reversed or removed by a level misalignment that also ruined the intensity distribution. The scanning Fabry-Perot readings in all these situations showed heavily multi-mode output. Even the spectrum from the laser operating with both the TeO_2 and the opposing FR with excellent spiral interference pattern was severely multi-mode. See *Fig. 3.14*.

We have shown that a chiral material can select a preferred handedness within a laser. This laser was operating multi-mode however, it was likely operating on less modes than a typical standing wave laser. This was also a low gain system. It is possible with more gain the other sense of handedness may still reach threshold and find gain from which to oscillate. We have also shown that the selecting factor from the TeO_2 crystal appears to

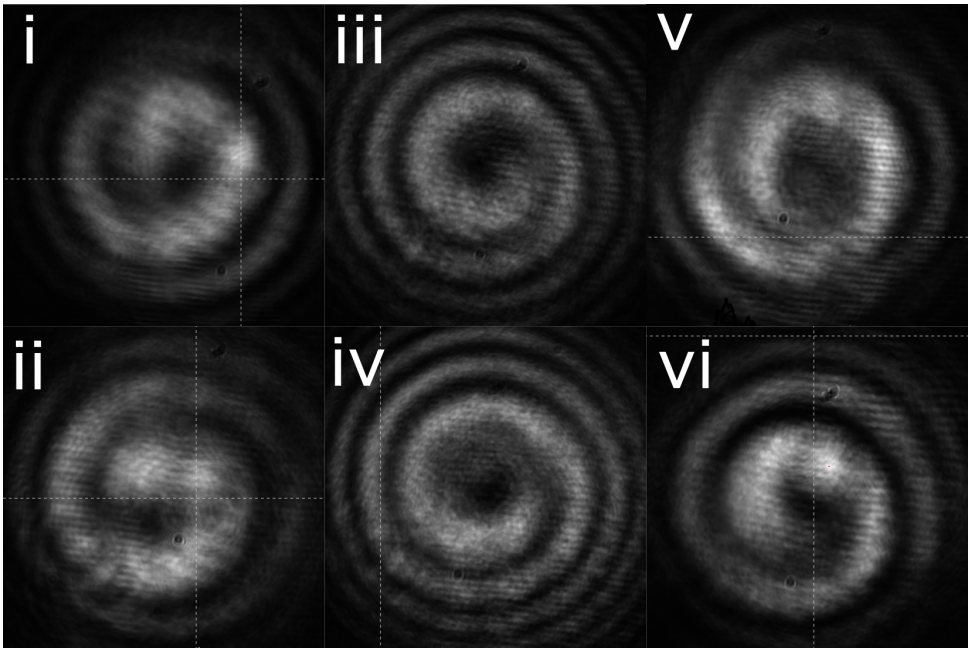

Figure 3.13: Spiral interference patterns for the retro-reflecting ring laser containing the TeO_2 crystal and/or the FR. i and ii show clear ACW handedness when contains the TeO_2 but not the FR. iii and iv show much stronger ACW spirals when the FR's magnetic field aligned with the cavity mode's propagation. v and vi similar quality ACW spirals to those with no FR when the magnetic field counter-propagated with the mode.

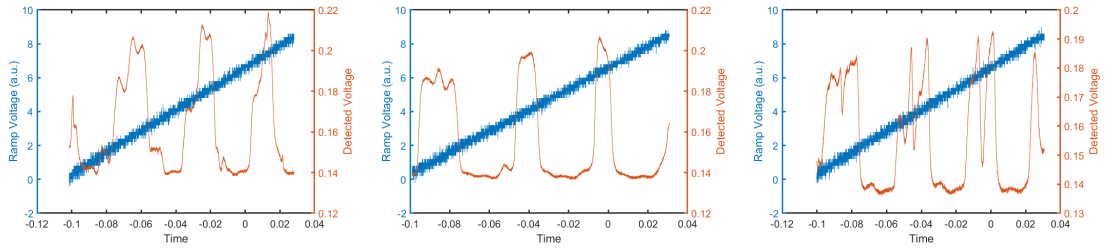

(a) *(b)* *(c)*

Figure 3.14: Fabry-Perot spectra for the retro-reflecting ring laser utilising TeO_2 as a handedness selector. *(a)* is the spectrum with no FR. *(b)* the spectrum with the magnetic field of the FR orientated with the cavity mode's direction of travel and *(c)* with the field orientated against the mode.

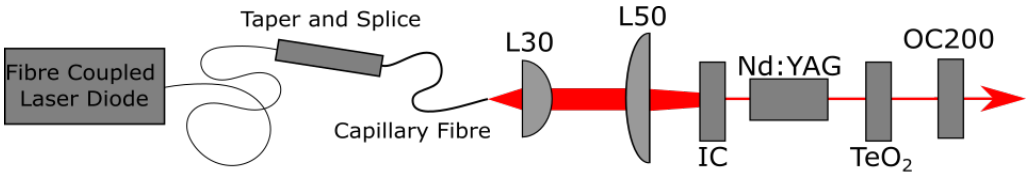

Figure 3.15: Schematic for the standing wave laser used to investigate handedness selection in higher gain systems. IC is the plane input coupler, OC200 the 5% transmission output coupler with a $200mm$ radius of curvature. The TeO_2 could be easily removed in order to test the handedness.

be stronger than that for the FR as it was able to more robustly select a handedness in the multi-mode ring laser. When both were used in tandem we also consistently observed the handedness preferred by the TeO_2. We still do not have a precise mechanism behind this observed orbital activity. The next steps are to attempt to measure its effect and test its efficacy within a standing wave cavity.

3.4.2 Tellurium Dioxide as a Handedness Selector Within a Standing Wave Cavity

We tested if orbital activity would work within a laser that is more multi-mode and has higher output power. To this end we constructed the laser seen in *Fig. 3.15*. This is a simple two mirror cavity using a 5% output coupler (the same transmission as the ring laser) with a $200mm$ radius of curvature. It was pumped using the same diode, taper and capillary fibre as the ring laser from this chapter. The same Nd:YAG crystal was also used. The additional output power comes from the large reduction in the number of cavity optics, greatly reducing the loss. The cavity length was adjusted to $132mm$, without the TeO_2 crystal for optimal matching of the LG_{01} mode with the ring shaped pump. We present the beams and spiral interference patterns from this system in *Fig. 3.16*. Here each beam is presented above its interference pattern. We can see we obtained reasonably high quality LG_{01} modes. i and iii are beams produced with no TeO_2 in the cavity. We can see i exhibits no clear sense of handedness and iii has a weak spiral indicating CW handedness. It was also possible to obtain ACW handedness with slight adjustments to the cavity alignments. This indicated there is no clear loss differential naturally in the two mirror cavity.

Inserting the TeO_2 crystal we found much the same result as without it. The cavity length was slightly shortened in order to maintain proper pump overlap. We see in v and vii of *Fig. 3.16* that the beam quality remained comparable, as did the spiral interference patterns. vi and viii show that both CW and ACW handedness were obtainable though

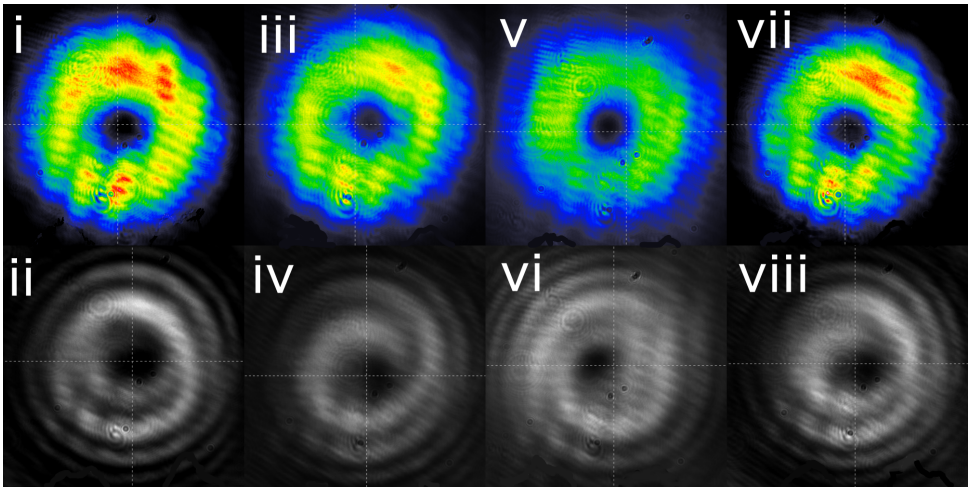

Figure 3.16: i and iii are examples of the transverse intensity profiles of the laser operating without the TeO_2. ii and iv are their corresponding Mach-Zehnder interference patterns. v and vii are beam examples with the TeO_2 and vi and viii are their interference patterns.

neither spiral is strongly convincing of a robust helical phase front. This indicates that in a more highly multi-mode and high power system, a $10mm$ length of TeO_2 is not a credible handedness selector. Similar experiments were done with the Faraday rotator described in Section 3.5, and again this was found not the be a viable handedness selector.

An interesting additional note is that the TeO_2 crystal's faces were likely parallel enough to each other for it to function as a weak etalon. This makes this experiment analogous to those done by Kim *et al.*, where they use the angle of an etalon within a cavity to select the handedness of a vortex mode [87]. We therefore altered the angle of the TeO_2 crystal in the cavity to see if we could enact a change in handedness. Whilst our experiments confirm that the handedness can be influenced by this it was never a robust change. We feel this effect is more closely linked to the misalignment of the cavity, like that which is achievable by re-aligning the cavity mirrors. We therefore do not feel our experiments support the claim that an etalon's interaction with the Poynting vector acts as a handedness selector.

3.5 Orbital Activity Measurement

Our hypothesis to explain the handedness selection in the ring laser involves FRs and TeO_2 having a property that causes a differential loss between the two senses of handedness of vortex modes. We have termed this orbital activity. In order to attempt to directly measure this we used the output from the ring laser with the FR to enforce unidirectionality detailed in Section 3.2. This provided $290mW$ of near pure LG_{01} mode with

a clear sense of handedness. The purity was assessed using the methods detailed in Section 4.4, as well as the implicit assumption that a single longitudinal mode beam will be of a single transverse mode. The beam was then split into two beam paths with an equal amount of power. This was ensured by inserting a linear polariser into one arm, and then using a half waveplate to re-orientate the polarisation in line with the other beam path. These beams were then fed into a amplified balanced detector. We used the PDB210A Si Photodetector from THORLABS^{TM}. This is a specialised photo-detector that receives two separate inputs, subtracts them from each other, then amplifies the subtracted signal. In this way it reveals any small differences between the two signals with high resolution. By using two arms of the same beam they will have the same pattern of noise from the laser. Any detected differences will therefore come from differences that arrise during their traversal of free space. In order to minimise any phase delay between the two signals it is important to keep the distance between the source and the detector equal in each arm. In one arm we can then introduce our orbitally active material and measure the difference in power detected. This measurement is unsuitable for the TeO_2 as we would need to be able to distinguish the loss incurred from traversing the crystal's two optical boundaries from that of the orbital activity. Whereas for the FR we can compansate for the losses incurred by the optical boundries in one arm by adjusting the balance of power in each arm with the polariser. The magnetic field can then be introduced to isolate the detection of any losses from orbital activity. We therefore initially measured the orbital activity of a FR. A schematic of this experiment is given in *Fig. 3.17*.

For this experiment we used a larger FR in order to try to increase the orbital activity, making it easier to detect. A TGG crystal $100mm$ in length was used in combination with a stack of ring magnets producing approximately $0.18T$ of uniform magnetic field over the length of the crystal. This should cause a 142^o rotation of the linear polarisation. In the arm without the polariser we inserted the TGG without the magnets then rotated the polariser until an even amount of power was registered in both arms of the detector, accounting for any loss caused by the optical surface of the TGG. The noise on the amplified signal was found to be $0.2V$, from a measured input signal of $1.25V$. As the gain factor on the amplifier in the detector at $1064nm$ was approximately $10,000$ this means we should have been able to detect a difference in power between the two arms of 0.001%. The magnet was then slowly translated over the TGG. If our theory is correct this will slowly increase the level of orbital activity. This was done with the magnetic field orientated in both directions. We expected to see a greater drop in transmission in one direction compared to the other. However no such drop was detected upon multiple repeats of the experiment. This could either be because we are mistaken by the cause of the handedness selection within the laser. Or alternatively the effect is too small to be

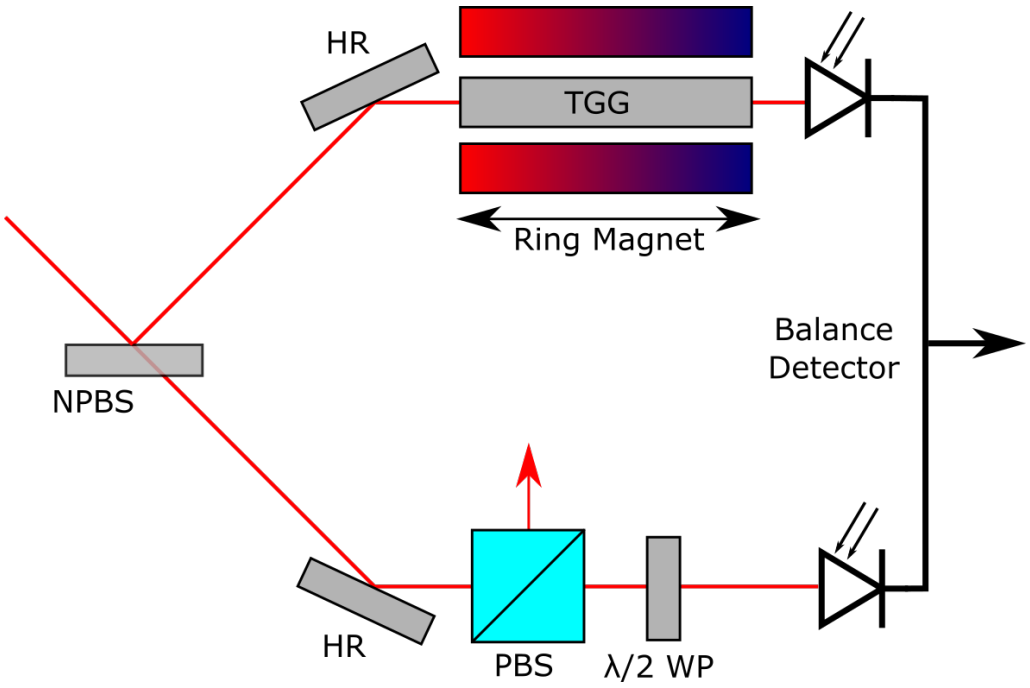

Figure 3.17: Schematic for the orbital activity measurements. NPBS is a 60:40 non-polarising beam splitter; the lower power beam goes towards the TGG. HR is a highly reflective mirror and PBS is a polarising beam splitter. This can be rotated to control the power in this arm. $\lambda/2$WP is a zero-order half waveplate. The ring magnet can be translated to vary the strength of the Faraday effect.

detected. Detection sensitivity was limited due to the difficulty in moving a strong magnet close to metallic objects. A rig was created to attach the magnets to a translation stage to minimise this problem. Despite this, it was still challenging to introduce the magnet without misaligning the FR. Nevertheless enough measurements were made that we feel reasonably confident that if orbital activity is present in FRs, it is not detectable in our system.

There are several improvements that could be made to this experiment. A more powerful vortex mode beam could be used to improve the signal to noise ratio. A FR offering more rotation might make the orbital activity effect stronger, increasing the size of the loss we are trying to detect. We should also attempt to test the TeO_2 for orbital activity. This would most easily be achieved with a source that could be reliably switched between either the two senses of handedness or a vortex mode and a Gaussian. It would need to do this whilst keeping the power in each arm of the detector exactly equal. This would be a challenging source to operate, however the best candidate might be to use a SLM to modify a Gaussian beam as described in Section 1.4.3. We have not undertaken these experiments to date.

3.6 Conclusions

In this chapter we sought to investigate a method for selecting the handedness of first-order vortex modes within a laser cavity. We built a single-vortex-mode ring laser in order to remove ambiguity from the system. In doing this, we discovered a link between the handedness of the vortex mode and the direction it traversed a Faraday Rotator within the cavity. It appeared the FR caused a loss differential between the two senses of handedness depending on whether the beam was either co-propagating or counter-propagating with the magnetic field. We named this effect orbital activity. It may be possible to amplify this beam up to machining powers, however the seed laser has very poor efficiency and is alignment sensitive, so this may not be practical.

This effect was shown to exist within a multi-mode, but still approximately unidirectional ring laser. However, the effect was less pronounced. We believe this was due to the loss differential being very small, allowing modes with the opposite or no handedness to access some of the gain. We introduced a crystal of $\alpha - TeO_2$ in order to investigate whether a chiral material would cause a similar effect. This was found to be true and appeared to give much more stable handedness selection in the multi-mode laser.

Both a FR and the TeO_2 were inserted into a standing wave laser operating on a

LG_{01} mode. Neither were found to have any impact on the handedness of the output. An attempt was made to measure the scale of orbital activity in these materials using a highly sensitive balanced detector. However, no loss differential between opposite senses of phase was uncovered. This leaves doubt as to the source of the handedness selection found in our ring laser. It is possible that it is due to another effect within the laser cavity or that it was interacting with another mechanism in the laser that was not found in free space. It also appears that this effect is unlikely to be strong enough to be practical in multi-mode lasers. More research is needed in order to understand these preliminary results, as well as a theoretical explanation for the source of the loss differential selecting the handedness. We must conclude that this is not a viable route for generating high power vortex modes with controllable handedness.

Chapter 4

Higher-Order Transverse Mode Purity

As we have seen there are many ways to generate vortex modes with varying advantages and disadvantages. One key metric that is often overlooked is the purity of the mode produced. This is important as any experiment or application involving a vortex mode is likely to be investigating or utilising one of the unique properties of the mode. Most impurities in a mode will not have the desired properties. This will limit the efficiency of a given application and obscure the results of a scientific investigation. Quantifying this purity more carefully is therefore critical to further development in this field.

In this chapter we will be discussing how to detect and identify impurities in higher-order transverse modes. We therefore need to state clearly what we mean by impurity. Impurities are the result of any phenomenon that causes the electric field of our beam to deviate from that of the mode we desire. These come in two broad categories, non-modal impurities and modal ones. Non-modal impurities primarily come from scattering effects and optical aberrations. Examples include scattering from particles smaller than the beam, spherical aberrations incurred from focussing and chromatic aberrations from interactions with matter that are wavelength dependant. Modal impurities are laser modes, other than our desired one, that are co-propagating or near co-propagating with the beam. We need not be concerned by modal-impurities that are not co-propagating with the beam as they will leave the beam path as it travels. An example of a beam with a modal impurity would have 80% of its power associated with the fundamental mode but 20% with an LG_{01}. Assuming it is the fundamental mode that is wanted for the application this would be a beam with a 20% modal impurity.

In reality, due to fourier theory, any non-modal impurity can be considered a modal

impurity; as any distibution of light can be constructed out of an infinite sum of HG or LG modes. One can therefore view, for example, scattering effects as changing the modal content of the beam. For our purposes however, the disctiction between modal and non modal is useful. It distiguishes between situations where the impurities are in a few distinct modes that individually cause enough distirtion to the beam that it can be relatively simply measured and quantified; and those where the distortion is the result of a potentially infinite sum of undesirable modes, each at a power level that is near undetectable.

We should also distinguish impurities from noise. We define noise as any phenomenon that, upon measurement, makes our beam appear less pure than it actually is. An example being background light picked up by a CCD camera. Whilst minimising noise is important to gain an accurate understanding of the purity of a given beam, it does not contribute as an impurity. In this chapter we will use the term impurity as an umbrella term for both modal and non-modal impurities. When quantifying purity we will state the percentage of the power in a given laser beam that is related to the desired mode. We will generally give the lower estimate of this value, as our methods will have measured the level of a specific impurity. This assumes all other impurities are minimal, however our methods cannot guarentee that there is not some portion of the power in impurities that are not quantified; hence using the lower estimate.

In order to gain a complete understanding of the purity of a mode it would be neccessary to know both the beams entire intensity and phase distribution. Detecting both simultaneously is exceptionally challenging and beyond the scope of this thesis. We will instead be looking either at a limited measurement of the phase and intensity or just the intensity profile. We will then combine this information with knowledge about how the beam was produced to predict what impurities might be present. We can then analyse the data to attempt to confirm this and in some cases quantify the level of impurity, provided are assumptions are correct.

4.1 Literature On Higher-Order Mode Purity

There have been many approaches to measuring higher-order mode purity. One of the most common is to quote the beam propagation factor of the beam, its M^2 [87, 88, 112, 113]. This is the most common way of stating the purity of the fundamental mode. The M^2 is defined so that it is 1 for a pure HG_{00} mode. Any M^2 larger than this is a clear sign of impurity and is correlated with its scale. A pure LG mode has $M^2 = 1 + 2p + l$ where p and l are the radial and azimuthal mode orders respectively [114]. For a HG mode the M^2 is often different in the two axes and given by $1 + 2n$ where n is the order in the

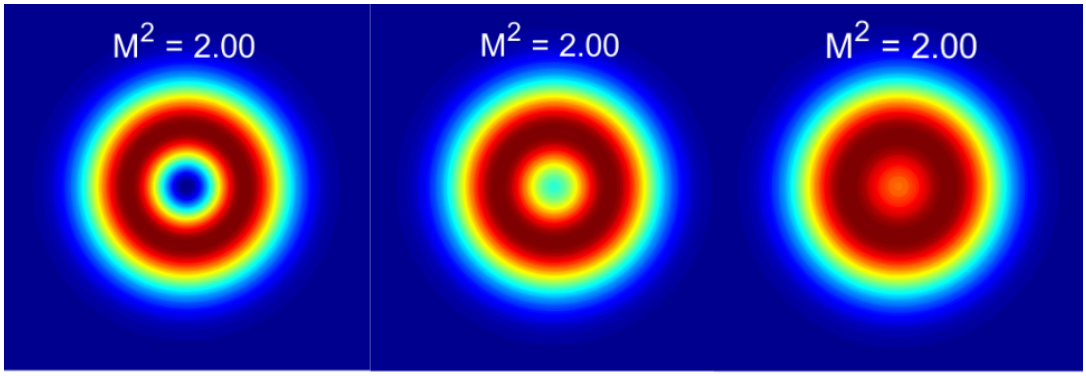

Figure 4.1: The three beams are all theoretically generated on the same scale, and propagated over three Rayleigh lengths either side of the focus of the the pure LG_{01} mode. The M^2 was determined by the beams second moment of intensity at 50 locations along this path. The left beam is a pure LG_{01} mode, the middle has both a LG_{00} and LG_{02} mode impurity at 20% the intensity of the main mode, while the right has the same impurities at 50%. They all have an identical M^2 of 2.

given axis. When considering modal-impurities in higher order modes it is possible for the impurities to have both higher and lower M^2 values. This makes the use of the beam propagation factor as a purity measurement limiting as impurities could be masked by both the presence of a higher and lower order impurity.

We demonstrate a theoretical example of this in *Fig. 4.1.* Here we have simulated an LG_{01} mode with various levels of modal impurity passing through a focus. The left image has no impurity, the middle both a LG_{00} and LG_{02} impurity. Both being 20% the power of the main mode, meaning only 71.4% of the total power is in the LG_{01} mode. The right image takes this to the extreme with the same LG_{00} and LG_{02} impurities being 50% of the total power. The right image is clearly impure losing its central intensity null. However the middle is less impure. In both cases the presence of the LG_{02} mode is unreadable from the image alone. We calculated the M^2 of these beams by taking the second moment of intensity at 50 points along the beam, up to three Rayleigh ranges either side of a focus with a $100\mu m$ radius. All the beams have an M^2 of 2, meaning that, for any given M^2, many combinations of modes are possible and it gives no clear indication of either the amount or kind of impurity present. Therefore, other methods must be used in addition to this.

One way to extract more information from an M^2 measurement was shown by Chard *et al.* [115]. They looked more closely at the radii of a LG_{01} beam as it propagated through a focus. They examined its evolution along two orthogonal axes and noted that the radii in each axis were nearly identical to each other along the beam's whole propagation. This

demonstrated their mode had high circularity, a key feature of a DM.

A more detailed method involves analysing the one-dimensional intensity profile [73, 116, 117]. This is generally done by either taking the intensity profile along one axis of a HG mode or the average radial profile of an LG mode. A numerical fit of the appropriate theoretical intensity distribution is then done. One can then compare the difference between the measured and theoretical beam. This has several uses, including highlighting any peaks with either excess or missing power as well as additional power in what should be intensity nulls. This comparison with theory makes such discrepancies much clearer than looking purely at the intensity profile in isolation. However it suffers from ignoring much of the data captured in an intensity profile. It also takes no consideration of the phase, for example whether the beam is changing as it propagates.

By only looking along one transverse axis of of the beam, one ignores all the information in the other axis. For example: if examining a HG_{01} mode that happened to have a HG_{11} mode impurity, its profile would be identical to a pure mode in one axis, but different in the other one. In the LG case averaging azimuthally about the beam can hide azimuthal asymmetry in the beam, a common sign of HG impurities. Furthermore, this technique does little to say what kind of impurity is present, other than that additional power in the centre of a mode is often an indication of the fundamental mode as an impurity.

A more powerful technique, is to use a SLM for modal decomposition [77, 118, 119]. This involves displaying a phase pattern that will reflect the power of given mode and scatter all others. One can then measure the power distribution between each mode. This can reveal both the kind and amount of each mode in a given beam. It is, however, cumbersome, with SLMs being both expensive and sensitive to damage from high incident powers. It also requires careful alignment and the foresight to test for what modes might arise as impurities in a given system. For example it may be that a HG mode is the major impurity in a predominantly LG beam. If one only scans for LG impurities this will be missed, the missing power likely attributed to additional loss in the diagnostic system. It is also not a single shot system, with time needed to record the data for each mode reflected by the SLM It also requires careful measurement of the power reflected for each change of the pattern on the SLM. This system can give a very accurate reading of modal-impurities but requires a significant investment of time and resources to implement. A less thorough but simpler diagnostic may be more useful in many situations.

A recent paper by Sroor *et. al.* has also done a thorough analysis on the purity of

cylindrical vector modes (i.e. radial, azimuthal and other exotic polarisation states of DMs) [120]. They analyse these states in a manner analogous to quantum entanglement. This allows, with the help of modal decomposition by an SLM, for any given LG_{01} mode's complete polarisation state to be broken down into a set of base states. This can then be compared to the desired state of the mode. This method whilst complex in theory, is only capable of distinguishing one kind of DM from another. Which, whilst important, is insufficient in the case where more than one order of transverse mode is present, which is often the case.

Therefore we seek to find an easily implemented yet powerful diagnostic for higher-order mode purity. This will improve the ability to compare the relative merits of various methods for creating higher-order modes. Furthermore it will help guide research in improving existing techniques in terms of mode purity.

4.2 Estimating Vortex Mode Purity By Analysing its Mach-Zehnder Interference Pattern

Several methods can be used to detect the presence of OAM within a beam. The two most common involve interfering the beam with a spherical wave generated from itself [81, 87, 88, 90, 121, 122]. This is generally done using a Mach-Zehnder interferometer see (3.1.4). If the beam is co-propagating with the spherical wave a spiral is formed with the handedness of the spiral corresponding with the handedness of the beam and the number of spirals the azimuthal order of the vortex mode. If the beam and wave are misaligned a pattern of fringes is observed. A fork in the fringes indicates the presence of OAM and the number of forks the azimuthal order. Images of these two patterns are given in *Fig. 4.2*. A third way to detect OAM is to astigmatically focus a vortex mode. Due to the Gouy phase shift (see Section 5.1) the mode will be converted to a corresponding HG mode at 45^o to the axis of astigmatism. A non pure-vortex mode will not result in a HG mode and simply show a 'squashed' doughnut profile. All of these methods are a binary measurement of whether OAM is present or not. In the case of a vortex mode with impurities they cannot by themselves tell us what percentage of the power carries OAM.

We have found it is possible to still observe spirals in an impure beam as *Fig. 4.3* demonstrates. Here three beams have been simulated that all have an identical intensity distribution to the LG_{01} vortex mode. They are in fact: a pure vortex mode; an incoherent superposition of the vortex mode and a DM containing no OAM, with the DM having half the power of the vortex mode; and another incoherent superposition of the vortex mode with a vortex mode of the opposite handedness, again at half the power of the main vortex

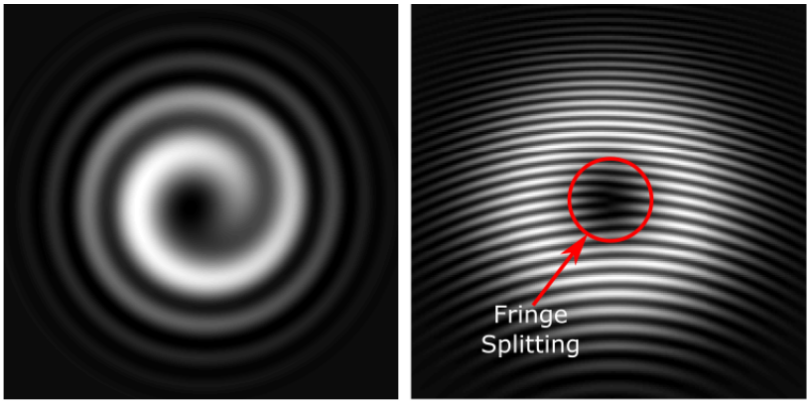

(a) (b)

Figure 4.2: (a) shows a typical fork interference pattern for the LG_{01} vortex mode. (b) shows a typical spiral interference pattern for the same mode.

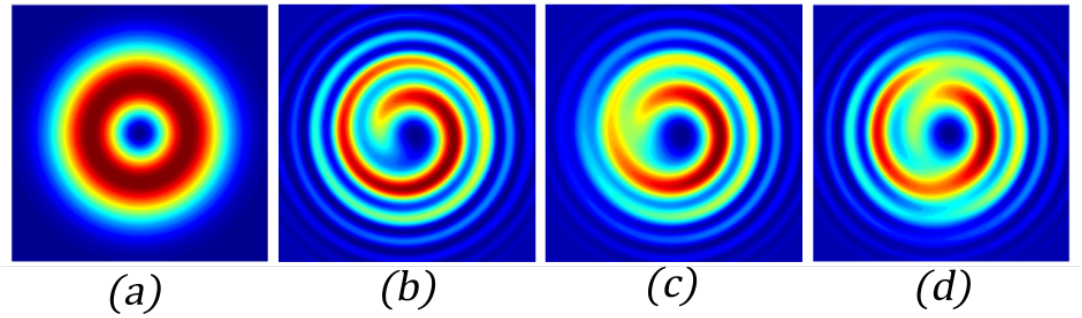

Figure 4.3: Simulated spiral interference patterns of DMs containing various amounts of OAM. *(a)* is the intensity profile of all the modes. *(b)* is the interference pattern of a pure vortex mode. *(c)* the interference pattern of an incoherent superposition of a vortex and a DM containing no OAM. *(d)* is the interference pattern for an incoherent superposition of two vortex modes with opposite handedness.

mode. This first superposition of modes only contains $^2/_3{}^{rds}$, and the second, half the OAM of the pure mode. All the beams are interfered with the same, coherent, spherical wave to get the three spirals. The interference pattern of the vortex and the no OAM mode has less contrast in the spiral due to the impurity. However, without the pure comparison this would easily be missed. The interference of the opposing vortex modes again has less contrast and a distorted spiral. Similar patterns to these, i.e. unlear spirals, have been observed experimentally in work throughout this thesis. Particularly in Chapter 3, with regards to the retro-reflecting ring laser in Section 3.9. This clearly shows the limits of a Mach-Zehnder interference pattern to detect OAM.

We consider a method to more quantitatively analyse these spiral patterns. Whilst it will not detect the impurities demonstrated in *Fig. 4.3*, it will detect another common impurity, HG modes. This method can give an indication of what fraction of the maximal

$l\hbar$ of OAM a vortex mode can contain, as well as the level of impurity in LG modes created by methods likely to cause HG_{01} impurities.

4.2.1 Relation Between HG and LG Modes

An $LG_{01}^{+/-}$ mode can be de-constructed into two orthogonal HG_{01} modes that are $\pi/2$ out of phase [70]. Therefore we know that any laser cavity capable of supporting a LG_{01} mode can support these as well. It follows that these are likely impurities to arise when generating doughnut modes via any method internal to a cavity. Furthermore, in an AMC (see Chapter 5), if the input HG_{01} mode is not perfectly orientated at 45^o, or the converter is misaligned, some residual HG_{01} mode content will be left in the output. We should examine what happens to the Mach-Zehnder interference pattern in the presence of additional HG_{01} mode content.

4.2.2 Simulating a Mach-Zehnder Interferometer

By making the z value in the equation for the electric field of a HG mode, equation (4.1), $\lambda/4$ greater for the HG_{01} mode than the HG_{10} mode we can simulate a $\pi/2$ phase shift. If these are of equal field strength and we take the sum of them, we create a LG_{01} vortex mode.

$$\begin{aligned} E_{HG}(x,y,z) = E_0 \frac{w_0}{w(z)} Hp^m\left(\frac{\sqrt{2}x}{w(z)}\right) Hp^n\left(\frac{\sqrt{2}y}{w(z)}\right) \\ exp\left(\frac{-x^2-y^2}{w(z)^2}\right) exp\left(\frac{i\pi\left(x^2+y^2\right)}{\lambda R(z)}\right) \\ exp\left(\frac{-i2\pi z}{\lambda}\right) exp\left(i\left(n+m+1\right)\zeta(z)\right). \end{aligned} \tag{4.1}$$

$$E_{HG}^{10}(x,y,z) + E_{HG}^{01}(x,y,z+\lambda/4) = 2E_{LG}^{10} \tag{4.2}$$

If we then reduce the total electric field strength of one mode, we add a controllable HG_{10} impurity whilst retaining a pure vortex mode of decreased power.

$$E_{HG}^{10}(x,y,z) + 1/2 E_{HG}^{01}(x,y,z+\lambda/4) = E_{LG}^{10} + 1/2 E_{HG}^{10}(x,y,z) \tag{4.3}$$

If we then multiply the summed electric fields by their complex conjugates, we can see their intensity profiles. This accurately simulates a vortex mode with a HG_{01} impurity. The first row of *Fig. 4.4* clearly shows how the mode evolves from a pure LG_{01}^{+} to a predominantly HG_{10} mode, as the power in the HG_{01} mode is reduced.

To simulate a Mach-Zehnder interferometer we need to sum the mode fields with a coherent a spherical wave. The electric field of a spherical wave is given in cylindrical

coordinates r, θ and z, by

$$E_{Sph} = \left(\frac{1}{r}\right) exp\,(ikr)\,. \tag{4.4}$$

The second row of *Fig. 4.4* depicts the interference patterns produced. In contrast to the beams, the spirals are less obviously impure and hold a clear sense of handedness even with a 40% HG_{01} impurity. Whilst these impure beams do contain some amount of OAM it is not the maximal $l\hbar$ per photon present in a pure vortex mode. In a given experiment that is reliant on OAM, a more robust measurement of its presence is needed to quantify the amount present.

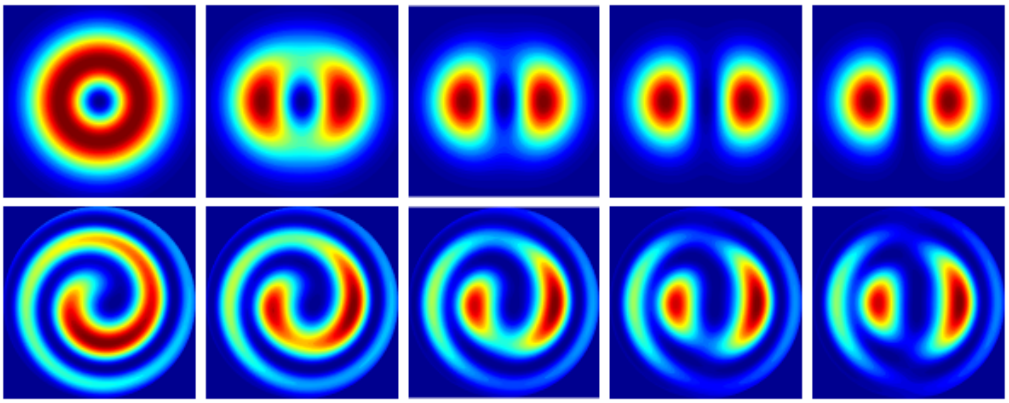

Figure 4.4: Theoretical intensity profiles generated by summing the electric fields of a HG_{10} mode with varying amounts of HG_{01}. All intensities are normalised. The top row is the intensity profile of the beam while the bottom is their corresponding Mach-Zehnder interference patterns. From left to right the HG_{01} impurity is 0%, 20%, 40%, 60% and 80% of the beam's total electric field strength. The spiral pattern is retained even for a highly impure beam.

4.2.3 Theoretically Measuring The Azimuthal Intensity Variation

If we look at the interference pattern created by the pure first-order vortex mode we can qualitatively see it is more azimuthally symmetric than those with the impurity. We can quantify this by taking a narrow slit the length of the pattern diameter and placing it in the centre of the image to sample only a small segment of the intensity. If we then rotate this through 180^o and sample the intensity at a number of angles we can plot the azimuthal dependence of the intensity. We have done this digitally though it could in principle be done physically. Doing this for our different levels of impurity we get the plots in *Fig. 4.5*. We can see that as the HG_{10} impurity increases the azimuthal intensity variation increases as well. This demonstrates a clear positive correlation between azimuthal symmetry and purity, certifying a clear diagnostic for detecting the presence of HG_{10} impurity, as well as other non azimuthally symmetric impurities. It is important to note this will not detect undesirable HG_{00} or non OAM LG_{01} mode content as these impurities are azimuthally

symmetric. Therefore, its application is limited to systems where HG_{01} mode impurities are the most likely, such as with AMCs.

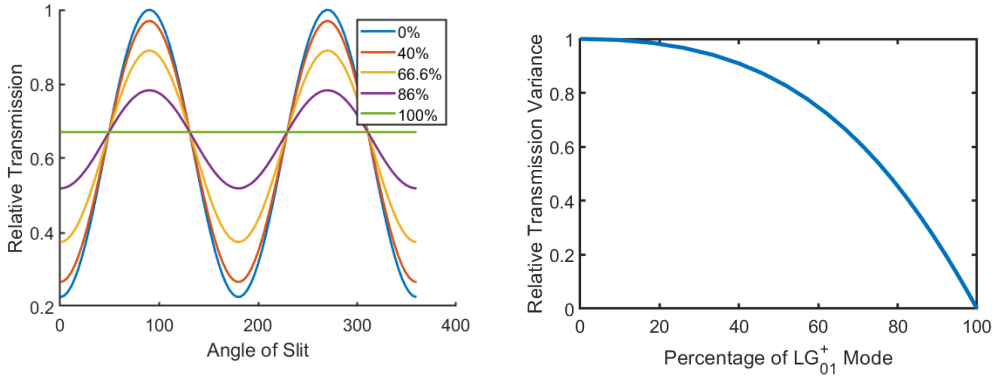

(a) *(b)*

Figure 4.5: (a) Plot of the azimuthal intensity distribution measured through a slit for the interference patterns in *Fig. 4.4*. The legend denotes the percentage of the power contained in the vortex mode. *(b)* A plot of the difference between the maximum and minimum intensity transmitted through the rotated slit.

4.2.4 Experimental Test of Azimuthal Intensity Variation

In order to confirm our theoretical results we generated LG_{01} vortex modes with controllable amounts of HG_{01} impurity. This was done using the twin pump spot laser and astigmatic mode converter outlined in 5.7. A HG_{01} mode was generated from a laser and passed through a dove prism to control its rotation. This prism was rotated through 40^o in 2.5^o increments, corresponding to an 80^o beam rotation in 5^o increments. Passing a HG_{01} mode not at 45^o through an AMC will generate a mode that can be seen as a coherent superposition of a HG_{01} and LG_{01} mode. This allows us to introduce a known amount of HG_{01} impurity. The percentage purity of the converted mode for a given rotation of the beam is shown in *Fig. 4.6a*. We measured the angle of the HG_{01} to the horizontal for each rotation allowing us to accurately estimate the vortex mode content after the converter. Example converted beam images and interference patterns are in *Fig. 4.6b*. The modes depicted correspond, from left to right, to approximately 100%, 85%, 50%, 30% and 0% vortex mode content. We can see that experimentally the spiral pattern is discernible, if degraded, even when only 50% of the power theoretically contains OAM. Therefore it is much more difficult to qualitatively evaluate a real spiral pattern. However, when we use the rotating slit analysis the azimuthal asymmetry is clearly apparent.

Fig. 4.7a shows that, as we decrease the purity, the greater the variance in trans-

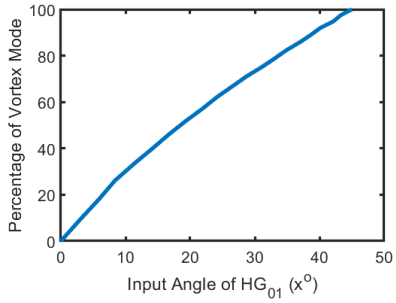

(a)

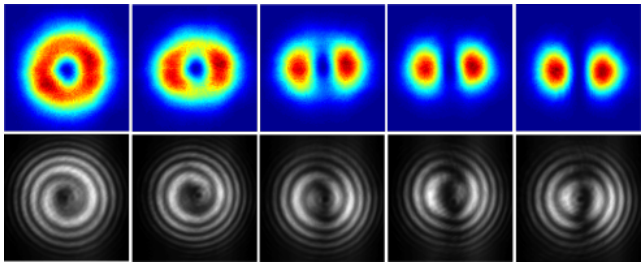

(b)

Figure 4.6: (a) shows the relation between the input angle of the HG_{01} mode and the expected percentage of LG_{01}^{+} contained in the converted modes. The top row of *(b)* depicts the LG_{01}^{+} modes converted from input HG_{01} modes at, from left to right, 45^o, 39^o, 25^o, 15^o and 1^o. The bottom row shows their corresponding Mach-Zehnder interference patterns.

mitted power we see. When we plot the difference in the maximum and minimum power transmitted against the rotation of the HG_{01} mode input, we get the curve in *Fig. 4.7b*. The transmitted power was normalised so the maximum power when a pure HG_{01} mode was fed into the analysis is set to 1. The measurement is sensitive to other impurities in either the beam or the coherent spherical wave, such as scattering from small particulates. Positioning the rotation point of the digital slit on the true centre of the spiral is also critical for an accurate measurement. This centering unfortunately had to be done by eye as we were not able to find a consistent computational way of determining the centre. This adds some error to our method and may explain the slight variations in the 'pure' beam. Alternatively it may be revealing that our beam is imperfect. The contrast between pure and impure beams was also found to be enhanced by limiting the power of the spherical wave interference pattern. This is because the amount of power in the spherical wave forms the background intensity of the image.

This method clearly differentiates between a virtually pure beam and one with more significant HG_{01} impurity. Furthermore, it is possible to estimate the percentage of the beam power that is a vortex mode by fitting the transmission variance to theory, as displayed in *Fig. 4.7c*. This demonstrates that a measurement of the intensity variance can be matched to a theoretical spiral pattern with a known impurity. This then allows one to estimate the percentage of power that is in the vortex mode, and therefore the amount of OAM contained in the beam. The accuracy of this will be strongly affected by other impurities in the beam, particularly azimuthally symmetric ones, that will not be detected by this method. Through this method, we can state that the laser and converter detailed in Section 5.7 is capable of producing modes where 94% of the power is in the LG_{01} vortex mode. The true value is probably slightly higher than this due to alignment errors in

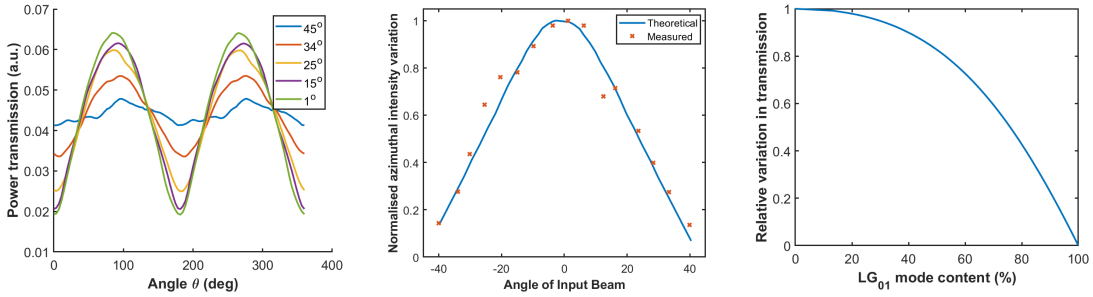

(a) *(b)* *(c)*

Figure 4.7: While not as even as the theoretical values, *(a)* shows the clear sine squared pattern emerging as we increase the beam impurity. *(b)* plots the difference between the maximum and minimum transmission through the slit for each rotation of the HG_{01} mode. We can see this fits the theoretical values very well. The theoretical values were normalised to the average intensity and image size of the measured results. The background level from the spherical wave was also subtracted. *(c)* Can then be used as a calibration curve to estimate the level of mode impurity.

the Mach-Zehnder diagnostic and extra asymmetries introduced by scattering at the CCD.

This technique means that vortex modes produced by an AMC can be of high purity and that a quantifiable measurement of this is possible. It also will have application in any other method of producing vortex modes that is liable to producing HG_{01}, or other non-azimuthally symmetric impurities. An additional advantage is that as this can be performed digitally, it applies retroactively on past work; provided a reasonable quality Mach-Zehnder interferometer pattern was recorded. Finally it has demonstrated that a spiral pattern from such an interferometer on its own is not sufficient evidence of significant OAM content. Any experiment reliant on OAM requires a more careful confirmation of its presence than has often previously been done.

4.3 Direct Measurement of Beam Purity from its Intensity Distribution

Whilst the rotating slit technique is powerful for determining the purity of a LG_{01} vortex modes, it is limited in scope to detecting primarily HG_{01} impurities. It also requires the assembly of a Mach-Zehnder interferometer which, while common practice in the field of vortex modes, can be cumbersome. Here we consider a broader more easily applicable set of techniques based on examining a beam's intensity profile.

First, we must acknowledge that for a diagnostic technique to be worthwhile it must be simple to implement. We, therefore, limit ourselves to analysing the intensity distribution

of the mode in a single plane using a CCD camera. Whilst this limits the available information, removing all data on polarisation, spatial and temporal coherence, these all have reliable diagnostic techniques already and are complemented by this analysis. Information on phase is also not assessed, though this technique could be complemented with the analysis in the previous section, for detecting OAM. A quantitative one-dimensional analysis of the intensity profile has been conducted by many authors in the past [83, 116, 117, 123], and a few have undertaken limited quantitative analysis of higher-order modes in two dimensions [68, 73]. The limitations of $1D$ analysis are discussed earlier in this chapter, whilst the two papers incorporating $2D$ analysis either compare the beam qualitatively with simulated beams, or only analyse the azimuthal variance of the beam. Our analysis seeks to investigate the purity more thoroughly. We do limit our analysis however, to the HG_{01} and LG_{01} modes, these being the modes of primary interest of this thesis. Many of these techniques would be applicable to other higher-order modes, with minor adjustments.

By limiting ourselves to analysing the intensity distribution in a single plane, we limit the situations in which our analysis will be applicable. Firstly, coherent modal-impurities will cause a change in the beams intensity profile as it propagates. To extract this information from an intensity profile we would need a minimum of two images of the beam and probably more. We will therefore largely ignore trying to detect coherent impurities. We are also primarily concerned with modal-impurities that are propagating on the same axis as the main mode, again because non coaxial impurities will cause the intensity profile to change as it propagates. These are also less of a concern with these impurities as they will eventually diverge from the beam path and can be spatially filtered. We are also limiting ourselves to beams that have majority of their power either in the HG_{01} or LG_{01} mode. This is because the analysis relies on calibrating itself on key features of these modes. Finally, our analysis involves comparing the measured beam with a theoretically generated pure mode. This simulated mode is assumed to be non-astigmatic. Therefore our analysis is only meaningful on stigmatic beams.

The following analysis is therefore only applicable to beams which have a stable intensity profile upon propagation, are predominantly either the HG_{01} or LG_{01} mode, are produced in a cylindrically symmetric system and can reasonably expected to have most of their modal impurities be incoherent. Looking at these constraints we can now predict what systems our analysis will be most applicable to. Generally HG_{01} modes have only been intentionally generated for mode conversion or coherent combination into vortex or radial modes. This has largely been done using cylindrically symmetric bulk solid-state or fibre lasers [32, 72, 73]. Understanding the cause of modal purities in fibres is beyond the scope of this thesis, however we know that a major cause of impurities in bulk systems is

unused regions of gain [85]. These regions cannot be spatially accessed by the main cavity mode but can by modal impurities. These will generally be of a different frequency to the main mode to also access gain left by spatial hole burning, and will therefore be incoherent with the main mode. They will also be coaxial with the main mode as they need to be stable within the laser cavity. LG_{01} modes are created in a broader variety of ways. We know both SPPs and SLMs create other modes besides the desired LG_{01} mode but these will be coherent with main mode as they are created from the same HG_{00} source. Our analysis is therefore less suitable than, for example, using a SLM to separate the modes. AMCs when aligned properly will create a pure, stigmatic, vortex mode. However, any impurity in the seed HG_{01} mode will carry though. We have seen that these are likely to be incoherent and coaxial so our analysis should apply provided the beam has been left free from astigmatism. Intracavity methods of generating LG_{01} modes are again mostly done in either cylindrically symmetric bulk solid-state or hybrid fibre/bulk lasers. For the same reasons we can therefore reasonably expect any impurities to be coaxial and incoherent, making our following analysis relevant.

With these limitations in place, we must identify features in the intensity profiles that we can reasonably associate with impurity. Looking first at the HG_{01} mode profile, we know for a pure mode, the line central between the two peaks should have zero intensity and the peaks should be symmetric and of equal height. Any deviation from this will indicate impurity. Furthermore, our beam should match a theoretically generated beam with the same beam radius and peak intensity. Therefore, subtracting such a theoretical intensity profile from our measured beam will resolve such impurities. As for a LG_{01} mode, the central point should be an intensity null and the ring of peak intensity should be even, as stated in [68]. The beam should also be circular. Again the same subtraction of a matching theoretical beam should reveal the spatial nature of any impurities.

To measure these in a consistent and repeatable manner it is useful to automate the process into an algorithm. This also necessitates the standardisation of any images used. As we will be simulating a matching theoretical mode to our measured beams, it simplifies the process to centre the beam in the image. The raw camera image is therefore cropped into a square, using an algorithm, with the beam centre. After this, the methods for analysing the two modes diverge. We will describe the techniques for the HG_{01} mode first.

4.4 Measuring the Purity of a HG_{01} Mode from its Intensity Distribution

4.4.1 Outline of techniques for Analysing a HG_{01} Mode

In order to analyse the beam we need to know both its size and centre. Initially we can do this by taking a weighted centroid for the beam centre. We can then initially define the beam width as the the average radial distance from this centre of every point that has $1/e^2$ of the maximum intensity reading of the image. These measurements are both somewhat inaccurate. The standard definition of beam radius is based on the second moment of the intensity distribution. For a fundamental mode this simplifies to measuring the distance from the beam axis to where the intensity falls to $1/e^2$ of the intensity on the beam axis. For higher order Gaussian modes this value can then be scaled by the root of the M^2 factor. As the HG_{01} mode is a fundamental Gaussian distribution in one axis, we can measure the $1/e^2$ points in this axis to get a more accurate size measurement for the beam. A centre defined by a weighted centroid will give a rough centre of the beam for a HG_{01} mode, but it is sensitive to the symmetry of the two peaks. As this is one of the variables we a trying to measure, we cannot assume they are symmetric. Therefore, for a HG_{01} mode we define the centre as the midpoint between the two peaks. This is only sensitive to the position of the peaks not their relative heights and is a more stable definition. For a pure HG_{01} these definitions yield the same result.

To derive the true beam width we now need to define the position of the two peaks in the image. We cannot simply take the two points of maximum intensity as these will likely sample the same peak twice. We therefore define a minimum separation of these points as a quarter of the initial beam radius. This measurement is also sensitive to noise spikes so we use a $2D$ smoothing algorithm to average this out. We can now find the location of the two peaks. This information is also used to rotate the image so its axes of symmetry lie in the horizontal and vertical axes of the image. We will define the axis of symmetry that crosses both the peaks as the 'long' axis and the axis that follows the central intensity null as the 'short' axis. The rotation simplifies the simulation of theoretical modes done later in this analysis. We can now accurately measure the centre point as the position between these two peaks.

We can now measure the relative height difference between the two peaks defined as

$$H_d = 100\frac{|H_1 - H_2|}{max\,(H_1, H_2)} \tag{4.5}$$

where H_d is the relative difference in the height of the two peaks as a percentage, and

H_1 and H_2 are the heights of each respectively. H_d should be 0 if the beam is pure. Though the exact cause of a mismatch in peak heights may be different in any given system, one potential cause would be a coherent Gaussian impurity, illustrated in *Fig.4.8*. We clearly see a large disparity in the peak heights caused by a minor coherent Gaussian impurity, $1/8th$ the power. Interestingly, there is no increase in the central minima, just a slight lateral displacement. This situation seems plausible when generating HG_{01} modes within a cavity. If there is less gain in the region corresponding to one peak than the other, it is feasible a coherent combination could be the mode with the lowest threshold. This should be easily avoided however by correct alignment of the cavity.

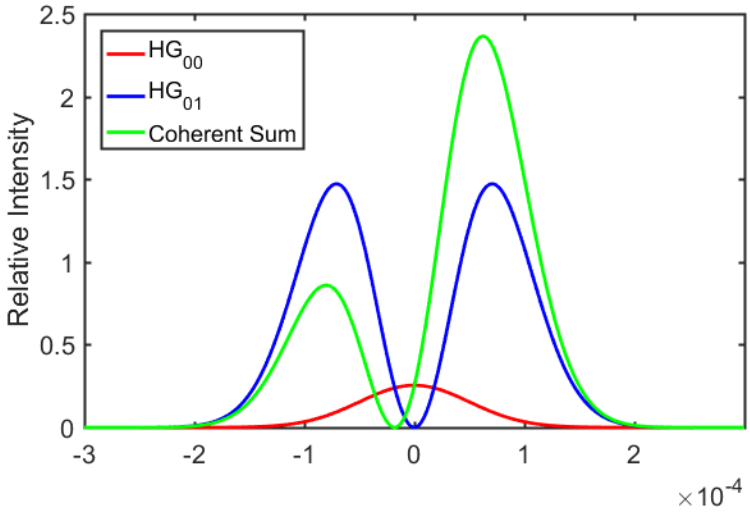

Figure 4.8: Depicts in 1D the coherent interference of a HG_{01} mode and a HG_{00} mode with $1/8^{th}$ the intensity. We clearly see that the central minima remains zero but shifted laterally slightly, however the two peak heights are substantially mismatched.

Further analysis of the mode requires generating a matching theoretical pure mode for comparison. The first step in this is working out a more accurate beam radius. This is done by taking a 1D intensity sample through the peaks parallel to the short axis of the beam. This gives us two Gaussian distributions from which we take the beam radii as defined above. We then take the average of these. This is demonstrated in *Fig. 4.9*. This measurement is sensitive to higher-order modal impurities that have the same mode order in the long axis; i.e. the HG_{11} mode. However, these modes do not seem likely to appear in most methods of generating HG_{01} modes, and this definition of the beam radius has been sufficient for all the modes we have analysed.

Now we know the beam size we can work out its Rayleigh range and Gouy phase shift using equations (4.6) and (4.7). We take z in these equations to be 0 as we are dealing

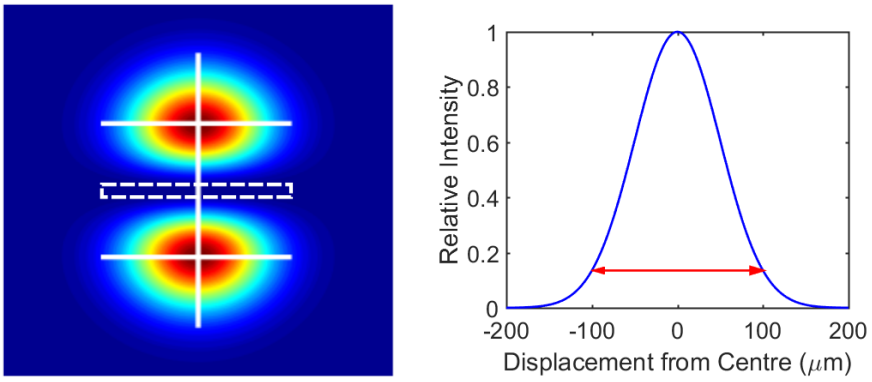

(a) *(b)*

Figure 4.9: These images demonstrate the beam widths of the HG_{01} mode as we define them for our intensity distribution analysis. *(a)* shows where we take the intensity cross sections from the beam in the short axis (the shorter lines), the longer line defines the long axis, and the central box is the region within which we measure the intensity of the central null. *(b)* and shows where the $1/e^2$ intensity point ideally lies defining the beam radius.

with a single image, and most stable laser modes hold their intensity distribution with displacement in z. This also allows us to take $w(z)$ in equation to be w_0 as defined by the the short axis radius. (Note: the beam image does not actually need to be taken at the focus.) We now plot a matching theoretical mode to the measured beam on the same axis. We define the origin of the plot to be the beam centre. We then use equation (4.1) to plot the electric field, setting m and n to 0 and 1. Multiplying this field by its complex conjugate we get a matching theoretical intensity distribution for our beam. This is then scaled to have the same peak intensity by taking the average height of the two measured peaks, I_{0m}, and multiplying the normalised theoretical intensity field by this value. See equation (4.8). We can now compare between the measured and theoretical beams.

$$z_R = \frac{\pi w_0}{M^2 \lambda} \tag{4.6}$$

$$\zeta(z) = arctan(\frac{z}{z_R}) \tag{4.7}$$

$$E_0\, E^{01}_{HG}(x,y,z) \text{ x } E_0\, \overline{E^{01}_{HG}}(x,y,z) = I_{0m}\, I^{01}_{HG}(x,y,z) \tag{4.8}$$

We compare the intensity null down the centre of our measured beam to a theoretical one. We know it should be zero, however simply measuring the intensity of the centre point of the beam is sensitive to noise and any misalignment in determining its position. To compensate for this, we define an area, centred on the mode, that is the width of the beam in the short axis and $1/20^{th}$ the beam width in the long. See *Fig. 4.9.* We can then

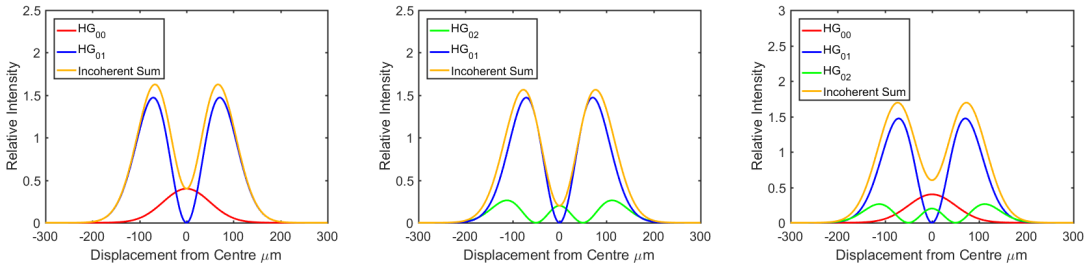

(a) *(b)* *(c)*

Figure 4.10: One dimensional depictions of the sum of intensity profiles of a HG_{01} mode with HG_{00} and HG_{02} impurities. Impurities are 20% the power of the main mode. Note that the increase in the central intensity null is equal to the peak intensity of the impurity.

take the average pixel (intensity) value in this area for both the measured and theoretical mode. Subtracting the theoretical average from the measured, gives us how much more power there is in the centre than we expect. We can compare this to the average peak height to get a normalised measure for the excess power in the central null.

4.4.2 Identifying Specific Impurities

The final and most powerful diagnostic technique is to subtract the matching pure intensity profile from the measured one. In so doing we are left with the residual intensity distribution which we will call the residuals. It is useful here to examine what the residual will look like for certain modal impurities. The two most likely impurities to arise from generating HG_{01} modes are the adjacent HG modes, HG_{00} and HG_{02}. It is easier to analyse this residuals in one dimension. We simulate three modes: a HG_{01}, fundamental and HG_{02}. The latter two have 20% the power of the HG_{01} mode. We then combine these into three impure beams: the HG_{01} plus the fundamental, the HG_{01} plus the HG_{02} and finally the sum off all three. These are displayed in *Fig. 4.10*.

We can see the fundamental impurity slightly contracts the position of the peaks, and adds power where the central null should be. Interestingly the height of this excess power matches the height of the Gaussian. The HG_{02} mode impurity slightly increases the spacing of the peaks and also adds to the central minima in the same manner as the fundamental. An even combination of the two keeps the peak separation the same but adds power to the centre and generally broadens the beam.

We continue our simulation by plotting a matching HG_{01} mode for our simulated impure beams in the same manner as described in the previous section. i.e. we have a pure

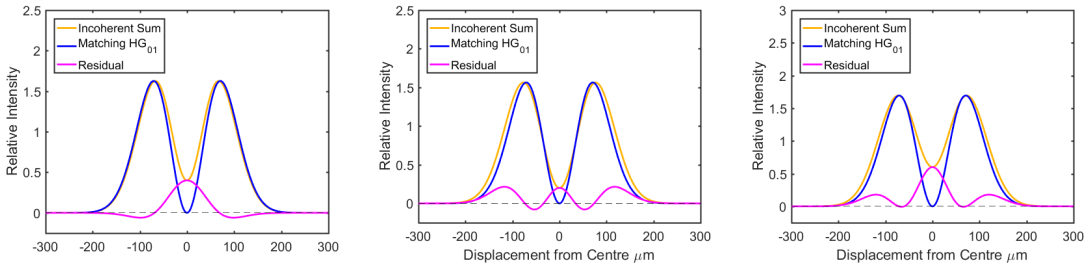

Figure 4.11: The 1D residuals for a HG_{01} mode combined with: *(a)* a fundamental mode impurity at 20% of the power of the HG_01 mode, *(b)* a HG_{02} impurity at 20% of the power, and *(c)* both impurities. Each exhibits a distinct structure.

HG_{01} mode with the same beam radius and peak intensity. Subtracting this from the sum we get the residuals in *Fig. 4.11.* When talking about residuals a 'peak' will be a positive region of residual intensity, whilst a 'valley' a negative one. We can see for a fundamental mode impurity we get a large peak surrounded by two valleys as a residual, whilst for HG_{02} impurity we get three peaks interspersed with smaller valleys. Combining the two equally reduces the size of the valleys and concentrates the power in the central peak. Following this procedure on real beams will allow us to examine the structure of their residuals in order to identify what impurities are prevalent in the beam. Furthermore we can estimate how much of a given impurity there is from this residual.

4.4.3 Identifying and Quantifying HG_{00} Impurities

The analysis in the following two sections, whilst powerful, is limited in scope. It allows us to identify and quantify the amount of incoherent fundamental or HG_{02} modal impurity there is in a given HG_{01} beam only under certain conditions. This includes all the conditions stated in Section 4.3, as well as the condition that the modal impurity is the only significant impurity in the beam. Small amounts of non-modal impurities can be tolerated; however if, for example, there is a significant coherent as well as incoherent HG_{00} mode impurity this method would not be able to successfully extract the quantity of HG_{00} impurity. This is also true if both significant incoherent HG_{00} and HG_{02} modal impurities are present; as we cannot easily distinguish how much of the central peak is from each impurity. In the case where only one coaxial, stigmatic, incoherent modal impurity is present however, we believe this technique provides an accurate estimation of the fraction of the power the impurity holds.

We have already see that for a beam with an incoherent HG_{00} impurity the height of

the central peak of the residual is equivalent to the impurities maximum intensity. As a HG_{01} mode will contribute no power along the axis of the impurities peak we can assume the width of the residuals central peak in the short axis is equivalent to width of the impurity. Therefore to quantify a HG_{00} mode impurity we measure the width of the central peak in the residual and use this with equation (4.1), where n and m both equal 0, to plot a matching theoretical mode to the HG_{00} impurity. This is then scaled to be the same peak intensity as the central peak of the residual. We can now calculate the total power of this impurity in relation to the total power of the measured beam. This will give us the total fraction of power associated with the impurity. This figure is an estimate but is still very useful for comparing between different measured beams.

In order to check if this estimation of the impurity was correct we can sum the theoretical impurity with a theoretical HG_{01} scaled to account for the power not in the impurity. See equation (4.9). Here Pt_{00} is the power in the fundamental mode impurity we have derived from the residual, Pt_{01} is the power in the theoretical HG_{01} mode it is being combined with and Pm is the measured power of the beam. We can now subtract this new theoretical match mode from the measured beam. We should see that most of the structure in the residual has gone and we are only left with patterns caused by non-modal impurities. We should also see a reduction in the total power left in the residual. To measure this we need to take an absolute sum (i.e. taking the modulus of each pixel and then summing them) due to the negative intensity values in the residual. The total power of the residual on its own means little as much of the power in it is from noise. However subtracting our theoretical match modes has no impact on the noise structure. This means a comparison of the absolute sum of residuals that result from subtracting two different theoretical match modes can tell us which was a better fit for the measured beam. In this context we can therefore see if by adding a fundamental mode impurity to our theoretical match, we more closely approximated the true beam. If this is the case the absolute sum of the residual will decrease and we obtain good evidence that our suggested type and level of impurity is present in the measured beam.

$$Pt_{00} + Pt_{01} = Pm \tag{4.9}$$

4.4.4 Identifying and Quantifying HG_{02} Impurities

Similar analysis for estimating the amount of HG_{02} mode impurity can also be performed. The identifying residual pattern for an incoherent HG_{02} mode impurity is three peaks interspersed by two valleys. Assuming the impurity is coaxial, we can again use the height of the central peak to estimate the peak height of the impurity. Analysing a pure HG_{02} mode we see that the width of the central peak is equal to its beam width in the short

axis and that this peak height is 76.14% of the height of the outer lobes. We can again use this information in conjunction with equation (4.1) to generate a theoretical model of the impurity. The total power of this gives us an estimation for the percentage of the beam associated with the impurity. We can then simulate a HG_{01} mode that accounts for the remainder of the power and sum this with the impurity to create a new theoretical match mode. When this is subtracted from the measured beam we should again see a residual with little to no structure left. The same limitations as for estimating a HG_{00} impurity apply.

4.4.5 Analysing Real HG_{01} Modes

To investigate the validity of the analysis described in the last four sections we apply it to three predominantly HG_{01} modes generated using the apparatus described in Section 5.7. In brief this involves using two adjacent pump spots to better overlap with the HG_{01} mode in a solid state laser. The impurities are generated by varying the separation between the spots by translating one of them. This should increase the overlap with either the HG_{00} or HG_{02} modes. Furthermore this moves one of the pump spots further away from the central axis of the laser cavity, slightly misaligning it. The measured intensity profiles, matching theoretical modes, peak height difference and excess central power of the modes are displayed in *Fig. 4.12*. *(a)* has a $128\mu m$ separation between the centres of the pump fibres (which have a $105\mu m$ core radius), *(b)* a $187\mu m$ separtion, and *(c)* a $215\mu m$. Many more beams were analysed than these three, however these serve as illustrative examples.

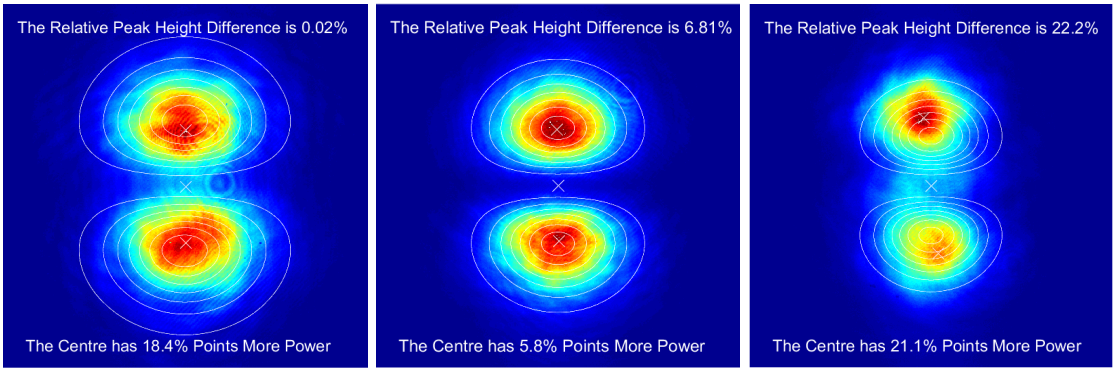

(a) *(b)* *(c)*

Figure 4.12: Three predominantly HG_{01} modes with their peak and centre locations marked by white 'xs', peak height difference, excess central power both written at the top and bottom of the images respectively), and matching theoretical mode (white contour lines) displayed.

We can see that our basic analysis yields powerful results. Whilst *Fig. 4.12c* is clearly impure, with different intensities in each lobe and lots of excess power between them; the

difference between *Fig. 4.12a* and *Fig. 4.12b* is less obvious. However, looking at our measurements for peak height difference and excess central power, we can see that *(a)* has near perfect peak symmetry but significant excess central power. This possibly indicates an incoherent modal impurity as we have seen that coherent modal impurites tend to not add power to the central null and give unequal powers in the peaks.. As with this beam the pump spots were placed closer together than in *Fig. 4.12b*, we might expect this to be a HG_{00} mode. This tells us we should experiment with increasing the separation between the pump spots. *(b)* has much less excess central power, but a 6.8% peak height mismatch. This probably indicates that either the laser needs to be re-aligned so the cavity mode sees equal gain from each pump spot, or the power in each pump spot is uneven. These different impurities and their subsequent remedies would be hard to pick up from the image alone. Our analysis however clearly reveals this. Determining how to take *(c)* to a purer mode is, however, more tricky as there are clearly several issues. There is a significant peak height discrepancy, large excess central power, and we can visually assess its peak spacing is much larger than a true HG_{01} mode.

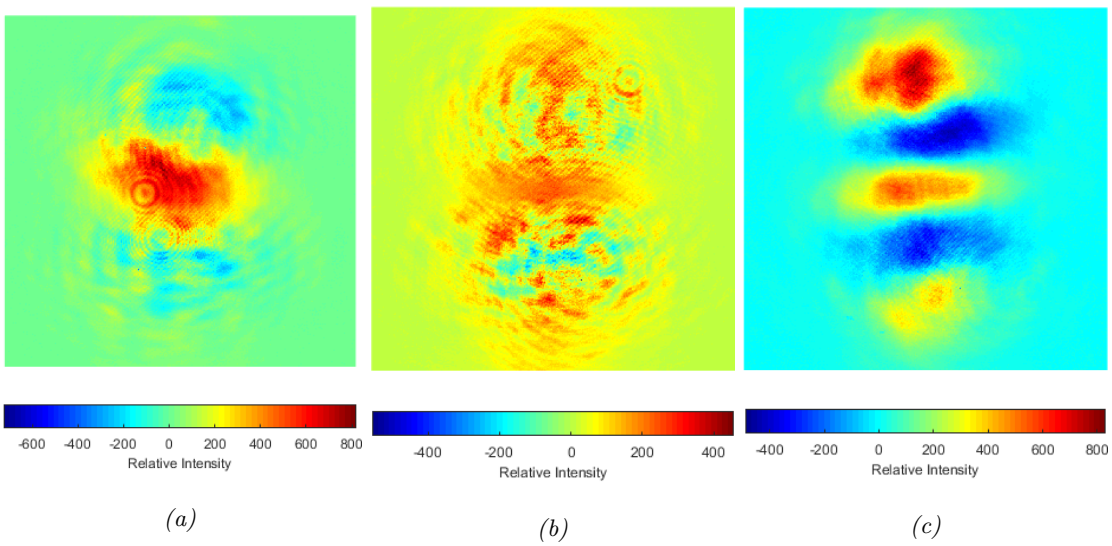

Figure 4.13: Plots of the residual power remaining after matching theoretical HG_{01} modes are subtracted from the beams in *Fig. 4.12*. Note the smaller scale in *(b)*.

Fig. 4.13 depicts the residuals for each mode. They each exhibit a distinct structure. *Fig. 4.13a* shows a central peak with two adjacent smaller valleys. *Fig. 4.13b* is mostly general noise and Airy rings created by scattering from small particulates, with a slight central peak. *Fig. 4.13c* shows three clear peaks interspersed by two valleys. We can therefore infer that *Fig. 4.13a* has a HG_{00} impurity, *Fig. 4.13b* no significant modal impurity and *Fig. 4.13c* a HG_{02} impurity.

We can now attempt to quantify the suspected HG_{00} impurity in the beam from *Fig. 4.12a*. We measure the peak height and width of the central peak in the residual and generate a simulation of it. Measuring the total power of this we find that accounts for approximately 38% of the power of the measured beam. This is much higher than one might expect from an initial look at the image. Even if this is an overestimation of the significance of the impurity it still shows that careful analysis of the mode purity is warranted. When we take the HG_{00} impurity into account for the matching theoretical mode we get a better match for the measured beam. The new residual is shown in *Fig. 4.14a*. It has significantly less structure as well as a reduced scale. What is left appears to mostly be from non-modal impurities such as the airy rings from scattering. Furthermore, when we compare the absolute sum of the power left in the residuals we find the remaining power has reduced. In this case the initial residual contains 24.6% of the power in the measured beam, while the second residual, created from subtracting the theoretical match mode that includes the HG_{00} impurity from the measured beam, contains only 16.3% of the power, a 33.7% reduction. This improvement is a strong validation that a significant portion of the beam's power is contained in an incoherent HG_{00} modal impurity. The measured beam, both theoretical match modes, residuals and the estimated impurity are all shown in three dimensions in *Fig. 4.15*.

We can perform the same analysis on the beam in *Fig. 4.12b*. The 3D plots are in *Fig. 4.16*. Here the beam is much closer to pure, with only an estimated 0.8% of the power in the HG_{00} impurity. This is small enough that it could be attributed to noise or to CCD blooming. This is a phenomenon where charge leaks from one pixel to others near it if they are under strong illumination for a sustained period. As a CCD conducts more easily in one axis than another, this leads to streaking in one dimension [124]. This may also explain the slight broadening of the peaks compared to the theoretical model, as power detected in the peaks leaks out. This shows the current limit of our analysis where it will struggle to accurately detect small impurities. However, looking at the 2D plot of the improved residual, we can see the central peak has diminished and there has been a 9.2% reduction in the absolute power of the residuals.

The analysis to estimate the quantity of the HG_{02} modal impurity in the beam from *Fig. 4.12c* was trialled. However, it proved unsuccessful in generating a better matching theoretical mode. It is suspected this was due to there being both HG_{00} and HG_{02} impurity present in this beam. More work is needed to find a useful metric to determine the ratio of these before this analysis can deal with multiple significant impurities. Another mode generated by the twin pump spot system outlined in Section 6.5 however, was found to have an impurity that appeared to be pure HG_{02}, see *Fig. 4.17*. This system used

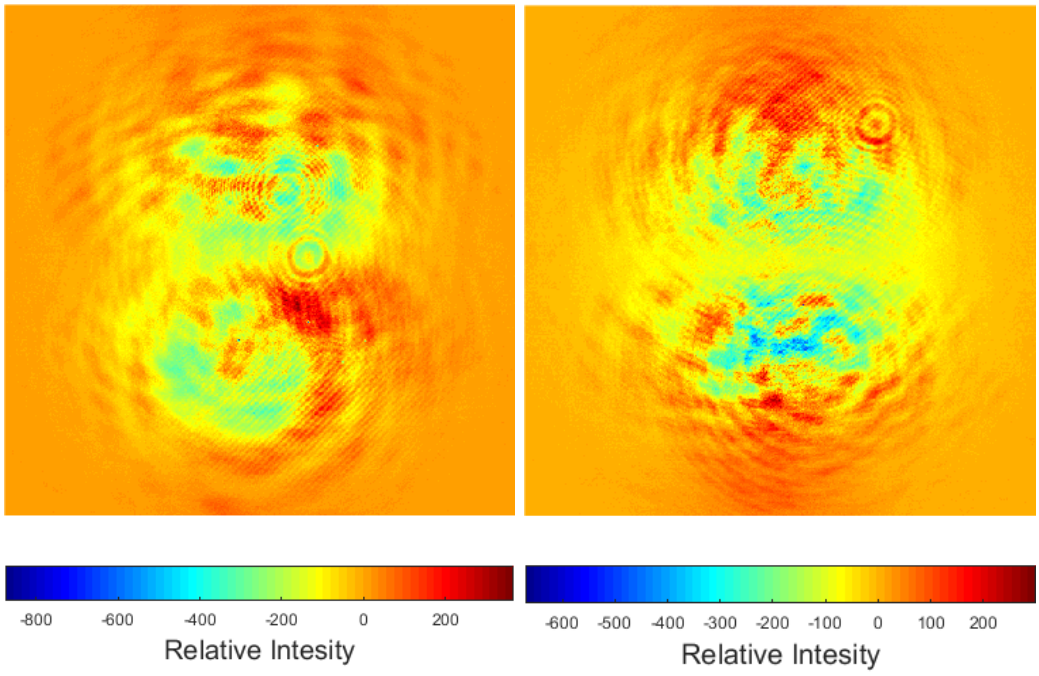

(a) *(b)*

Figure 4.14: The residuals for the beams in *Fig. 4.12a* and *Fig. 4.12b* after the estimated Gaussian impurity has been taken into account in the theoretically matching beam.

the same twin pump spot technique to select for the HG_{01} mode as that for the modes analysed above, but used a shorter laser cavity. We therefore used this, amongst other modes produced by this system, to test our ability to detect and quantify HG_{02} impurities. Looking at the residual left after a matching HG_{01} mode is subtracted from the measured beam, *Fig. 4.17b*, we see the clear three peaks interspersed with valleys pattern we expect from a HG_{02} impurity. To identify the scale of this impurity we again measure the height and width of the central peak of the residual. We found that measurements of the width of the central peak of the residual gave an inaccurate beam width for the theoretical HG_{02} mode, in that it gave an impurity much larger than that of the main HG_{01} mode and did not qualitively match what was observed in the measured beam. We therefore used the width of the measured beam in the short axis to estimate the spot size of the impurity. The peak intensity of the theoretical was then scaled to be 1.313 times the height of the central peak in the residual, as this is the ratio between the heights of the central and outer peaks of a pure HG_{02} mode. The total power of the imputityas then measured to estimate how much of the total measured power the impurity is responsible for. We can then generate a matching theoretical mode that is a combination of the HG_{01} and HG_{02} modes

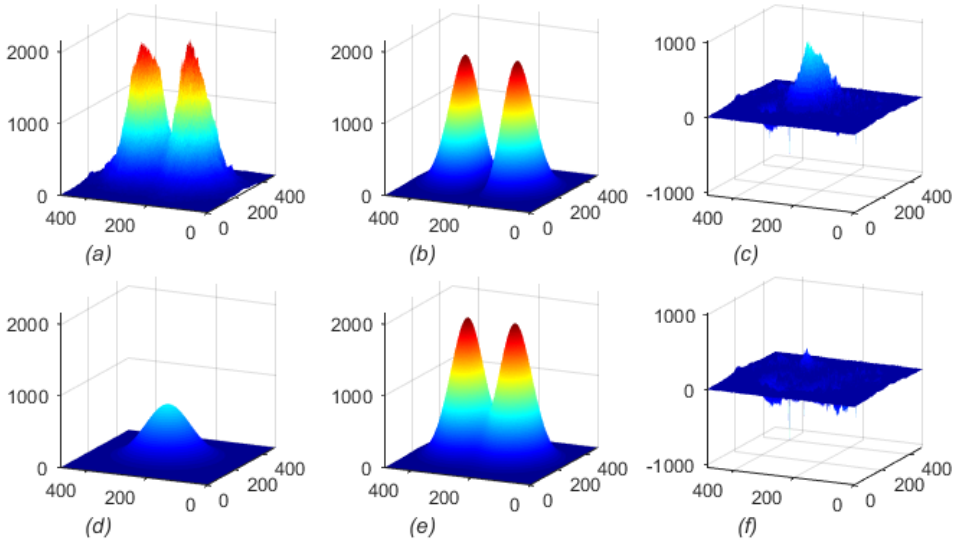

Figure 4.15: 3D plots of the beam from *Fig. 4.12a*. All images are on the same scale; *(a)* is the measured beam, *(b)* the initial matching theoretical HG_{01} mode, *(c)* the residuals. *(d)* is the estimated HG_{00} mode impurity, it is 38% of the total measure power. *(e)* is the new matching theoretical beam which is the estimated HG_{00} impurity summed with a HG_{01} at 72% of the total power. *(f)* is the new residual, its absolute intensity is reduced by 33.7%.

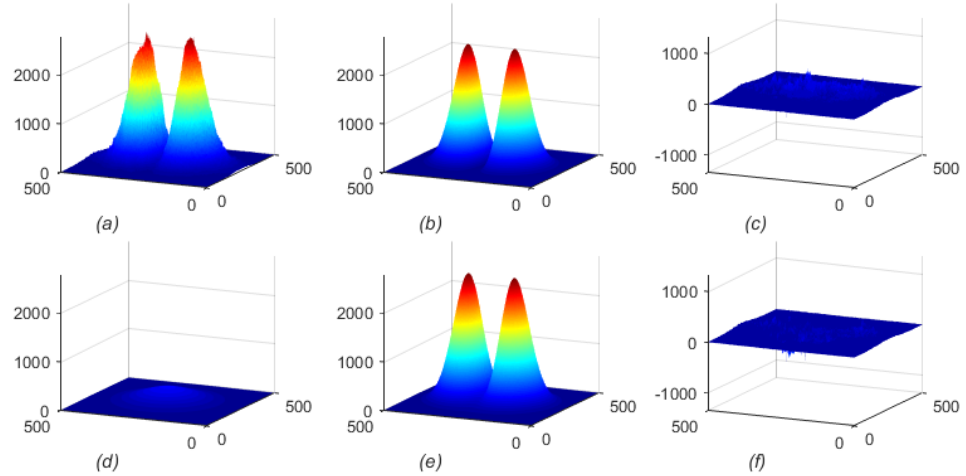

Figure 4.16: 3D plots of the beam from *Fig. 4.12b*. All images are on the same scale. *(a)* is the raw beam, *(b)* the initial matching theoretical HG_{01} mode, *(c)* the residuals. *(d)* is the estimated HG_{00} mode impurity, it is 0.8% of the total measured power. *(e)* is the new matching theoretical beam which is the estimated HG_{00} summed with a HG_{01} at 99.2% of the total power. *(f)* is the new residual, its absolute intensity is reduced by 4.5%.

and subtract this from the measured mode to see if there's an improvement in the residual.

We estimate that the HG_{02} impurity is 31.7% of the total beam power. Combining this with a theoretical HG_{01} mode and subtracting it from the measured beam we get the residual in *Fig. 4.17c*. We see a dramatic improvement from the previous residual. There is 54.7% less power in the new residual and also significantly less structure. The peaks and valleys are still there, though inverted, but have significantly less intensity. This suggests that we may have overestimated the amount of power in our impurity or it could be due to how the impurity is interacting with what is causing the peak height mismatch. It is also possible that there is some small amount of Gaussian impurity that is causing this discrepancy. Despite this we feel this is an accurate model of the beam. It indicates that a smaller gap between the pump spots is needed, or that the cavity mode size is too small for optimal gain matching. The accuracy of this model is highlighted in the 3D plots in *Fig. 4.18*. We can see the second theoretical mode is visually a much better fit for the measured beam and the subsequent reduction in structure of the residual.

4.4.6 Conclusions

We have found that we can analyse any given predominantly HG_{01} mode and identify some common impurities. If these are either a incoherent HG_{00} or HG_{02} mode we can make a reasonable estimate of their percentage power within the beam. However, if multiple impurities are present we cannot extract this information. A possible solution would be to iterate through various ratios of suspected impurity and find which is the best fit. This would be reasonably easy to implement but we were constrained by both time and computing power; so this is not presented here.

As we can see this analysis of a HG_{01} mode's intensity profile is powerful. Being able to identify several key signs of mode impurity. We can detect peak height difference which is a possible indication of coherent mode impurity. We can also measure excess central power, a sign of incoherent mode impurity. Furthermore by creating a matching theoretical HG_{01} mode and subtracting it from the measured beam we can gain important information on the types of impurities present in a beam. This can greatly inform how to improve the beam quality in a given system. Furthermore if the impurity is Gaussian or HG_{02} we can obtain a decent estimation of its fractional contributions though more work is needed to confirm this. With more work it should be possible to expand this estimation to other forms of impurity. Furthermore the accuracy of this method could be improved with better understanding of typical noise profiles from CCD cameras, particularly blooming. Being able to identify and compensate for this in a given beam image would improve our ability to detect small impurities.

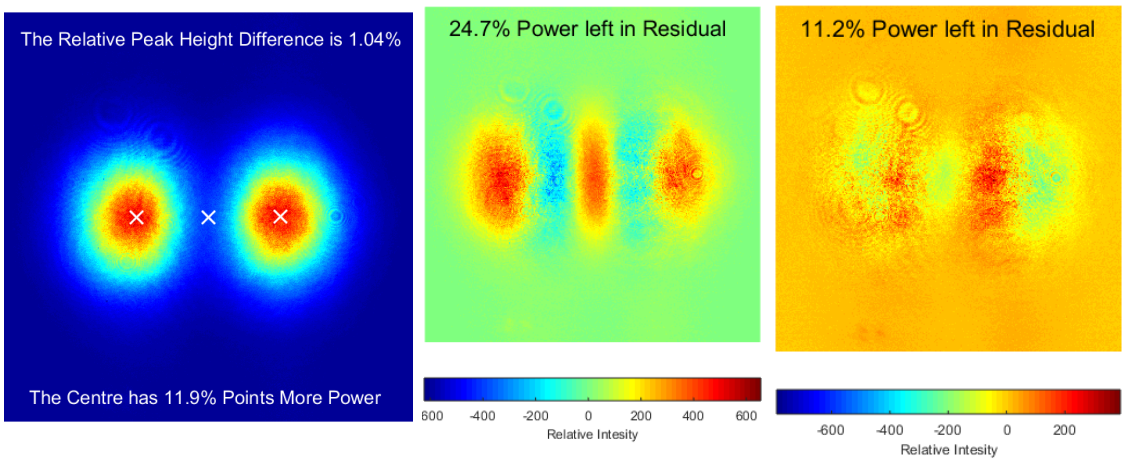

(a) *(b)* *(c)*

Figure 4.17: (a) displays a beam produced by the twin pump spot system. *(b)* is the residual after a matching HG_{01} mode has been subtracted from the beam. *(c)* is the residual when 31.7% of the power in the matching theoretical mode is HG_{02}.

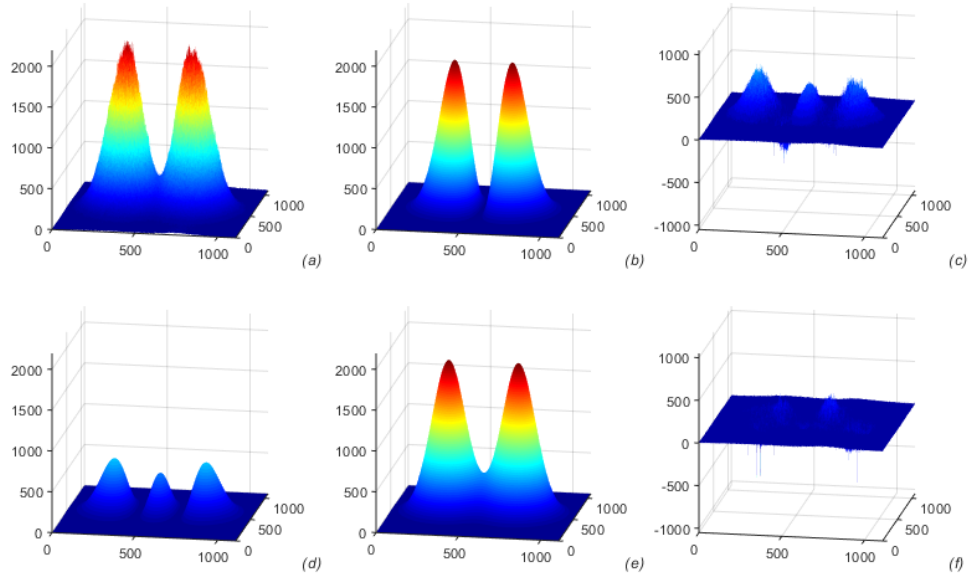

Figure 4.18: 3D plots of the beam from *Fig. 4.17a*. All images are on the same scale. *(a)* is the raw beam, *(b)* the initial matching theoretical HG_{01} mode, *(c)* the residual. *(d)* is the estimated HG_{02} mode impurity, it is 31.7% of the total measured power. *(e)* is the new matching theoretical beam which is the estimated HG_{02} summed with a HG_{01} at 68.3% of the total power. *(f)* is the new residual.

4.5 Measuring the Purity of a LG_{01} Mode from its Intensity Distribution

4.5.1 Outline of techniques for Analysing an LG_{01} Mode

We can follow much of the same methodology as in the last section to assess the purity of LG_{01} modes. As cylindrical symmetry is generally required in order to create LG_{01} modes, we can expect any modal impurities to be cylindrically symmetric. We can therefore expect the most common impurities to be the HG_{00} and LG_{02} mode. The one exception to this is vortex modes made by an AMC. In this case combining the following techniques with the analysis of the spiral interference pattern outlined in Section 4.2 will prove more powerful at identifying and quantfying the impurities in the beam. The key metrics we are seeking to analyse here are the beams circular symmetry, both in terms of beam width and the evenness of the peak intensity ring, how close to zero the central intensity null is, and finally the beam's similarity to a matching theoretical mode.

After the beam has been centred on the image there is one key difference in the methodology of analysing LG_{01} modes. We still define the beam radius using the point at which the intensity has fallen to $1/e^2$ of its maximum value, however there is no axis in an LG_{01} mode along which the intensity follows a Gaussin distribution. To measure the beam width we first use a weighted centroid to define the centre of the beam. This is appropriate as the symmetry of both the mode and its likely impurities helps stabilise the central position. To measure the beam width we take a 1D cross section of the beam through the centre and then identify the points of $1/e^2$ intensity measured against the average height of the two peaks. This should give a beam width $\sqrt{M^2}$ larger than the fundamental beam width defined in (4.6). The key difference is to measure this along multiple axes in order to build a picture of how the beam width varies azimuthally. Taking an average of these will give a good measure for the beam size needed to make a matching theoretical mode. A pure LG_{01} mode's beam width does not vary about its circumference. A mismatch in beam width along two transverse axes can be a sign of astigmatism. We can take an estimate of the astigmatism by taking the minimum and maximum beam widths. Rather than just taking the minimum and maximum values as is, we averaged them with the values of beam width adjacent to them about the circumference in order to minimise the impact of noise. For a more accurate measurement of the astigmatism readings, of the beam's width should be taken as it passes through a focus, as with an M^2 measurement. A severely astigmatic beam will break the conditions we set out at the start for when our analysis is applicable. Reducing astigmatism in vortex modes is critical as astigmatic focussing can convert them into a corresponding HG mode. This is a phenomenon caused by the Gouy

phase shift and is explained thoroughly in Section 5.1.

Next we wish to measure the azimuthal symmetry of the intensity. This should provide complementary information to that obtained by doing the analysis on a spiral interference pattern outlined in Section 4.2. Here we have to compromise between two factors. We want to include as much of the beam as possible so not to miss information. However we also want to avoid looking at regions of the beam with low intensity, as this is highly susceptible to noise. We also want to identify the peak intensity of the mode for scaling the theoretical match mode. For this we want to average the power in the peak intensity ring. In the latter case we want to minimise the thickness of this ring, so that we measure the peak intensity as accurately as possible. However, we also want to average enough data to minimise the effect of noise spikes. To achieve this we measure the intensity variance of two ring shaped cross sections of the beam. The first cross section has a width of half the beam width, and is positioned so it includes the maximal intensity of the beam. This includes the majority of the beam's intensity whilst avoiding the edges of the beam that are most sensitive to noise. It is skewed to the outer edge of the beam as there is a greater percentage of the total intensity further from the centre. We use this region to measure the general azimuthal intensity distribution of the beam. The second cross section is 5% of the beam width and is positioned to include the maximum power per unit area. This finds an accurate measure of the peak intensity, Ip_{LG}, of the mode and also informs us of the azimuthal symmetry of the peak region. This is the most critical part of the beam for many machining applications [49]. We can see these regions outlined in *Fig. 4.19*.

We measure the intensity variance by setting the pixel values of the beam outside each region of interest to zero. This image is then divided up into even angular sections. The mean intensity of each section is then taken. We can then plot this against the angle from the vertical to examine the variation. Subtracting the mean value from this and taking the modulus gives us the azimuthal intensity variation. The mean of this variation is a useful single number indication of the azimuthal symmetry.

From here we again need to simulate a matching theoretical mode. This time we use the electric field formula of an LG mode, (4.10), setting p to 0 and l to 1. We set $w_{(z)}$ to be the average beam width measured earlier, divided by $\sqrt{2}$ so that it is eqivalent to the fundamental mode beam width w_0 as used in (4.10). We can set z to 0 as the beam profile should be stable under propagation so this is arbitrary. We position the centre of our measured beam and the central phase singularity in the theoretical mode to the origin of our plots. We also set the phase of the central point of the LG_{01} modes electric field to be zero even though technically it is undefined. We multiply this electric field by its complex

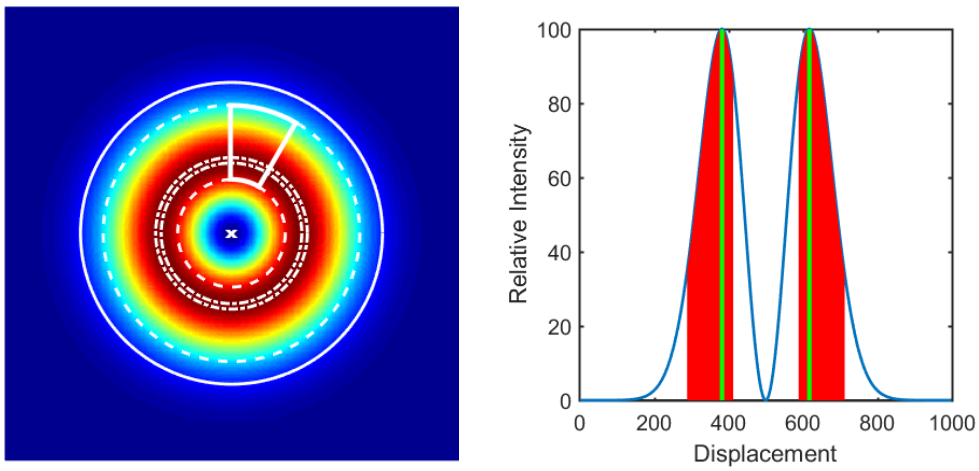

(a) *(b)*

Figure 4.19: Here we can see our definitions for the two beam cross sections used to measure the azimuthal intensity variance, as well as the definition of the beam width. The centre point as measured by the weighted centroid is also marked. In *(a)* the solid ring shows the $1/e^2$ point that defines the beam width, $\sqrt{2}w_0$. The dashed lines show the boundary of the first cross section that includes most of the beam's intensity. The dashed and dotted line is the peak intensity ring. The white box is an example of an angle slice taken for the first cross section. In reality this would be much thinner. The red area in *(b)* demonstrates the region for the wider cross section; we can see this is skewed to the outer edge of the beam. The green section shows where the peak intensity region is defined.

conjugate to get a theoretical LG_{01} vortex mode, see equation(4.11). We then scale the theoretical mode to have a maximum intensity equal to the average peak intensity Ip_{LG}. This is our matching theoretical mode.

$$E_{(r,\phi,z)} = \frac{E_0}{w_{(z)}^2}\left(\frac{r\sqrt{2}}{w_{(z)}}\right)^{|l|}\exp\left(\frac{-r^2}{w_{(z)}^2}\right)L_p^{|l|}\left(\frac{2r^2}{w_{(z)}^2}\right)\exp\left(-ik\frac{r^2}{2R_{(z)}}\right)\exp\left(il\phi\right) \tag{4.10}$$

$$E_0\, E_{LG}^{01}(x,y,z)\ \text{x}\ E_0\,\overline{E_{LG}^{01}}(x,y,z) = Ip_{LG}\, I_{LG}^{01}(x,y,z) \tag{4.11}$$

We measure any excess power in the central null using a similar method as for the HG_{01} mode. We define a box about the centre point that is 5% the average beam size in each axis. We then take the mean intensity within this and subtract the mean intensity of the same region in the theoretical mode. This tells us how much more power is in the central intensity null than we would expect if the mode was a pure LG_{01}.

We can then subtract the theoretical mode from the measured to look at the residuals. If we generate two theoretical LG_{01} modes, one with an incoherent HG_{00} impurity at 20% of the power of the main mode; and another with an incoherent LG_{01} impurity also at 20% of the power, we get the beams in *Fig. 4.20a* and *Fig. 4.20c*. We can see the fundamental mode impurity appears to have little impact on the look of the LG_{01} mode except to significantly raise the power in the centre. The power level in the centre of the beam is now equal to the peak power of the HG_{00} impurity. The LG_{02} impurity at first glance appears to have made no difference, however it is has actually widened the beam and increased the thickness of the ring slightly. If we now subtract a matching theoretical LG_{01} mode from both these beams we get the residuals in *Fig. 4.20b* and *Fig. 4.20d*. We can see the HG_{00} impurity leaves a central peak surrounded by a small valley. Whilst the LG_{02} impurity leaves a valley in the shape of the LG_{01} mode with a small peak around this. These are both distinctive patterns we can use to identify these impurities in LG_{01} modes.

It is more difficult to estimate the scale of these impurities. Whilst the central peak in the residual of the HG_{00} impurity will give us the impurities peak intensity, we cannot easily determine the mode's beam radius. The opposite is true for the LG_{02} impurity. We have no clear feature off which to measure the peak intensity but if we knew this we could measure the beam radius from the outside of the residual's peak ring to the beam centre. We might be able to quantify the level of impurity by simulating a large number of residuals and plotting trends in the structures left behind. A real residual could then

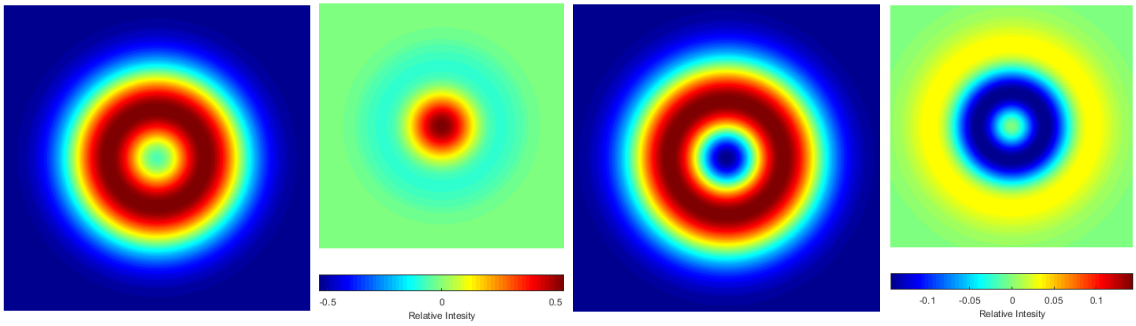

(a) *(b)* *(c)* *(d)*

Figure 4.20: (a) is a theoretical LG_{01} modes with a HG_{00} impurity at 20% the power and *(b)* its residual. *(c)* is a theoretical LG_{01} modes with a LG_{02} impurity at 20% the power and *(b)* its residual.

be fitted to this curve. However, this has fallen outside the scope of this thesis and we will not attempt to quantify the level of these incoherent modal impurities in real beams.

4.5.2 Analysing Real LG_{01} Modes

We can now apply this analysis to real beams, see *Fig. 4.21*. We have selected three beams, each produced via a different method. *4.21a* is made by using an AMC to mode convert a HG_{01} mode from the twin pump spot system described in Section 5.7. The middle beam comes from applying the same converter to a HG_{01} mode produced using the the intra-cavity slit method outlined in Section 5.6.2. The final beam is from the single longitudinal mode, uni-directional, ring laser outlined in Section 3.2. The beams made via an AMC have common sources of impurity from misalignment of the converter itself. As discussed earlier this will produce a HG_{01} impurity. This should manifest as an azimuthal intensity variance. Misalignment of the converter can also leave the beam astigmatic. Furthermore any impurity in the input HG_{01} mode will carry over into the converted mode. A HG_{00} impurity should remain unchained but any higher-order, or coherent, modal impurities could behave in complex ways. In theory the beam from the ring laser should be pure as it is operating on a single longitudinal mode, however it may be possible for there to be coherent impurities. Furthermore the beam is not immune to astigmatism or non-modal impurities.

We can see clearly that *Fig. 4.21a* and *Fig. 4.21c* are much more azimuthally symmetric than *Fig. 4.21b*. This is reflected in the azimuthal intensity distribution, with the twin pump beam varying the least and the intracavity-slit beam the most. We therefore have evidence that the twin pump beam was converted with minimal AMC misalignment. Its lower astigmatism estimation is also a good indication of this. The intensity variance

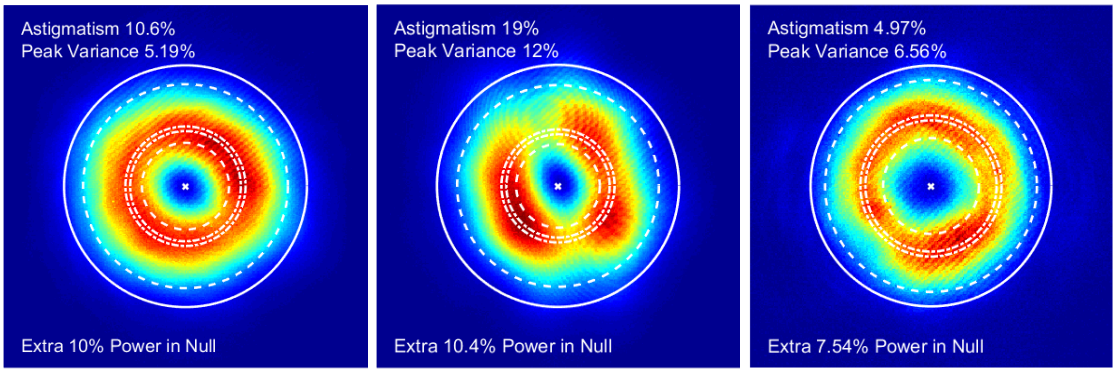

(a) *(b)* *(c)*

Figure 4.21: (a) is from the twin pump spot and AMC system described in Section 5.7. *(b)* is from the wire and slit with AMC system decribed in Section5.6. *(c)* is from the ring laser described in Section 3.2. On each beam the cross represents the centre of the beam as determined by a weighted centroid. The solid line is the measured beam width. The dashed line is the boundary of the cross section measuring the overall azimuthal intensity distribution and the dotted and dashed for the peak intensity distribution.

in the beam from the ring laser is more of a mystery, however the slight astigmatism might explain it. The beam was imaged onto a camera via a series of spherical lenses. If these were slightly off axis they may have produced a slight astigmatism and therefore a differential in the Gouy phase shift in the two axes. This would begin to convert the beam towards a HG_{01} mode. Its also possible that scattering effects could be disrupting the azimuthal symmetry.

Taking a more detailed look at the intensity variance, (*Fig. 4.22*), we can see *Fig 4.21c* has a relatively flat azimuthal profile with some intensity drops flanked by spikes. This is consistent with there being some azimuthally variant scattering. *(a)* has a very slight sinusoidal variance, in accordance with a minor misalignment in the AMC causing a HG_{01} mode impurity and the associated variation in azimuthal intensity. *(b)* has high variance in its azimuthal symmetry. There is no clear pattern to this, indicating that any combination of AMC misalignment, scattering and impurity in the source mode could be the source.

Looking more closely at the variance in the beam width, we can see a similar pattern. These are plotted in *Fig. 4.23*. The beam from *Fig. 4.21a* has a slightly sinusoidal beam width variation. This is again consistent with a misaligned converter, as a HG_{01} mode has a smaller beam width in one axis than the other, and we would expect the measured beam width to be an average of this impurity with the main mode. The beam from *Fig.*

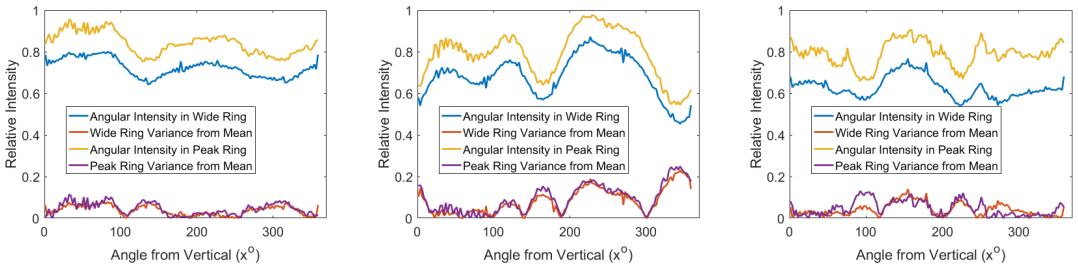

(a) *(b)* *(c)*

Figure 4.22: The angular intensity variation for the beams from *Fig. 4.21*. *(a)*, *(b)* and *(c)* correspond between these two figures. The angles are measured from the vertical. The blue lines are the mean intensity of each section of the wide cross-sections of the beams, and the red their absolute variances from the mean value. The yellow lines are the mean intensity of each section of the peak rings and the purple their variances from the mean. The y axes are scaled so that the maximum intensity value in each beam is equal to 1.

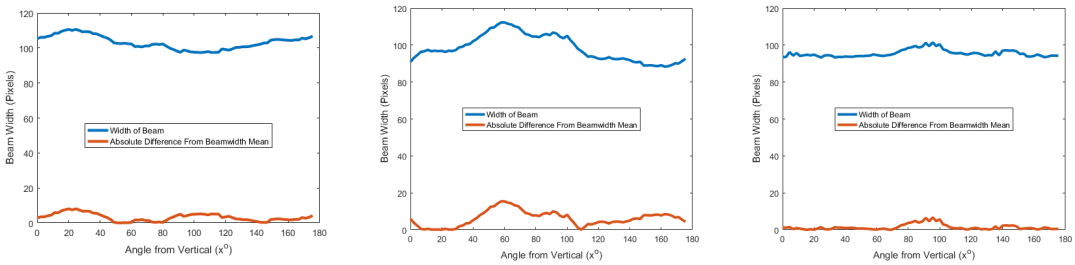

(a) *(b)* *(c)*

Figure 4.23: The angular variation in the width of the beams from *Fig. 4.21*. The blue lines are the measured width of the beam, measured in pixels. The orange lines are the absolute variance in this about the mean width.

4.21b has a more widely varying beam width with no clear pattern. This is likely a sign of several competing impurities, such as an impure input mode and misaligned converter. Finally the beam from *Fig. 4.21c* has a nearly flat beam width with two small increases. This is probably where scattering particles have pushed power out from the peak to the edges. This is consistent with the evidence from the azimuthal intensity variation. These two measurements combine to give key information about the purity of the LG_{01} mode.

Finally we will look at the residuals when a matching theoretical LG_{01} mode has been subtracted from the measured beams. We can see that both the twin pump converted mode and the ring mode have $18 - 19\%$ of the total beam power left in the residual. As discussed earlier this is not a good indication of the total purity of the beam as it is exceptionally sensitive to noise. However it is useful for comparison. Here it shows that the modes from *Figures. 4.21a* and *Fig. 4.21c* are of similar purity, while the beam from

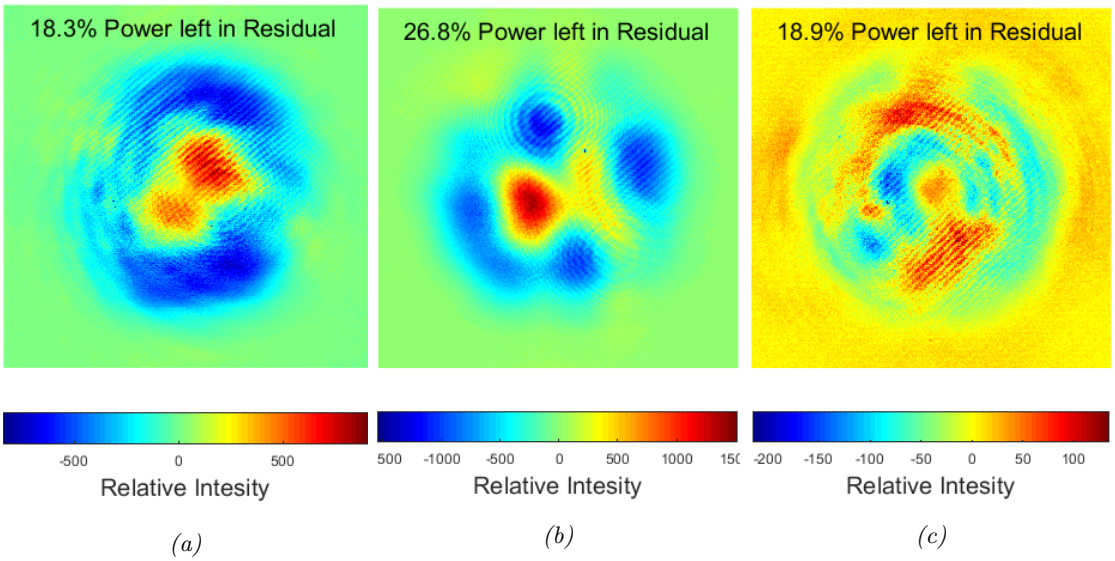

(a) *(b)* *(c)*

Figure 4.24: The residuals for *(a)* the LG_{01} mode made using the twin pump laser, *(b)* the intra-cavity slit laser and *(c)* the ring laser.

Fig. 4.21b is substantially worse. What is interesting to note is the colour scale on the figures, with the ring laser's colour bar being over a significantly smaller range, indicating the individual deviations from an ideal LG_{01} mode are much smaller. We can also see that much of the structure of the image resembles airy rings. These two factors combine to suggest that much of the mismatch of this beam with theory is caused by scattering. Looking at the residuals from *(a)* and *(b)* we can see there is excess power in the centre and missing power from around the main intensity ring. This suggests that some of the peak intensity may be from a HG_{00} impurity, as it resembles the structure seen in *Fig. 4.20b*. The height of the central peak and the depth of the ring shaped valley are roughly equal however, whereas in the theory the peak height is much greater in magnitude. This suggests that this may not be only source of of impurity. It is also possible that an entirely different impurity we have not considered could cause this structure in the residuals. Furthermore, the central structure in the residual of both modes is not a single peak but split into two regions. The outer valley in *Fig. 4.24a* is shallower in one axis that the others. This is likely the result of the slight sinusoidal azimuthal intensity variation in the beam. *Fig. 4.24b* has its outer valley severely fragmented which is again consistent with its beam's large azimuthal intensity variance.

We have therefore been able to obtain less useful information from analysing the residuals of LG_{01} modes compared to those of the HG_{01} modes. This has largely been due to the beams we've been measuring having either non-modal impurities or modal impurities we have not been able to identify from the structure in the residual. We believe this to be

mostly due to the additional complexities in generating LG_{01} modes compared to HG_{01}, leaving more areas where impurities can arise, meaning it is more likely for multiple impurities to be in play at once. We therefore need to improve our analysis to account for these situations.

4.5.3 Conclusions on LG_{01} Intensity Analysis

More work is needed in order to be able to quantify specific impurities in a given LG_{01} mode purely from its intensity profile. This may require either simulating, or creating laser beams with known amounts of different impurities. This will allow us to understand how incoherent modal-impurities effect the intensity profile of a LG_{01} mode. Measurements of the circularity of the beam and azimuthal intensity distribution do seem to correlate well with different levels of impurities, particularly in modes generated from AMCs. This combined with the analysis of spiral intensity profiles will help us determine the quality of modes generated this way. Whilst this technique hasn't given us an indication to the absolute amount of power in the beam that corresponds to the desired mode, it does allow us to compare different LG_{01} modes. This allows us to more meaningfully compare the relative merits of differing methods to produce such modes. Within a given method, it can also help detect errors from alignment and indicate what steps can be taken to improve purity.

To improve this technique a better understanding of what impurities commonly afflict LG_{01} laser systems and how they affect the intensity profile is needed. Using the second moment definition of beam width may also help us improve the measurement of the beam radius. These techniques could also be easily extended to higher-order DMs due to there similar structure. Furthermore both the LG_{01} and HG_{01} intensity distribution analysis could both be applied to the transmission through a polariser of radially or azimuthally polarised DMs. This would then extend the analysis to looking at the polarisation purity these modes.

4.6 Conclusions

We have seen how taking a more careful look at the purity of higher order mode is both necessary and challenging. We have been able to detect the presence of HG_{01} impurities by analysing the azimuthal symmetry of spiral interference patterns. This is key for estimating the amount of OAM is actually present in a beam. It is however mostly limited to use with vortex modes generated via astigmatic mode converters. One improvement to this technique would be to standardise the power and size of the spherical wave used to

interfere with the main mode.

This can be supported by our analysis of the intensity distribution of LG_{01} modes. We can again measure the azimuthal symmetry of the mode itself along with its circularity. A discrepancy in either of these is a good sign of HG_{01} impurity or a misaligned mode converter. The intensity distribution has had mixed results in identifying specific impurities. We have seen residual patterns that roughly correspond with that of an incoherent HG_{00} impurity, and later in this thesis we will see beams which more exhibit this. However, we have been unable to quantify these impurities. We should also be able to identify incoherent LG_{02} impurities but we have not created a real laser beam that contains this impurity. We can improve the analysis of these mode by moving to a second moment definition of the beam radius.

Looking at HG_{01} beams has been more successful with us being able to identify and quantify two different incoherent modal impurities. We can also easily detect and quantify a peak height mismatch, which is a key sign of impurity. To improve this analysis we should more carefully analyse the beam in the short axis in order to identify modal impurities that have an order greater than 0 in this axis. We should also attempt to understand more carefully how the beam is effected by coherent modal impurities in order to identify when these are present.

The intensity distribution analysis will be improved in general with a better understanding of various noise sources. For example background noise could be sampled from the cameras being used. We could use this information to simulate a common noise spectrum for the camera and take account for this in the beam image. Effort should also be made to detect and remove the effects of CCD blooming from the images. Unfortunately solving these issues fell outside the time scale of this thesis.

Chapter 5

Spherical Mirror Astigmatic Mode Converters

Astigmatic mode converters (AMCs) use a surprising relation between HG and LG modes to convert one to the other by exploiting the Gouy phase shift. They introduce a relative phase shift between the 'component' modes of a HG mode at 45^o to the principle axes by astigmatically focussing them [70]. In general this converts a HG_{mn} mode into a corresponding LG_{pl} mode. Here the p and l orders in the LG mode are related to the m and n orders by

$$p = min(\ m\ ,\ n\ ) \qquad l = |n - m| \tag{5.1}$$

Unlike SLMs and SPPs, AMCs have the potential to produce pure LG modes. The only requirements being correct alignment of the converter and a pure HG input. Both SLMs and SPPs introduce an azimuthal $2n\pi$ phase delay to a Gaussian beam which causes the majority of the power to transform into a beam resembling the desired mode. In principle, however, a pure mode cannot be made when only acting upon the phase in a single plane; therefore in both systems significant portions of the power are scattered into other modes, meaning the resultant beam is actually a modal superposition [39, 66, 77, 78]. This can mean the appearance of the beam is changes upon propagation, only maintaining its DM appearance in either the focal plane or the far field. This is acceptable in many applications but not all. AMCs, however, manipulate the phase over an extended region allowing for lossless conversion into a pure LG mode.

This lossless conversion opens the potential for generating very high purity modes with controllable OAM. This control comes from being able to rotate the input HG mode by 90^o in order to change the sign on phase delay. This provides clear advantages in terms of purity and efficiency over other external methods of generating vortex modes (See Section

1.4.3), whilst also providing controllable OAM unlike most methods internal to a laser cavity.

5.1 The Gouy Phase Shift

The Gouy phase shift, ζ, is an often overlooked part of the electric field equation of Gaussian beams. It is mathematically given by

$$\zeta(z) = arctan\left(\frac{z}{z_R}\right). \tag{5.2}$$

where z is the distance from the beam waist. It ultimately represents a π phase shift that occurs as a Gaussian beam moves from the far-field, though a focus and back out to the far-field. The physical explanation for this is subtle and complex [125], however an intuitive explanation is given by Robert W. Boyd in [126]. As phase is a relative measurement we must always state what we are measuring phase against. In the case of Gaussian beams we can use a plane wave of the same frequency, that has zero phase delay with the Gaussian beam where the beam's radius of curvature is infinite, i.e. at the beam waist. Plane waves can be treated using the geometric model of optics. As we know Gaussian beams do not behave as described by ray optics. It is the difference in the path length through a focus of the Gaussian beam compared to plane wave that can be attributed as the Gouy phase shift. We see this in *Fig. 5.1.* Here we have plotted the Gaussian beam path, BCD and AE, marked according to its beam width w_z, with points of equal phase, one Rayleigh length from the focus, marked as AB and DE. A corresponding geometric ray traces AE. We find that the difference in these paths tends to π as we move away from the focus. This holds for all focussing powers except when the beam is exceptionally tightly focussed, however this occurs at the same point that the Gaussian beam solution fails to satisfy the wave equation.

5.2 Mode Diagonalisation

It is possible to decompose an LG_{pl} mode into a set of HG modes of the same order N. Here N is defined as

$$N = m + n = 2p + l \tag{5.3}$$

where p and l are defined as in (5.1). The initial equations were presented in the appendix of the paper by Abramochkin and Volostnikov in [127] but are presented more clearly in both [32] and [70]. Equation (8) from [70] is given in (5.4). It states the decomposition of an LG mode's electric field into an equivalent set of HG modes. However

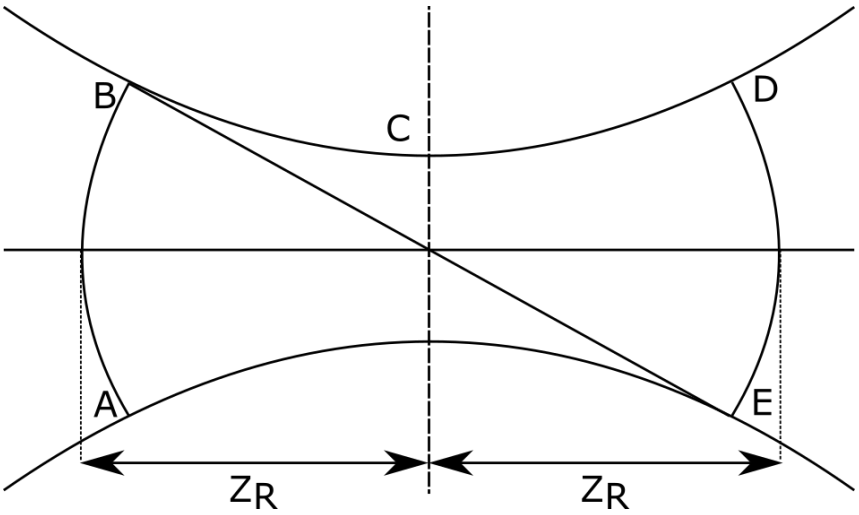

Figure 5.1: Here we see the difference in path length taken by a Gaussian beam, BCD, compared to the plane wave BE. This is attributed as the Gouy phase shift.

as equation (9) from that paper contains a slight error and we present a corrected version derived from equations (11) and (12) in [32].

$$u^{LG}_{p,l}(x,y,z) = \sum_{k=0}^{N} i^k b(n,m,k)\ u^{HG}_{N-k,k}(x,y,z) \tag{5.4}$$

where u is the electric field and b is a real coefficient given by

$$b(n,m,k) = \left(\frac{(-2)^k(-1)^k}{2^k k!}\right) \frac{d^k}{dt^k}\left[(1-t)^n\,(1+t)^m)\right]_{\ t=0} \tag{5.5}$$

We shall refer to the HG modes that can be summed to make a given LG mode as component modes. Note that the i^k term in (5.4) corresponds to a successive phase difference of $\pi/2$ between the components. Coincidently, a HG mode aligned at 45^o to the principal x and y axes can be broken down into the same set of constituent modes. We shall from now on denote this diagonal HG mode as HG^{45}_{nm}.

$$u^{HG^{45}}_{n,m}\left(\frac{x+y}{\sqrt{2}}, \frac{x-y}{\sqrt{2}}, z\right) = \sum_{k=0}^{N} b(n,m,k) u^{HG}_{N-k,k}(x,y,z) \tag{5.6}$$

The key difference here is the lack of the i^k term causing the phase shift between the terms. So all the component modes are in phase. We can therefore see it is possible to convert from a HG mode to its corresponding LG mode if we can introduce the correct phase delays. We show the constituent modes for both HG^{45} and LG modes with $N = 1, 2$ & 3 in *Fig. 5.2*. It is interesting to note that a mode will normally be formed of $N+1$ constituent modes. However in the case of the LG_{10} mode the intensity contribution from the HG_{11} mode is 0. Also of note is that for the modes with $p = 0$ all the coefficients from

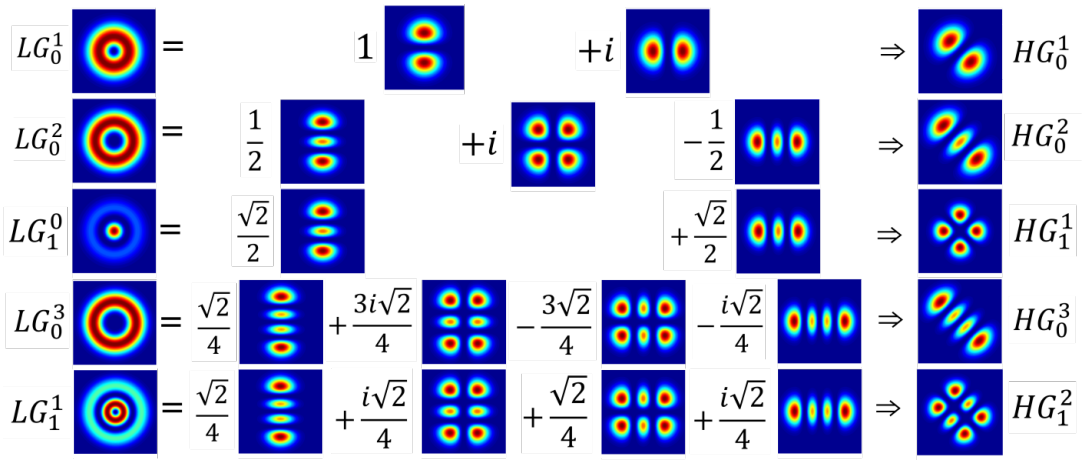

Figure 5.2: LG modes with $N = 1$ to $N = 3$ and there corresponding decomposition into HG modes. On the right is the HG_{nm}^{45} mode with the same component modes. The relative intensity and phases are given.

(5.6) are positive. This means all the component modes are phase delayed by $\pi/2$ from the previous one.

5.3 Astigmatic Mode Converter Fundamentals

One way to take advantage of this surprising relation between LG and HG modes is to use an astigmatic mode converter. This allows the conversion of a LG mode to its corresponding diagonal HG mode and vice versa (See *Fig. 5.2*). An AMC is made by simply placing two astigmatic optics a fixed distance apart. Passing a mode matched (i.e. mode with the correct beam diameter and radius of curvature to achieve conversion) LG or diagonal HG mode through this will perform a perfect conversion providing the input mode is pure. This exploits the behaviour of the Gouy phase shift discussed earlier by creating an astigmatic focal region. The electric field for a HG_{nm} mode is given in Cartesian coordinates x, y and z as [1]

$$\begin{aligned} E_{HG}(x,y,z) = E_0 \frac{w_0}{w(z)} Hp^m\left(\frac{\sqrt{2}x}{w(z)}\right) Hp^n\left(\frac{\sqrt{2}y}{w(z)}\right) \\ exp\left(\frac{-x^2-y^2}{w(z)^2}\right) exp\left(\frac{i\pi\left(x^2+y^2\right)}{2\lambda R(z)}\right) \\ exp\left(\frac{-i2\pi z}{\lambda}\right) exp\left(i\left(n+m+1\right)\zeta(z)\right). \end{aligned} \tag{5.7}$$

Where E_0 is a scaling factor, w_0 is the beam radius of the fundamental mode at the beam waist and z_R is its Rayleigh range given in (5.8). $w(z)$ is its beam radius at z, given in (5.9). m and n are the mode order in x and y respectively. From now on we

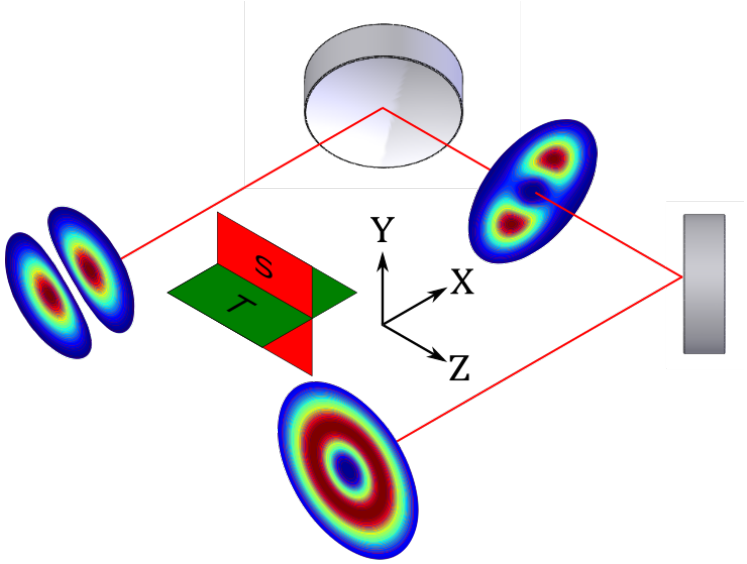

Figure 5.3: Coordinate system used for the astigmatic mode converter.

will correspond the x axis with the tangential plane, T and the y axis with the sagittal, S. The coordinate system and planes for an AMC are displayed in *Fig. 5.3*. Hp is the Hermite polynomial and λ is the wavelength. $R(z)$ is the fundamental mode's radius of curvature for its wavefront at z and $\zeta(z)$ is the Gouy phase shift.

$$z_R = \frac{\pi w_0^2}{\lambda} \tag{5.8}$$

$$w(z) = w_0\sqrt{1 + \left(\frac{z}{z_R}\right)^2} \tag{5.9}$$

Decomposing the Gouy phase shift term for a HG mode along the Cartesian axes gives the following (see [70] for a full derivation of this),

$$\Psi(z) = (n + 1/2)\zeta_S + (m + 1/2)\zeta_T. \tag{5.10}$$

Where $\Psi(z)$ is the total phase delay, ζ_S and ζ_T are the Gouy phase delays in the sagittal and tangential planes respectively. We can apply this to our HG_{nm}^{45} modes. Take the HG_{01}^{45} mode as an example. As the HG_{01} and HG_{10} component modes have the same total mode order they would normally experience the same Gouy phase shift. If we equate their total phase shifts and simplify we get the following formula.

$$\begin{aligned} \frac{3}{2}\zeta_S + \frac{1}{2}\zeta_T &= \frac{1}{2}\zeta_S + \frac{3}{2}\zeta_T \\ \zeta_S &= \zeta_T \end{aligned} \tag{5.11}$$

We can see that if we want a different total phase shift for each component we need $\zeta_S \neq \zeta_T$. Looking at (5.2) we can see that the phase delay is dependant on the Rayleigh

range. If we focus the HG_{01}^{45} astigmatically we will therefore create a different Gouy phase shift in each plane and cause a relative phase delay between its component modes. By controlling the ratio of the Rayleigh ranges in each plane we can tune this for a $\pi/2$ relative phase shift allowing us to convert from a HG_{01}^{45} to a LG_{01} vortex mode.

A second condition for successful conversion is to ensure the LG_{01} vortex mode is stigmatic after the converter. Otherwise, it will continue to experience a relative phase shift between its component modes and will start to convert back to a HG_{01}^{45} mode as it approaches the far field. One way to satisfy this condition is to make the AMC symmetric. This involves constructing it out of two identical astigmatic optics, and then ensuring the focal points in both the sagittal and tangential planes are coincident in the centre of the converter, see *Fig. 5.4*. We can see from symmetry arguments that the output from the AMC must be stigmatic provided the input mode is as well. This is due to the second optic doing the exact opposite transformation upon the beam as the first optic. This situation is presented by Beijersbergen *et. al.* in [70]. However their analysis only holds for cylindrical lenses. Here we expand it in principle to any given astigmatic focussing optics. Though in reality this is most likely to be off-axis spherical mirrors.

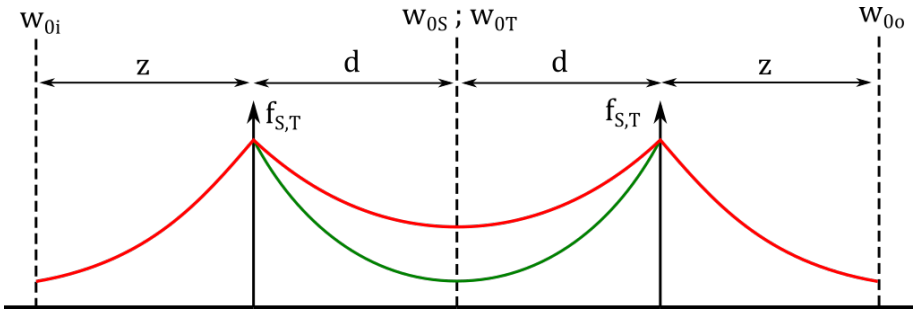

Figure 5.4: This clearly demonstrates that by symmetry arguments an AMC with identical focussing optics and a centrally located beam waist in both planes will produce a non-astigmatic output. Here the red line is the sagittal/combined beam radius as it traverses the converter. The green is the tangential beam radius.

5.4 Mode Converter Theory

The relative phase shift between successive component modes in *Eqn. (5.6)* created by a symmetric AMC is given in (5.12). A full derivation can be found in [70].

$$\Delta\Psi = 2\arctan\left(\frac{d}{z_{RT}}\right) - 2\arctan\left(\frac{d}{z_{RS}}\right) \tag{5.12}$$

Where $\Delta\Psi$ is the relative phase shift, d is the distance from an optic to the coinci-

dent waists, and z_T and z_S are the Rayleigh ranges in the tangential and sagittal planes respectively. To convert from HG^{45}_{nm} to a LG_{pl} mode we need to set $\Delta\Psi$ to $\pi/2$. We then make the substitutions in (5.13) and rearrange to get (5.14).

$$A = \arctan\left(\frac{d}{z_{RT}}\right) \quad B = \arctan\left(\frac{d}{z_{RS}}\right) \tag{5.13}$$

$$\frac{\tan(A) - \tan(B)}{1 + \tan(A)\tan(B)} = 1 \tag{5.14}$$

we can now undo our substitutions and rearrange to obtain an expression for z_{RT} in terms of z_{RS} and d.

$$z_{RT} = d\frac{z_{RS} - d}{z_{RS} + d} \tag{5.15}$$

For the beam to be stigmatic outside the converter the spot size at the optic surfaces, $w(d)$, in both planes must be equal. From this and the formulae in (5.8) and (5.9) we derive the relation

$$\frac{z_{RT}^2 + d^2}{z_{RT}} = \frac{z_{RS}^2 + d^2}{z_{RS}} \tag{5.16}$$

which can be rearranged to give z_{RS} in terms of d, and z_{RT}:

$$z_{RS} = \frac{d^2}{z_{RT}} \tag{5.17}$$

substituting (5.15) into this we get the following two relations

$$z_{RS} = d\left(\pm\sqrt{2} + 1\right) \tag{5.18}$$

$$z_{RT} = d\left(\pm\sqrt{2} - 1\right) \tag{5.19}$$

Our final boundary condition is that the radius of curvature of the beam in both planes must be equal after the astigmatic optic. In practice this means that the difference of the inverse focussing power of the optic in each plane (which we denote Δf_{inv}) must match the difference in the inverse radii of curvature in each plane of the beam incident upon it. This is shown mathematically as

$$\Delta f_{inv} = \frac{1}{f_T} - \frac{1}{f_S} = \frac{1}{R_T(d)} - \frac{1}{R_S(d)} \tag{5.20}$$

where f_T and f_S are the focal length of the optic in the tangential and sagittal planes respectively. $R_T(d)$ and $R_S(d)$ are similarly the mode's radii of curvature at the optic and are given in full as

$$\begin{aligned} R_T(d) &= \frac{d^2 + z_{RT}^2}{d} \\ R_S(d) &= \frac{d^2 + z_{RS}^2}{d} \end{aligned} \tag{5.21}$$

substituting in (5.18), (5.19) and (5.21) into (5.20) we get the simple relation

$$d = \frac{\sqrt{2}}{2\Delta f_{inv}} \tag{5.22}$$

This relates the spacing required between the optics in the converter in order to achieve a $\pi/2$ phase change, to parameters only dependant on the optics themselves. We can then use equations (5.18), (5.19) and (5.8) to calculate the spot sizes of the modes within the converter. Simple Gaussian beam propagation formula can then be used to locate the required position and size of the input beam waist w_{0i}. It is important to note here that we are dealing with higher order modes. Therefore when measuring the spot size of the input mode on a camera it will be scaled by the square-root of the beam propagation factor, M^2, compared to the fundamental mode size defined in (5.9).

5.5 Spherical Mirrors in AMCs

The relation in (5.22), in the case of cylindrical lenses, simplifies to that given by Beijersbergen *et. al.*. However this extension of the theory allows us to consider off-axis spherical mirrors. These have several advantages, including the lower losses and higher damage thresholds of highly reflective optical coatings; compared to the anti-reflective coatings used on lenses. This means they are potentially more suitable for high power applications. It also allows for greater wavelength flexibility as we are not limited by the absorption spectrum of suitable optical substrates. Furthermore the mechanical tolerances in the manufacture of spherical optics tends to be better than for cylindrical ones. This should reduce any aberrations in the beam by ensuring the two optics are closer to identical.

If we take a look at the focal lengths of off-axis spherical mirrors, f_T and f_S [1]

$$\begin{aligned} f_T &= \frac{R}{2cos(\theta)} \\ f_S &= \frac{Rcos(\theta)}{2} \end{aligned} \tag{5.23}$$

where R is the radius of curvature of the mirror and θ is the angle of incidence upon them. We can see the degree of focussing is dependant on the angle of incidence. Therefore by choosing a very high angle we can increase the difference between f_T and f_S . This then reduces d allowing for the construction of a compact converter. It is now trivial to design an AMC knowing only the radii of curvature of the mirrors you are using and the desired angle of incidence. An additional note is that a spherical mirror AMC is achromatic, as the focal length is only dependant on the curvature and not the refractive index of the

substrate as with lenses. This gives it additional advantages when being used with a pulsed system or widely tunable laser.

5.6 First Order Hermite-Gaussian Laser Using an Intra-Cavity Slit

In order to test this system experimentally, we, like most others, elected to generate the simplest HG mode to test the system. There are additional benefits to going to higher orders such as the resulting LG mode having greater OAM per photon, a steeper intensity profile and greater-intensity concentration. All of which are discussed more thoroughly in Chapter 2. The HG_{01} mode is however much simpler to generate than higher orders.

To generate a pure LG_{01} vortex mode we need a pure HG_{01} source. If this is to have future use for laser processing it also needs to have the potential for power scaling. Previously HG_{01} modes have been generated by two main methods. The first is by inserting a thin wire or mask into a cavity to create a central loss and suppress the Gaussian mode [70, 72, 73]. This, however, suffers from scattering effects that can lead to mode impurities, especially when operating in mediums with high gain. HG_{mn} modes can also be produced through off-axis laser diode pumping [74, 75, 112, 128]. This however is exceedingly alignment and thermally sensitive and is likely to produce several HG_{mn} modes simultaneously. We initially chose to try and improve on the masking technique by using an intra-cavity slit.

5.6.1 Two Mirror Capillary Pumped Laser

Most previous attempts to make a HG_{01} mode were based on introducing a spatial loss to a laser operating on the fundamental mode. We have built a laser that operates on a LG_{01} (but not necessarily a pure vortex) mode. This was done using the same capillary fibre from Chapter 3, spliced using the same taper to the same fibre coupled diode laser. This fibre had an outer diameter twice that of the inner diameter to give it a strong overlap with the LG_{01} mode. The output was re-imaged via a $4f$ system into a two mirror standing wave cavity, see *Fig. 5.5*. The same Nd:YAG crystal was used from Section 3.2. The cavity length was scaled for optimal LG_{01} mode quality, indicating good overlap with the pump. An image of the beam was put through the purity analysis detailed in Section 4.5. Results are given in *Fig. 5.6*. We can see the beam has very low astigmatism and azimuthal intensity variation, with only a slight break in the symmetry due to an increase in the peak power on the left of the beam. Substantial power remains in the centre however, there being 12.6% more power than expected. This is probably the main source of

the large amount of remaining power in the residual. A fundamental mode impurity is the most likely source of this. It could possibly be minimised by increasing the cavity mode size to obtain better overlap. However this risks exciting the LG_{02} mode. We also have no control over the handedness of the OAM. A quick test for OAM was done by reflecting the beam off an off-axis spherical mirror to astigmatically focus the beam, see Section 4.2. If this was a vortex mode it would undergo a phase shift into a HG_{01}^{45} mode. However in this case it simply became an elliptical ring, indicating either that fairly even amounts of each handedness, incoherently combined, are present, or that another form of non-vortex DM has been produced.

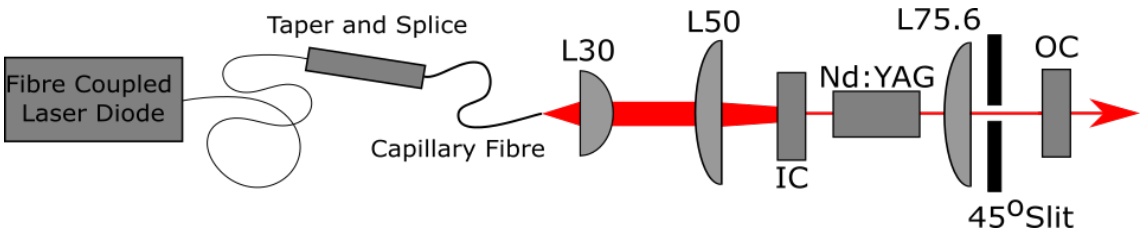

Figure 5.5: Schematic for the HG_{01} slit laser. IC is an input coupler with high transmission at $808nm$ and $> 99.5\%$ reflectance at $1064nm$. OC is the output coupler with 96% transmission at $1064nm$. LXX is a spherical lens with its focal length in mm. The slit is angled to 45^o from the plane of the optical bench.

5.6.2 HG_{01} Intra-Cavity Slit Laser

In order to force this laser to operate on a HG_{01} mode, an adjustable slit was introduced to the cavity. This was centred on the beam and the gap closed until the wings of the DM were being clipped inducing a loss (See *Fig. 5.7a*). We know the HG_{01} mode is supported by the cavity as it is a component mode of the DM. Furthermore the fundamental mode should also be suppressed due to the lack of gain in the centre of the pump. However as we've seen there is a significant amount of Gaussian in the LG_{01} mode which is likely to remain as we are doing nothing additional to suppress this mode. Nevertheless a clear HG_{01} intensity distribution was observed. 3D depictions of the beam and its estimated impurity are given in *Fig. 5.8*.

Introducing this slit at 45^o to the plane of the bench generated the mode seen in *Fig. 5.7*. This mode is orientated to -45^o to resemble a backslash. A maximum output power of $242mW$ was achieved. Analysing this with the method outlined in Section 4.4 we find a relatively pure mode, see *Fig. 5.7* and *Fig. 5.8*. We can see that the power in the centre of the mode has carried over. However other than this the mode quality is high with near equal power in each peak. If we look at the residuals we can see the pattern indicating a

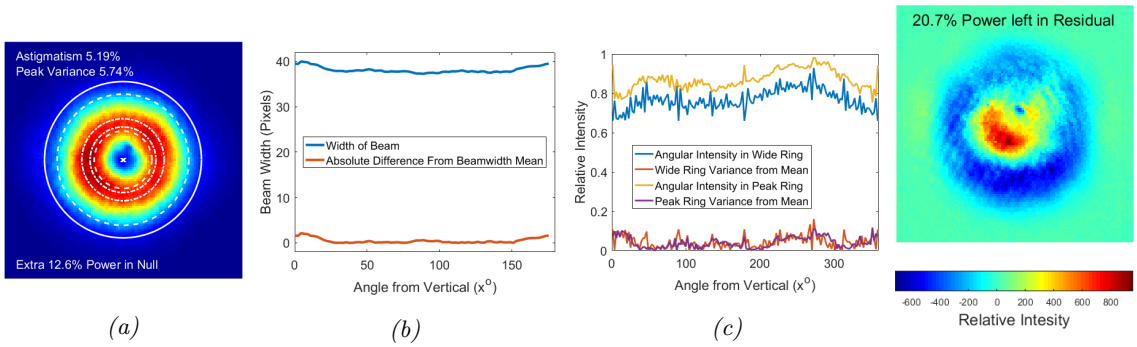

(a) *(b)* *(c)* *(d)*

Figure 5.6: Results of the mode purity analysis on the LG_{01} mode produced by the standing wave cavity pumped by the 0.5 aspect ratio capillary fibre. *(a)* is the beam with the beam radius, centre and regions used for azimuthal intensity measurement. *(b)* is a plot of the azimuthal variation in the width of the beam, *(c)* is the azimuthal intensity variance and *(d)* is the residual after a matching pure LG_{01} mode is subtracted from the measured beam.

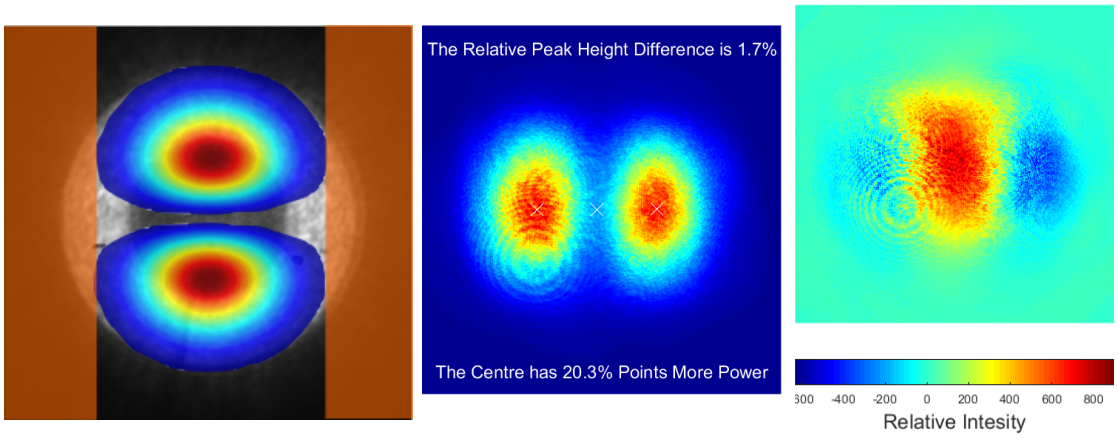

(a) *(b)* *(c)*

Figure 5.7: (a) is an illustration of how the intra-cavity slit works as a mode selector. We can see the pump ring in the background with its wings being blocked by the orange slit. This induces a loss in these regions leaving the HG_{01} mode with the best overlap. *(b)* The resultant HG_{01} mode from the laser. *(c)* The residual of the mode shows a pattern consistent with a Gaussian mode impurity.

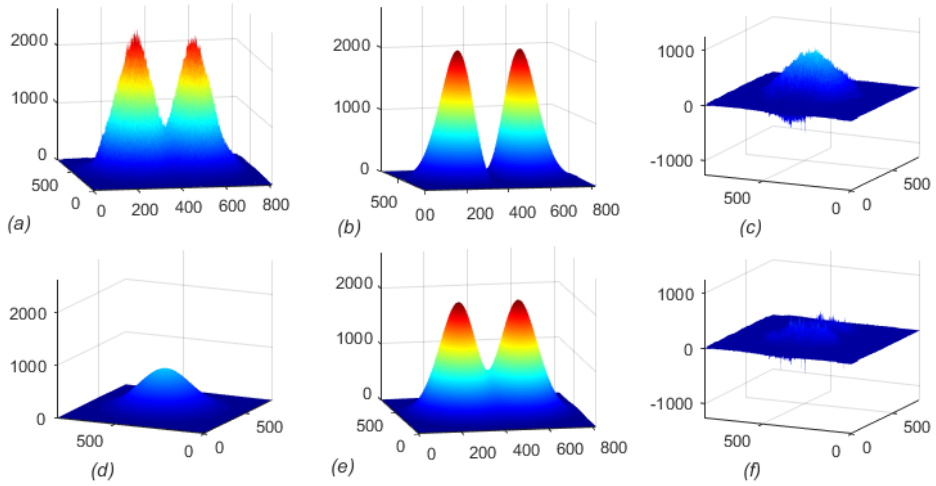

Figure 5.8: *(a)* depicts the measured HG_{01} beam from the slit laser. *(b)* is our initial matching theoretical mode. *(c)* is the initial residual with the characteristic pattern indicating a fundamental mode impurity. *(d)* is our estimated HG_{00} impurity. *(e)* Is our new theoretical match mode including the impurity. *(f)* is the residual from the improved theoretical match mode.

Gaussian impurity as we might expect due to its appearance in the original LG_{01} mode. Following the method outlined in Section 4.4.2 we identified a HG_{00} modal-impurity that accounted for 37% of the total power. The results of this are found in *Fig 5.8*. We can see the residual has been reduced to mostly noise with a 44.4% decrease in the total power in the residual. This shows the mode is likely less pure than it initially appeared, as an estimated 37% of the power in the unwanted fundamental mode impurity. This will carry over into the LG_{01} mode as it passes through the AMC. This will remove the central intensity null of the converted mode and reduce the amount of OAM per photon. This mode was then fed into an AMC to confirm this.

5.6.3 Intra-Cavity Slit Laser Mode Conversion

For the AMC we used mirrors with a $150mm$ radius of curvature and a input angle of 45^o for ease of alignment. These mirrors were coated to be highly reflective at $1064nm$ at 45^o. A telescope was then used to re-size the beam waist of the HG_{01}^{45} mode to precisely $202\mu m$, $96mm$ away from the first mirror. These values were calculated using the method detailed in Section 5.4. The slit was then rotated to precisely 45^o to the plane of the bench. The output was then fed through the AMC outlined in *Fig. 5.9*. Loss from the converter was below the noise threshold of the thermal power meter used, less than 0.3%.

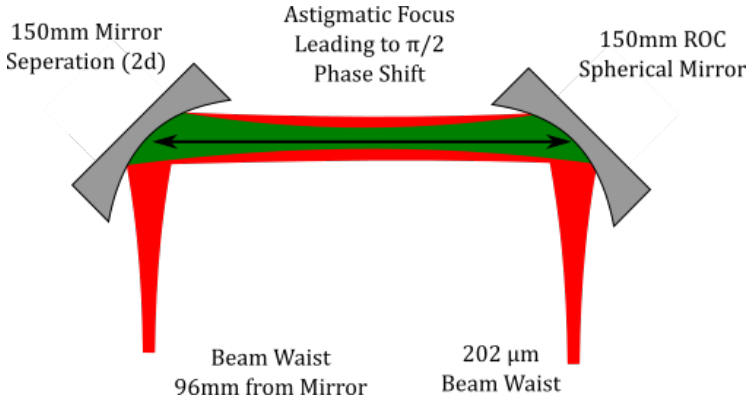

Figure 5.9: Schematic of the AMC used to conduct the experiments detailed in this paper. The mirrors are coated to be highly reflective at $1064nm$ at 45^o. The mirror separation and calculated beam waist and sizes are marked. The red represents the beam in the sagittal or combined planes, green the beam in the transverse plane.

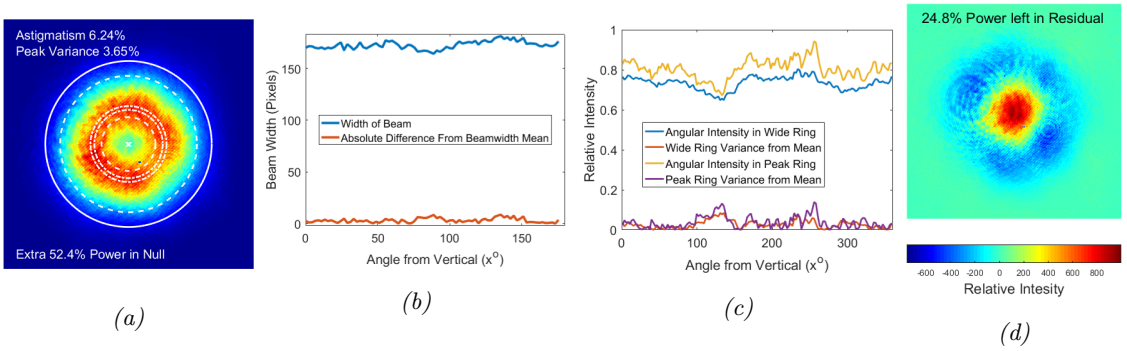

(a) *(b)* *(c)* *(d)*

Figure 5.10: Results of the mode purity analysis on the LG_{01} mode produced by passing the beam from *Fig. 5.7b* through the AMC. It has very low astigmatism and azimuthal intensity variation. Looking at the residual however, is substantial power remaining in the centre. This shows the HG_{00} impurity has carried through the converter.

The resulting LG_{01} and its analysis are presented in *Fig. 5.10*. We can see the Gaussian impurity has carried over as there is more power in the centre than we would expect. This is confirmed in the residual. However the beam has similar astigmatism and lower peak variance to that created directly by the cavity without the slit, showing that a very pure mode is attainable with this method if we can remove the HG_{00} impurity.

We then rotated the slit through 90^o so it was orientated to $+45^o$ to resemble a forwardslash. This switches the handedness of the vortex mode. This produced the beam seen in *Fig. 5.11a* which was converted to produce the beam in *Fig. 5.11b*. Again the only major impurity is from additional Gaussian content. In order to improve this we need to find a way to generate a HG_{01} mode without this impurity. One way might be to insert a nano-wire into the cavity as described earlier. This would induce a loss for the Gaussian.

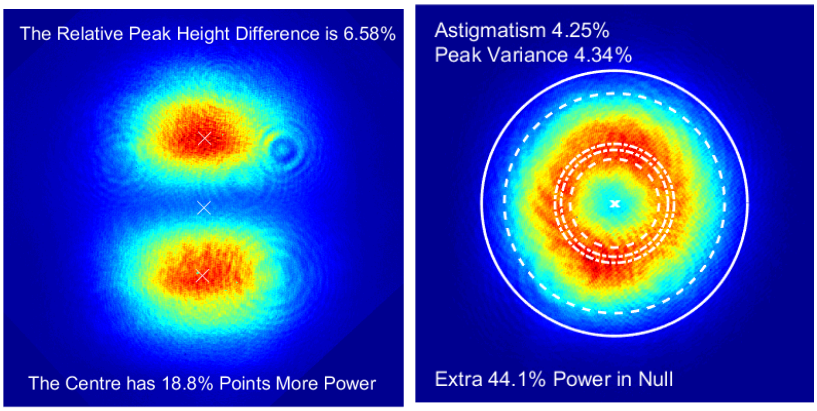

(a) *(b)*

Figure 5.11: Here we see both the output of the intra-cavity slit laser and the resultant converted beam after a 90^o rotation of the intra-cavity slit. We can see that in both cases the beam quality is once again high with the exception of the HG_{00} impurity.

It does not address the fundamental cause however, as the source of this impurity is the unused gain in the cavity. This additionally causes the system to be less efficient as not all the available pump power is converted into laser output. This is a concern for the lasers eventual viability in applications where cost is an important factor. A different approach may therefore yield better results.

The output from both orientations was fed through a Mach-Zehnder interferometer in order to confirm the change in handedness, *Fig. 5.12*. The handedness change was confirmed however the spiral for the $+45^o$ beam was severely degraded. This was confirmed with the analysis outlined in Section 4.2. Looking at *Fig. 5.12c* we can see the azimuthal intensity variation of both beams compared with a matching spiral generated from a pure LG_{01} and HG_{01} mode. We see the -45^o spiral from the first beam has a nearly even azimuthal intensity variation while the $+45^o$ has significant variation. This is surprising as the mode quality was high. It was found this was caused because the $+45^o$ mode had a spatially variant polarisation, *Fig. 5.12d*, that resembled that of a radial mode. This caused a spatially variant loss due to the high-angle reflections in the interferometer. The cause of this unusual polarisation is unknown. This could may be alleviated by adding a polarisation selecting element to the cavity.

5.6.4 Conclusions and Improving the HG_{01} Mode Quality

We can see that the mode converter is working as expected, however improvements are needed in the seed mode. Particularly with regards to the polarisation state and suppressing the Gaussian mode. Whilst this may be achievable by adding a wire, or spot defect

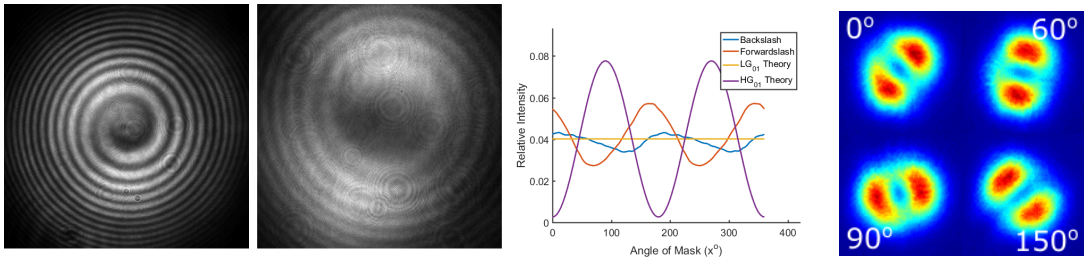

(a) *(b)* *(c)* *(d)*

Figure 5.12: Here we see the Mach-Zehnder interference patterns for both the -45^o *(a)* and $+45^o$ *(b)*. There azimuthal intensity variation is plotted agants matching patterns generated from a pure HG_{01} and LG_{01} mode. We can see there is significant intensity variation in the $+45^o$ beam. This is caused by spatially variant polarisation depicted in *(d)*.

mirror, to the cavity to suppress the fundamental mode, and adding a Brewster's window to achieve linear polarisation, this will further increase the loss in an already inefficient cavity. Furthermore it is difficult to see how this technique could be extended to produce higher order modes. We therefore sought a more elegant method of generating HG modes other than loss shaping.

5.7 Twin Pump Spot HG_{01} Laser

5.7.1 Gain Shaping

In order to improve the purity of our HG_{01} mode we explored the technique of gain shaping. This allows us to more accurately target our desired mode whilst suppressing all others. If we pump a solid state laser with a gain profile that more closely resembles a HG_{01} mode it will see the highest gain and be selectively excited. Furthermore by ensuring all the gain overlaps with the HG_{01} mode, all other modes will be suppressed. We have already explored this in regards to LG modes with capillary fibres (see Chapter 3 and Chapter 2) with reasonable success. One way to achieve this is to take the output of two fibre coupled diodes and re-image them so they are adjacent in the gain medium. The separation could then be varied to optimise the overlap with HG_{01} mode. We therefore constructed the laser seen in *Fig. 5.13*.

Two BWT^{TM}, $4W$, $808nm$, fibre coupled laser diodes with inbuilt thermoelectric cooling units were used as the pump. The output fibres had a $105\mu m$ core diameter and $125\mu m$ cladding diameter and were highly multimode at the pump wavelength. These were mounted on the same water cooled copper heat sink and connected in parallel to the same electronic power supply for thermoelectric cooling. With a water temperature of 15^oC the cooling current was tuned for maximum absorption in the laser crystal when

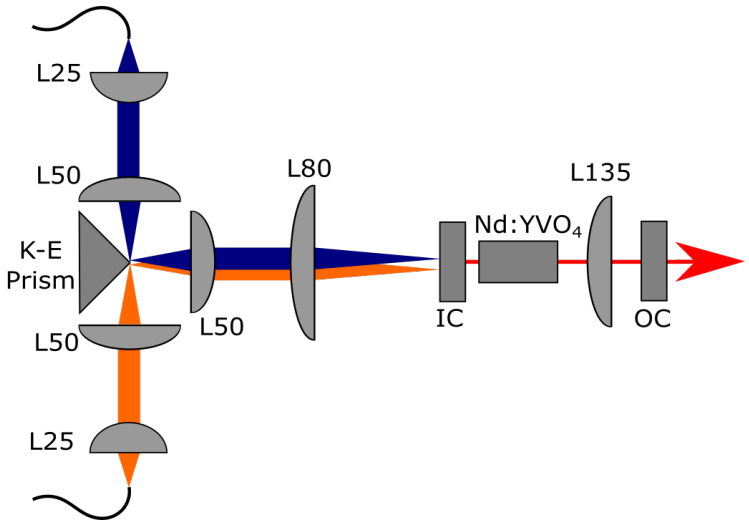

Figure 5.13: Schematic of the twin pump HG_{01} laser. LXX are spherical lenses with focal lengths, XX, in mm. IC and OC are the input and 95% reflectivity output couplers respectively. The prism is used to re-direct the two coaxial but counter-propagating pump beams, a second pair of lenses then re-image the two adjacent pump spots into the Nd:YVO_4 crystal. The spacing between the pump spots and mode matching the cavity to them is critical to suppress both HG_{00} and higher order HG_{nm} modes. However once this is achieved alignment for good mode quality is trivial.

$3.5W$ of current was supplied to each diode. We can see in *Fig. 5.14* that each diode had an almost identical output at all powers. The thresholds were $0.85A$ and $0.90A$ with slope efficiencies of $0.81W/A$ and $0.82W/A$. The measurement was taken at the laser gain crystal after the pump optics. The slight differences may be accounted for by the different power supplies used for each diode, or slight differences in the losses of the pump optics before the prism. Separate diode drivers were used so independent control could be maintained for each pump spot. The outputs from the fibres diodes are aligned so they propagate along the same optic axis but in opposite directions. The fibre tips are then re-imaged with identical lens pairs onto the knife-edge prism which is highly reflective at the $808nm$ pump wavelength. By translating the prism orthogonal to the pump axis we can then vary the separation of the pump spots to find the best overlap with the HG_{01} mode. The tip of the prism is then re-imaged into a $5mm$ long square-rod of 1% doped Nd:YVO_4 crystal. We moved from Nd:YAG to vanadate due to its short absorption length at the pump wavelength and polarised output. The polarised output will ensure minimum loss going through the converter when combined with a half-waveplate external to the cavity. The waveplate is used to orientate the polarisation so it is s-polarised with respect to the mirrors. The much higher absorption coefficient of Nd:YVO_4 means we can expect an absorption length of $22.8cm^{-1}$, meaning $1/e^2$ of the power will be absorbed within the first $0.88mm$ of the crystal. This assists with mode selection as the pump beam only remains

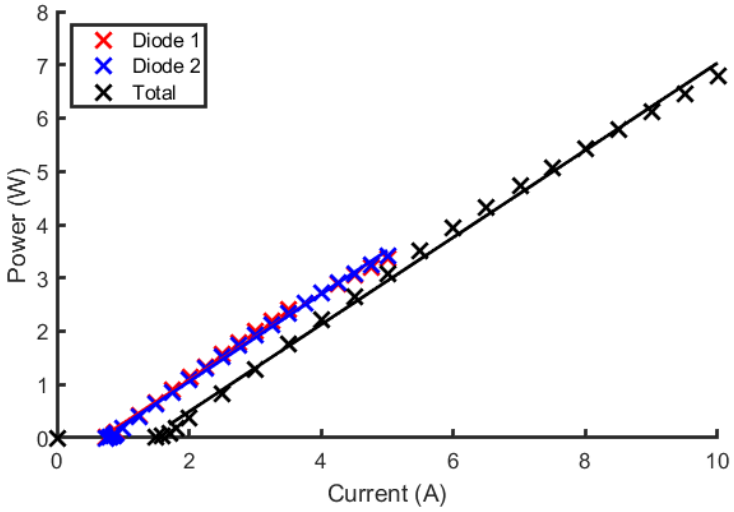

Figure 5.14: Power curves for the two BWT^{TM} diodes as measured at the laser gain crystal. We see they have matching thresholds and slope efficiencies.

as two distinct spots close to the focal plane. The crystal is contacted along its four, non-optical edges to a water cooled copper heat sink via a thin sheet of pyrolytic graphite. The laser cavity is formed of two plane mirrors and a spherical lens with a focal length of $135mm$ to match the cavity mode size to the pump spot. Optimal mode matching was achieved when the calculated mode size in the Nd:YVO_4 was approximately $170\mu m$.

In order to optimise the pump spots we adjusted the separation between the pump spots and analysed the output of the laser using the methods outlined in Section 4.4. We found the highest quality mode was produced when the separation between the two pump spot centres, is 1.6 times that of the diameter of the individual pump spot, in this case the separation being approximately $531\mu m$ and the pump spot diameter roughly $336\mu m$. The total pump power used was approximately $1W$ giving a linearly polarised output of $175mW$ at $1064nm$. More pump was available but the HG_{01} mode quality appeared reduced at higher powers when thermal effects became more prominent. Images of the focused pump beam and laser output are in *Fig. 5.15*.

The beam intensity profile was assessed and found to have almost precisely even peaks and very limited excess central power of 3.1%. Potentially within the noise of either the camera or analysis. Some of the central power can likely be as a result of blooming. This is reinforced as by trying to add a simulated HG_{00} impurity to the model of the matching mode, we increased the percentage power in the residual rather than decreased it. We believe the unusual, two central peaks winged by valleys structure, in the residual is due to blooming in the camera. Removal of blooming effect from images in order to better

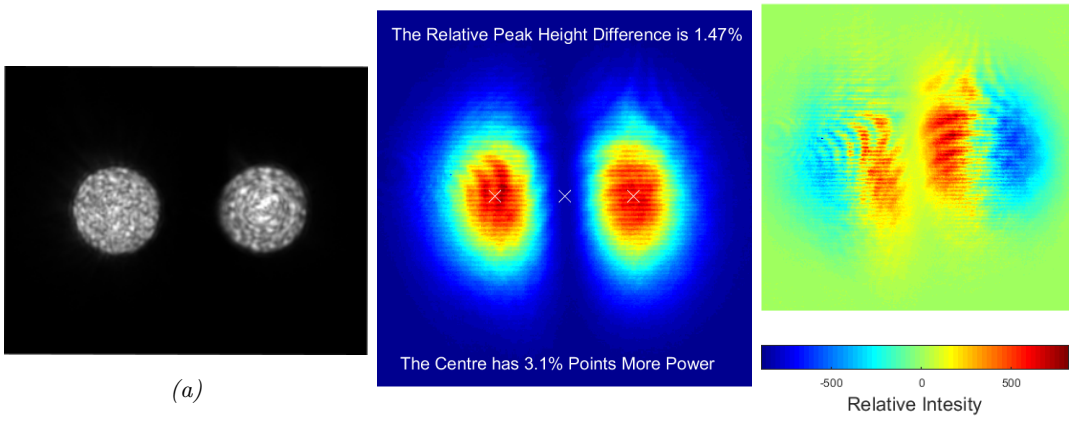

(a) *(b)* *(c)*

Figure 5.15: CCD images of the pump beam at the focus, *(a)* and the resulting laser output, *(b)*. The residual, *(c)*, has an unusual structure but we expect this largely due to blooming noise.

asses beam quality is ongoing. Still, this highlights the importance of obtaining aberration free images in order to properly assess beam quality.

5.7.2 Mode Converting the Twin Pump Spot HG_{01} Mode

This beam was then angled at 45^o to the Cartesian axes via a dove prism. Two steering mirrors were placed after this to correct for the beam walk caused by rotating this prism during fine adjustments. This beam was then fed into the same AMC as in Section 5.6.3. The conversion losses were again below our ability to detect them, giving $175mW$ of vortex mode. The converted mode is presented in *Fig. 5.16a*. We can see it has little variation in either beam width or azimuthal intensity, being comparable with both the mode converted from the intra-cavity slit laser and the raw output of the two-mirror capillary pumped laser. However the excess central power is lower, only the ring laser output from Section 3.2 having less.This proves that with a high quality source the AMC is capable of producing high purity vortex modes.

To confirm the presence of OAM we used the standard method of a Mach-Zehnder interferometer described in Section 3.1.4. The interference pattern we produced is shown and analysed in *Fig. 5.16c*. We can see it is a very clear spiral with less azimuthal variation than that from the slit laser source. This indicates either that the AMC was better aligned or that there was less non-HG_{01} mode content in the new source. We believe both the power and structure left behind in the residual to be due to a combination of a small fundemental mode impurity and noise. By rotating the dove prism by 45^o (dove prisms rotate an image by twice the angle they are rotated to) we can reorientate the input from

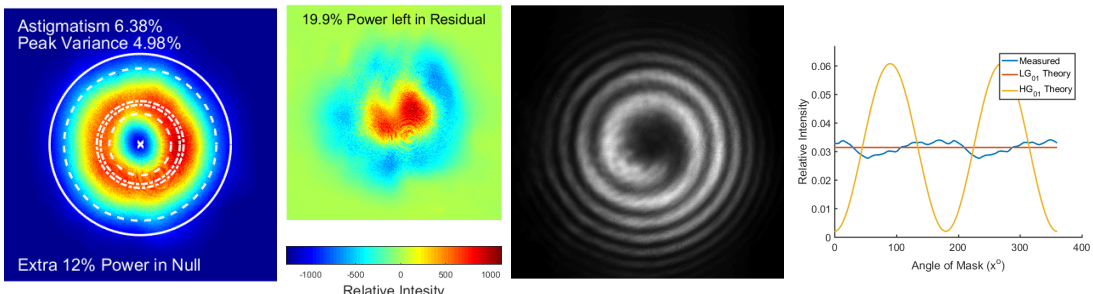

Figure 5.16: The LG_{01} mode produced by the AMC with the seed beam in *Fig. 5.15b*. We can see it has low astigmatism and peak variance and relatively low excess central power. The quality of the beam is further assured by the azimuthal symmetry of the spiral interference pattern from the Mach-Zehnder interferometer.

$+45^o$ to -45^o angle. This changes the handedness of the mode as demonstrated in *Fig. 5.17*. The azimuthal symmetry has dropped slightly, this is likely due to misalignment. This is probably caused by slight adjustments in the steering mirrors needed to compensate for beam walk during rotation. This will have slightly changed the optical path length the beam traverses before the AMC, changing the input mode size. The result will be a minimal amount of residual HG_{01} mode content. There is however, less excess central power compared to the $+45^o$ mode. The cause of this drop is unknown. Looking at the interference pattern (*Fig. 5.17c*) we see a clear spiral with the opposite handedness. Again it has excellent azimuthal symmetry.

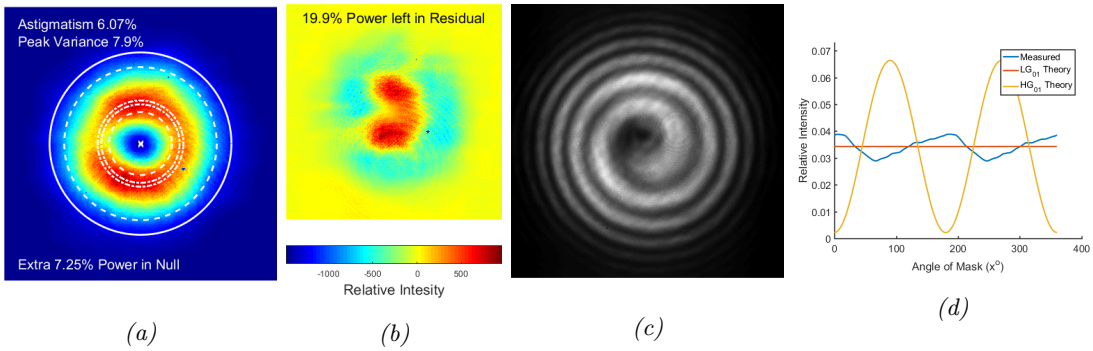

Figure 5.17: The LG_{01} mode produced after a 90^o rotation of the input mode. We can see it has low astigmatism and peak variance and relatively low excess central power. The quality of the beam is further assured by the azimuthal symmetry of the spiral interference pattern from the Mach-Zehnder interferometer.

5.7.3 Summary and Future Work

We can see that this technique of gain shaping has dramatically improved our beam quality. It also increased the maximum output power and efficiency of the system. The main limitation on the output power was the mode quality. A better match between the pump and cavity mode is therefore desirable. this could possibly be achieved by using a 'D' shaped fibre output to more closely resemble the lobes of a HG_{01} mode. Furthermore the introduction of a dove prism to rotate the beam has simplified handedness selection. Taking the rotation external to the cavity maintains the quality of the source meaning the HG_{01} purity does not need re-analysing. Gain shaping could be further extended to generate higher order HG modes. Simply adding a third fibre could allow for the selection of the HG_{02} mode, though the prism pump delivery system would need to be revised. Stacking another pair of fibres above the two in our current system would select the HG_{11}. These could then be fed through the AMC to create a variety of higher order LG modes.

Improvements to the pump delivery system would help realise this. Currently it is cumbersome and has a large footprint on the optical bench. A better method may be to use fibre splitters. Provided these can split the power evenly one can imagine designing a custom mount to align the multiple fibre ends in relation to each other. The whole system could then be run with a single pump diode. It may also be possible to mount a large array of fibres and then by switching the power to each one select between many different modes in a single device. However, it would be challenging to design a cavity stable to all these modes. A theoretical analysis of the thresholds of each transverse mode for a given multi-pump distribution should be done in order to better understand the processes behind the mode selection. Gain shaping is however promising as a more reliable way to generate high-order HG modes.

5.8 Conclusions

We have developed a novel design for the generation of vortex modes with measurably high purity. This has built on previous work using astigmatic mode converters. We have improved its efficiency and wavelength flexibility with the use of off-axis spherical mirrors to replace the cylindrical lenses. In addition we have expanded the theory of mode converter design to spherical mirrors as well as any other possible astigmatic focussing optics. We have also developed a new high purity HG_{01} source suitable for use with an AMC. This utilises gain shaping by using two circular laser diode beams, adjacent to each other, to pump a solid state laser. Furthermore we have the ability to select for the handedness of the vortex mode with the simple rotation of one optic. We have also seen how both the Mach-Zehnder, and intensity distribution purity analysis can be applied to a real system.

This has helped direct the course of our experiments towards better purity and furthermore confirmed the quality of our results.

We believe the combination of an advanced HG laser with a spherical mirror AMC is a strong candidate for a route to OAM beams at machining powers. Being a solid state laser it is not dependant on specialist, expensive equipment and has a strong basis for both power scaling and moving to a pulsed regime, which is critical for many potential laser processing applications. Furthermore the high beam quality may provide of interest in other areas such as optical trapping or microscopy. Moving forward the critical step is to prove that the beam quality can be maintained upon amplification.

Chapter 6

Amplifying First Order Hermite-Gaussian Modes

As noted in the previous chapter, mode impurities begin to appear in the double pump method of producing HG_{01} modes at higher pump powers. This limits the maximum attainable power of HG modes and, correspondingly, vortex modes by this method. It may be possible to improve on this with better cavity and pump profile design. An amplification stage greatly improves the theoretical maximum power attainable. The key will be maintaining the mode purity. There are two main possible routes.

The first amplification approach would be to amplify the vortex mode after the converter. This has advantages in that any distortions to the mode brought in by amplification will not be exacerbated by the mode converter. It also means less optics are likely to be between the amplifier output and the application; reducing the number of optics where the damage threshold of the coatings is a factor. However modern optical coatings can withstand damage of $10s$ of J/cm^2 from laser pulses on the order of $10ns$ [129, 130], equivalent to several kW of instantaneous power for a spot size of $100\mu m$. Clearly a lot of work will be needed before we can obtain vortex modes where the damage threshold of optical coatings will be the limiting factor. The main concern with amplifying vortex modes is the potential for scattering into the many degenerate annular intensity distributions. While we know of no mechanism that is certain to cause this, it is still a possibility. Furthermore, the fact that vortex modes are unstable to astigmatism is also a concern in systems likely to contain a strong non-spherical thermal lens.

The second approach is to amplify the HG mode. This is stable to astigmatism in its principal axes, and has no modes with similar intensity profiles to scatter into. The main disadvantage is that any impurities gained in the amplification process may behave

unexpectedly in the mode converter. A further consideration is the amplifier geometry. Much like in laser design, each geometry has distinct advantages and disadvantages and favours certain applications. It is therefore likely that an amplifier suitable for a HG_{01} mode, will not be for the LG_{01}.

6.1 Core Principles of Amplifier Design

Fundamentally, an optical amplifier is a laser without the feedback mechanism. To achieve optical amplification one needs to create a region of gain from which stimulated emission can occur. The key difference is that, instead of designing a cavity that provides feedback for spontaneous emission and eventually selects for a laser mode, an amplifier requires a seed source. This seed source sweeps through the gain region causing stimulated emission. Ideally, the output of the amplifier is identical to the seed source, but at a higher power. However, any impurities in the seed may also be amplified, especially if they overlap with areas of the gain not utilised by the desired mode. Furthermore, one must be careful to manage the thermal effects that come with higher pump powers. There must also be no feedback to the gain region or to the seed source . Feedback to the amplifier gain medium can instigate unwanted lasing, and feed back to the seed can distort the seed or cause damage to the low power laser.

Feedback to the seed source is normally minimised with the use of an optical isolator described in Section3.1.2. This is key to the common amplifier design of a 'master oscillator power amplifier' (MOPA). Here an isolator separates the seed source and each amplifier stage to prevent feedback, see *Fig. 6.1*. The seed source will be normally be low power with high beam quality, with each amplifier stage ideally only adding power without effecting either the beam's modal content or pulse attributes. Each amplifier can be of any given design depending on the application.

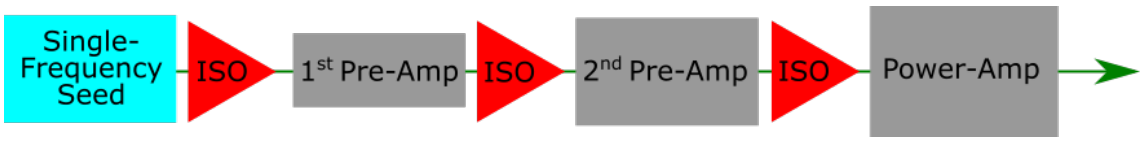

Figure 6.1: Schematic of a MOPA with three amplifier stages, separated by isolaters (ISO), though any number is possible

Early amplifier designs, much like early lasers, were primarily based on a rod architectures due to the relative ease of manufacture [131]. These are limited when pushed to high power due to thermal effects, particularly thermally induced birefringence, thermal lensing and eventually thermal fracture. The advent of diode lasers as pump sources

represented a massive improvement in both lasers and amplifiers. This allows for end pumped geometries that have a better overlap with the cavity mode and a more uniform pump distribution. However, the fundamental thermal effects still remain a problem. These are especially hard to mitigate in a rod architecture as they are mostly dependent upon the material properties of the gain crystal [131, 132]. In order to improve this different architectures have been developed that either increase the rate of heat removal or mitigate these thermal distortions by compensating for the birefringence or lensing effects.

One way to increase heat removal is to reformat the gain medium into a thin disc with an average thickness of a few hundred microns [133, 134, 135]. This is then cooled from one of the large, flat surfaces which also serves as a mirror. This causes the temperature gradient to vary linearly between the two flat faced rather than radially out from the centre, removing most of the thermal distortion effects. The downside is a massive reduction in the interaction length with the pump beam. In order to achieve a sufficient population inversion, multiple passes of the pump are needed through the gain medium. This means that whilst this architecture is capable of producing high quality beams with average powers $> 1kW$, it is cumbersome and expensive to construct and operate.

Despite fibre lasers being proposed [136] not long after the invention of the laser [11] it is only since the late $80s$ that fibre lasers have seen extensive improvements in output power [137]. The basic advantages of fibre lasers are their high surface area, allowing for greatly improved heat removal, and the fixing of the mode quality to the wave-guide nature of the fibre. This means that the condition for single mode operation is given by the normalised frequency or 'V-number' [138]

$$V = \frac{2\pi}{\lambda} a \sqrt{n_{core}^2 - n_{cladding}^2} \tag{6.1}$$

where λ is the wavelength, a is the fibre core radius, and n is the refractive index. It can be shown that, for a step index fibre, if $V < 2.405$ it can only support the fundamental mode. As V increases more modes are supported. As we can see, this is independent of the pump architecture and thermal properties of the amplifier. This limits the core size and therefore the cross section of the pump light. This problem was minimised with the use of double clad fibres first proposed in 1974 [139]. However, it still presents limits on the total energy storage of fibres for pulsed operation. Furthermore the long interaction lengths between the cavity mode and host material promote non-linear effects. Stimulated Brillouin scattering (SBS) and stimulated Ramen scattering (SRS) in particular, have placed the upper limit on power from single-mode fibre amplifiers and lasers [140, 141, 142, 143, 144]. The power limit for all fibre, near diffraction limited beam quality fibre laser recently hit the multi-kilowatt mark [29, 144], with powers up to $10kW$ theorised to be possible with

more pump power being available [145]. This makes them begin to rival the powers of disc lasers. These lasers are however spectrally broadened at high powers by SRS. Many applications require a narrower linewidth for which MOPA architectures are being used [146]. As of 2017 the power limit for an all fibre single mode MOPA design is in the tens to hundreds of watts. By moving to a hybrid fibre/free-space design, powers have been increased further at several key wavelengths of around 1, 1.5 and 2 microns [147, 148, 149]. Further work in increasing the threshold of the non-linearities is needed to further extend the powers of fibre lasers.

A third common amplifier geometry is the slab. This abandons cylindrical symmetry with the gain medium being rectangular, generally with a high aspect ratio between its width and height. A diagram of the faces of a slab gain medium is given in *Fig. 6.2*. In general, one needs to focus into this gain medium with a cylindrical lens breaking the cylindrical symmetry of the beam. For some applications this is either not an issue or a desirable trait. Nevertheless, for many it needs correction after the amplifier/laser. Two common ways to implement this geometry are either in a linear or zig-zag configuration. The linear has flat end faces and the beam propagates along the z axis. It is typically both cooled and pumped on the top faces [131]. This, much like the disc laser, sets up a thermal gradient purely in the y direction, removing thermally induced birefringence as a problem, provided the laser is linearly polarised along either x or y. The top surface also provides a large area for cooling. However, the gain medium still acts as a cylindrical thermal lens and will, in general, produce an astigmatic output. In the zig-zag configuration, shown in the lower half of *Fig. 6.2*, total internal reflection off the top faces is utilised to confine the mode. The edge faces are often at Brewster's angle, either to enforce linear polarisation in a laser, or to reduce Fresnel losses in an amplifier and remove the need for anti-reflection coatings. The medium is then pumped and cooled via the top and bottom faces. This tends to eliminate thermal distortion of the beam, as the beam's path means the entire beam sees the same thermal gradient [150]. Zig-zag amplifiers have recently seen interest for applications in space based remote sensing [151, 152]. This is due to their potential for combining high energy storage with high beam quality. One disadvantage of slab amplifiers is they typically need two pump sources in order to pump two faces. If only one is used the beam will see a highly uneven gain region which can lead to beam distortion.

6.2 Generation and Amplification of Vortex modes in Various Solid-State Geometries

There has only been limited research into the amplification of higher order modes in solid-state systems. In order to assess what geometry will be most appropriate for our needs

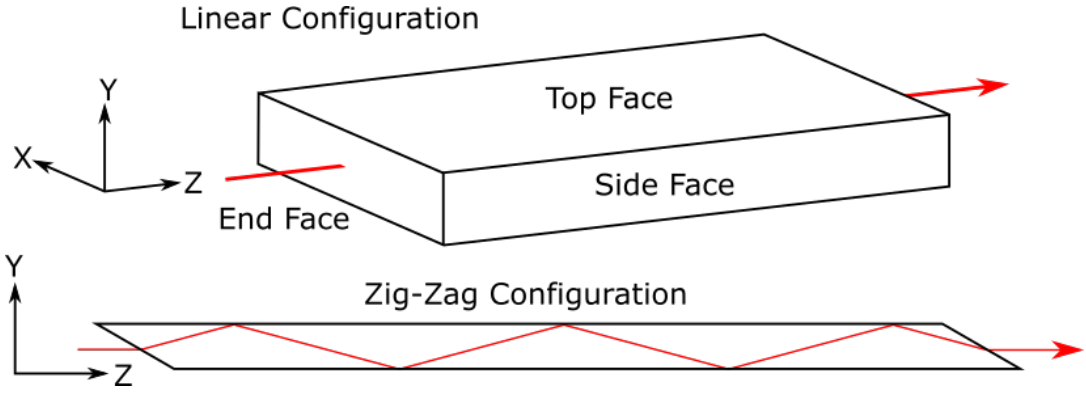

Figure 6.2: Diagrams of typical linear and zig-zag slab geometry gain media. The end face of the zig-zag slab is often at Brewster's angle in order to enforce linear polarisation in a laser or reduce losses in an amplifier. For a linear slab the ends would typically be at right angles compared to the other faces.

we now conduct a literature review of the use of these geometries as both lasers operating on higher order modes, as well as amplifying them. Though the laser systems are not completely analogous to how we would use them as an amplifier, it may highlight some advantages or issues when they are used with higher order modes.

Disc lasers have been used to produce high quality DMs at powers in the 100s of watts by utilising a mirror that selects for radial polarisation [153]. As this polarisation is only possible for modes containing a central intensity null, the LG_{01} mode is selected. This was later assisted by the introduction of a capillary fibre to deliver the pump and improve the gain overlap (see Section 2.1) [86]. These are however radial modes that do not contain OAM. Vortex modes have been excited in a disc laser using a novel dual pump scheme but efficiencies were poor and there is no evidence of handedness selection [83]. This method also produced various high order HG modes at low power. To the best of our knowledge, a disc laser has never been used to amplify a vortex mode. It is certainly possible to amplify a vortex mode seed in this configuration, however it is not clear that this method holds distinct advantages over an amplifier geometry that is simpler to construct, unless multi-hundreds or kilowatts of power are required. The same holds true for amplifying the HG_{01} mode, though this would be more challenging due to the modes lack of cylindrical symmetry.

The transverse mode solutions that propagate in an optical fibre are not the same as those in free space, though they are analogous. A minimum of a two mode fibre is needed to support a vortex mode [122]. It is possible to excite second order (i.e. modes analogous to either HG_{01} or LG_{01} modes) in these fibres through off-axis pumping. This has been demonstrated in several systems [91, 122, 154], but the coupling efficiency is poor,

typically less than 30%. It is also possible to excite more than one mode at a time, so we return to our problem of mode purity. Handedness selection in vortex modes has been shown by exciting both the PM_{11o} and PM_{11e} (analogous to HG_{10} and HG_{01} modes) simultaneously and controlling their phase relation with active feedback [121, 154]. This created up to $25W$ of vortex mode in a Yb double clad fibre amplifier, though the mode quality is poor. The TM_{01}, TE_{01}, HE_{21}^{odd} and HE_{21}^{even} fibre modes that are analogous to radial DMs have all been generated directly from a laser in research by Sun *et al.* , though at only a few mW of power [155]. Wavelength tuning in conjunction with a few-mode fibre Bragg grating was used to select between these modes.

Moving away from an all fibre system $36W$ of LG_{01} mode was produced by Lin *et al.* by using a free-space feedback cavity in a fibre laser [156]. A linear polariser and half waveplate are used to rotate the polarisation within the feedback arm. The LP_{01} (HG_{00}) and LP_{11} (LG_{01}) modes interact differently with the Stokes parameters of the fibre, driving a differential loss between the two modes. Lin then developed the system to generate a radially polarised OAM mode using an S-waveplate (see Section 1.4.2) [117]. Fibre amplifiers seem promising for reaching high power vortex modes. Maintaining the mode quality however, appears to be challenging. All the known examples are based around exciting a higher order mode within the fibre from a fundamental mode source [121, 122, 157]. How coupling in a higher order mode directly into a fibre will perform in terms of mode quality is unclear. We have, therefore, elected not to use a fibre amplifier for the time being.

To the best of our knowledge there has only been one demonstration of amplifying a DM within a slab [158]. A radial seed source was constructed using a capillary fibre to select for the LG_{01} mode. Thermal birefringence can then be used to select between azimuthal and radial polarisation as they see different focussing powers in a peripherally cooled, uniformly pumped, isotropic gain medium [159, 160]. One can then design a cavity such that only the radial mode is stable. This radial seed was then focussed by a cylindrical lens into a linear Yb:YAG slab laser. The polarisation was transformed by the Gouy phase shift but could be easily corrected with a quarter waveplate. This produced up to $4.4dB$ of gain and $4W$ of output power. The need for cylindrical lenses means that this style of amplifier is unsuitable for our converted vortex mode, as astigmatically focussing it would return it to a HG_{01}^{45} mode. However, it could be suitable for amplifying the mode before the converter, as a non-circularly symmetric beam is likely less prone to error in non-circularly symmetric amplifier.

We decided to construct an amplifier for the HG_{01} mode before it is converted in a slab amplifier. This is due to the possibility of exciting other modes in a fibre laser, the

practical obstacles of constructing a disc laser and the thermal limitations of traditional rod amplifiers. Mode coupling and thermal effects seem more likely to degrade the purity of a vortex mode than the HG mode. Amplifying before the converter may allow us to correct for any minor impurities that are incurred after amplification, such as astigmatism or higher order mode content that can be spatially filtered. We therefore have elected to construct a slab amplifier for the HG mode. Specifically we have decided to use a bounce geometry design.

6.3 Bounce Geometry Lasers and Amplifiers

One variation on the zig-zag slab is the bounce geometry. This uses a trapezoidal prism shaped gain medium, initially demonstrated by Bernard and Alcock [161]. It is side pumped on its base, see *Fig. 6.3*. It is cooled on the top and bottom faces giving it a near linear thermal gradient. The seed is fed in through an edge face, parallel or at a small angle to the pump face. This then refracts off the angled face to then undergo total internal reflection off the pump face at a grazing incidence. This means the seed source is effectively stretched in one dimension, allowing for a much greater overlap with a diode bar pump source. This removes the need to either reformat the diode output into a more even aspect ratio or couple it into a fibre. Fast axis collimation is all that is required. As our HG_{01} mode is already in a roughly $3:2$ aspect ratio this will also help improve pump overlap. The reflection off the face also means the entire beam sees an even gain distribution. This is one of the main appeals of the bounce geometry. The seed is commonly focussed by a vertical cylindrical lens (VCL) into the gain crystal. This is to limit the scale of the seed in the vertical direction so it sees less of the aberrated thermal lens. The thermal lens, without dedicated compensation, is much stronger in this dimension. The angle on the edge faces also helps to reduce parasitic lasing when used as an amplifier.

The main advantages of the bounce geometry are its high gain and potential for high beam quality (for the fundamental mode) [162, 163, 164, 165]. Output powers in the 10s of watts with slope efficiencies of $50-70\%$ have been produced utilising a single stage MOPA. With a mode-locked seed and a triple pass of the amplifier, pulses as short as $8.8ps$ have also been demonstrated with high mode quality at average powers of $44.5W$ by Abe *et al.* [113]. The output from this was subsequently converted to an LG_{01} vortex mode by using a spiral phase plate. This was achieved with a 95% conversion efficiency giving greater than $40W$ of vortex mode. However, the mode quality was poor with clear azimuthal intensity variation and a changing mode profile with propagation.

Chard *et al.* have also demonstrated the production of a first order vortex mode within

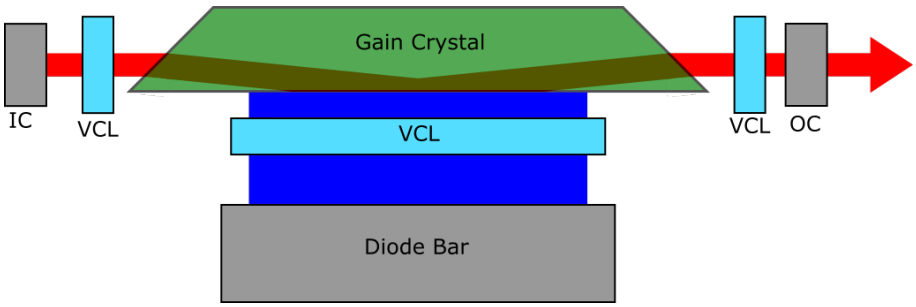

Figure 6.3: Basic layout of the bounce geometry laser. An amplifier is made simply by removing the IC and OC. The pump source is typically a diode bar focussed with a VCL. The cavity mode/seed enters an edge face then reflects off the pump face at grazing incidence. The crystal is cooled the top and bottom faces.

a bounce geometry laser [115]. This was generated from a laser where the pump had been defocussed and the input angle to the gain crystal adjusted until a roughly equal thermal lens was generated in each axis. This initially produced a high quality Gaussian mode. One arm of the cavity is then extended until the fundamental mode became more unstable. The instability comes from the fact that the thermal lens is much stronger in the centre of the gain crystal. As the vortex mode has a null in this region it sees a smaller lens and is better supported by the cavity. A DM is selected over other higher order modes, due to the cylindrical symmetry of the gain region. The handedness was found to be stable, though no known mechanism for this is presented. The mode suffered from a substantial Gaussian impurity and has azimuthal asymmetries in the intensity distribution. However, it has very little astigmatism, demonstrating that such a laser can support higher order modes. This gives further credence to the idea of amplifying a high order mode in such a design.

6.4 Q-switching

Q-switching is a very common method of pulsing a laser cavity. Pulsing a laser allows for significantly higher peak powers to be reached without significant additional pump power. This is essential for processes that have particularly high power or energy requirements such as materials processing, surgery, tattoo removal and non-linear optics [166, 167, 168, 169]. The pulse length of Q-switched lasers is largely determined by the cavity poton lifetime; this means pulsescan be sub nanosecond [170], though pulse durations of a few nanoseconds and higher are more typical. This allows for very accurate distance measurements to be made by timing how long it takes for a pulse to return in LIDAR or remote sensing applications [171, 172]. Q-switching works by alternating the attenuation (losses) within a laser cavity. The quality, or Q-factor, of a cavity is defined as the energy stored within the cavity divided by the the energy dissipated per cycle of the cavity.

$$Q = 2\pi f_r U_{sig} \frac{dU_a}{dt} \tag{6.2}$$

where Q is the Q-factor, f_r is the resonant frequency of the cavity, U_{sig} is the time averaged energy per unit volume in the gain medium, and $\frac{dU_a}{dt}$ is the time averaged rate of energy transfer per unit volume [1]. Effectively a low Q laser will have high losses for a given cavity mode whilst a high Q cavity will have low losses. Therefore a Q-switch is initially set to give the cavity high losses and prevent the laser from reaching threshold. The gain will therefore rise until the maximum energy storage is reached and the cavity is said to be gain saturated. The initial loss from the Q-switch must be high enough to prevent lasing or parasitic lasing may occur. This loss is then rapidly removed to provide the feedback to the gain medium and initiating stimulated emission. This will extract the gain rapidly into a single laser pulse. The cavity losses are then dramatically increased again to prevent the gain from recovering enough to cause a secondary pulse.

There are two ways to Q-switch a cavity: actively or passively. Active Q-switching occurs when the cavity Q is being controlled actively by the user, generally with an electrical signal. The actual Q-switch tends to be either an acousto-optic modulator or an electro-optic device such as a Pockels or Kerr cell. Pulses from these devices tend to be of the order of many round trips of the cavity. The optical switch needs to operate on a similar time-scale, otherwise secondary pulses can arise. The main advantage of such devices is a controllable pulse repetition rate. This will be linked exactly to the frequency of the switching, provided gain never builds so high as to facilitate parasitic lasing. In general as the repetition rate increases the pulse energy drops and the pulses lengthen.

Passive Q-switching utilises a saturable absorber. This is a material whose transmission is dependent on the intensity of light it is exposed to. At high intensities, the electrons in the ground state are rapidly excited into the upper state. The upper state lifetime is then long enough that the ground state becomes depleted, increasing the transmission at a given wavelength. This means saturable absorbers are significantly wavelength dependent. Under low intensity, a saturable absorber must exhibit a high loss in the cavity in order to increase the cavity losses, but not so high that it prevents all lasing. Once high enough gain is reached, low level lasing occurs which rapidly increases the transmission of the absorber, until the cavity gain is extracted into a single pulse. The recovery time of the absorber should ideally be longer than the pulse so as not to create additional losses, but not so long that the gain recovers fast enough to lase again. The main advantage of passive Q-switching is its simplicity, normally only requiring the addition of a single optic to a cavity. They are also suitable for very high repetition rates, as they are not limited by the speed at which an electrical signal can be modulated. However, the pulse energy and

duration tend to be fixed, with the pump power only effecting the repetition rate. They also can reduce laser efficiency as non saturable losses in the absorber tend to be high.

As we are aiming for an end application of laser processing, we should Q-switch our laser as this will greatly broaden the potential uses for our system. This is particularly relevant as it concentrates the photons into a short time period, increasing the instantaneous torque that can be applied when a vortex mode is absorbed. A laser operating on HG modes has been passively Q-switched before by Bagdasarov *et al.* [72]. They used intra-cavity masks to select for modes up to HG_{12} in a Nd:Phosphate glass rod laser. This was then amplified in another Nd:Phosphate glass rod to produce pulses with energy up to $100mJ$. This mode is then passed through an astigmatic mode converter. The mode quality for the LG_{01} mode is hard to assess as no spiral interference pattern is given and the intensity pattern saturated the camera (it seems superficially reasonable however). No image of the HG_{01} is provided, and the neither the repetition rate nor the average power are given. However, this demonstrates that it is possible to Q-switch, amplify and then mode convert a HG_{01} mode. Therefore we decided to passively Q-switch our double pump HG_{01} laser. Passive Q-switching was chosen for both its simplicity and as it would allow for a more compact cavity.

6.5 Q-Switched HG_{01} Seed Laser

In order to generate shorter pulses and, therefore, higher peak powers, we need to shorten the double pump laser cavity. To do this we removed the cavity lens and replaced the plane OC with a 5% transmission spherical OC with a $70mm$ radius of curvature. This required a change in the telescope used to focus the pump into the crystal from Section 5.7 in order to maintain a good overlap with the HG_{01} mode. The telescope now consisted of a $100mm$ collimating lens after the prism and a $50mm$ focussing lens. This dramatically reduced the pump spot diameter to $105x270\mu m$. These changes allowed us to shorten the cavity down to an optical length of $74.9mm$ giving it a round trip time of $250ps$ (This includes the passive Q-switch). We used a Cr^{4+}:YAG passive Q-switch with 70% initial transmission and AR coated at $1064nm$ to pulse the cavity. The doping concentration was not given by the manufacturere but the sample was approximately $4mm$ long. This was placed $10mm$ away from the rear of the Nd:YVO_4 crystal. It could not be placed closer due to the size of the cooling block and the mount for the Q-switch. Better pulse operation was found when the Q-switch was placed at this end of the cavity. We believe this is because the smaller mode size increased the intensity incident upon it, more effectively saturating the absorption. A schematic of the cavity is given in *Fig. 6.4*.

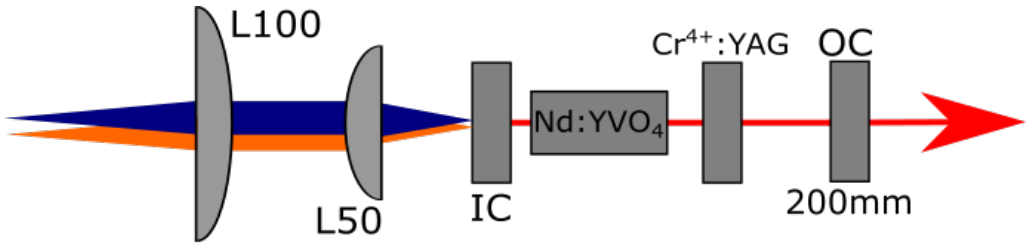

Figure 6.4: Schematic of the double pump Q-switched HG_{01} laser. The optical cavity length is $74.9mm$ and the Cr^{4+}:YAG passive Q-switch has an initial transmission of 70%

A pulse train and example pulses were measured with a fast photodetector and are shown in *Fig. 6.5*. These were taken with $5.06W$ of total pump power giving a repetition rate of $147kHz$. The pulses varied between $22ns$ and $26ns$ in length. This is 96 times the round trip time of the cavity, this is within the bounds of what we might have expected given the higher than normal reflectivity of the output coupler used for a Q-switched laser. This is something that could be easily improved in the next version of this laser. Occasional secondary pulses were observed. This phenomenon was found to occur much more regularly at higher pump powers, particularly above $5.42W$. This is likely due to the gain recovering quicker than the saturable absorption of the Cr^{4+}:YAG, leading to a second pulse forming. These 'double pulses' were typically separated by $100 - 200ns$, a finding consistent with other Cr^{4+}:YAG Q-switched solid-state lasers [173].

Unexpectedly the beam quality was maintained at much higher pump powers when the Q-switch was included within the cavity. This may be due to the additional intensity dependant losses from the Cr^{4+}:YAG crystal. We propose that the regions of the cavity mode that are solely associated with the modal impurity have a lower intensity and therefore never fully saturate the crystal, therefore experiencing higher losses compared to the main mode. This suppresses the mode impurities meaning we can pump harder without degrading the beam quality. *Fig. 6.6* shows beams produced before the Q-switch was added, with pump powers of $0.37W$ and $0.57W$ respectively. This produced $149mW$ and $277mW$ of output. We can see the higher power beam has a significant peak mismatch of 7% of the peak of the higher power lobe, whilst the lower has only an approximately 1% mismatch. They have 7.7% and 10.0% excess central power respectively. Looking at their residuals we see no clear pattern for the lower power beam whilst a clear pattern indicating HG_{02} impurity emerges for the higher power beam. Quantifying this using the method outlined in Section 4.4.4, we find there to be a 22% HG_{02} mode impurity. This is significant and could cause problems in the amplifier with the HG_{02} being amplified alongside the HG_{01}. As they have different intensity distributions the HG_{02} may be able to extract gain not available to the main mode, meaning the two modes may not be am-

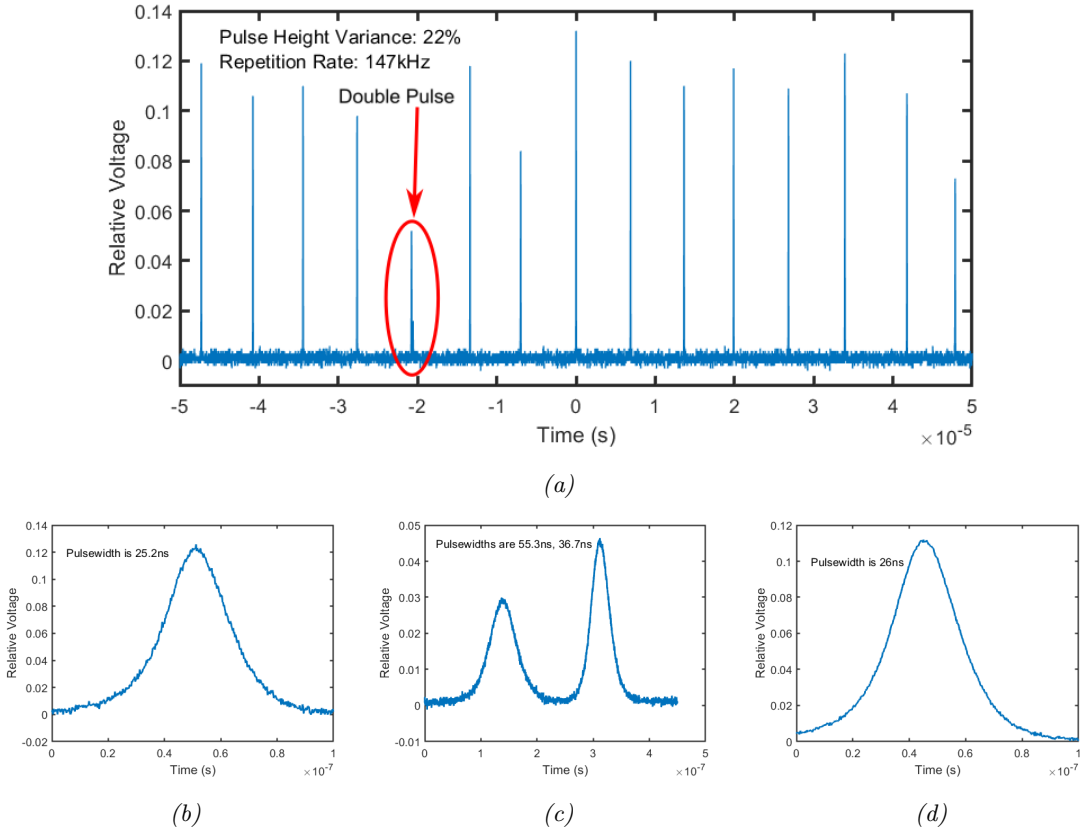

Figure 6.5: (a) shows a typical pulse train, exhibiting one double pulse. *(b)*, *(c)* and *(d)* show individual pulses. The pulsewidth was consistently between $22ns$ and $26ns$ for the single pulses.

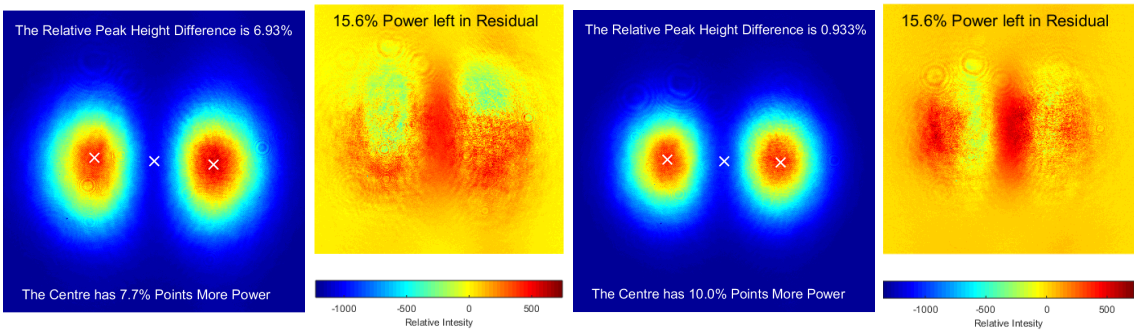

(a) *(b)* *(c)* *(d)*

Figure 6.6: Beams and residuals from the seed laser without a Q-switch. *(a)* is the $149mW$ beam and *(c)* the $277mW$. *(b)* and *(d)* are their respective residuals. The higher power beam exhibits a HG_{02} beam impurity as is clear from the residual.

plified equally. They might also see slightly different thermal lenses. All of this would degrade beam quality. Furthermore, any HG_{02} mode fed into an AMC will not necessarily be mode matched correctly, as it may not have exactly the same mode size (as in the mode size of the fundamental mode, w_0, used in equation (4.1)) after the amplifier. This would lead to a HG_{02} impurity in a predominantly LG_{01} beam, leading to a reduction in the concentration of OAM and a disturbance of the cylindrical symmetry. If we were to amplify the output from the seed without the Q-switch, we would need to limit the output power to less than $200mW$ without improving the overlap between the gain and the pump. We see that we can obtain similar powers of HG_{01} mode as with the lens stabilised double pumped laser from Section 5.7. Lower pump was needed due to the lower cavity losses. This demonstrates the consistency of the double pump method.

If we now add the Q-switch to the cavity we can look at the beam created at a pump power of $5.06W$ producing an average output power of $434mW$, *Fig. 6.7a*. We see a fairly dramatic drop in the lasers efficiency, however we have achieved a much higher power beam of usable quality. This loss in efficiency is not unexpected as the passive Q-switch was expected to add substantial loss to the cavity even when saturated. Though this loss was not able to be quantified. The output with the Q-switch at this pump level is of much higher quality than it was without it. The only clear discrepancy from a pure HG_{01} mode is the CCD blooming. This was largely linked to the use of a different camera for this portion of the experiment. This however does interfere with our ability to estimate the level of impurity. The peak height mismatch is low at 3% and we believe that much of the excess central power is linked to the blooming. This is affirmed by looking at the residual, *Fig. 6.7b*, which has central peaks that add to our definition of the excess central power and are in line with the blooming streaks above and below the beam. That the very centre

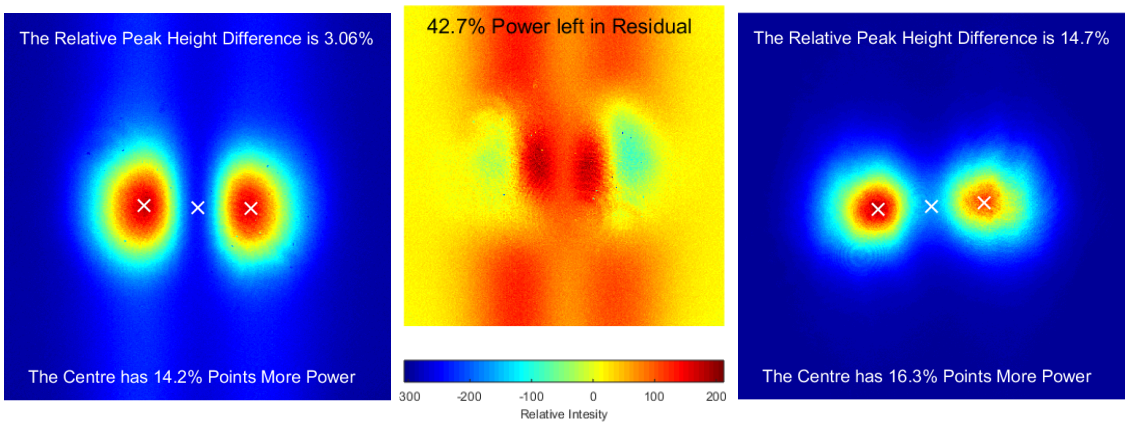

(a) *(b)* *(c)*

Figure 6.7: (a) is the seed mode used for the amplifier. *(b)* is its residual. We can see most of what remains is from CCD blooming. *(c)* is a mode at near equivalent pump power produced with the Q-switch removed.

of the residual does not drop to zero, may indicate some low level Gaussian impurity but this seems insignificant. This shows the need in future either minimise CCD blooming or find a way to identify and remove it from beam images. Finally, we can compare this to a beam made without the Q-switch at a similar pump power of $4.73W$, giving $2.38W$ of output, *Fig. 6.7c.* There is a significant peak mismatch and excess central power. Furthermore, the peaks have rounded out indicating other modes are present. We believe the improvement in beam quality from the Q-switch is due to the additional cavity losses it causes. This raised the thresholds of the impurities to the extent they didn't lase till much higher pump powers. This was critical, as it allowed us to operate in a regime with both good beam quality and stable pulse operation; as at lower pump powers pulses were skipped and pulse variance was higher. This is similar to findings by Lucianetti *et al.* in another passively Q-switched $1064nm$ laser [174].

6.6 Amplifying First Order Hermite Gaussian Modes

After the laser, the beam is collimated with a $135mm$ spherical lens, the remaining pump is filtered out, and the polarisation rotated with a half waveplate for maximum transmission through an isolator. This isolator was found to have near-perfect transmission with only a $1mW$ drop in power from $403mW$ of input. This small loss was partially due to slightly imperfect polarisation purity in the seed, the rest probably due to losses in the optical coatings. The polarisation is then reorientated with another half waveplate to align it with the c-axis of the amplifier gain crystal. The 1.1% doped, a-cut Nd:YVO_4 gain crystal

has dimensions of a $20mm$ x $2.5mm$ x $2mm$ slab with its end faces angled at 14^o and AR coated at $1064nm$. The longer of the two edge faces is polished and AR coated at $808nm$. The top and bottom faces are conduction cooled by 13.0^oC water pumped through a copper heat sink. This is run off the same supply as the cooling for the gain crystal in the seed laser to roughly couple their temperatures and match their emission spectra. This ensured high gain for the seed. The pump source for the amplifier is a DILAS^{TM} $808nm$ bar diode. The pump light fills approximately 70% of the pump face width. The diode's maximum output power was originally $60W$ however the central emitter had failed, reducing its output to $54.9W$. This should not be of concern with regards to amplification of the seed, as it should still see even gain due to its beam path through the amplifier. The diode cooling water temperature was held at 32.0^oC for optimal overlap with the absorption of Nd:YVO_4. This diode was fast axis collimated and a $12.7mm$ VCL is used to focus the pump into the diode. Two steering mirrors are used to direct the seed into the amplifier and two $50mm$ VCLs are placed either side of the gain medium in order to focus, and then collimate the seed in the vertical axis. A full schematic is given in *Fig. 6.8*.

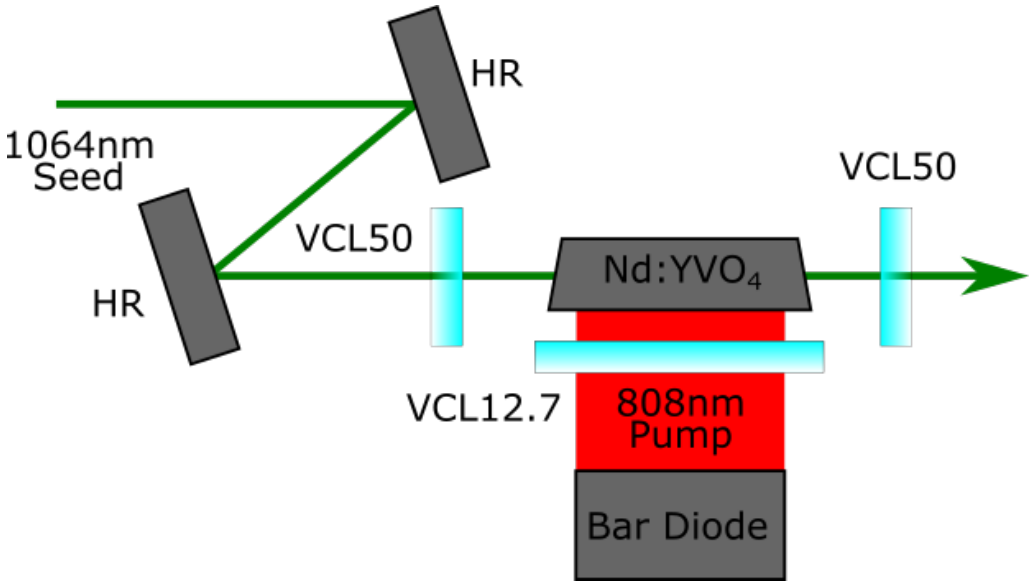

Figure 6.8: Schematic of the bounce geometry amplifier. VCLXX is a vertical cylindrical lens and its focal length in *mm*. HR is a highly reflective mirror at the seed wavelength.

6.6.1 Single-Pass Amplification

The two steering mirrors can be used to alter the bounce angle through the amplifier and the position of the bounce on the pump face. Alignment was optimised for a combination of beam quality and output power. We initially ran the amplifier in a single-pass configuration. The seed power at the amplifier was $0.42W$ and the best operation was found with

the bounce position roughly centred in the gain crystal as expected. Power curves for both the amplifier pump and output are given in *Fig. 6.9*. We can see the amplifier output is not entirely linear, with a change in the slope between $20W$ and $32W$ of pump power. The gain is still increasing as we reach maximum pump power, topping out at $15.86dB$ with $15.8W$ of output. However, the mode quality from the amplifier is suboptimal. We show the beam as it evolves with greater pump power in *Fig. 6.10*. We can see initially, just above the amplifier threshold, one lobe of the mode appears to be amplified more than the other. This quickly evens out as the gain increases, however we can see some extra structure in the wings of the mode at $22.0W$ of pump. This structure suddenly gains power at $24W$ of pump and merges with one lobe and then slowly splits from it as the gain increases. The inner lobe disappears around $28W$ and the two remaining wider lobes then steadily diverge until the two lobes of power are very widely spaced at $52W$ of pump. All these outputs were stable provided the pump power remained constant. At mid-high pump powers significant astigmatism in the beam was observed that could not be easily corrected with the collimating VCL. We can think of no clear physical explanation as to why this lobe splitting and then spreading would occur within the amplifier.

This splitting of the mode's lobes was unexpected and makes the higher power modes unsuitable for mode conversion. The output power at all pump powers was found to be strongly dependent on the position of the VCLs focussing both the pump and the seed into the gain crystal, and more weakly dependent on the bounce angle. None of these variables significantly effected the mode quality for better or worse. Nor did the seed power, however the position of the bounce in the crystal did heavily influence the transverse intensity distribution. Moving away from the centre tended to favour amplification in one lobe compared to the other causing peak height mismatch. It also affected the pump power at which the lobe splitting occurred, with it happening at higher pump powers as the bounce moved towards the edges of the gain crystal. This non-central alignment introduced other unwanted beam features such as a distortion in the lobe closer to the edge of the crystal and additional structure outside the other lobe. As these phenomena were largely dependent on the pump power and the symmetry of the path the seed took through the amplifier we concluded these effects were caused by the thermal lens within the amplifier. In order to lessen the effects of this we decided to implement a telescope before the amplifier.

6.6.2 Single-Pass With Seed Demagnified

As the thermal lens is not necessarily spherical, a larger beam will see more distortion from it as different parts of the beam see differing effective focal lengths. We installed a tele-

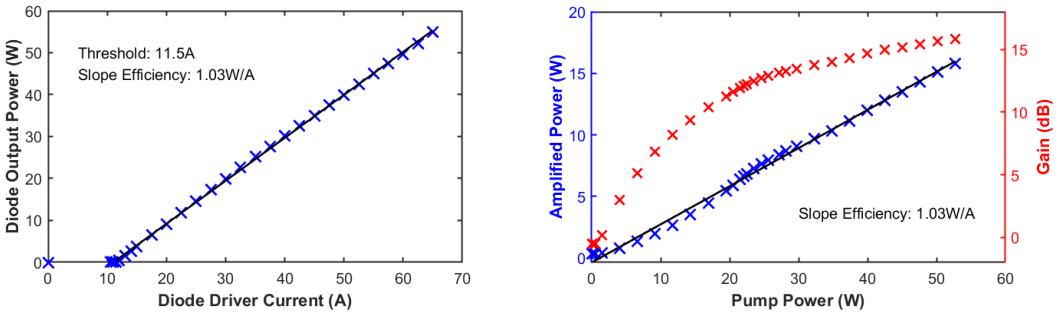

(a) *(b)*

Figure 6.9: (a) power curve for the amplifier bar diode. The bar diode has a linear power curve, despite the broken emitter. *(b)* power curve for the single-pass amplifier with no telescope.

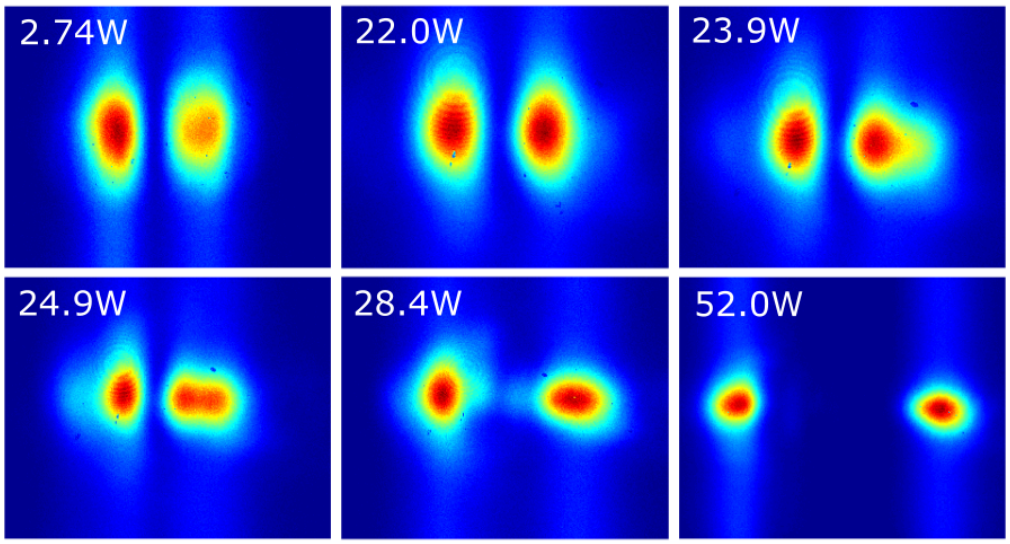

Figure 6.10: Beam images of the $0.42W$ HG_{01} seed when amplified in a single-pass configuration with no telescope. Values in white are the pump power being emitted from the bar diode for each image.

scope consisting of a $150mm$ and $70mm$ lens to reduce the beam size and pseudo-collimate the seed through the amplifier. This was not a $4f$ system, as there is a $290mm$ spacing between the lenses. Exact imaging of the seed is not necessary as it is an incoherent sum of Gaussian modes. The lenses were instead aligned to place a beam waist approximately central within the amplifier crystal. This symmetry should reduce distortion if the bounce location is also approximately central in the gain crystal. A schematic of the beam delivery with lens spacings is given in *Fig. 6.11*.

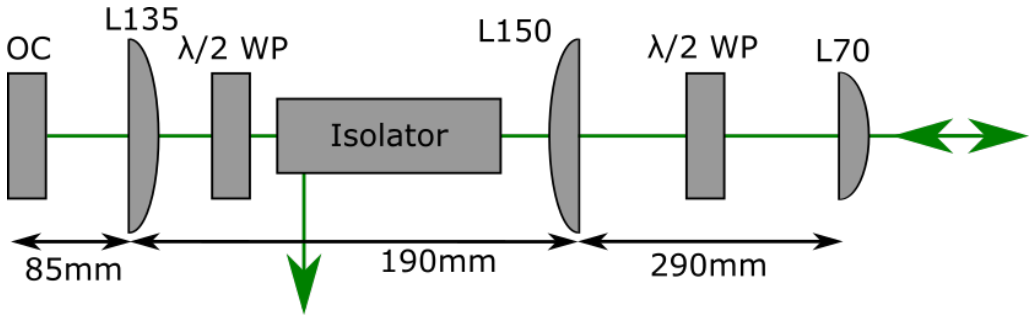

Figure 6.11: Schematic of the beam delivery optics before the bounce amplifier. LXX is a spherical lens with focal length XX in mm. When the amplifier is in double-pass configuration, the return beam is filtered out by the isolator.

We can then once again look at how the amplified beam evolves with increasing pump power, see *Fig. 6.12*. Again all the beams were astigmatic. This is especially clear from our camera placement for the beams at $29.8W$ of pump power where the lobes are elongated.. Initially at low pump powers the mode quality is reasonable. As it increases, however we see significant peak height mismatch, which starts at around $20W$ of pump power. We found that by increasing the bounce angle we could largely correct for this as well as increase the output power at higher pump powers. However, reducing the pump below $27W$ in this alignment reduced both the output power and beam quality. This is illustrated in the power curve given in *Fig. 6.13a*. The re-alignment causes a significant improvement in the slope efficiency at higher pump powers, though at a lower pump we observe less output power than the previous alignment. We can see the difference this realignment makes with the beams pumped with $29.8W$. We see that before the re-alignment (top right of *Fig. 6.12*) the two lobes have different shapes with the right lobe being taller and thinner. After re-alignment the lobes are much more even and there has been a $700mW$ improvement in output power, see *Fig. 6.13*. As the pump increases, some asymmetry in the lobes begins to reappear, however it is fairly minimal. The two lobes drifting further apart in the x axis (though no splitting of the lobes) is again observed at higher pump powers starting at $45W$. This is a substantial improvement in the mode quality at the expense of some output power and gain. The maximum output power being reduced to

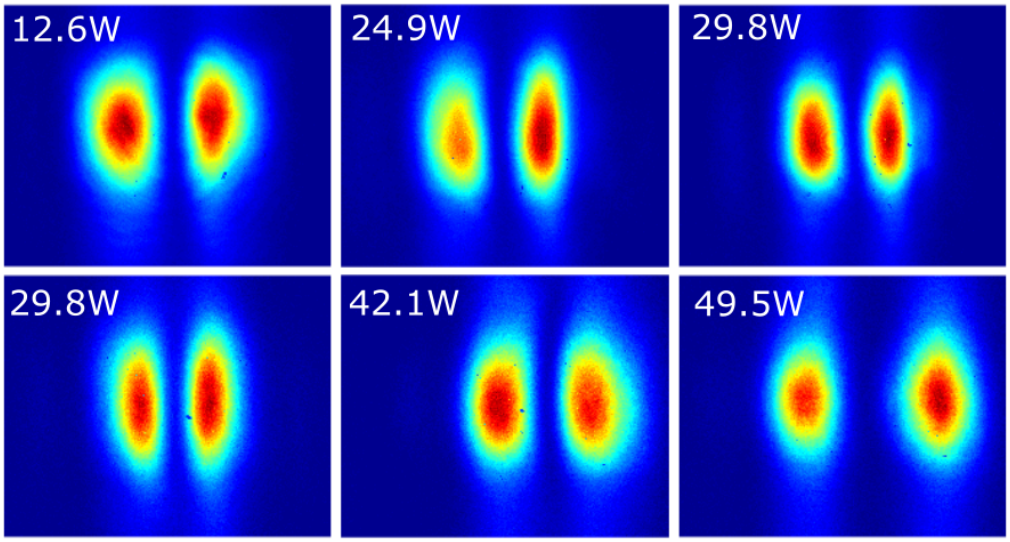

Figure 6.12: Beam images of the $0.42W$ HG_{01} seed when amplified in single-pass configuration, after passing through a demagnifying telescope. Values in white are the pump power being emitted from the bar diode for each image. The second row depicts beams after the cavity was realigned to improve both mode quality and output power.

$13.7W$ at $15.35dB$ of gain. However, the maximum output power for a mode that is of quality potentially suitable for mode conversion is much higher: going from $6.6W$ to $11.4W$. The pulse structure of the seed has also been maintained as we can see in *Fig. 6.13b*. There is still low pulse to pulse variation and few double pulses.

Examining the two highest quality modes from our two single-pass configurations with our intensity distribution analysis, see *Fig. 6.13 (c), (d), (e)* and *(f)*; we can see that the beam generated before demagnifying the seed has even peak heights but some reasonably significant excess central power. This is most likely from the blooming effect. Of more concern is the structure in the wings of the beam. There is a small amount of power either side of the two lobes. This is just visible in the residuals as two slight peaks on the outside of the valleys. This is also apparent in the output after the telescope was added, however only outside the right lobe. This has the appearance of widening this lobe compared to the other. This may also be linked to the significant peak height mismatch. There is less excess central power, but this is due to the larger image size on the CCD, meaning less blooming has leaked into the central region. Both these modes, if their significant astigmatism can be compensated, may produce reasonable vortex modes via the mode converter. However, this was not tested, due to the considerable difficulty in removing the astigmatism and the time constraints of this project. We instead chose to see if we can improve the beam quality and output power by using a double-pass configuration.

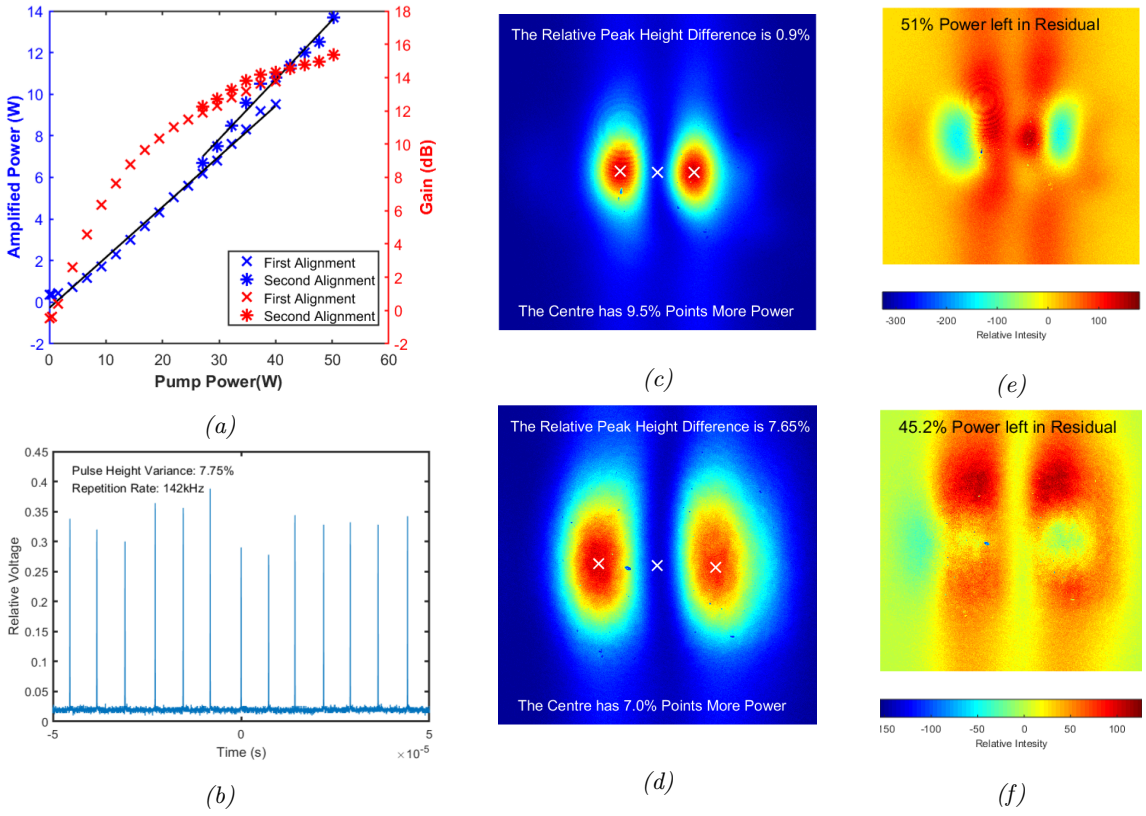

Figure 6.13: (a) shows the both the gain and output power of the single-pass amplifier when operated with the telescope. The higher bounce angle alignment is plotted with asterisks. We see we have less overall power and gain than without the telescope. *(b)* is the pulse train from the amplifier. *(c)* is the 6.6W output from the amplifier with no telescope. *(d)* is the 11.4W output from the amplifier with the telescope. *(e)* and *(f)* are their respective residuals.

6.6.3 Double-Pass Amplifier

For the double-pass configuration, a HR mirror was placed after the collimating VCL. The position of both the rear mirror and the VCLs are critical to mode match the amplified seed with the gain. Furthermore, these optics control the size of the beam as it is reflected back through the system. In order to extract the amplified beam, we utilise the non-reciprocity of the isolator. Provided the amplifier has not modified the polarisation of the beam it will be reflected out the side of the isolator by the second polarising beam splitter within it. As the aperture for the isolator had a diameter of $2mm$, we are limited in the size of the return beam. This constrains the position of the amplifier optics. We found it was not possible to maintain both good amplification and a small enough beam diameter to pass through the optics. Therefore we added a horizontal cylindrical lens (HCL) between the second VCL and the HR mirror retro-reflecting the output. The positions of these optics are given in *Fig. 6.14*. This allowed for passage through the isolator with minimal clipping. The amplifier was misaligned slightly in order for the output power to be measured before passage through the isolator. Before the isolator, the maximum output power was $17.2W$, with $17.0W$ transmitted through it. Some of the lost power is due to clipping of some additional structure outside the main beam on the isolator aperture. A power curve taken after the isolator is given in *Fig. 6.15a* and a pulse train in *Fig. 6.15b*. The maximum gain achieved was $16.28dB$ with $17.0W$ of output. There was an increase in the variation in pulse height and an increase in the average pulse width to $36ns$, as well as a destabilisation of the pulse train, with a greater variation in the time between the pulses. The cause for this is unknown, though it may be due to feedback into the seed laser, despite the isolator.

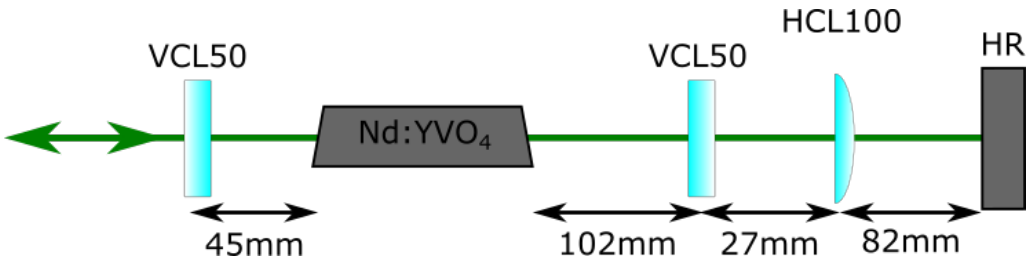

Figure 6.14: Schematic for the double-pass amplifier. HCL100 is a horizontal cylindrical lens with a $100mm$ radius of curvature.

The beam quality was degraded further in the double-pass of the amplifier. The beam also remained exceptionally astigmatic. We focussed the output through a $200mm$ focal length spherical mirror and took beam images at various power levels in three locations: approximately $100mm$ before the vertical focus, at the vertical focus and $100mm$ after it. With this focussing the vertical and horizontal foci were separated by up to $112mm$,

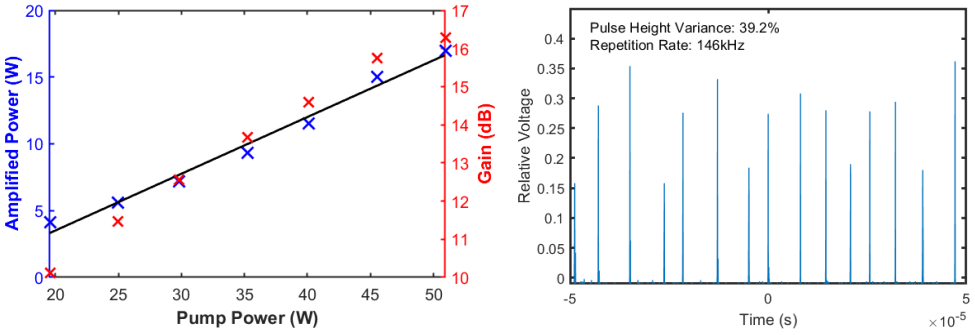

(a) *(b)*

Figure 6.15: (a) is the power curve and gain for the double-pass amplifier. *(b)* is an example pulse train from the double-pass amplifier.

depending on pump power. Beam images at three pump powers are presented in *Fig. 6.16*. The top row is at $30W$ of pump power producing $7.2W$ of output. We see that after the focus, the beam appears of reasonable quality. However, there is a large mismatch between the peaks before this. Before the focus there is also a severe excess structure in the mode. This variation as the beam propagates clearly shows there is some form of impurity that is either not co-linear with the main beam, or is coherent with it. This pattern continues as the pump is increased to $40W$ and $50W$ producing $11.5W$ and $17.0W$ of output respectively. We observe a reversal in the lobe with more power as we move through the focus at $11.5W$ though not at $17.0W$. We see an excess of central power in all the beams and additional power above and below the beams away from the vertical focus. It is possible that this unwanted structure and variation upon propagation is caused by amplifying impurities in the seed. However, re-aligning the seed cavity and changing its power had no substantial effect on the amplified mode quality. Nor did changing the bounce angle of the amplifier; this only influenced the output power. As the nature of these impurities is again primarily dependent on the pump power, we conclude that they are likely caused by thermal aberrations in the gain crystal. The double-pass has amplified this unusual effect further making the output unusable. None of these modes, even if the astigmatism can be compensated for, are suitable for mode conversion.

After operating the amplifier in the double-pass configuration. We noticed damage to the gain crystal. We are unsure when this occurred, as there was no sudden change in performance from the amplifier. It may have occurred at the start of the amplification experiments. An image of the damage is shown in *Fig. 6.17*. This may be the source of our poor beam quality: either by amplifying scattering from it or due to aligning around it, worsening the thermal distortions. The cause of the damage is unknown but it is likely from the seed source machining the corner of the crystal during alignment. In the future

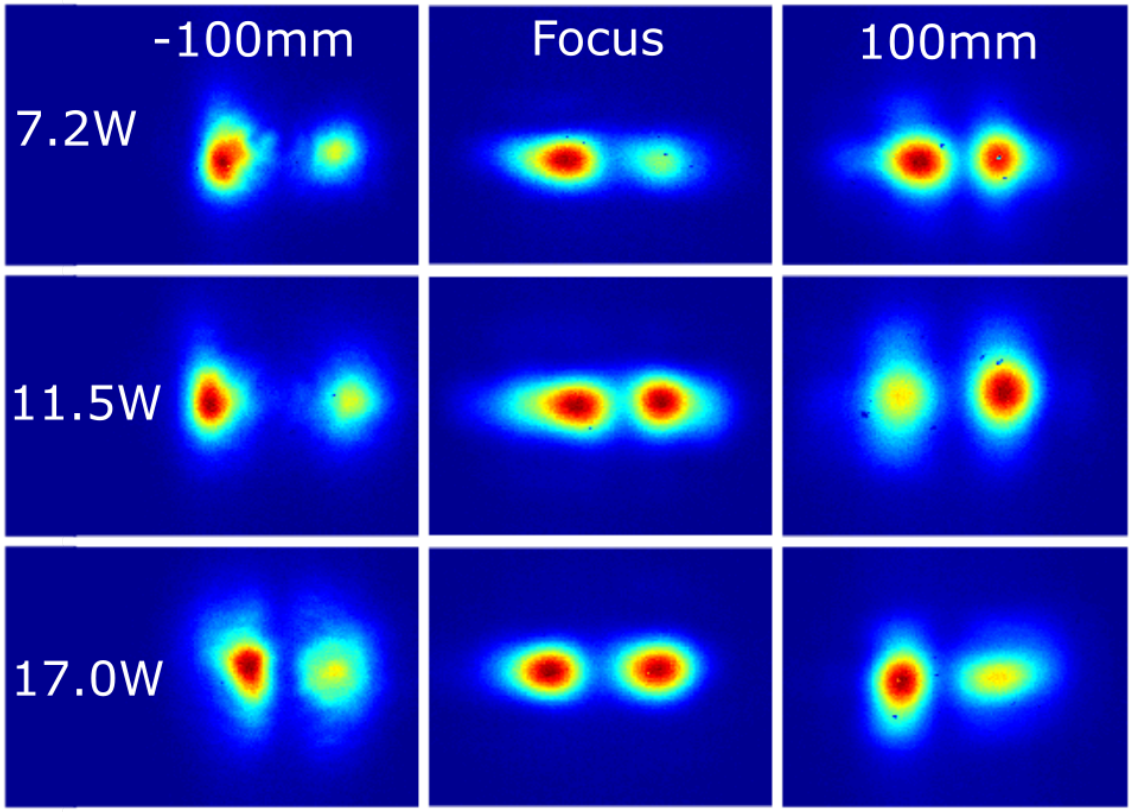

Figure 6.16: Outputs from the double-pass amplifier. Each row is a different output power level, the central column is taken in a focal plane, the left and right columns $100mm$ either side of this.

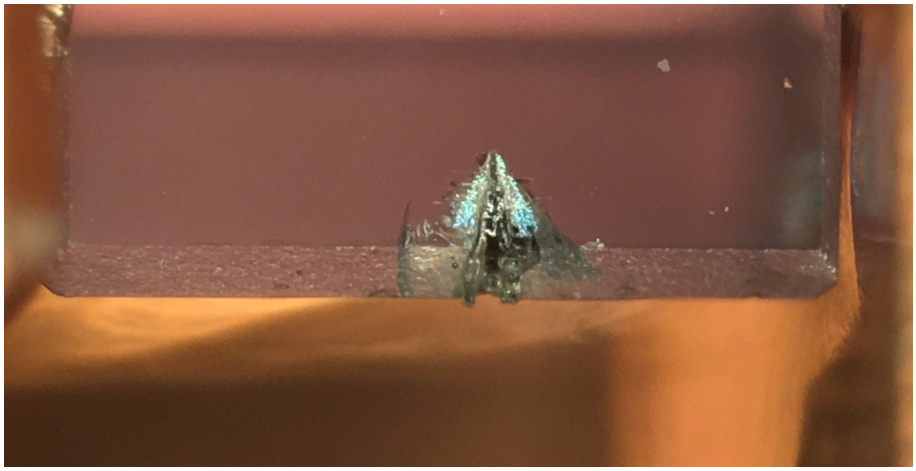

Figure 6.17: Magnified photograph of the damage to the amplifier gain crystal.

more effort should be made to keep the crystal clean and to use a lower power seed for initial alignment.

6.7 Conclusions

6.7.1 Possible Improvements to the Bounce Geometry Amplifier

Ultimately we were not able to scale the power of a HG_{01} mode using a bounce geometry amplifier, without compromising the beam quality or causing significant astigmatism. We may have been able to mode convert an $11.4W$ HG_{01} mode successfully to a vortex mode if we were able to componsate for the astigmatism, though this fell outside the time scope of this thesis. More work on this system may have yielded better results, but this again went beyond the scope of this project. An obvious improvement would be to keep the gain crystal free from damage and possibly by using a purer seed source. Widening the apertures on the isolator would also allow for more flexibility in the position of the amplifier optics. This may minimise the distortion and improve the gain. Alternatively a non-retro reflecting deign may be used. Here the return angle of the beam into the amplifier would be different to the initial entrance angle. This means the amplified beam would not counter-propagate with the seed and can be extracted with a pickoff mirror. The may extract the gain better and reduce thermal effects, as well as fully prevent the amplified beam from interfereing with the seed. Better cooling could also be used to try to reduce the thermal lensing. Another option would be to try to replicate the stigmatic bounce geometry amplifier created by Chard *et al.* [115]. This had the property of a circular gain profile as seen by the seed and a spherical thermal lens. This was achieved by varying the bounce angle on the pump face and the focussing of the pump. This may not work for a HG_{01} seed however as for optimal gain overlap an elliptic pump shape is

needed, this may be challenging to balance with a spherical thermal lens.

We may have more success if we sacrifice gain for mode quality and run the amplifier in a single-pass configuration. In single-pass the beam distortion was less significant leaving compensation of the astigmatism as the major hurdle. However as a condition for astigmatic mode conversion is a non-astigmatic input beam this would need near perfect compensation. This in addition to the other mode matching conditions would require a significant number of beam delivery optics capable of withstanding the high peak powers of the amplified beam. This may make this route impractical compared to other options. This can only be avoided by operating the amplifier with a near perfect spherical thermal lens. As the thermal lens is dependant on almost every aspect of the amplifier design this would be exceedingly challenging and limit flexibility in its operating parameters. Either approach greatly adds to the complexity of obtaining a high quality vortex mode. Other amplification approaches may prove more practical.

6.7.2 Other Possible Amplifier Geometries

Our seed begins non-astigmatic. We have seen the severe astigmatism produced when using a non cylindrically symmetric medium that would appear to favour amplifying a HG_{01} mode. A better approach maybe to amplify in a cylindrically symmetric medium. An example would be an end pumped rod geometry such as that used to generate the seed. To maintain a spherical thermal lens however a cylindrically symmetric pump is required which would lead to poor overlap with the seed. This will leave unused regions of gain that may either amplify any impurities in the seed or be susceptible to parasitic lasing. It will also reduce the efficiency of our amplifier. It may therefore be better to amplify the LG_{01} mode after the AMC.

There are very few example of amplifying vortex modes. It is not clear they will hold their OAM upon amplification though we know no mechanism that would cause them not to in a bulk design. In a fibre design it is possible the seed vortex mode may couple into other modes supported in the waveguide if it is not launched correctly. This is unfortunate as astigmatism is practically eliminated in a fibre amplifier. The most likely amplification geometry to succeed may therefore be an end pumped rod design. This could be pumped by a capillary fibre for excellent gain overlap. Care would be needed to be taken with the cooling to manage thermal effects however, as rods have a limited cooling surface. This could be improved by reducing the gain in any given amplifier stage and using a multiple stage MOPA architecture to achieve the desired output power. Another alternative would be to use doped glass as a gain medium and draw it into a long thin rod. This would increase the cooling surface but, provided the diameter was large enough, not act

as a waveguide. Pumping such a geometry evenly would be challenging. It is unlikely a capillary fibre could be used as the output only remains doughnut shaped near a focus. However, one could use a a top hat pump with a relatively long Rayleigh range.

Overall there are still many amplification geometries to explore in order to realise high purity vortex modes at machining powers. It has fallen beyond the scope of this thesis to realise this, nevertheless we believe using an astigmatic mode converter, HG_{01} source and an amplifier to be a viable route towards this. It presents particular advantages in terms of mode purity and handedness control, provided purity can be maintained through the amplification stage.

Chapter 7

Conclusions and Future Work

The aim of this thesis was to investigate and develop a method for generating power-scalable vortex modes with controllable handedness, with a particular focus on these modes' applications to laser processing of materials. This led us to experiment with several different approaches of generating these modes and weigh there various benefits and limitations. We also sought to improve the methods used to detect and identify these modes. This final chapter seeks to summarise our key findings and discuss how well we met these aims. Suggestions will also be made as to future work that could be done to better meet and expand upon our aims. The approaches we took include: using high aspect ratio capillary fibres to pump a bulk solid-state laser and generate high order doughnut modes (DMs); an investigation into what causes handedness selection of vortex modes within a cavity through experiments with a vortex mode ring laser; a presentation of some new techniques to estimate the purity of higher-order transverse modes; the generation of high purity first order Hermite-Gaussian (HG) modes so they can be converted to vortex modes using an astigmatic mode converter (AMC); the power amplification of first order HG modes before their conversion to vortex modes.

Through our experiments the purity of LG_{01} (as well as other higher-order transverse modes) became apparent as major issue that had, so-far, not been fully addressed. Its importance is easily underestimated as, unlike with more conventional fundamental transverse modes, there are many different modes that all give a LG_{01} intensity profile. This means that one needs to achieve not only single transverse mode operation, but also that this is the right kind of LG_{01} mode. Our research therefore followed a pattern of trying different ways to first achieve creating a pure vortex mode, followed by ways to confirm this.

We began this thesis with a review of the literature aimed to both explain the desire for making vortex modes, as well as the various methods, and challenges. in creating them. We explain how the properties of vortex modes are useful for applications in laser

processing, remote sensing, optical tweezing and more. We also highlight how an impurity in the vortex mode will diminish these desirable properties. We then expand upon the many ways of making DMs with a particular focus on vortex modes. We find that external methods of generating vortex modes: spiral phase plates and spatial light modulators, but with the exception of AMCs, will create a vortex mode like beam. However, it will contain significant impurities and the beam will not hold its intensity profile as it propagates, making it not a true mode. Most methods internal to the cavity will not necessarily create a vortex mode. Instead creating a radially or azimuthally polarised mode, or an incoherent superposition of DMs that may not contain OAM. Sometimes OAM is observed, but whether all the beams power is contained within a vortex mode of a specific handedness is rarely confirmed. Furthermore, the handedness of the vortex mode is almost never controllable, nor is it necessarily reliable. We also see how most attempts to make high azimuthal order DMs result in undesirable petal modes that are a coherent superposition of vortex modes with opposite handedness.

We now begin a summary of this thesis, chapter by chapter.

7.1 Generation of High Order Laguerre-Gaussian Modes

In this chapter we go into more detail on the benefits of DMs for machining besides their ability to have exotic polarisation states and OAM. This is mostly due to the differing thermal behaviour of materials illuminated by a beam with a central intensity null and steeper intensity profile. These benefits can also scale with higher azimuthal mode order. We then describe the mechanisms by which pumping with a ring shaped profile can preferentially select for a DM. Furthermore, we show how a thinner ring with a higher aspect ratio between its outer and inner radii will preferentially select for higher azimuthal orders; and derive an equation that can predict a given modes threshold. We then use a capillary fibre, with an outer to inner radii ratio of 0.8, to pump a bulk solid-state laser. This results in high-order petal modes up to $LG_{0,23}$. This highlights the difficulty in selecting for a single handedness of vortex mode. Some form of intra-cavity handedness selection would need to be discovered and implemented in order to make this approach viable for generating vortex modes.

7.2 Investigating Handedness Selection in Vortex Mode Ring Lasers

In an attempt to find an intra-cavity handedness selector we elected to build a single longitudinal mode, uni-directional, ring laser. Before this we explain that having a single

longitudinal mode should also force single transverse mode operation, and that this, when pumped with a capillary fibre, will produce a vortex mode. We then explain how a Mach-Zehnder interferometer can be used to test for the presence of OAM, and how a scanning Fabry-Perot etalon can be used to confirm single longitudinal mode operation. We found, unexpectedly, that in the uni-directional ring laser the handedness of the vortex mode was associated with the direction the intra-cavity mode traversed the Faraday rotator. This laser could then be used as the seed source for an amplifier, however its low efficiency and sensitivity to alignment may make this impractical.

We then built a semi-unidirectional ring laser using retro-reflection of one of the outputs to enforce the directionality. This did not operate on a single longitudinal mode. This allowed us to isolate the handedness selecting effect to the Faraday rotator, however it appeared to be a much weaker selecting device than when used in the single longitudinal mode ring laser. We also discovered a similar effect in the highly chiral material tellurium dioxide. Attempts to replicate this effect in a standing wave cavity were unsuccessful. We were also unable to measure any differential loss between the two handednesses, caused by this effect, in free space. We therefore conclude this effect is exceptionally small and appears to only be practical in single longitudinal mode, uni-directional ring lasers. This effect warrants more research into what causes the effect. Once this is understood it may be possible to scale it to a level where it will be useful within a typical laser cavity.

7.3 Higher-Order Transverse Mode Purity

Here we address the problem of higher order mode purity directly. We first review the literature on the various methods currently used to measure higher order mode purity and assess their merits and limitations. In general the techniques are either limited in scope or are generally qualitative in nature. We then present two new techniques for measuring the purity of higher order modes. We chose these methods due to their ability to be done digitally on data that was already routinely collected, meaning the techniques, once understood, are relatively simple to implement.

The first of these measurements assesses the azimuthal symmetry of the Mach-Zehnder interference patterns used test for OAM in vortex modes. This allows us to detect any azimuthal asymmetry in the vortex mode that must come from some form of impurity. This is mostly applicable when generating vortex modes using an AMC, as the most common impurity from these will be a HG_{01} mode. In this case it also gives us a reasonable estimation as to the amount of OAM content within the beam compared to the theoretical

maximum. This was experimentally tested and the experimental results were found to fit well with theory. One improvement to this would be to calibrate the power of the spherical wave electric field used in the simulations with the power of the spherical wave actually used to create the measured interference pattern.

We then moved to analysing the intensity profiles of LG_{01} and HG_{01} modes. We initially set some limitations to when this analysis was applicable such as; the beam must be stigmatic, incoherent modal-impurities must be the most likely impurities, and the beam must be predominantly either a HG_{01} or LG_{01} mode. We then looked for key features that were indicators of impurity such as excess power in the centre of the beam, peak height differences for the HG_{01} mode and azimuthal symmetry for the LG_{01}. We then generated theoretical matching modes to these and subtracted this from the measured intensity profile. This left a residual intensity distribution that allowed us to identify certain modal impurities in the beam. In the case of the HG_{01} beam, when there was predominantly only one modal impurity, we were also able to estimate what quantity of the power was associated with the impurity.

This intensity analysis is still in development. We want to look at ways to account for the noise in beam images, and then to remove it. We also wish to improve the definition of beam width used to incorporate the second moment of inertia. Simulating more impurities in these modes may also reveal more insight into what features in the residual indicate what impurities. We also wish to develop a technique that can estimate the amount of incoherent modal impurities in LG_{01} modes as well as when there is more than one modal impurity present. All of this could then be more thoroughly tested with both general HG_{01} and LG_{01} laser beams as well as by specifically creating these modes with known amounts of impurity. Finally more work could be done to apply this technique to other higher order modes such as the $LG02$ or HG_{02} mode.

7.4 Spherical Mirror Astigmatic Mode Converters

In this chapter we investigate the use of AMCs as a source of high-purity vortex modes. These, unlike other methods external to a laser, can theoretically produce pure vortex modes, provided they are properly aligned and the seed HG_{01} mode is also pure. The handedness of the resultant vortex mode is dependant on whether the input seed is aligned at $+45^o$ or -45^o to the axis of astigmatism. We first explain how vortex modes can be decomposed into a HG_{01} and HG_{10} mode with a $^{pi}/_2$ phase shift between them. Then it is shown how the Gouy phase shift can be exploited to produce this phase shift in an AMC. We then extend the theory of AMCs to include those built with off-axis spherical

mirrors rather than cylindrical lenses. This accrues additional benefits to the system such as: wavelength independence, higher transmission and more flexibility in design. We then explored two methods of generating HG_{01} modes.

The first relied on loss shaping by using an intra-cavity slit in a laser pumped via a capillary fibre. The cavity was initially set up for a LG_{01} mode that was found not to contain OAM. The slit then causes losses in the wings of this to select the HG_{01} mode. Using our analysis from chapter four, we found this produced a beam with a significant, estimated at 37% of the total power, fundamental mode impurity. When converted, this impurity carried over to the vortex mode. Handedness control was obtained by rotating the the intra-cavity slit to change the orientation of the HG_{01} beam. Whilst it would be possible to mitigate the beams impurities by introducing a wire or spot defect mirror to the laser cavity, it would not solve the key problem of there being spatially unused gain in the cavity.

We improved on this method by moving to gain shaping. By pumping the laser with two adjacent pump spots, from two identical fibre-coupled laser diodes, we could produce a much purer HG_{01} mode. This appeared to prevent a fundamental mode impurity from oscillating. This was again confirmed with our intensity distribution analysis from chapter four. This method also improved the maximum output power for a high purity HG_{01} mode. When converted this produced high purity vortex modes as measured by our spiral interference pattern analysis. Handedness control was achieved by rotating the input HG_{01} mode with a dove prism. Improvements could be made to the pump architecture by using a fibre beam splitter so that only one pump diode is needed. This may also improve the overall efficiency of the system. Further investigation should also be done to see if other higher order modes can be generated at high purity by using multiple pump spots. This would allow for the generation of other higher order LG modes via an AMC.

7.5 Amplifying First Order Hermite-Gaussian Modes

Our final chapter records our attempt to amplify a first order HG mode. We first discussed the various advantages and limitations of different amplifier geometries and conducted a brief review of the literature on how both vortex modes and HG_{01} modes have been either created or amplified in these geometries. We then discuss the mechanics behind q-switching and the relative advantages of using either passive or active methods to achieve this. We then implement a passive Q-switch into our twin pump spot HG_{01} mode laser. This produced $24ns$ pulses at $434mW$ of average power.

To amplify this beam we used a bounce geometry amplifier as its inherent cylindrical asymmetry should complement our asymmetric beam. Furthermore, the inversion of the seed through the gain profile means it sees an even gain distribution. We were successful in amplifying the power of a $400mW$ seed to $13.7W$ in a single pass configuration and to $17.0W$ in a double pass configuration. The mode quality was not maintained however. At high pump powers in the single pass configuration a spreading of the two lobes of the HG_{01} mode was observed. We have no understanding of the mechanism behind this, other than it correlated with the thermal lens in the amplifier. This effect was mitigated by reducing the size of the seed beam using a telescope which allowed us to create a $11.4W$ output mode with acceptable mode quality. This output was however astigmatic and without correction was not suitable for mode conversion. In a double pump configuration the mode quality deteriorated further, with the beam profile remaining highly astigmatic and changing upon propagation. Damage to the amplifier gain crystal was observed that occurred at an unknown time during the experiments. This may be part of the reason why the mode quality was not maintained upon amplification but we believe there is a more fundamental problem.

The amplifier could potentially be improved by carefully controlling the thermal lens of the amplifier to be cylindrically symmetric, this can be done by defocussing the pump diode and controlling the bounce angle of the seed. We feel a better method of generating high power vortex modes will be to move to a cylindrically symmetric amplifier geometry and amplify the output of an AMC. We still believe that using a combination of a high purity HG_{01} laser, AMC and solid-state amplifier is the best method for creating high power vortex modes for laser processing.

7.6 Final Comments

Vortex modes clearly have significant potential applications. A major one being how their unique feature of OAM will interact with material during machining. We sought a way to generate vortex modes at high enough power to investigate their potential for machining. The challenges in doing this eventually meant actually doing machining experiments fell outside the scope of this thesis, however we feel we have identified a clear route towards this goal. Astigmatic mode converters present clear advantages over other methods both internal and external to the laser cavity. AMCs provide robust handedness control as well as a guaranteed near pure vortex mode as opposed to another non-OAM doughnut mode, unlike most intra-cavity methods. They can also do this at reasonable efficiency and output power unlike our experiments in chapter three. Unlike the other extra-cavity methods of spiral phase plates and spatial light modulators they are also capable of producing a true

vortex mode that is unchanging upon propagation. The only remaining challenge to realising machining power vortex modes is to amplify them without compromising beam quality.

We have also clearly shown both the need for, and two methods of, assessing the beam quality of higher order modes. These techniques need more work to both expand their scope of applicability as well as their accuracy. We also demonstrated an intracavity method of selecting vortex mode handedness using a Faraday rotator within a uni-directional, single longitudinal mode ring laser. It is however, limited to this style of laser which is inherently inefficient and is unlikely to prove practical outside a laboratory.

So whilst not all the initial aims of this thesis have been reached, most notably achieving good vortex mode beam quality at high power, we do feel we have laid the ground work for a practical way of doing this moving forward, whilst also furthering a much needed discussion of what constitutes a vortex mode carrying OAM, and how to accurately identify and detect this.

References

7.7 Bibliography

[1] A.E. Siegman. *Lasers*. University Science Books, 1986.

[2] Orazio Svelto and D.C. Hanna. *Principles of Lasers*. The language of science. Springer, 1998.

[3] M. Grau, C. Lin, O. Dier, C. Lauer, and M.-C. Amann. Room-temperature operation of 3.26μm GaSb-based type-I lasers with quinternary AlGaInAsSb barriers. *Applied Physics Letters*, 87(24):241104, dec 2005.

[4] H. Morkoç, S. Strite, G. B. Gao, M. E. Lin, B. Sverdlov, and M. Burns. Large-band-gap SiC, III-V nitride, and II-VI ZnSe-based semiconductor device technologies. *Journal of Applied Physics*, 76(3):1363–1398, aug 1994.

[5] Lawrence livermore deploys world's highest peak-power laser diode arrays — lawrence livermore national laboratory.

[6] Guenter Huber, Christian Kränkel, and Klaus Petermann. Solid-state lasers: status and future [Invited]. *Journal of the Optical Society of America B*, 27(11):B93, nov 2010.

[7] Lasers and manufacturing - Science and Technology Facilities Council.

[8] Annual Laser Market Review & Forecast: Lasers enabling lasers - Laser Focus World.

[9] John R. Whinnery, Jesse H. Ausubel, and H. Dale Langford. *Lasers: Invention to Application*. The National Academies Press, Washington, DC, 1987.

[10] Kerri T Vierling, Lee A Vierling, William A Gould, Sebastian Martinuzzi, and Rick M Clawges. Lidar: shedding new light on habitat characterization and modeling. *Frontiers in Ecology and the Environment*, 6(2):90–98, mar 2008.

[11] T. H. MAIMAN. Stimulated Optical Radiation in Ruby. *Nature*, 187(4736):493–494, August 1960.

[12] C.M. Banas and R. Webb. Macro-materials processing. *Proceedings of the IEEE*, 70(6):556–565, 1982.

[13] J. Dutta Majumdar and I. Manna. Laser processing of materials. *Sadhana*, 28(3-4):495–562, June 2003.

[14] Alexandros Selimis, Vladimir Mironov, and Maria Farsari. Direct laser writing: Principles and materials for scaffold 3D printing. *Microelectronic Engineering*, 132:83–89, jan 2015.

[15] Wenpeng Wang, Baifei Shen, Xiaomei Zhang, Lingang Zhang, Yin Shi, and Zhizhan Xu. Hollow screw-like drill in plasma using an intense Laguerre-Gaussian laser. *Scientific reports*, 5:8274, January 2015.

[16] Michael D. Perry, Brent C. Stuart, Paul S. Banks, Booth R. Myers, and Joseph A. Sefcik. Laser machining of explosives, April 1998. US Patent 6150630A.

[17] Marti Duocastella and Craig B Arnold. LASER & PHOTONICS REVIEWS Bessel and annular beams for materials processing. *Laser Photonics Rev*, 6(5):607–621, 2012.

[18] Anoop N. Samant and Narendra B. Dahotre. Laser machining of structural ceramics, A review. *Journal of the European Ceramic Society*, 29(6):969–993, April 2009.

[19] C Y Yap, C K Chua, Z L Dong, Z H Liu, D Q Zhang, L E Loh, and S L Sing. Review of selective laser melting: Materials and applications. *Citation: Applied Physics Reviews*, 2:41101, 2015.

[20] Avanish Kr. Dubey and Vinod Yadava. Experimental study of Nd:YAG laser beam machining—An overview. *Journal of Materials Processing Technology*, 195(1-3):15–26, January 2008.

[21] Jian Cheng, Chang-Sheng Liu, Shuo Shang, Dun Liu, Walter Perrie, Geoff Dearden, and Ken Watkins. A review of ultrafast laser materials micromachining. *Optics and Laser Technology*, 46:88–102, 2012.

[22] Gregg D. Sucha and Heinrich Endert. Ultrafast fiber lasers: alternative light sources for industrial material processing. In Isamu Miyamoto, Koji Sugioka, and Thomas W. Sigmon, editors, *Proc. SPIE*, volume 4088, pages 201–204. International Society for Optics and Photonics, nov 2000.

[23] D. Bruneel, G. Matras, R. Le Harzic, N. Huot, K. König, and E. Audouard. Micromachining of metals with ultra-short Ti-Sapphire lasers: Prediction and optimization of the processing time. *Optics and Lasers in Engineering*, 48(3):268–271, mar 2010.

[24] Martin Kraus, Marwan Abdou Ahmed, Andreas Michalowski, Andreas Voss, Rudolf Weber, and Thomas Graf. Microdrilling in steel using ultrashort pulsed laser beams with radial and azimuthal polarization. *Optics Express*, 18(21):22305, oct 2010.

[25] Mark Ramme, Jiyeon Choi, Troy Anderson, Ilja Mingareev, and Martin Richardson. Sub-micron machining of semiconductors: femtosecond surface ripples on GaAs by 2 μm laser light. In Mary Ann Maher, Jung-Chih Chiao, and Paul J. Resnick, editors, *Proc. SPIE*, volume 7590, page 759004. International Society for Optics and Photonics, feb 2010.

[26] Ayşe S. Kabaş Sarp and Murat Gülsoy. Etching of enamel for direct bonding with a thulium fiber laser. In Peter Rechmann and Daniel Fried, editors, *Proc. SPIE*, volume 7884, page 78840K. International Society for Optics and Photonics, feb 2011.

[27] Nils Gehlich, Tobias Bonhoff, Laura Sisken, Mark Ramme, Christian Gaida, Martin Gebhardt, Ilya Mingareev, Lawrence Shah, and Martin C. Richardson. Utilizing the transparency of semiconductors via "backside" machining with a nanosecond 2 μm Tm:fiber laser. In Udo Klotzbach, Kunihiko Washio, and Craig B. Arnold, editors, *SPIE LASE*, page 89680W. International Society for Optics and Photonics, March 2014.

[28] Lin Li Juan Carlos Hernandez*, Philippus Crouse. High-power Yb-doped Fibre Laser for Cutting Dry Pine Wood. In *Proceedings of the World Congress on Engineering*, London, U.K, 2007.

[29] Shinya Ikoma, Keisuke Uchiyama, Yuya Takubo, Masahiro Kashiwagi, Kensuke Shima, and Daiichiro Tanaka. 5-kW single stage all-fiber Yb-doped single-mode fiber laser for materials processing. In Adrian L. Carter and Ingmar Hartl, editors, *Fiber Lasers XV: Technology and Systems*, volume 10512, page 11. SPIE, feb 2018.

[30] Bill Shiner. Fiber lasers for material processing. In J. Thomas Schriempf, editor, *Proc. SPIE*, volume 5706, pages 60–68. International Society for Optics and Photonics, mar 2005.

[31] Francesco Pampaloni and Joerg Enderlein. Gaussian, Hermite-Gaussian, and Laguerre-Gaussian beams: A primer. *eprint arXiv:physics/0410021*, Oct 2004.

[32] L. Allen, M. Beijersbergen, R. Spreeuw, and J. Woerdman. Orbital angular momentum of light and the transformation of Laguerre-Gaussian laser modes. *Physical Review A*, 45(11):8185–8189, June 1992.

[33] Richard A Beth. Mechanical Detection and Measurement of the Angular Momentum of Light. *Physical Review*, 50:115–125, 1936.

[34] A. T. O'Neil, I. MacVicar, L. Allen, and M. J. Padgett. Intrinsic and Extrinsic Nature of the Orbital Angular Momentum of a Light Beam. *Physical Review Letters*, 88(5):053601, January 2002.

[35] S. Franke-Arnold, L. Allen, and M. Padgett. Advances in optical angular momentum. *Laser & Photonics Review*, 2(4):299–313, August 2008.

[36] Igor A Litvin, Sandile Ngcobo, Darry Naidoo, Kamel Ait-Ameur, and Andrew Forbes. Doughnut laser beam as an incoherent superposition of two petal beams. *Optics letters*, 39(3):704–7, February 2014.

[37] Vincent L Y Loke, Theodor Asavei, Alexander B Stilgoe, Timo A Nieminen, and Halina Rubinsztein-Dunlop. Driving corrugated donut rotors with Laguerre-Gauss beams. *Optics express*, 22(16):19692–706, August 2014.

[38] Jian Wang. Advances in communications using optical vortices. *Photonics Research*, 4(5):B14, oct 2016.

[39] Miles Padgett and Richard Bowman. Tweezers with a twist. *Nature Photonics*, 5(6):343–348, jun 2011.

[40] H. He, M. E. J. Friese, N. R. Heckenberg, and H. Rubinsztein-Dunlop. Direct Observation of Transfer of Angular Momentum to Absorptive Particles from a Laser Beam with a Phase Singularity. *Physical Review Letters*, 75(5):826–829, July 1995.

[41] Mohammad Vaziri (Khamedi), Sozha Sohailya, and Alireza Bahrampour. Resonant second harmonic generation in plasma by self-focused twisted beam. *Optics Communications*, 341:295–301, April 2015.

[42] Ze-Di Cheng, Zhao-Di Liu, Xi-Wang Luo, Zheng-Wei Zhou, Jian Wang, Qiang Li, Yi-Tao Wang, Jian-Shun Tang, Jin-Shi Xu, Chuan-Feng Li, and Guang-Can Guo. Degenerate cavity supporting more than 31 Laguerre-Gaussian modes. *Optics Letters*, 2017.

[43] Yuanying Zhang, Jikang Wang, Wuhong Zhang, Shuting Chen, and Lixiang Chen. LED-based visible light communication for color image and audio transmission utilizing orbital angular momentum superposition modes. *Optics Express*, 26(13):17300, jun 2018.

[44] Shimao Li, Wen Yu, Laura Meriggi, Qingsheng Xiao, Zhichao Nong, Xinlun Cai, Marc Sorel, and Siyuan Yu. High-directional vortex beam emitter based on Archimedean spiral adiabatic waveguides. *Optics Letters*, 42(5):975, mar 2017.

[45] Wen Cheng, Joseph W Haus, and Qiwen Zhan. Propagation of vector vortex beams through a turbulent atmosphere. *Optics express*, 17(20):17829–36, sep 2009.

[46] Chien-Yuan Han, Chien-Wa Ho, Chih-Wei Kuo, and Ruey-Shyan Chang. Simple Triangular Path Interferometer for Generation of an Inhomogeneously Polarized Beam. *Japanese Journal of Applied Physics*, 48(9):092402, sep 2009.

[47] Martynas Beresna, Mindaugas Gecevičius, and Peter G. Kazansky. Polarization sensitive elements fabricated by femtosecond laser nanostructuring of glass [Invited]. *Optical Materials Express*, 1(4):783, aug 2011.

[48] Shakeel Safdar, Lin Li, M. A. Sheikh, and Zhu Liu. The Effect of Nonconventional Laser Beam Geometries on Stress Distribution and Distortions in Laser Bending of Tubes. *Journal of Manufacturing Science and Engineering*, 129(3):592, jun 2007.

[49] C.E. Protasov and A.V. Gusarov. Modeling the Effect of Beam Shaping at Selective Laser Melting. *Procedia IUTAM*, 23:147–154, jan 2017.

[50] Rudolf Weber, Andreas Michalowski, Marwan Abdou-Ahmed, Volkher Onuseit, Volker Rominger, Martin Kraus, and Thomas Graf. Effects of Radial and Tangential Polarization in Laser Material Processing. *Physics Procedia*, 12:21–30, jan 2011.

[51] G. Costa Rodrigues and J.R. Duflou. Effects of Different Polarization Strategies on Laser Cutting with Direct Diode Lasers. *Physics Procedia*, 83:302–309, jan 2016.

[52] A V Nesterov and V G Niziev. Laser beams with axially symmetric polarization. *Journal of Physics D: Applied Physics*, 33(15):1817–1822, August 2000.

[53] V G Niziev and A V Nesterov. Influence of beam polarization on laser cutting efficiency. *Journal of Physics D: Applied Physics*, 32(13):1455–1461, July 1999.

[54] Marwan Abdou Ahmed, Joachim Schulz, Andreas Voss, Olivier Parriaux, Jean-Claude Pommier, and Thomas Graf. Radially polarized 3kW beam from a CO_2 laser with an intracavity resonant grating mirror. *Optics Letters*, 32(13):1824, jul 2007.

[55] Marwan Abdou Ahmed, Andreas Voß, Moritz M. Vogel, Armin Austerschulte, Joachim Schulz, Volker Metsch, Tobias Moser, and Thomas Graf. Radially polarized high-power lasers. In *Proc. SPIE*, volume 7131, page 71311I. International Society for Optics and Photonics, oct 2008.

[56] O J Allegre, W Perrie, S P Edwardson, G Dearden, and K G Watkins. Laser microprocessing of steel with radially and azimuthally polarized femtosecond vortex pulses. *Journal of Optics*, 14(8):085601, aug 2012.

[57] Junichi Hamazaki, Ryuji Morita, Keisuke Chujo, Yusuke Kobayashi, Satoshi Tanda, and Takashige Omatsu. Optical-vortex laser ablation. *Optics Express*, 18(3):2144, feb 2010.

[58] Fuyuto Takahashi, Katsuhiko Miyamoto, Hirofumi Hidai, Keisaku Yamane, Ryuji Morita, and Takashige Omatsu. Picosecond optical vortex pulse illumination forms a monocrystalline silicon needle. *Scientific Reports*, 6(1):21738, apr 2016.

[59] M. G. Rahimian, F. Bouchard, H. Al-Khazraji, E. Karimi, P. B. Corkum, and V. R. Bhardwaj. Polarization dependent nanostructuring of silicon with femtosecond vortex pulse. *APL Photonics*, 2(8):086104, aug 2017.

[60] Takashige Omatsu, Keisuke Chujo, Katsuhiko Miyamoto, Masahito Okida, Kazuki Nakamura, Nobuyuki Aoki, and Ryuji Morita. Metal microneedle fabrication using twisted light with spin. *Optics Express*, 18(17):17967, aug 2010.

[61] Kohei Toyoda, Katsuhiko Miyamoto, Nobuyuki Aoki, Ryuji Morita, and Takashige Omatsu. Using Optical Vortex To Control the Chirality of Twisted Metal Nanostructures. *Nano Letters*, 12(7):3645–3649, jul 2012.

[62] S. Syubaev, A. Zhizhchenko, A. Kuchmizhak, A. Porfirev, E. Pustovalov, O. Vitrik, Yu. Kulchin, S. Khonina, and S. Kudryashov. Direct laser printing of chiral plasmonic nanojets by vortex beams. *Optics Express*, 25(9):10214, may 2017.

[63] Eungjang Lee, Yannick Petit, Etienne Brasselet, Thierry Cardinal, Seung-Han Park, and Lionel Canioni. Sub-diffraction-limited fluorescent patterns by tightly focusing polarized femtosecond vortex beams in a silver-containing glass. *Optics Express*, 25(9):10565, may 2017.

[64] Darryl Naidoo, Kamel Aït-Ameur, and Andrew Forbes. Intracavity vortex beam generation. In Andrew Forbes and Todd E. Lizotte, editors, *SPIE Optical Engineering + Applications*, pages 813009–813009–10. International Society for Optics and Photonics, September 2011.

[65] Jianjun Guo, Banghong Guo, Ronghua Fan, Wenjie Zhang, Yu Wang, Litao Zhang, and Panpan Zhang. Measuring topological charges of Laguerre–Gaussian vortex beams using two improved Mach–Zehnder interferometers. *Optical Engineering*, 55(3):035104, mar 2016.

[66] M.W. Beijersbergen, R.P.C. Coerwinkel, M. Kristensen, and J.P. Woerdman. Helical-wavefront laser beams produced with a spiral phaseplate. *Optics Communications*, 112(5-6):321–327, dec 1994.

[67] K. Sueda, G. Miyaji, N. Miyanaga, and M. Nakatsuka. Laguerre-Gaussian beam generated with a multilevel spiral phase plate for high intensity laser pulses. *Optics Express*, 12(15):3548, jul 2004.

[68] Steve C. Tidwell, Dennis H. Ford, and Wayne D. Kimura. Generating radially polarized beams interferometrically. *Applied Optics*, 29(15):2234, may 1990.

[69] Xudong Chen, Chengcheng Chang, and Jixiong Pu. Amplification of vortex beam in Nd:YAG power amplifiers. In *2016 Progress in Electromagnetic Research Symposium (PIERS)*, pages 989–992. IEEE, aug 2016.

[70] M.W. Beijersbergen, L. Allen, H.E.L.O. van der Veen, and J.P. Woerdman. Astigmatic laser mode converters and transfer of orbital angular momentum. *Optics Communications*, 96(1-3):123–132, February 1993.

[71] Chr. Tamm and C. O. Weiss. Bistability and optical switching of spatial patterns in a laser. *J. Opt. Soc. Am. B*, 7(6):1034–1038, Jun 1990.

[72] V Kh Bagdasarov, Sergei V Garnov, N N Denisov, A A Malyutin, Yu V Dolgopolov, A V Kopalkin, and F A Starikov. Laser system emitting 100 mJ in Laguerre—Gaussian modes. *Quantum Electronics*, 39(9):785–788, sep 2009.

[73] A A Malyutin and V A Ilyukhin. Generation of high-order Hermite–Gaussian modes in a flashlamp-pumped neodymium phosphate glass laser and their conversion to Laguerre–Gaussian modes. *Quantum Electronics*, 37(2):181–186, feb 2007.

[74] Shu-Chun Chu and Kenju Otsuka. Doughnut-like beam generation of Laguerre–Gaussian mode with extremely high mode purity. *Optics Communications*, 281(6):1647–1653, March 2008.

[75] Takayuki Ohtomo, Shu-Chun Chu, and Kenju Otsuka. Generation of vortex beams from lasers with controlled Hermite- and Ince-Gaussian modes. *Optics Express*, 16(7):5082, mar 2008.

[76] J. Courtial and M.J. Padgett. Performance of a cylindrical lens mode converter for producing Laguerre–Gaussian laser modes. *Optics Communications*, 159(1):13–18, 1999.

[77] Bereneice Sephton, Angela Dudley, and Andrew Forbes. Revealing the radial modes in vortex beams. *Applied Optics*, 55(28):7830, oct 2016.

[78] Andrew Longman and Robert Fedosejevs. Mode conversion efficiency to Laguerre-Gaussian OAM modes using spiral phase optics. *Optics Express*, 25(15):17382, jul 2017.

[79] M.A Clifford, J Arlt, J Courtial, and K Dholakia. High-order Laguerre–Gaussian laser modes for studies of cold atoms. *Optics Communications*, 156(4-6):300–306, nov 1998.

[80] Cyril Hnatovsky, Vladlen G Shvedov, Wieslaw Krolikowski, and Andrei V Rode. Materials processing with a tightly focused femtosecond laser vortex pulse. *Optics letters*, 35(20):3417–9, October 2010.

[81] M Harris, C A Hill, and P R Tapster. = 1, 2,. *Physical Review A*, 49(4), 1994.

[82] Y.F. Chen, Y.P. Lan, and S.C. Wang. Generation of Laguerre–Gaussian modes in fiber-coupled laser diode end-pumped lasers. *Applied Physics B*, 72(2):167–170, January 2001.

[83] Koki Shimohira, Yuichi Kozawa, and Shunichi Sato. Transverse mode control by manipulating gain distribution in a Yb:YAG ceramic thin disk. *Optics letters*, 36(21):4137–9, November 2011.

[84] D. J. Kim and J. W. Kim. High-power TEM00 and Laguerre–Gaussian mode generation in double resonator configuration. *Applied Physics B*, 121(3):401–405, oct 2015.

[85] J.W. Kim and W.A. Clarkson. Selective generation of Laguerre–Gaussian (LG0n) mode output in a diode-laser pumped Nd:YAG laser. *Optics Communications*, 296:109–112, June 2013.

[86] Tom Dietrich, Martin Rumpel, Thomas Graf, and Marwan Abdou Ahmed. Investigations on ring-shaped pumping distributions for the generation of beams with radial polarization in an Yb:YAG thin-disk laser. *Optics express*, 23(20):26651–9, October 2015.

[87] D. J. Kim and J. W. Kim. Direct generation of an optical vortex beam in a single-frequency Nd:YVO_4 laser. *Optics Letters*, 40(3):399, feb 2015.

[88] Qiyao Liu, Bin Zhang, Sisheng Qi, Yaocheng Li, Xuliang Fan, Yongguang Zhao, Wei Zhou, and Deyuan Shen. Integration of helicity-control and pulse-modulation for vortex laser based on a black phosphorus plate. *Optics Express*, 24(26):30031, dec 2016.

[89] Di Lin, J M O Daniel, and W A Clarkson. Controlling the handedness of directly excited Laguerre-Gaussian modes in a solid-state laser. *Optics letters*, 39(13):3903–6, July 2014.

[90] Alexander Volyar, Vladlen Shvedov, Tatyana Fadeyeva, Anton S. Desyatnikov, Dragomir N. Neshev, Wieslaw Krolikowski, and Yuri S. Kivshar. Generation of single-charge optical vortices with an uniaxial crystal. *Optics Express*, 14(9):3724, may 2006.

[91] Yuichi Tanaka, Masahito Okida, Katsuhiko Miyamoto, and Takashige Omatsu. High power picosecond vortex laser based on a large-mode-area fiber amplifier. *Optics Express*, 17(16):14362, aug 2009.

[92] Megumi Okamoto and Hiroyuki Sasada. Generation of Optical Vortices by Converting Elegant Hermite Gaussian Beams Generation of Optical Vortex Using a Spiral Phase Plate Fabricated in Quartz by Direct Laser Writing and Inductively Coupled Plasma Etching Generation of Optical Vortices by Conve. *Japanese Journal of Applied Physics Megumi Okamoto and Hiroyuki Sasada Jpn. J. Appl. Phys*, 44, 2005.

[93] Larry C. Andrews and Ronald L. Phillips. Spot size and divergence for Laguerre Gaussian beams of any order. *Applied Optics*, 22:643–644, Mar 1983.

[94] CLaser. Nd:YAG properties. Date Accessed 04/01/2019 http://www.claser-sh.com/index.php?m=content&c=index&a=show&catid=38&id=14.

[95] Norman Barnes and Brian Walsh. Quantum efficiency measurements of Nd:YAG, Yb:YAG, and Tm:YAG. *Advanced Solid State Lasers*, 68:284–287, 02 2002.

[96] RAYLEIGH. On the Magnetic Rotation of Light and the Second Law of Thermo-Dynamics. *Nature*, 64(1667):577–578, oct 1901.

[97] B.E.A. Saleh and M.C. Teich. *Fundamentals of Photonics*. Wiley Series in Pure and Applied Optics. Wiley, 2007.

[98] Dirk Jalas, Alexander Petrov, Manfred Eich, Wolfgang Freude, Shanhui Fan, Zongfu Yu, Roel Baets, Miloš Popović, Andrea Melloni, John D. Joannopoulos, Mathias Vanwolleghem, Christopher R. Doerr, and Hagen Renner. What is — and what is not — an optical isolator. *Nature Photonics*, 7(8):579–582, aug 2013.

[99] J. F. Dillon. Origin and Uses of the Faraday Rotation in Magnetic Crystals. *Journal of Applied Physics*, 39(2):922–929, feb 1968.

[100] John Ballato and Elias Snitzer. Fabrication of fibers with high rare-earth concentrations for Faraday isolator applications. *Applied Optics*, 34(30):6848, oct 1995.

[101] E. A. Ballik. The Response of Scanning Fabry-Perot Interferometers to Atomic Transition Profiles. *Applied Optics*, 5(1):170_1, jan 1966.

[102] J. M. Vaughan. *The Fabry-Perot interferometer : history, theory, practice, and applications.* A. Hilger, 1989.

[103] RP-Photonics. Encyclopedia of laser physics and technology - free spectral range resonator - cavity - axial mode spacing. https://www.rp-photonics.com/free spectral range.html. 2016-01-20.

[104] P. Hariharan. *Basics of interferometry.* Academic Press, 1992.

[105] J.M. Green, J.P. Hohimer, and F.K. Tittel. Travelling-wave operation of a tunable cw dye laser. *Optics Communications*, 7(4):349–350, apr 1973.

[106] F. R. Faxvog. Modes of a unidirectional ring laser. *Optics Letters*, 5(7):285, jul 1980.

[107] Benjamin A. Thompson, Ara Minassian, and Michael J. Damzen. Unidirectional single-frequency operation of a Nd:YVO_4 ring laser with and without a Faraday element. *Applied Optics*, 43(15):3174, may 2004.

[108] H. Abitan, H. Bohr, and C. F. Pedersen. Fiber ring laser with a feedback mirror. *Applied Optics*, 44(36):7802, dec 2005.

[109] Peter Charles Shardlow. *Enhancement of Self-Organisation and Adaptivity in Laser Systems.* PhD thesis, Imperial College London, 2010.

[110] L.D. Barron. *Molecular Light Scattering and Optical Activity.* Cambridge University Press, 2009.

[111] P A Thomas. The crystal structure and absolute optical chirality of paratellurite, $\alpha - TeO_2$. *Journal of Physics C: Solid State Physics*, 21(25):4611–4627, sep 1988.

[112] Y.F. Chen, T.M. Huang, C.F. Kao, C.L. Wang, and S.C. Wang. Generation of Hermite-Gaussian modes in fiber-coupled laser-diode end-pumped lasers. *IEEE Journal of Quantum Electronics*, 33(6):1025–1031, jun 1997.

[113] Masashi Abe, Hiroki Seki, Maya Kowa, Yuta Sasaki, Katsuhiko Miyamoto, and Takashige Omatsu. High average power, diffraction-limited picosecond output from a sapphire face-cooled Nd:YVO_4 slab amplifier. *Journal of the Optical Society of America B*, 32(4):714, apr 2015.

[114] Anthony E. Siegman. New developments in laser resonators. volume 1224, page 2. International Society for Optics and Photonics, jun 1990.

[115] Simon Peter Chard. *Development of versatile high power bounce geometry lasers.* PhD thesis, Imperial College London, 2011.

[116] J. W. Kim, J. I. Mackenzie, J. R. Hayes, and W. A. Clarkson. High power Er:YAG laser with radially-polarized Laguerre-Gaussian (LG_01) mode output. *Optics Express*, 19(15):14526, jul 2011.

[117] Di Lin, J. M. O. Daniel, M. Gecevičius, M. Beresna, P. G. Kazansky, and W. A. Clarkson. Cladding-pumped ytterbium-doped fiber laser with radially polarized output. *Optics Letters*, 39(18):5359, September 2014.

[118] Igor A. Litvin, Angela Dudley, Filippus S. Roux, and Andrew Forbes. Azimuthal decomposition with digital holograms. *Optics Express*, 20(10):10996, may 2012.

[119] Sandile Ngcobo, Kamel Aït-Ameur, Nicolas Passilly, Abdelkrim Hasnaoui, and Andrew Forbes. Exciting higher-order radial Laguerre-Gaussian modes in a diode-pumped solid-state laser resonator. *Applied optics*, 52(10):2093–101, April 2013.

[120] Hend Sroor, Nyameko Lisa, Darryl Naidoo, Igor Litvin, and Andrew Forbes. Purity of Vector Vortex Beams through a Birefringent Amplifier. *Physical Review Applied*, 9(4):044010, apr 2018.

[121] Robert D. Niederriter, Mark E. Siemens, and Juliet T. Gopinath. Continuously tunable orbital angular momentum generation using a polarization-maintaining fiber. *Optics Letters*, 41(14):3213, jul 2016.

[122] V.V.G. Krishna Inavalli and Nirmal K. Viswanathan. Switchable vector vortex beam generation using an optical fiber. *Optics Communications*, 283(6):861–864, mar 2010.

[123] G. Ruffato, M. Massari, and F. Romanato. Generation of high-order Laguerre–Gaussian modes by means of spiral phase plates. *Optics Letters*, 39(17):5094, sep 2014.

[124] Barry Burke, Paul Jorden, and Paul Vu. CCD Technology. *Experimental Astronomy*, 19(1-3):69–102, jul 2006.

[125] E H Linfoot and E Wolf. Phase Distribution near Focus in an Aberration-free Diffraction Image. *Proceedings of the Physical Society. Section B*, 69(8):823–832, aug 1956.

[126] Robert W. Boyd. Intuitive explanation of the phase anomaly of focused light beams. *Journal of the Optical Society of America*, 70(7):877, jul 1980.

[127] E. Abramochkin and V. Volostnikov. Beam transformations and nontransformed beams. *Optics Communications*, 83(1-2):123–135, May 1991.

[128] Kenju Otsuka and Shu-Chun Chu. Microchip solid-state cylindrical vector lasers with orthogonally polarized dual laser-diode end pumping. *Optics Letters*, 38(9):1434, may 2013.

[129] Detlev Ristau, Marco Jupé, and Kai Starke. Laser damage thresholds of optical coatings. *Thin Solid Films*, 518(5):1607–1613, dec 2009.

[130] Cheng Xu, Peng Yi, Heliang Fan, Jianwei Qi, Shuai Yang, Yinghuai Qiang, Jiongtian Liu, and Dawei Li. Preparation of high laser-induced damage threshold Ta2O5 films. *Applied Surface Science*, 309:194–199, aug 2014.

[131] Walter Koechner. *Solid-state laser engineering*. Springer, 1999.

[132] Sakae Kawato and Takao Kobayashi. Design of End-Pumped Thin Rod Yb:YAG Laser Amplifiers. *Japanese Journal of Applied Physics*, 42(Part 1, No. 5A):2705–2710, may 2003.

[133] A. Giesen, H. Hügel, A. Voss, K. Wittig, U. Brauch, and H. Opower. Scalable concept for diode-pumped high-power solid-state lasers. *Applied Physics B*, 58(5):365–372, may 1994.

[134] C. Stewen, K. Contag, M. Larionov, A. Giesen, and H. Hugel. A 1-kW CW thin disc laser. *IEEE Journal of Selected Topics in Quantum Electronics*, 6(4):650–657, jul 2000.

[135] Y. B. Tian, Z. H. Tian, H. M. Tan, and X. Y. Liu. Laser diode array pumped Yb:YAG/BIBO 515 nm thin disc laser with four-pass optical coupling system. *Laser Physics*, 20(4):793–798, apr 2010.

[136] Charles J. Koester and Elias Snitzer. Amplification in a Fiber Laser. *Applied Optics*, 3(10):1182, oct 1964.

[137] Cesar Jauregui, Jens Limpert, and Andreas Tünnermann. High-power fibre lasers. *Nature Photonics*, 7(11):861–867, nov 2013.

[138] D. Gloge. Weakly Guiding Fibers. *Applied Optics*, 10(10):2252, oct 1971.

[139] S. Kawakami and S. Nishida. Characteristics of a doubly clad optical fiber with a low-index inner cladding. *IEEE Journal of Quantum Electronics*, 10(12):879–887, dec 1974.

[140] R. Y. Chiao, C. H. Townes, and B. P. Stoicheff. Stimulated Brillouin Scattering and Coherent Generation of Intense Hypersonic Waves. *Physical Review Letters*, 12(21):592–595, may 1964.

[141] D. Cotter. Observation of stimulated Brillouin scattering in low-loss silica fibre at 1.3 μm. *Electronics Letters*, 18(12):495, 1982.

[142] Andrey Kobyakov, Michael Sauer, and Dipak Chowdhury. Stimulated Brillouin scattering in optical fibers. *Advances in Optics and Photonics*, 2(1):1, mar 2010.

[143] N. Bloembergen. The Stimulated Raman Effect. *American Journal of Physics*, 35(11):989–1023, nov 1967.

[144] Yasuhiro Mashiko, Huy Khanh Nguyen, Masahiro Kashiwagi, Tomoharu Kitabayashi, and Kensuke Shima. 2 kW single-mode fiber laser. Technical report, Fujikura, 2016.

[145] Yoonchan Jeong, Alexander J Boyland, Jayanta K Sahu, Seunghwan Chung, Johan Nilsson, and David N Payne. Multi-kilowatt Single-mode Ytterbium-doped Large-core Fiber Laser. *Journal of the Optical Society of Korea*, 13(4):416–422, 2009.

[146] Shijie Fu, Wei Shi, Yan Feng, Lei Zhang, Zhongmin Yang, Shanhui Xu, Xiushan Zhu, R. A. Norwood, and N. Peyghambarian. Review of recent progress on single-frequency fiber lasers. *Journal of the Optical Society of America B*, 34(3):A49, mar 2017.

[147] Craig Robin, Iyad Dajani, and Benjamin Pulford. Modal instability suppressing, single frequency photonic crystal fiber amplifier with 811W output power. *Optics Letters*, 39(3):666, feb 2014.

[148] Daniel Creeden, Herman Pretorius, Julia Limongelli, and Scott D. Setzler. Single frequency 1560nm Er:Yb fiber amplifier with 207W output power and 50.5% slope efficiency. In John Ballato, editor, *Proc. SPIE*, volume 9728, page 97282L. International Society for Optics and Photonics, mar 2016.

[149] Gregory D. Goodno, Lewis D. Book, and Joshua E. Rothenberg. Low-phase-noise, single-frequency, single-mode 608 W thulium fiber amplifier. *Optics Letters*, 34(8):1204, apr 2009.

[150] J.M. Eggleston, L.M. Frantz, and H. Injeyan. Deviation of the Frantz-Nodvik equation for zig-zag optical path, slab geometry laser amplifiers. *IEEE Journal of Quantum Electronics*, 25(8):1855–1862, 1989.

[151] A. K. Sridharan, S. Saraf, and R. L. Byer. Yb:YAG master oscillator power amplifier for remote wind sensing. *Applied Optics*, 46(30):7552, oct 2007.

[152] Xiuhua Ma, Jinzi Bi, Xia Hou, and Weibiao Chen. High efficiency diode-pumped slab oscillator and amplifier for space-based application. *Optics & Laser Technology*, 43(3):559–562, apr 2011.

[153] Marwan Abdou Ahmed, Matthias Haefner, Moritz Vogel, Christof Pruss, Andreas Voss, Wolfgang Osten, and Thomas Graf. High-power radially polarized Yb:YAG thin-disk laser with high efficiency. *Optics Express*, 19(6):5093, mar 2011.

[154] Mio Koyama, Tetsuya Hirose, Masahito Okida, Katsuhiko Miyamoto, and Takashige Omatsu. Power scaling of a picosecond vortex laser based on a stressed Yb-doped fiber amplifier. *Optics Express*, 19(2):994, jan 2011.

[155] Biao Sun, Anting Wang, Lixin Xu, Chun Gu, Yong Zhou, Zhongxi Lin, Hai Ming, and Qiwen Zhan. Transverse mode switchable fiber laser through wavelength tuning. *Optics Letters*, 38(5):667, mar 2013.

[156] Di Lin and W. A. Clarkson. Polarization-dependent transverse mode selection in an Yb-doped fiber laser. *Optics Letters*, 40(4):498, feb 2015.

[157] Xiangqing Jin, Fufei Pang, Yu Zhang, Sujuan Huang, Yingchun Li, Jianxiang Wen, Zhenyi Chen, Min Wang, and Tingyun Wang. Generation of the First-Order OAM Modes in Single-Ring Fibers by Offset Splicing Technology. *IEEE Photonics Technology Letters*, 28(14):1581–1584, jul 2016.

[158] C. R. Smith, S. J. Beecher, J. I. Mackenzie, and W. A. Clarkson. Amplification of a radially polarised beam in an Yb:YAG thin-slab. *Applied Physics B*, 123(8):225, aug 2017.

[159] Inon Moshe, Steven Jackel, and Avi Meir. Production of radially or azimuthally polarized beams in solid-state lasers and the elimination of thermally induced birefringence effects. *Optics Letters*, 28(10):807, may 2003.

[160] Akihiko Ito, Yuichi Kozawa, and Shunichi Sato. Selective oscillation of radially and azimuthally polarized laser beam induced by thermal birefringence and lensing. *Journal of the Optical Society of America B*, 26(4):708, apr 2009.

[161] J. E. Bernard and A. J. Alcock. High-efficiency diode-pumped Nd:YVO_4 slab laser. *Optics Letters*, 18(12):968, jun 1993.

[162] A. Minassian and M.J. Damzen. 20 W bounce geometry diode-pumped Nd:YVO4 laser system at 1342 nm. *Optics Communications*, 230(1-3):191–195, jan 2004.

[163] G. Smith, P. C. Shardlow, and M. J. Damzen. High-power near-diffraction-limited solid-state amplified spontaneous emission laser devices. *Optics Letters*, 32(13):1911, jul 2007.

[164] Chunhua Wang, Lifeng Shen, Zhiliang Zhao, Bin Liu, Hongbo Jiang, Jun Chen, and Chong Liu. 1.2 MW peak power, all-solid-state picosecond laser with a microchip

laser seed and a high gain single-passing bounce geometry amplifier. *Optics & Laser Technology*, 85:14–18, nov 2016.

[165] D. Sauder, A. Minassian, and M. Damzen. High efficiency laser operation of 2 at.% doped crystalline Nd:YAG in a bounce geometry. *Optics Express*, 14(3):1079, feb 2006.

[166] Y. Lawrence Yao, Hongqiang Chen, and Wenwu Zhang. Time scale effects in laser material removal: a review. *The International Journal of Advanced Manufacturing Technology*, 26(5-6):598–608, sep 2005.

[167] Mark A Latina, Santiago A Sibayan, Dong H Shin, Robert J Noecker, and George Marcellino. Q-switched 532-nm Nd:YAG laser trabeculoplasty (selective laser trabeculoplasty): A multicenter, pilot, clinical study. *Ophthalmology*, 105(11):2082–2090, nov 1998.

[168] Suzanne L. Kilmer, Margaret S. Lee, Joannes M. Grevelink, Thomas J. Flotte, and R. Rox Anderson. The Q-Switched Nd:YAG Laser Effectively Treats Tattoos. *Archives of Dermatology*, 129(8):971, aug 1993.

[169] John M. Dudley, Goëry Genty, and Stéphane Coen. Supercontinuum generation in photonic crystal fiber. *Reviews of Modern Physics*, 78(4):1135–1184, oct 2006.

[170] Xiaoyang Guo, Koichi Hamamoto, Shigeki Tokita, and Junji Kawanaka. 160ps Yb:YAG/Cr:YAG microchip laser. *Laser Physics Letters*, 15(10):105001, oct 2018.

[171] Russell Targ, Michael J. Kavaya, R. Milton Huffaker, and Roland L. Bowles. Coherent lidar airborne windshear sensor: performance evaluation. *Applied Optics*, 30(15):2013, may 1991.

[172] Brian M. Walsh, John M. McMahon, William C. Edwards, Norman P. Barnes, Randy W. Equall, and Ralph L. Hutcheson. Spectroscopic characterization of Nd:Y_2O_3: application toward a differential absorption lidar system for remote sensing of ozone. *Journal of the Optical Society of America B*, 19(12):2893, dec 2002.

[173] J.D. Park, C.H. Cho, C.H. Lim, K.H. Ko, D.H. Kim, H. Cha, and Y. I. Kang. Additional Laser Pulses due to Different Saturation Characteristics of Gain and Absorption in Passively Q-switched Lasers. In *2007 Conference on Lasers and Electro-Optics - Pacific Rim*, pages 1–2. IEEE, aug 2007.

[174] Antonio Lucianetti, Rudolf Weber, Walter Hodel, Heinz Peter Weber, Alexander Papashvili, Vladimir A. Konyushkin, and Tasoltan T. Basiev. Beam-quality im-

provement of a passively Q-switched Nd:YAG laser with a core-doped rod. *Applied Optics*, 38(9):1777, mar 1999.